Structure and Stability of Ultrathin Polymer and Nanocomposite Films at the Air-Water Interface

Struktur und Stabilität von ultradünnen Polymer und Nanokomposit Filmen an der Wasser-Luft Grenzfläche

Zur Erlangung des Grades eines Doktors der Naturwissenschaften (Dr. rer. nat.)
genehmigte Dissertation von Christian Appel aus Seligenstadt
Tag der Einreichung: 26.09.2018, Tag der Prüfung: 12.11.2018
Darmstadt 2018 — D 17

1. Gutachten: Prof. Dr. B. Stühn
2. Gutachten: Prof. Dr. R. Feile

TECHNISCHE
UNIVERSITÄT
DARMSTADT

Fachbereich Physik
Exp. Physik kondensierter Materie

Structure and Stability of Ultrathin Polymer and Nanocomposite Films at the Air-Water Interface
Struktur und Stabilität von ultradünnen Polymer und Nanokomposit Filmen an der Wasser-Luft Grenzfläche

Genehmigte Dissertation von Christian Appel aus Seligenstadt

1. Gutachten: Prof. Dr. B. Stühn
2. Gutachten: Prof. Dr. R. Feile

Tag der Einreichung: 26.09.2018
Tag der Prüfung: 12.11.2018

Darmstadt 2018 — D 17

Structure and Stability of Ultrathin Polymer and Nanocomposite Films at the Air-Water Interface

The main part of this work focuses on the structural investigations at the air-water interface using two different approaches. The first one is an indirect approach that aims for a structural characterization at the interface using thermodynamic quantities such as surface coverage, surface pressure and isothermal compressibility using the Langmuir-Blodgett technique. In the second approach the structural characterization is performed using local visualizing techniques like Brewster-Angle-Microscopy or X-ray surface scattering techniques. The systems studied for this purpose are all confined into a quasi-2D conformation including ultrathin polymer films, single nanoparticle films and polymer nanocomposites at the air-water interface.

The indirect approach mainly focuses on the investigation of quasi-2D polymer films at the air-water interface. From the in water insoluble polymer's point of view, the air-water interface represents a solvent that can provide either good or θ solvent conditions. The interface can be characterized using 2D scaling laws from polymer physics. In one of the systems a remarkable effect is found. The solvent properties at the air-water interface can be tuned from θ to good conditions in amphiphilic block copolymers by increasing the volume fraction of the hydrophilic block. This result was quite astonishing since the volume fractions of the hydrophilic block were less than 5 %. The same system exhibits a unique phase transition that can be linked to the hydrophobic part in the block copolymers. X-ray surface scattering reveals that upon compression to a critical surface pressure, the hydrophobic part in the blocks is able to dewet from the air-water interface. Lateral structures of several micrometer are formed within the film which can be observed by optical and scattering techniques. However, the existence of the hydrophilic block is crucial for their observation because their lateral size seems to depend on the mobility of the chains at the interface.

The *in-situ* structural development of single nanoparticle films was observed for different particle sizes. It was possible to directly observe a structural transition that is also apparent in the indirect measurement of the thermodynamic quantities of the particle film. Finally, nanoparticles were successfully introduced in a polymer matrix at the air-water interface. Depending on the nanoparticle size, they seem to be evenly distributed or forced out of the polymer film upon increasing the area fraction of the particles.

Struktur und Stabilität von ultradünnen Polymer und Nanokomposit Filmen an der Wasser-Luft Grenzfläche

Der Schwerpunkt dieser Arbeit liegt auf strukturellen Untersuchungen der Wasser-Luft Grenzfläche. Dabei werden zwei unterschiedliche Ansätze verfolgt. Bei dem ersten Ansatz handelt es sich um eine indirekte Charakterisierung der Struktur an der Grenzfläche anhand thermodynamischer Messgrößen. Mit Hilfe der Langmuir-Blodgett Technik werden Flächenabdeckung, Oberflächendruck und die isotherme Kompressibilität bestimmt. Im zweiten Ansatz wird die Struktur der Grenzfläche durch lokale optische Methoden, wie Brewster-Winkel-Mikroskopie, und durch Streuexperimente, wie Röntgenreflektometrie, aufgelöst. Ultradünne Polymerfilme, Filme einzelner Nanopartikel und Polymer-Nanokomposit-Filme werden an der Wasser-Luft Grenzfläche präpariert und damit in eine quasi-2D Konformation gezwungen.

Bei der indirekten Charakterisierung liegt der Fokus auf den quasi-2D Polymerfilmen an der Wasser-Luft Grenzfläche. Für die in Wasser unlöslichen Polymere stellt die Wasser-Luft Grenzfläche ein Lösemittel dar, welches entweder gute oder θ Lösemitteleigenschaften aufweisen kann. Die Grenzfläche kann nun mit Hilfe von Skalengesetzen der Polymerphysik in zwei Dimensionen charakterisiert werden. Dabei zeigt sich in einem der Systeme ein sehr interessanter Effekt. Die Lösemitteleigenschaften der Grenzfläche können von θ zu guten Lösemitteleigenschaften durch das Blockverhältniss eines amphiphilen Blockcopolymers verändert werden. Des Weiteren ist es erstaunlich, dass dies für Volumenanteile von weniger als 5 % bereits deutlich nachweisbar war. Im selben System kommt es auch zu einem außergewöhnlich stark ausgeprägten Phasenübergang, welcher in Zusammenhang mit dem hydrophoben Block gebracht werden kann. Der hydrophobe Block entnetzt die Wasser-Luft Grenzfläche, sobald der Oberflächendruck einen kritischen Wert erreicht. Dieser Prozess hat zur Folge, dass sich laterale Strukturen mit einer Ausdehnung von einigen Mikrometern bilden. Brewster-Winkel-Mikroskopie und Röntgenreflektometrie konnten beide diese Strukturen nachweisen. Dennoch spielt der hydrophile Block eine entscheidene Rolle, da die Größe der Strukturen durch die Mobilität der Ketten bestimmt wird und ohne diesen nicht detektiert werden kann.

Verschieden große Nanopartikel wurden erfolgreich in Monolagen präpariert und ihre strukturelle Entwicklung wurde *in-situ* mit Röntgenreflektometrie aufgelöst. Eine Änderung der Konformation im Nanopartikelfilm konnte unmittelbar beobachtet werden, die sich ebenfalls im Oberflächendruck und der Kompressibilität identifizieren lässt. Abschließend konnten die Nanopartikel und Polymere in einem Komposit-Film an der Wasser-Luft Grenzfläche präpariert werden. Je nach Größe der Partikel verteilten sich diese gleichmäßig in der polymer matrix oder wurden mit steigendem Flächenanteil aus dem Film gezwungen.

Contents

1 Introduction

The interface between air and water has peaked the interest of scientists already in the 19th century since Agnes Pockels invented a device to measure the surface tension of hydrophobic or amphiphilic molecules at the water surface[1]. Pockels invention has been improved later on by Irving Langmuir and Katharine Blodgett to transfer layers of molecules on solid substrates[2]. From this point on, assembled layers of molecules at the interface were called *Langmuir films*. A variety of systems from simple carboxylic acids, biological peptides or complex polymers to liquid crystals and nanoparticles have been intensely studied ever since. The experiments gave insights in intermolecular interactions at hydrophobic/hydrophilic interfaces[3], orientation of surfactant molecules[4], emulsions and colloid and interface science[5,6]. Part of this work is related to the conformation of a polymer chain that is confined to the water surface. The air-water interface itself acts as a solvent for the water insoluble polymer chains resulting in a swollen or collapsed conformation of the chain. The chain conformation can be explained using the scaling theory for polymer solutions. It can be expressed by power laws of molecular weight, concentration and solvent properties of the interface[7]. These concepts help to understand the constitution of the film in terms of thermodynamic quantities, however the exact molecular structure can not be revealed.

In recent years, the advancement of experimental techniques to characterise interfaces with atomic resolution has once again led to an increasing interest in the assembly of a broad range of systems at the interface. To precisely know and control the structure and morphology of monomolecular (ultrathin) films is also very important for modern nanotechnology. Most of the time the arrangement of the molecules perpendicular to the interface can be well controlled due to their amphiphilic nature. However, understanding the key factors in the formation of lateral structures in more complex ultrathin films is an even more important challenge. Microphase separation and crystallisation have been observed by neutron reflectivity experiments and Brewster-Angle Microscopy for block copolymers with PEG as a block partner[8–10]. Morphology control of polymer films transferred on solid substrates by Langmuir-Blodgett film deposition has been investigated using Transmission-Electron-Microscopy and Atomic-Force-Microscopy[11–13]. However, these techniques can only be used on solid substrates and yield to local information over scales of several hundreds of nanometers. X-Ray and neutron surface scattering averages over a much larger length scale and can be implemented directly on the water surface. Als-Nielsen et al. give an extensive review on diffraction from organic molecules at the air-water surface[14]. In this work, the morphology of a thin polymer film was investigated using a X-Ray reflectometer for laboratory use. The technique is used to investigate the structural changes parallel and perpendicular to the interface during a phase transition in the polymer film.

Another interesting topic is the assembly of nanoparticles at the air-water interface. Monolayers of magnetic nanoparticles are of significant technical importance as catalysts, sensors or high capacity bit-patterned information storage carriers. Being able to con-

trol the assembly of single particle films at the interface is the first step to manufacture future nanoelectronic devices [15,16]. Furthermore, nanoparticle-based structures often reveal new physical phenomena that are interesting for fundamental science because they have no analogies in bulk materials. Iron oxide nanoparticles have been successfully prepared in highly ordered monolayers at the air-water interface and also transferred on solid substrates [17]. The iron oxide nanoparticles need to be stabilised by a shell to avoid agglomeration of the particles. The shell also controls the spacing between particles in a close packed monolayer [17,18]. To obtain nanoparticles in an arrangement with spacings on larger length scale, they can be introduced into a polymer matrix to form a polymer nanocomposite film [6]. However, it is challenging to understand the influence of polymer size, particle size and interactions on the morphology [19]. This thesis gives insights on Langmuir monolayers of highly ordered iron oxide nanoparticles. Two different particles sizes are introduced into a polymer matrix and their influence on the behaviour and structure of the film is investigated.

Outline of this Thesis

This thesis consists of two main parts: Theoretical concepts and experimental methods on the one hand and experimental results on the other. In chapter 2 and 3, theoretical concepts to investigate soft matter at the air-water interface are introduced. Chapter 2 focusses on the thermodynamics of the systems while the concepts for surface scattering are presented in chapter 3. In chapter 4 introduces experimental methods, data processing and sample preparation used in this work. The second part starts in chapter 5 with the study of the solvent properties of the air-water interface for three different polymer systems. One of the systems shows a remarkable phase transition that is characterised in chapter 6. The influence of the hydrodynamics between subphase and film is studied for a range of molecular weights in the system. Chapter 7 deals with the assembly of iron oxide nanoparticles into monolayers at the air-water interface. Two particle sizes are introduced into a polymer matrix to investigate their ability to form polymer nanocomposite films.

2 Theoretical Concepts I: Soft Matter at the Aqueous Interface

A lot of interesting phenomena can be observed at the aqueous (air-water) interface. Soft matter molecules arrange themselves at the interface and self-assemble into monolayers. Whether they have this ability or not can often be related to their amphiphilic character. In the human body a lot of different examples show how soft matter is able to self-assemble at interfaces (e.g. lipids). But soft matter is not only limited to the human body, certain polymers are also able to form monolayers due to their amphiphilic nature. The air-water interface provides ideal properties to simulate the behaviour of soft matter molecules at interfaces. Another important group are nanoparticles which can also arrange themselves at the aqueous interface under certain conditions, even though they do not necessary have an amphiphilic character.

This chapter gives an introduction into concepts that are important to understand the behaviour of soft matter at the aqueous interface. After briefly characterising amphiphilic molecules the focus of the chapter shifts towards polymers and basic models to describe their configuration. The theory of Langmuir isotherms at the air-water interface will be introduced for amphiphilics and polymers. The surface pressure scaling for polymers will be explained by polymer scaling laws in two dimensions before the chapter finishes with a short summary on why nanoparticles are able to form stable monolayers at the air-water interface.

2.1 Amphiphilic Molecules

The word amphiphil stems from the greek language and it literally means "both-loving". This basically describes their composition because they are a combination of a polar and a non-polar group in one molecule. Water and oil are in general immiscible, however they can be emulsified by adding amphiphilic molecules to the solution. Part of the molecule is soluble in water while the other part is soluble in oil. As surfactants, amphiphilic molecules self-assemble at the interface in order to reduce the surface tension. This leads to the formation of surfactant films or more complex morphologies (for example microemulsion [20]). To understand how surfactants are able to accomplish this it is important to understand why water and oil do not mix.

The free energy for the mixing of two species can be written as the sum of two terms. Its gain in configurational entropy in the mixed state and a second term for the energy of mixing. The next neighbor interaction in liquid water is dominated by a network of hydrogen bonds ($\sim 25-100\,k_\mathrm{B}T$). When a foreign molecule which cannot form hydrogen bonds is introduced in this network, the water molecules around the foreign molecule rearrange into a network maximizing the number of hydrogen bonds, thus, forming a cage around it. Since the water molecules adopt a more ordered state locally in order to satisfy their hydrogen bond requirements it leads to a decrease in entropy. This effect is

called the hydrophobic interaction and it leads to a phase separation between for example oil and water. Amphiphilic molecules can act as a surfactant between both species leading to a process of mixing on a microscopic length scale [21]. Lipids are a classic example for amphiphilic molecules but there are also certain polymers that fulfill these conditions.

2.1.1 Polymers

Synthetic and natural polymers, also known as macromolecules, are necessary components in our regular life every day. They are built up of a large number of identical repeat units (*monomer unit*) that are linked together by covalent bonds, thus forming a long chain. Polymers can help to understand the structure in many materials of biological origin including proteins and nucleic acids such as DNA due to their similarity in molecular architecture. Furthermore, natural and synthetic polymers are important to form complex composite materials such as glass-reinforced plastics, wood and tissue. Most polymers are based on a carbon chain, however, a variety of possible structures still emerges. Each structure can lead to different properties based on the chemical constitution of the monomer unit. The most simplest polymer is polyethylene $(C_2H_4)_n$, while a more complex structure can be easily obtained by changing the side groups, for example poly(methyl methacrylate) $(C_5H_8O_2)$.

When the polymer has different types of chemical groups attached to one of the main carbon atoms, different spatial orientations of the groups are possible. Two regular arrangements of the side groups are called isotactic and syndiotactic. In isotactic polymers the similar side groups appear on the same side of the chain or on alternating sides for syndiotactic polymers. If the side groups are randomly arranged the polymer is called atactic. It is interesting to note that atactic arrangement in polymers involves a quenched disorder which makes it usually impossible to crystallise, thus, they form glasses at low temperatures [21]. It is also not possible to find polymers in the gaseous state. Polymer solutions and melts are liquids which are often very viscous. Most of the polymers prefer a glassy instead of a crystalline state with polystyrene or poly(methyl methacrylate) as common examples. However, some polymers can crystallise but crystallisation is usually not complete. They form semi-crystalline structures where small crystals exist in a matrix of amorphous material in a glassy or liquid state, such as polyethylene or in some natural materials.

Block Copolymers

So far only homopolymers have been discussed which are formed by a single type of monomer unit. Chemically combining two different monomer units in one chain leads to a new species called copolymers. Due to the arrangement of the different monomer units, the properties of the copolymer can vary greatly. Randomly arranging monomer units leads to a group of polymers with a quenched disorder called random copolymers, which usually do not crystallise due to the same arguments as for atactic polymers. However, if the monomer units are arranged in blocks the properties of the material can dramatically change. These block copolymers have a tendency to microphase separate. Since both blocks are covalently bonded they can microphase separate in a variety of morphologies. The microphase separated structures can be formed on a length scale of few to several hundreds of nanometers [22]. Controlling the length scale depends on many dif-

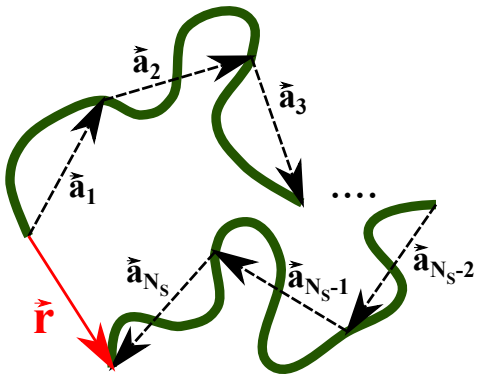

Figure 2.1: Low resolution sketch of a polymer chain splitted in N_S freely jointed segments. The segments connect the junction points from 0 to N_S. $\vec{r}$ is the end-to-end distance vector.

ferent parameters (e.g. molecular weight, monomer structure, temperature). As already mentioned the self-assembly of the block copolymers leads to a variety of morphologies that mainly depend on the volume fractions of the participating monomer units.

Statistical Description of Polymer Coils

Polymers in solution or the melt occupy different energy states which are populated according to the laws of Boltzmann statistics. Most of the conformations of polymers in the fluid state represent random coils. For a lowered resolution corresponding to length scales of some nanometers, the dependence on the microscopic chemical structure (e.g. bond angles, rotational potentials, presence and length of sidegroups, etc.) vanishes. Polymer chains exhibit a common behaviour and they become equivalent to each other. The chain can be splitted in N_S subchains of uniform length and the chain can be associate with a sequence of vectors

$$(\vec{a}_1, \vec{a}_2, ..., \vec{a}_{N_S}), \tag{2.1}$$

connecting the junction points of the chain. The interesting quantities can now be discussed statistically using the distribution function for the vectors connecting any two junction points. Particular interesting is the end-to-end distance vector $\vec{r}$. As long as the subchains are large compared to the persistence length l_{ps}, which is a parameter that measure the stiffness of the chain, the successive steps $\vec{a}_i$ show no orientational correlations. This freely jointed segment chain can formally be described equivalently to the motion of a Brownian particle suspended in a liquid. The segments of the chain perform a motion of perfectly uncorrelated steps and their distribution function is [23]

$$p(\vec{r}) = \left(\frac{3}{2\pi\langle\vec{r}^2\rangle}\right)^{3/2} \exp\left(-\frac{3\vec{r}^2}{2\langle\vec{r}^2\rangle}\right). \tag{2.2}$$

The end-to-end distance vector $\vec{r}$ can also be calculated directly for the freely jointed segment model to

$$\langle\vec{r}^2\rangle = N_S\langle|a_l|^2\rangle. \tag{2.3}$$

When $a_S = \langle|a_l|^2\rangle^{1/2}$ is used as the mean segment length and if the persistence length of the polymer is small, then N_S and a_S are equivalent to the degree of polymerization N and the monomer size a leading to

$$\langle\vec{r}^2\rangle = Na^2. \tag{2.4}$$

It is known from basic chemistry that an assumption of the freely jointed chain model is rather unphysical. In a polymer chain successive links are not free to rotate but constraint to certain definite bond angles. Surprisingly the fundamental results do not change and the size of the chain is given by $\langle \vec{r}^2 \rangle = N b^2$ with an effective monomer size b [21]. Usually this effective monomer size is given by a characteristic ratio $C_\infty = b^2/a^2$ which is for example $C_\infty = 6.9$ for poly(methyl methacrylate).

So far it has been completely neglected that comparing the conformation of a single polymer chain in solution with the Brownian motion is only allowed if the volume of the monomers can be disregarded. However, this is not correct and a chain with non-vanishing monomer size cannot occupy a given location in a random walk twice. The already occupied space will be taken into account by the excluded volume v which obviously results in a chain expansion (*excluded volume effect*). Mathematically solving this problem is much more complicated and instead of the results for a random walk it leads to

$$\langle \vec{r}^2 \rangle = k^2 N^{2\nu} \tag{2.5}$$

with the Flory-exponent ν and k as a mean segment length (Kuhn length). This radius is also referred to as the Flory-radius $R_F = \langle \vec{r}^2 \rangle^{1/2}$. In order to understand the effect of the excluded volume, the combined contribution of the excluded volume effect and solvent interaction energies, characterized by the interaction parameter χ, has to be calculated: [21]

$$F = k_B T v (1 - 2\chi) \frac{N^2}{2\vec{r}^3} \tag{2.6}$$

There are three possible cases that need to be discussed.

- The good solvent case with $\chi > 1/2$: The polymer chain is swollen and $\nu = 3/5$ for three dimensions.
- The θ-solvent case with $\chi = 1/2$: The repulsive effect of the excluded volume is cancelled out by the polymer/solvent interaction. The polymer chain is an ideal random walk with $\nu = 1/2$. The same situation occurs in a polymer melt.
- The bad solvent case with $\chi < 1/2$: The polymer/solvent interaction outweighs the repulsive excluded volume interaction and the polymer collapses. In this case the Flory-exponent is $\nu = 1/3$ in three dimensions.

2.2 The Air-Water Interface: Langmuir Monolayer

Molecular interactions in the bulk and at the interface are different. In a bulk liquid, each molecule exhibits a force by its surrounding molecules. The net force on the molecule averages to zero over time scales larger than the relaxation time of the molecular neighborhood. However, at the surface the net force does not vanish. In order to increase the surface area, work has to be performed to transfer molecules to the surface. The necessary work dW to increase the surface area by a small quantity dA is $dW = \gamma dA$. The coefficient γ is the surface tension which has the dimension force per length. In the thermodynamic

description of interfaces, the surface tension can be defined using the derivative of the *Gibbs free energy* G per surface area [24]

$$\gamma = \left(\frac{\partial G}{\partial A}\right)_{T,p} \tag{2.7}$$

at constant temperature T and pressure p. The surface tension is an analogy to the 3D vapor pressure.

Molecular films on a liquid surface are called Langmuir monolayers and have been studied for more than 100 years. Amphiphilic molecules are an ideal system to form Langmuir monolayers because they arrange themselves perpendicular to the interface and allow the study of 2D ordering. Model systems to imitate the behaviour of biomembranes can be investigated but also transferred on solid substrates as Langmuir-Blodgett films. Multilayers with a high level of molecular ordering can be accomplished by this technique.

In a Langmuir monolayer the surface pressure Π is the important quantity to be measured. A liquid has a surface tension γ_0, for example $\gamma_0 = 72.8\,\mathrm{mN/m}$ for water. Adding molecules to the interface always reduces the surface tension of the liquid which means that once a monolayer is formed at the interface, the surface tension reduces to γ. The surface pressure

$$\Pi = \gamma_0 - \gamma \tag{2.8}$$

is now given by the difference of the two surface tensions.

Whether it is possible for molecules to form a monolayer on an interface can be predicted by the *spreading coefficient* S. A convenient definition for S can be given in terms of the interfacial tensions [25]

$$S = \gamma_{\mathrm{air/water}} - (\gamma_{\mathrm{oil/air}} + \gamma_{\mathrm{oil/water}}) \tag{2.9}$$

which can be measured independently. Here, it is illustrated for the example of an oil droplet at the air-water interface. If S is positive the molecules spread on the interface. However, if it is negative the molecules try to minimize the contact area thus they dewet the interface and form droplets or aggregates. The oil droplet spreads on water because the spreading coefficient is $S = 8.9\,\mathrm{mN/m}$.

Pressure-Area Isotherms

The surface pressure in a monolayer depends on the number of molecules per area. In analogy to the 3D pressure/volume phase diagram, a surface-pressure/area phase diagram for the 2D monolayer can be recorded. Figure 2.2 shows a schematic isotherm of an amphiphilic molecule to illustrate different possible phases at the interface. In the gaseous state (G), the area available for each molecule is large. The molecules are well separated and there is almost no interaction between them, similar to an ideal gas. Consequently, the surface pressure in this regime is very low ($\Pi < 1\,\mathrm{mN/m}$). Reducing the area leads to a plateau in the isotherm that can be associated with a phase transition from the gaseous (G) state into an expanded (E) state. This constant pressure plateau is very characteristic for the coexistence of the two phases in the monolayer. Reducing the area shifts the ratio between the phases until all the molecules are in the expanded (E) state

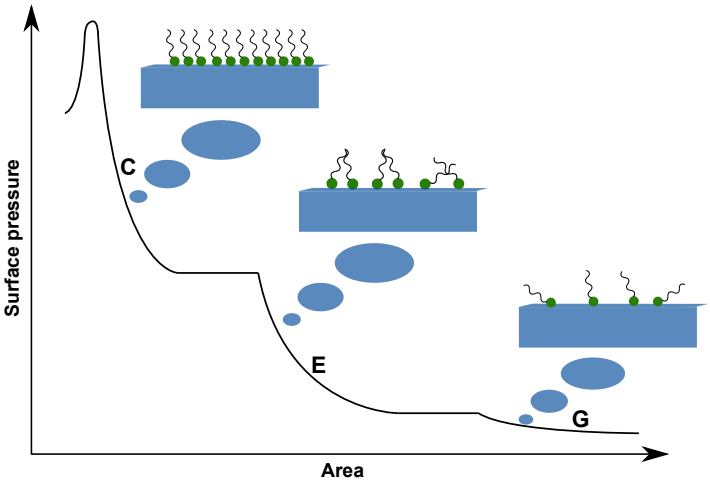

Figure 2.2: Pressure-area isotherm sketch for an arbitrary amphiphilic molecule. The molecules at the interface exhibit different phases G,E and C which correspond to the gaseous, the expanded and the condensed phase. The conformation of the molecules changes in dependency of the phase they are in.

and the pressure starts to rise again. In the expanded state the molecule interactions are similar to that in a liquid. However, there is still no long-range order in the monolayer. This changes once the area is reduced and the molecules are in the condensed (C) state. The molecules in the condensed phase are highly ordered and their order is comparable to the one in a solid. The surface pressure sharply rises upon reducing the area until the monolayer collapses in a maximum or a kink. The collapse strongly depends on various factors and is in general not well reproducable because the 2D order can be broken in many different ways (e.g. formation of multilayers, micelles, holes etc.) It is important to note that the specific form of an isotherm strongly depends on the type of molecule leading to a variety of measurable isotherms.

It is possible to record the surface-pressure/area isotherm of Langmuir monolayers in two different ways. In the first scenario the non-equilibrium surface pressure is recorded versus the available area. For this a certain number of molecules will be spreaded at the interface and two barriers continuously compress the monolayer with a constant velocity. A lot of data points can be recorded, however, the molecules are being constantly compressed during the recording. The isotherms are called *compression isotherms*. In the second approach, the *concentration isotherms*, the number of molecules is increased by subsequently spreading more molecules at the interface. After each spreading, the monolayer is given time for the molecules to arrange themselves and then the surface pressure is recorded. The advantage is that the true equilibrium pressure can be measured, but the number of points is quite limited and it is also difficult to increase the number of molecules in an already densely packed monolayer.

Isothermal Compressibility

From the data recorded for a compression isotherm it is possible to directly calculate the isothermal compressibility

$$C_S = -\frac{1}{A}\left(\frac{\partial A}{\partial \Pi}\right)_{T,p}. \tag{2.10}$$

Its value is an indicator for the elasticity of the monolayer which can help to differentiate phases in a monolayer. Typical values for amphiphilic molecules are between $5-10\,\mathrm{m/N}$

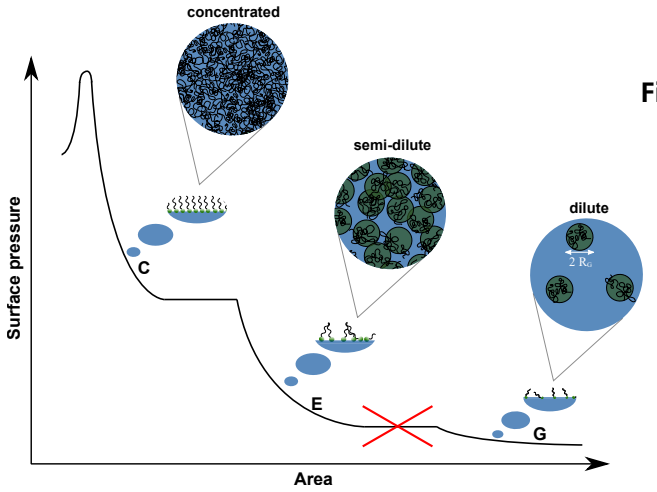

Figure 2.3: Top: Compression pressure-area isotherm in the case of a polymer film. Three different concentration regimes for polymer solutions are presented corresponding to the earlier mentioned G,E and C (gaseous, expanded and condensed phases). Bottom: Two-dimensional sketch of the polymer conformation at the air-water interface. In the dilute regime the Flory radius R_F represents the size of a single polymer chain extended at the interface.

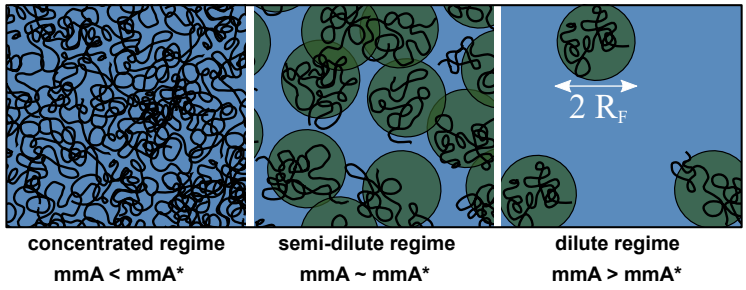

for fatty acids in the expanded phase[26], while they range between 10 m/N and several 100 m/N for more complex molecules like polymers.

Polymer Monolayers at the Air-Water Interface

The ability of a polymer to form a uniform monolayer free of impurities can be linked to its amphiphilic nature. An important aspect is the number of water-attracting groups. However, with increasing number of water-attracting groups the polymers may become soluble in water. One example for this is poly(2-vinylpyridine) (P2vP). The pyridine compound (C_5H_5N) is a ring structure similar to *benzene* with delocalized electrons, thus able to form hydrogen bonds with water molecules. Unfortunately, pyridine is protonated in a slightly acidic environment (pH = 4.9) and under these conditions soluble in water. Consequently, it is crucial to have a balance between hydrophobic and hydrophilic parts of the polymer to form a monolayer. Polymers that fulfill these conditions are confined to the surface. This results in a reduced dimension for chain conformation. Good examples are polyacrylates and polymethacrylates where the ester bond is the hydrophilic part and the remaining carbon atoms in the monomer represent the hydrophobic part. The adapted conformation at the interface is fundamentally different from the one for small amphiphilic molecules, but it is possible to directly compare the discussed phases.

In figure 2.3 (upper panel) the schematic isotherm for a flat polymer chain at the air-water interface is shown. In the *dilute regime*, the polymer chains are well separated from each other and each chain occupies a large area and the situation is comparable to that of an ideal gas. Each chain occupies a disk shaped space with a radius $R_F = \langle \vec{r}^2 \rangle^{1/2}$ (see equation (2.5)). Reducing the area will reduce the space between those disks

until all of them start to overlap at the area $A^* = \pi R_F^2$ corresponding to the overlap concentration $c^* \sim 1/A^*$. Now the chains are in the *semi-dilute regime*. There cannot be a coexistence between the dilute and semi-dilute regime which excludes the possibility of a coexistence plateau in the isotherm. Upon further compression, the polymer chains strongly interact with each other leading to an increasing pressure until separated chains cannot be distinguished from each other. The chains are in the *concentrated regime* where the 2D conformation is usually broken. A coexistence plateau may occur in the isotherm during the transition from a 2D to a 3D conformation. The bottom panel of figure 2.3 provides a top view of the conformation in the three regimes.

So far the solvent quality of the air-water interface has been neglected, however, for the conformation of the polymer chain it is an important property. While the area occupied by a disc-shaped polymer chain for a θ-solvent in the dilute regime is the same as in the melt, it increases for good solvent conditions. The characteristic area $A^* = \pi R_F^2$ defines the overlap concentration where R_F is given by $\langle \vec{r}^2 \rangle^{1/2}$ (taken from equation 2.5) with the solvent quality characterized by the Flory exponent ν. For bad solvent conditions, polymers do not form flat monolayers in general but adopt a *mushroom conformation*. A good example for bad solvent conditions is polystyrene that forms mushrooms upon spreading on water, however, its spreading coefficient is $S_{PS} = -8\,\mathrm{mN/m}$ indicating that it already dewets from the interface upon spreading [27].

In 1979 de Gennes found a solution to solve the mathematically challenging problem of polymer chains in solution taking into account the existence of an excluded volume [7]. In the scaling theory for polymer solutions, chain conformation can be expressed by power laws of number of monomers N, monomer concentration c_m, dimension d and solvent quality characterized by the Flory-exponent ν. Here, the introduction of the power laws in the dilute and semi-dilute regime will be performed using the concentration c instead of the area A, however they are proportional to each other ($c \sim 1/A$).

2.2.1 Surface Pressure Scaling in 2 Dimensions

A fundamental distinction between the dilute polymer solution and more concentrated solutions exists in form of the overlap concentration c_m^*. At concentrations $c_m \approx c_m^*$ the chains begin to be densely packed instead of well separated from each other like in the dilute regime. Therefore, it is legitimate to expect c_m^* to be comparable to the local concentration inside a single polymer chain. For a two dimensional system this leads to

$$c_m^* \cong \frac{N}{R_F^2} = k^{-2} N^{1-2\nu} \tag{2.11}$$

with R_F being the Flory-radius as defined in equation (2.5) [7].

Dilute Regime

For concentrations $c_m < c_m^*$, the polymer chains are in a dilute solution. The surface pressure Π becomes an important property in the discussion of solution parameters. A virial expansion can be used to express it as

$$\frac{\Pi}{k_B T} = \frac{c_m}{N} + A_2 c_m^2 + O\left(\frac{c_m}{N}\right)^3 \tag{2.12}$$

which is only extended to the second virial coefficient for the purpose of this discussion[23]. The first virial coefficient has already been inserted as $A_1 = 1/N$ for dissolved polymers. Equation (2.12) gives us a prediction for the scaling behaviour of the surface pressure in the dilute regime. The second order term can be interpreted as an increase of surface pressure due to the interactions between separated polymers. It vanishes completely for a θ-solvent and neglecting higher order terms one can expect an ideal gas behaviour for a solution of polymers in this limit. For good solvent conditions, the second virial coefficient can be expressed as $A_2 \simeq R_F^2 N^{-2}$. The chains essentially behave like hard spheres of radius R_F that tend to repel each other and increase the surface pressure in this limit[7].

Semi-dilute Regime

In the semi-dilute regime the polymer chains overlap but are not densely packed yet. The monomer-monomer interaction can still be explained by the excluded volume υ. The scaling of the surface pressure can be obtained from a generalization of equation (2.12) given by[28]

$$\frac{\Pi}{k_\mathrm{B}} = \frac{c_m}{N} \cdot f_\Pi\left(\frac{c_m}{c_m^*}\right) \tag{2.13}$$

where the function $f_\Pi(x)$ is dimensionless and has two limiting properties. In the dilute regime (for small x), $f_\Pi(x)$ is expressed as $f_\Pi(x) = 1 + \text{constant} \cdot x$. For large x (semi-dilute regime), all thermodynamic properties become independent of the degree of polymerization N and only depend on the concentration of monomers c_m. It means that a single chain with N monomers has the same local properties like a solution of chains with N monomers. This is a strong requirement because $f_\Pi(x)$ must be independent of N and behave like a simple power law of x

$$\lim_{x\to\infty} f_\Pi(x) = \text{constant} \cdot \left(\frac{c_m}{c_m^*}\right)^t = \text{constant} \cdot c_m^t \cdot N^{t(2\nu-1)} \tag{2.14}$$

using equation (2.11) for c_m^*. The surface pressure can now be expressed as

$$\frac{\Pi}{k_\mathrm{B}T} = \text{constant} \cdot c_m^{t+1} \cdot N^{t(2\nu-1)-1} \tag{2.15}$$

and since the condition was that Π must be independent of N, the condition for t is $t = 1/(2\nu-1)$. The surface pressure in 2 dimensions scales as

$$\Pi \sim c_m^{\frac{2\nu}{2\nu-1}} \tag{2.16}$$

with c_m being the monomer concentration and ν the 2D Flory-exponent. For good solvent conditions the 2D Flory-exponent is $\nu = 0.75$ and for a θ-solvent $\nu = 0.5$. Experimentally $\nu \approx 0.55$ has been found to be the limit for the 2D Flory-exponent of a θ-solvent[29,30].

In a different approach that considers the spatial properties of the chains, a much better picture of what happens in semi-dilute solutions can be obtained. Upon reaching the

overlap concentration c_m^*, the polymer chains can be described as an ideal gas of *blobs* of size ξ. The size of these blobs scales as

$$\xi \approx a n^{\nu} \tag{2.17}$$

with n being the number of monomers inside of the blob. Using the monomer density $c_m \approx n/\xi^2$ of a blob and equation (2.17) leads to

$$\xi \sim c_m^{-\frac{\nu}{2\nu-1}}. \tag{2.18}$$

At the overlap concentration c_m^* the size of the blobs must be comparable to the size of one polymer chain, however it decreases rapidly with increasing concentration $c_m > c_m^*$. The scaling of the surface pressure for an ideal gas of blobs in 2D can now be expressed as

$$\Pi = \frac{k_B T}{\xi^2} \sim c_m^{\frac{2\nu}{2\nu-1}} \tag{2.19}$$

which matches equation (2.16) [31].

2.3 Nanoparticles at the Air-water Interface

Placing a single particle (P) with an effective radius of r at the interface between air (A) and water (W) leads to a decrease of the energy of the system. A schematic illustration is shown in figure 2.4. The energy of the system reduces from the energy of the air-water interface E_0 to E_1 which is the energy with particles located at the interface. The adsorption free energy can be expressed in terms of particle size and penetration depth [32]

$$\Delta E = \pi r^2 \gamma_{A/W} \left(1 - |\cos\theta|\right)^2. \tag{2.20}$$

The energy difference is dominated by two main factors. The size of the particle r plays an important role but also the wettability of the particle surface characterized by the contact angle θ. First the influence of the particle size r will be discussed.

Generally, for microscopic particles the decrease in total free energy is much larger than the thermal energy ($k_B T$) which leads to a permanent confinement of them to the interface. This effect is also known as *pickering effect* [33]. In emulsions and foams solid particles are used to stabilize two immiscible liquids. However, for smaller particles in the nanometer range the energy reduction can be comparable to $k_B T$. The desorption of smaller particles at the interface is dynamically driven with a characteristic time $\tau_{\text{off}} = A\exp(-\Delta E/k_B T)$ [34]. The stability of nanoparticles at the interface strongly depends on maximizing the adsorption free energy ΔE so that the wettability of the particle surface becomes increasingly important. The wettability of a particle at the air-water interface can be described by the contact angle θ given by Young's equation: [35]

$$\cos(\theta) = \frac{\gamma_{A/W} - \gamma_{P/W}}{\gamma_{P/A}} \tag{2.21}$$

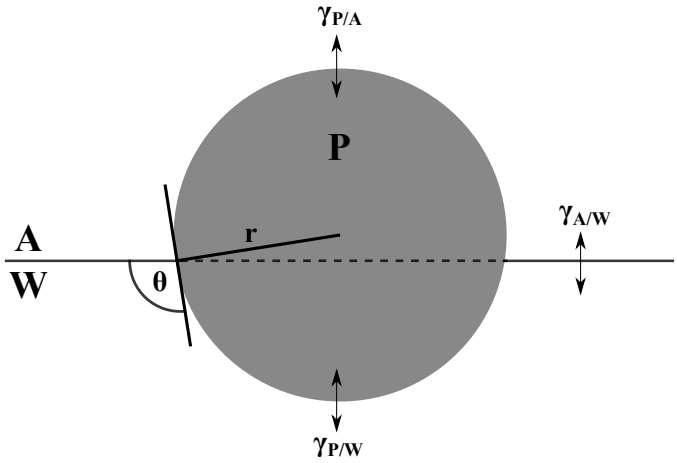

Figure 2.4: A spherical particle (radius r) at the air-water interface. The interfacial tensions between the interfaces is given by $\gamma_{X/Y}$ with P for particle, A for air and W for water.

For a contact angle of $\theta = 90\,°$, the adsorption energy has its maximum for a particle with homogeneous wettability. Increasing or decreasing the contact angle has a destabilizing effect. In this work iron oxide nanoparticles of different size are investigated on their ability to form monolayers at the air-water interface. The wettability of the particles is modified by an oleic acid shell around the particles. This leads to an increased hydrophobicity of the particles, thus an absorption of the particles at the air-water interface.

Dispersion of Nanoparticles in a Polymer Matrix

When mixing polymers and nanoparticles the question is whether the nanoparticles phase segregate/aggregate or homogeneously disperse in the 2D polymer matrix. The interesting case is obviously when nanoparticles homogeneously disperse in the thin polymer films and it is important to understand their dispersion laterally and along the thickness of the thin films. The goal of this work is to investigate the distribution of nanoparticles in a thin polymer film. The thickness of the polymer film is smaller than the particle size which leads to the question of their dispersion in the polymer film. The particles can for example be surrounded by polymers or dispersed on top of the polymer film[36].

If there are no specific interaction between polymer and particles, the entropy of mixing promotes mixing of nanoparticles. Its contribution to the total free energy F_{mix} of the system increases with decreasing particle size and is given by[36]

$$F_{\text{mix}} = \frac{\phi_P}{r^2} ln(\phi_P) \tag{2.22}$$

in 2D with the particle radius r and the particle area fraction ϕ_P. Likewise, the polymers have to stretch themselves for the nanoparticles to be accommodated in the matrix. The stretching energy increases with increasing particle size r with a contribution of F_{stretch} to the free energy[36]

$$F_{\text{stretch}} = \left(\frac{r}{R_F}\right)^2 \tag{2.23}$$

with R_F as the Flory radius of the matrix polymers. This consideration is obviously quite simple because it does not only neglect interaction between particles and polymers but

also depletion interaction between particles. Taken these interactions into account structuring and ordering of polymer chains at the particle-polymer interface have been observed [37] as well as aggregation of particles due to bridging interactions of the polymers [38].

3 Theoretical Concepts II: Scattering from Ultrathin Soft Matter Films

In the last 30 years several techniques have been invented that are able to directly probe local properties of interfaces (*AFM, STM and TEM*). At the air-water interface the most prominent direct imaging technique is the Brewster-Angle-Microscopy which is able to provide live images of monolayers with a lateral resolution down to a few μm. Investigating surfaces and interfaces with X-ray scattering methods averages over much larger lateral length scales and is therefore able to complement imaging techniques. Surface X-ray scattering provides complementary information in reciprocal space with a lateral resolution of up to several μm and a few hundred nm perpendicular to the surface. The lower limit for surface X-ray scattering is on an atomic scale making it a powerful tool to investigate soft-matter surfaces.

This chapter starts with an overview about scattering of particles in solution introducing the form and structure factor. This is used to determine the structure and size of iron oxide nanoparticles in solution. Then it shifts to surface X-ray scattering from soft matter interfaces. The specular reflectivity will be explained using the Fresnel equations for single and multiple ideal flat surfaces before an approximation method is introduced (kinematical approximation). It follows a statistical description of surfaces that is necessary to understand the complete scattered profile from real interfaces including the off-specularly scattered intensity. X-ray scattering in raw data form cannot be directly compared to model calculations, therefore, experimental considerations taking into account finite resolution are introduced before a description of off-specular intensity can be provided. At the end of the chapter the concepts important for Brewster-Angle-Microscopy are briefly summarized.

3.1 Small Angle X-ray Scattering: Particles in Solution

The general setup of a scattering experiment is shown in figure 3.1. Monochromatic X-ray radiation with a wave vector $\vec{k}_i$ is scattered at the sample at an angle 2θ. The angle 2θ is called *scattering angle*. After being scattered the radiation can be detected in the detector (D) far away from the sample with a wave vector $\vec{k}_f$. The scattering process can be assumed to be purely elastic which means $|\vec{k}_i| = |\vec{k}_f|$. The *scattering vector* $\vec{q}$ can then be expressed as the difference of the incoming and scattered radiation [39]

$$q = |\vec{q}| = |\vec{k}_f - \vec{k}_i| = \frac{4\pi n}{\lambda} \sin\theta \tag{3.1}$$

with the wave length λ of the radiation and the refractive index n which is 1 in case of a SAXS experiment. The scattering vector $\vec{q}$ provides information on the momentum transfer in the sample while the energy transfer during the scattering process is zero

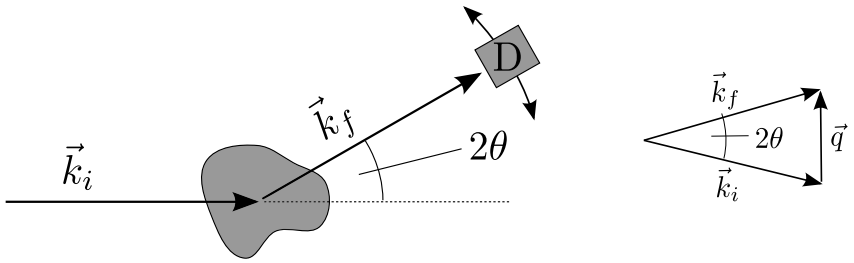

Figure 3.1: Sketch of the scattering geometry for a scattering experiment with definition of the scattering vector $\vec{q}$. The scattered intensity is detected at the detector (D).

(elastic scattering). Therefore, measuring the scattered radiation in dependency of the scattering angle 2θ fully describes the scattering process [40].

The scattered radiation in the detector can only be measured as the scattered intensity $I(\vec{q})$. In general, the intensity is defined using the squared complex amplitude $A(\vec{q})$ as

$$I(\vec{q}) = |A(\vec{q})|^2 = \left| \int_V \rho(\vec{r}) e^{-i\vec{q}\vec{r}} \, d\vec{r} \right|^2 \tag{3.2}$$

with the electron density distribution $\rho(\vec{r})$ and the scattering volume V. The important information is that the scattered intensity solely depends on the electron density distribution. For a solution of monodisperse particles the density can be written as a convolution of the distribution in a single particle $\rho_P(\vec{r})$ with the correlation between neighbours $n_L(\vec{r})$ [41].

$$\rho(\vec{r}) = \rho_P(\vec{r}) \otimes n_L(\vec{r}) \tag{3.3}$$

In the fourier transformation (see equation (3.2)) this convolution leads to a product of two scattering processes. The first process can be understood as the scattering from a single particle and is therefore called *form factor* $F(\vec{q})$. It is given by the fourier transformation of the electron density distribution of a single particle $\rho_P(\vec{r})$. The second term is related to the correlation between two different particles and called *structure factor* $S(\vec{q})$. Now, the scattered intensity $I(\vec{q})$ is proportional to both terms

$$I(\vec{q}) \sim F^2(\vec{q}) \cdot S(\vec{q}). \tag{3.4}$$

In the following the structure factor will be 1 which is equivalent to no correlation between neighbouring particles. For dilute solutions of particles as investigated in this work, this is a valid assumption. Consequently, the scattered intensity directly measures the squared form factor of our particles. Furthermore, the samples are isotropic meaning it is sufficient to use absolute values for the scattering vector q. The form factor of a sphere and a cylinder are used to demonstrate the expectations for the scattered intensity.

- Consider a sphere with a radius R and constant electron density ρ_S. The form factor $F_S(\vec{q})$ of the sphere in a solution with an electron density ρ_m is given by [40]

$$F_S(q) = 4\pi(\rho_S - \rho_m)R^3 \frac{\sin qR - qR\cos qR}{q^3R^3}. \tag{3.5}$$

  The limit for $F_S(q \to 0)$ is the sphere volume $(4/3\,\pi R^3)$ multiplied by the electron density contrast $(\rho_S - \rho_m)$.

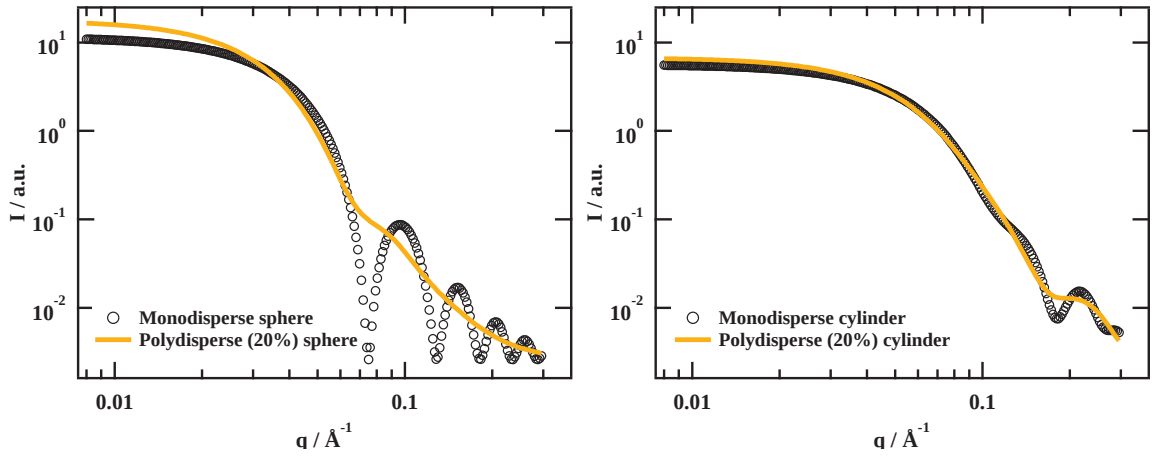

Figure 3.2: Model functions for the intensity profile of a dilute system of monodisperse and polydisperse spheres in the left panel and cylinders in the right panel. The intensity is given by the squared form factor of the particles.

- Consider a cylinder of radius R and length L with an electron density ρ_C. If the cylinders are not oriented, the squared form factor $F_C^2(\vec{\mathrm{q}})$ of the cylinder in a solution with an electron density ρ_m is given by [41]

$$|F_C(\mathrm{q})|^2 = (\rho_C - \rho_m)^2 \int_0^{\pi/2} \left(\frac{2J_1(\mathrm{q}R\sin\alpha)}{\mathrm{q}R\sin\alpha} \frac{\sin(\mathrm{q}L\cos\alpha/2)}{\mathrm{q}L\cos\alpha/2} \right)^2 \sin\alpha \,\mathrm{d}\alpha \qquad (3.6)$$

  with $J_1(x)$ being the Bessel function of the first kind.

The form factor of a sphere is plotted in the left panel of figure 3.2. The oscillations characteristic for the form factor are clearly visible for monodisperse spheres with a radius of $R = 6\,\mathrm{nm}$ (black points). However, realistic systems are usually described by a distribution of particle sizes. Introducing a polydispersity of 20 % into the model smears out the clear minima of the monodisperse form factor (orange curve). This can be similarly observed in the form factor for the cylinders. The cylinders have an ratio of 2:1 so that their radius R and length L are both 4 nm in the plotted form factor. The minimum characteristic for the length of the cylinder smears out if the polydispersity is increased to 20 %.

3.2 Surface X-ray Scattering from Soft Matter Interfaces

The previous section about SAXS showed that it is sufficient to know the electron density distribution in the sample to calculate the scattered intensity. In case of a reflectivity experiment it is possible to approach the problem using a complex refractive index n known from optics. The following gives a selection of the for this work important theory provided and explained in detail in the book *X-Ray Scattering from Soft Matter Thin Films* written by Metin Tolan [42]. Equations without an explicit reference can be found in the book of Tolan.

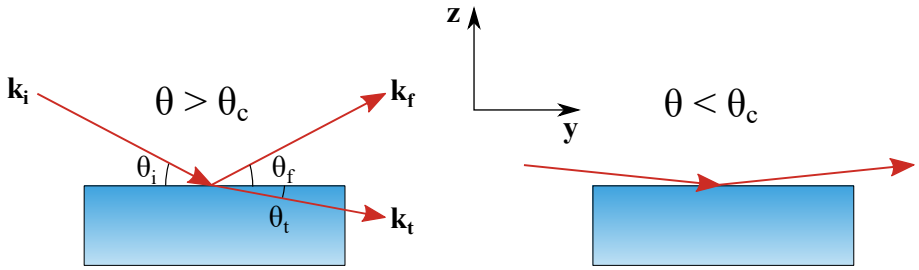

Figure 3.3: Reflection of X-rays at the air-water interface for angles larger and smaller than the critical angle θ_C (total external reflection).

3.2.1 Specular Scattering from Ideal Flat Surfaces

In a homogeneous reflecting medium the complex refractive index n can be expressed as

$$n = 1 - \frac{\lambda^2}{2\pi} r_e \rho + i \frac{\lambda}{4\pi} \mu = 1 - \delta + i\beta \tag{3.7}$$

with δ as the dispersion term characterized by the electron density ρ and the electron radius r_e. For X-rays δ is always positive and usually very small ($10^{-5} - 10^{-6}$) so that n is always close to 1 with the refractive index of the vacuum being 1. The absorption of the medium is characterized by β which is most of the time even smaller ($\sim 10^{-8}$) and therefore often neglected in the description of reflectivity from an interface.

For X-rays vacuum/air is the optically denser medium due to the higher refractive index n. Therefore, radiation that is coming from the vacuum/air and reflected at an interface of a single medium shows the phenomenon of total external reflection. For $\theta < \theta_C$ the X-rays do not penetrate far into the medium and all incoming radiation is reflected at the interface (see figure 3.3). The critical angle θ_C can be calculated using Snell's law of refraction

$$\theta_C \approx \sqrt{2\delta} = \lambda \sqrt{r_e \rho / \pi}. \tag{3.8}$$

There is almost no difference between s and p-polarization due to the refractive index being practically always 1 for X-rays. Considering a s-polarized incoming wave, the reflection r_s and transmission t_s coefficient can be calculated using the *Fresnel equations*

$$r_s = \frac{k_{i,z} - k_{t,z}}{k_{i,z} + k_{t,z}} \qquad t_s = \frac{2k_{i,z}}{k_{i,z} + k_{t,z}} \tag{3.9}$$

with $k_{i,z} = k \sin\theta_i$ and $k_{t,z} = nk \sin\theta_t = k(n^2 - \cos^2\theta_i)^{1/2}$. Figure 3.4 shows the Fresnel reflectivity $R_F = |r(\theta)|^2$ and transmission $T_F = |t(\theta)|^2$ as a function of the incident angle θ_i normalized by the critical angle θ_C. Three different ratios of δ/β are displayed to illustrate the role of the absorption β. Apparently, only the vicinity around the critical angle θ_C is influenced by absorption and it can be neglected for larger angles. The function R_F decreases rapidly once the incident angle θ_i is larger than θ_C. It is also interesting to take a closer look at the transmission function that has a pronounced maximum at $\theta_i = \theta_C$. This maximum originates from a constructive interference of the reflected and

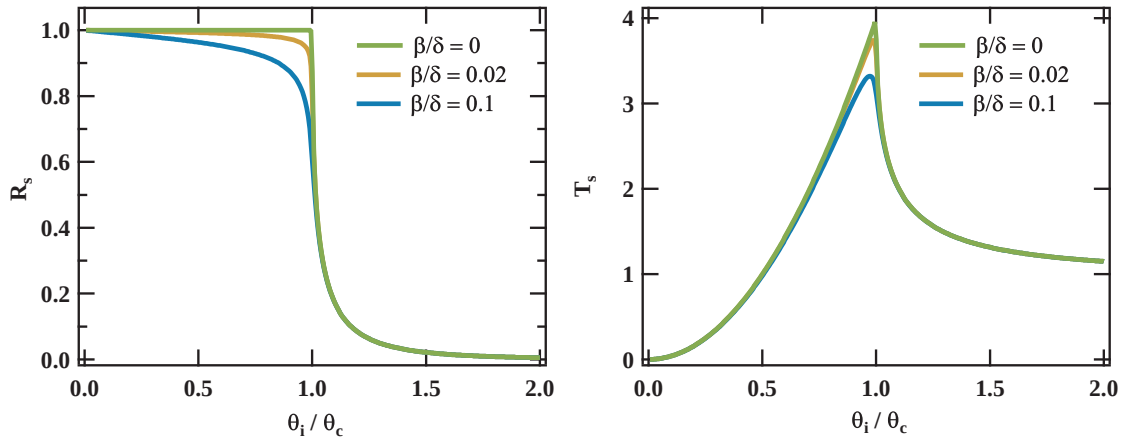

Figure 3.4: Fresnel reflectivity $R_F = |r(\theta_i)|^2$ and transmission $T_F = |t(\theta_i)|^2$ as a function of the incident angle θ_i normalized by the critical angle θ_C. Three different absorption/dispersion ratios δ/β are plotted. The curves are only influenced by absorption in the vicinity of the critical angle θ_C.

transmitted wave enhancing the amplitude of the transmitted wave. For larger angles the transmission function becomes 1.

For an ideal flat surface, an incoming wave towards the interface is reflected under the same angle $\theta_r = \theta_i$ (specular condition). The scattering vector $\vec{q}_z = \vec{k}_f - \vec{k}_i$ has the absolute value of

$$q_z = \frac{4\pi}{\lambda} \sin\theta_i. \tag{3.10}$$

The critical angle θ_C can also be expressed as a critical wave vector $q_c \approx 4\sqrt{\pi\rho_e r_e}$ and the Fresnel reflectivity (reflected intensity) is now given by

$$R_F(q_z) = |r_s|^2 = \left| \frac{q_z - \sqrt{q_z^2 - q_c^2}}{q_z + \sqrt{q_z^2 - q_c^2}} \right|^2 \approx \left(\frac{q_c}{2q_z} \right)^4 \quad \text{for } q_z \gtrsim 3q_c. \tag{3.11}$$

The reflectivity decreases very fast (see figure 3.4), so that the limiting factor of a setup is given by its reliability to measure small values of R_F.

Multiple Interfaces

The case of reflection from a single interface is the simplest one. However, in nearly all experiments the situation is far more complex, so it is necessary to consider the reflectivity of a stratified medium with multiple layers. For simplicity reason, the scattering is considered to be at sharp interfaces as also assumed in the previous discussion. Two different methods can be used to calculate the reflectivity for a multiple layered system. A theoretical treatment using a transfer matrix for each layer published by Abelés [43] in 1950 or a recursive method introduced in 1954 by Parratt [44]. In this work a brief introduction to Parratt's recursive method will be given.

The reflection of a multilayer system consisting of N interfaces at the positions $z_j \leq 0$ is schematically shown in figure 3.5. The vacuum counts as the first layer with the first interface located at $z_1 = 0$. A semi-infinite substrate is located under the last layer at the position z_N. Each layer has a thickness of $d_j = z_{j-1} - z_j$ with a refractive index n_j.

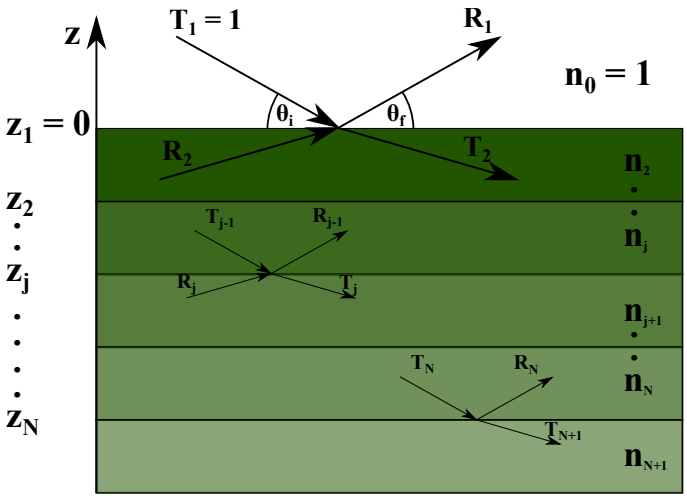

Figure 3.5: Sketch of a system consisting of $N+1$ layers with refractive indexes n_j and N interfaces. For the specular condition θ_i and θ_f are equal. The amplitude of the incident wave is normalized ($T_1 = 1$) and there is no reflected wave from the substrate ($R_{N+1} = 0$).

T_j and $k_{i,j}$ are the amplitude and the wave vector of the transmitted wave and R_j and $k_{f,j}$ are the corresponding values for the reflected wave inside layer j. The amplitude of the incident incoming wave is $T_1 = 1$ and hits the first interface under the angle θ_i. The total reflectivity of the multilayer system is given by R_1, however in order to calculate R_1 it is necessary to know the reflected amplitudes R_j inside each layer j. From the Maxwell equations it is known that the tangential components of the electric and magnetic field vectors have to be continuous at each of the interfaces. By using this relation the amplitudes of the reflected and transmitted wave can be calculated.

Parratt formulated a method that recursively defines the reflectivity of layer j by the reflectivity of layer $j+1$. The ratio between reflected and transmitted wave of layer j is given by

$$X_j = \frac{R_j}{T_j} = e^{-2ik_{z,i,j}z_j} \frac{r_{j,j+1} + X_{j+1}e^{2ik_{z,i,j+1}z_j}}{1 + r_{j,j+1} + X_{j+1}e^{2ik_{z,i,j+1}z_j}} \tag{3.12}$$

with the Fresnel coefficient from equation (3.9) customized for the interface between layer j and $j+1$:

$$r_{j,j+1} = \frac{k_{z,i,j} - k_{z,i,j+1}}{k_{z,i,j} + k_{z,i,j+1}}. \tag{3.13}$$

The z component of the wavevector in layer j is given by $k_{z,j} = k(n_j^2 - \cos^2(\theta_i))^{1/2}$. The bottom layer is assumed to have an infinite thickness so that no reflection has to be taken into account from the bottom of the sample ($X_{N+1} = 0$). The reflectivity of the whole sample is given by the coefficient for the top layer

$$R = |X_1|^2. \tag{3.14}$$

3.2.2 Kinematical Approximation and Influence of Surface Roughness

The theoretical results for reflectivities so far are based on Snell's and Fresnel's law and no direct reference to scattering has been given yet. However, reflection does indeed occur due to the scattering of radiation by individual particles and is in general no different than in any other scattering experiment. A very handy way to describe the scattering from X-rays at an interface is the *kinematic (first Born) approximation*. It is valid for incident angles θ_i much larger than the critical angle θ_c and the scattered intensity can be calculated without using the full Parratt formalism. However, the kinematic approximation describes the *weak scattering regime* in which interactions between the incident and scattered waves can be neglected. It is not valid in the vicinity of the critical angle where total external reflection occurs. It has also been shown for the transmission function T_F in figure 3.4 that the pronounced maximum at $\theta_i = \theta_C$ originates from a constructive interference of reflected and transmitted wave. For small angles the approximation is not correct and leads to the wrong results compared to the exact solution in equation (3.14). In general, the kinematic approximation is still a good approximation for angles $\theta_i > 3\theta_C$ where the amplitude of the scattered wave is sufficiently small [45]. A very useful interpretation is given by

$$R(\mathrm{q_z}) \approx R_F(\mathrm{q_z}) \left| \frac{1}{\rho_\infty} \int \frac{\mathrm{d}\rho(z)}{\mathrm{d}z} e^{i\mathrm{q_z}z}\, \mathrm{d}z \right|^2 = R_F(\mathrm{q_z}) \left| F(\mathrm{q_z}) \right|^2 \tag{3.15}$$

where $F(\mathrm{q_z})$ is the Fourier transform of the derivative of the electron density profile $\rho(z)$ and ρ_∞ is the density of the material. A big advantage of this approach is that the contribution of the reflectivity curve by various features in the structure can now be identified and interpreted. For example if the electron densities in a multilayer system are well known, the resulting reflectivity curve can be calculated with a total electron density that consist of different boxes corresponding to the different materials in the layered system [40]. In case of a single layer of thickness d this leads to

$$\begin{aligned} R(\mathrm{q_z})/R_F(\mathrm{q_z}) &= \left| F_1(\mathrm{q_z}) + e^{i\mathrm{q_z}d} F_2(\mathrm{q_z}) \right|^2 \\ &= \left| F_1(\mathrm{q_z}) \right|^2 + \left| F_2(\mathrm{q_z}) \right|^2 + 2 \left| F_1(\mathrm{q_z}) \right| \left| F_2(\mathrm{q_z}) \right| \cos(\mathrm{q_z}d + \Delta\Phi(\mathrm{q_z})) \end{aligned} \tag{3.16}$$

with $F_{1,2}(\mathrm{q_z})$ as the Fourier transforms of the derivative of the electron density distribution and the phase differences $\Phi(\mathrm{q_z})$ between the two interfaces. The last term is interesting because it represents the interference between the top and bottom interface leading to oscillations that are directly related to the thickness of the layer (the so-called *Kiessig fringes*) [46]. The phase difference $\Phi(\mathrm{q_z})$ between the two interfaces depends on the profile of the density distribution perpendicular to the interface and can lead to a $\mathrm{q_z}$ dependency of the Kiessig fringes. However, for two sharp interfaces its value is $\Phi(\mathrm{q_z}) = 0$.

For X-rays the assumption of an ideal flat surface cannot hold for the reflection at real surfaces. Due to the small wavelength in the nanometer range, all surfaces are considerably rough for X-rays. The differences between the reflection at an ideal and a rough surface is illustrated in the top panel of figure 3.6. For X-rays scattered at a rough interface, the radiation scattered under specular condition ($\theta_r = \theta_i$) reduces while the

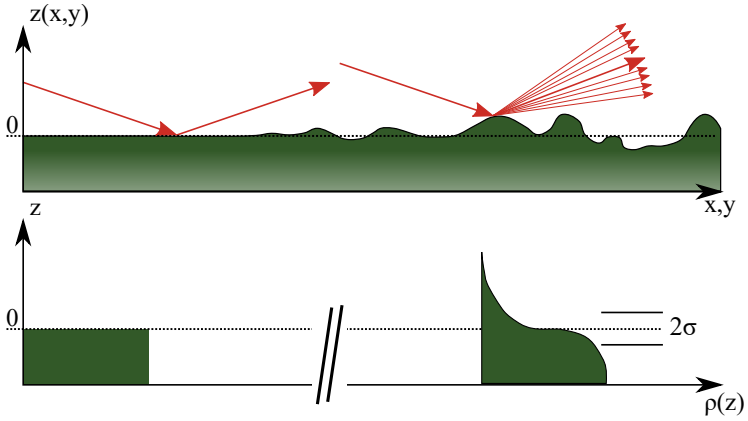

Figure 3.6: In the top panel, a sketch of the height profile of an interface for two different situation is shown. On the left the reflection at an ideal flat surface is illustrated while the right hand side represents a real (rough) surface. The bottom panel shows the corresponding electron density profiles for the two situations with σ being the *rms roughness*.

intensity in $\theta_r \neq \theta_i$ direction increases (off-specular intensity). The electron density profile $\rho(z)$ for a rough surface can be understood as the average over an (x, y) area at a given z. The result for the specular reflectivity is a reduction given by

$$R(q_z) = R_F(q_z)e^{-\sigma^2 q_z^2} \tag{3.17}$$

with the *root mean squared* (*rms*) roughness σ of the interface. It is common to describe the continuous variation of the electron density by a random variable with a Gaussian distribution. Then the average electron density distribution as a function perpendicular to the interface (z component) is given by an error function. When the reflectivity is calculated the error function leads to a Gaussian function modulating the specular reflectivity of the interface. The bottom panel of figure 3.6 shows the difference between the electron density distribution $\rho(z)$ for an ideal flat and a rough surface. As already mentioned, the roughness of the interface influences the amount of off-specular intensity. So far only the laterally averaged structure (*rms* roughness) has been considered. However, to understand and interpret the whole scattering profile it is important to thoroughly describe the lateral structure of the surface. Therefore, a model for the statistical description of interfaces is necessary.

3.2.3 Statistical Description of Interfaces

Nowadays, many techniques are able to yield to real-space images of surfaces with atomic resolution such as *Scanning-Tunneling-Microscopy, Atomic-Force-Microscopy* and *Transmission-Electron-Microscopy*. However, those techniques only illustrate local properties of the interface while X-ray scattering averages over a lateral length scales of several micrometres. Therefore, the techniques are very well suited to complement each other. The following gives an introduction into the statistical description of interfaces necessary to interpret X-ray surface scattering data.

Height-Height Correlation Function

For a description of a single interface it is necessary to first define the contour function $z(\vec{r}_{xy})$ that provides the height of the interface for a lateral vector $\vec{r}_{xy}$. The contour function is the height of the surface at each position with respect to the mean interface

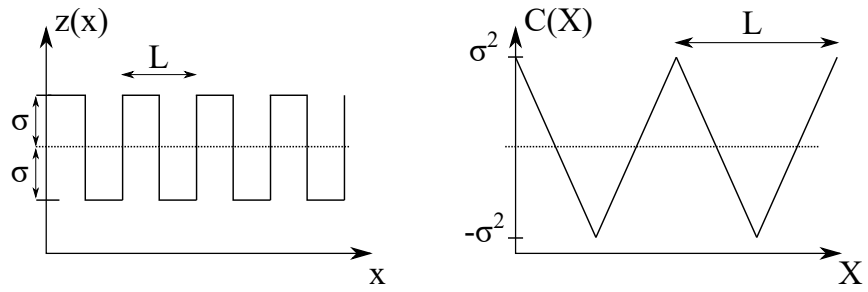

Figure 3.7: Interface contour $z(x)$ and height-height correlation function $C(X)$ of a periodic surface with periodicity L. σ is the *rms roughness*.

location, however, it would be more suitable to describe the main features of the interface by only a few parameters. A simple way to describe a surface by its statistical properties is given by the height-height correlation function

$$C(\vec{R}) = \frac{1}{A}\int_A z(\vec{r}_{xy})z(\vec{r}_{xy}+\vec{R})\,\mathrm{d}\vec{r}_{xy} = \left\langle z(\vec{r}_{xy})z(\vec{r}_{xy}+\vec{R})\right\rangle_{\vec{r}_{xy}} \tag{3.18}$$

where $\vec{R} = (X, Y)$ is a lateral vector and A the considered area. The correlation function $C(\vec{R})$ describes the probability of finding a point P at position $\vec{R}$ with the same height $z(P)$ above the mean interface location as at the origin. This is illustrated in figure 3.7. An important parameter to characterize interfaces has already been mentioned before as the *rms roughness* σ which is defined as

$$\sigma^2 = \left\langle z^2(\vec{r}_{xy})\right\rangle_{\vec{r}_{xy}} = C(0). \tag{3.19}$$

Another useful function that will become important later on is the *mean quadratic height difference function* [47]

$$g(\vec{R}) = \left\langle \left[z(\vec{r}_{xy}) - z(\vec{r}_{xy}+\vec{R})\right]^2\right\rangle_{\vec{r}_{xy}} = 2\sigma^2 - 2C(\vec{R}) \tag{3.20}$$

which can be used together with equation (3.19) to form

$$\frac{C(\vec{R})}{C(0)} = 1 - \frac{g(\vec{R})}{2\sigma^2}. \tag{3.21}$$

This relation guarantees that $C(\vec{R}) \leq C(0) = \sigma^2$ since $g(\vec{R}) \geq 0$ always holds. Furthermore, if two points are uncorrelated $C(\vec{R})$ becomes 0 because $g(\vec{R}) = 2\sigma^2$. For statistically rough surfaces an intermediate behaviour is expected: $C(\vec{R})$ decreases monotonically until all correlations vanish for very large distances ($C(\vec{R}) \to 0$ for $|\vec{R}| \to 0$).

For scattering experiments it is more convenient to use the description of interfaces in reciprocal space. The height-height correlation function can be transformed into reciprocal space using a Fourier transformation, the so-called power spectral density (PSD)

$$\tilde{C}(\vec{q}_{xy}) = \int C(\vec{R})e^{-i\vec{q}_{xy}\vec{R}}\,\mathrm{d}\vec{R}, \tag{3.22}$$

which is equivalent to

$$\tilde{C}(\vec{\mathrm{q}}_{xy}) = \left|\tilde{z}(\vec{\mathrm{q}}_{xy})\right|^2. \tag{3.23}$$

In the second definition the PSD is computed using the Fourier transform of the contour function

$$\tilde{z}(\vec{q}_{xy}) = \int z(\vec{r}_{xy}) e^{-i\vec{\mathrm{q}}_{xy}\vec{R}}\,\mathrm{d}\vec{R} = \left|\tilde{z}(\vec{q}_{xy})\right| e^{i\phi(\vec{q}_{xy})} \tag{3.24}$$

where modulus $\left|\tilde{z}(\vec{q}_{xy})\right|$ and phase $\phi(\vec{q}_{xy})$ are already separated. The free choice of phases $\phi(\vec{q}_{xy})$ in reciprocal space corresponds to the fact that the height-height correlation function in real space only depends on the spatial separation characterized by $\vec{R}$. Therefore, the statistical description in real space (averaging in equation (3.18)) corresponds to the loss of phase information in reciprocal space.

The *rms roughness* σ can now be calculated using the PSD

$$\sigma^2 = \int \tilde{C}(\vec{\mathrm{q}}_{xy})\,\mathrm{d}\vec{\mathrm{q}}_{xy}. \tag{3.25}$$

However, in an experiment the equation or rather the limits in the integral have to be adjusted to the accessible $\vec{\mathrm{q}}_{xy}$ range. A lower and an upper cutoff for the accessible region in reciprocal space are introduced leading to

$$\sigma^2 = \int_{\mathrm{q}_{min}}^{\mathrm{q}_{max}} \tilde{C}(\vec{\mathrm{q}}_{xy})\,\mathrm{d}\vec{\mathrm{q}}_{xy}. \tag{3.26}$$

The measured roughness depends on the experimental setup due to limits from the accessible q-range. One has to take this into account while comparing the experimental measured roughness of the same sample at different setups.

Correlation Functions of Solid Interfaces

Coastlines, tree trunks or other examples in nature have similar surface structures on different length scales. They appear as fractals where parts of them show the same statistical properties on many scales. Still, their vertical dimension often scales differently compared to their lateral dimensions. Such a behaviour is called self-affine. This can also be the case for an isotropic solid surface. Sinha et al. proposed a simple correlation function that is suited for many isotropic solid interfaces [48]

$$C(R) = \sigma^2 e^{-(R/\xi)^{2h}} \tag{3.27}$$

with the cutoff (correlation) length ξ and the *Hurst parameter* h. If $R \ll \xi$ the surface is self-affine rough while it appears to be smooth for $R \gg \xi$. Therefore, ξ can be interpreted as the length scale on which the surface appears to be rough. The second parameter $0 < h \leq 1$ defines the fractal dimension $D = 3 - h$ of the interface. For h=1 the interface consists of smooth hills and valleys. The problem with this correlation function is that the limit for $h \to 0$ is not properly defined. Palasantzas et al. have been investigating height-height correlation functions and were able to find a class of functions that lead to the correct limit for $h \to 0$ [49–51]. These are the so-called K-correlation functions leading to a new class of functions. Details on their specific form can be found in the references [45].

Soft Matter Thin Films: Liquid and Polymer Surfaces

On each liquid surface wave excitations are always present. In an ocean, the waves are called surface gravity waves that are wind-generated. However, there are also internal waves on each liquid surface that cannot be seen by the naked eye. The internal waves are separated into two kinds which are gravity and capillary waves. As the name implies, the effect of gravity is predominant in gravity waves while the surface tension plays an important role for capillary waves. A characteristic feature of capillary waves is that their amplitude is much smaller than their wavelength and they are important for most soft matter surfaces.

Capillary waves are related to the surface tension of a liquid but in order to understand how they are excited, it is necessary to formulate the *excess free energy per unit area* $\Delta F(z)$. In the simplest case of a bulk-liquid surface this is done by

$$\Delta F(z(\vec{r}_{xy})) \simeq \frac{\gamma}{2} \int \left(|\nabla z(\vec{r}_{xy})|^2 + q_{l,c}^2 z^2(\vec{r}_{xy}) \right) \mathrm{d}\vec{r}_{xy} \tag{3.28}$$

with the contour function of the surface $z(\vec{r}_{xy})$, the surface tension γ and the lower cutoff vector for the capillary wave $q_{l,c} = \sqrt{\rho g/\gamma}$. Here, ρ is the density of the liquid and g the gravitational constant ($2\pi/q_{l,c} \approx 0.27\,\mathrm{cm}$ for water). Introducing the Fourier transform $\tilde{z}(\vec{\mathrm{q}}_{xy})$ leads to [52]

$$\Delta F(z(\vec{r}_{xy})) \simeq \frac{\gamma}{2} \int \left(q_{xy}^2 + q_{l,c}^2 \right) \left| \tilde{z}(\vec{q}_{xy}) \right|^2 \mathrm{d}\vec{q}_{xy}. \tag{3.29}$$

The argument of the integral is equivalent to the energy of each oscillation mode with wavevector $\vec{q}_{xy}$. Taking into account the density of states (factor of $4\pi^2$) and using the equipartition theorem (energy per mode $= k_\mathrm{B}T/2$) yields to

$$\tilde{C}(\vec{q}_{xy}) = \left| \tilde{z}(\vec{q}_{xy}) \right|^2 = \frac{k_\mathrm{B}T}{4\pi^2\gamma} \frac{1}{\vec{q}_{xy}^2 + \vec{q}_{l,c}^2}. \tag{3.30}$$

Now, it is clear that for a bulk-liquid interface the capillary waves are thermally excited waves. The height-height correlation function in real space can be written as [53]

$$C(R) = \frac{k_\mathrm{B}T}{2\pi\gamma} K_0(q_{l,c}R) \simeq -\frac{k_\mathrm{B}T}{2\pi\gamma} \left[ln(q_{l,c}R/2) + \gamma_E \right] \tag{3.31}$$

with $K_0(x)$ as a modified Bessel function of the second kind and $\gamma_E \approx 0.5772$ as the Euler's constant. The approximation is legitimate as long as gravity is present as the only background potential. The roughness σ generated by capillary waves can now be calculated using equation (3.26) and (3.31), where $q_{l,c} \approx 0$ is used as the lower cutoff and $q_{u,c} = \pi/\kappa$ as the upper cutoff [54,55]. The upper cutoff is limited by the molecule diameter κ which means that there cannot exist any wavelength for capillary waves smaller than the molecule size. For a liquid surface the roughness is now given by

$$\sigma^2 = \int_0^{q_{u,c}} \tilde{C}(\vec{\mathrm{q}}_{xy})\, \mathrm{d}\vec{\mathrm{q}}_{xy} = \frac{k_\mathrm{B}T}{4\pi\gamma} \left(\frac{\mathrm{q}_{u,c}^2 + \mathrm{q}_{l,c}^2}{\mathrm{q}_{l,c}^2} \right). \tag{3.32}$$

There has been some work on liquid interfaces stating the existence of another *intrinsic roughness* σ_{in} in addition to the thermically induced capillary wave roughness σ [56,57]. The intrinsic roughness has its origin in the density fluctuation of the molecules at the interface. These density fluctuation are not thermically induced but an intrinsic roughness of the interface. The effective roughness is simply given by the square sum $\sigma_{\text{eff}}^2 = \sigma_{\text{in}}^2 + \sigma^2$ of the two components [56–58].

3.2.4 Experimental Considerations

In the previous chapters two different approaches illustrated how to calculate the reflectivity of X-rays at an interface. An exact solution using the in optics well known Fresnel equations and the first Born approximation (kinematical approximation). However, X-ray scattering in raw reflectivity form cannot be directly compared with those model calculations. One reason for this is that the finite resolution of the experimental setup has to be taken into account. Another influence is that the data may contain artifacts stemming from the scattering geometry. In the following, the effect of the setup will not only be presented for the specular conditions ($\theta_f = \theta_i$) but also extended to off-specular scattering ($\theta_f \neq \theta_i$).

Experimental Geometry

The general setup of the experiment used in this work is presented in section 4.2. The scattering geometry for an incoming wave $\vec{k}_i$ in the yz-plane is illustrated in the left panel of figure 3.8. The wave is scattered at the interface and the scattered wave has a wave vector $\vec{k}_f$ with $k = |\vec{k}_{i,f}|$ (elastic scattering). Due to the roughness of the interface the scattered wave may also be scattered out of the yz-plane, thus gaining an extra x component. The scattering vector $\vec{\mathrm{q}} = \vec{k}_f - \vec{k}_i$ can be splitted into two components, the lateral scattering vector $\vec{\mathrm{q}}_{xy}$ and the component $\vec{\mathrm{q}}_z$ perpendicular to the surface. In our setup the lateral scattering vector $\vec{\mathrm{q}}_{xy}$ can be simplified to $\vec{\mathrm{q}}_y$ because the detector automatically integrates over all $\vec{\mathrm{q}}_x$ (Våntec-1 line detector). Therefore, the angle ϕ of figure 3.8 can be neglected in the following discussion and the geometry simplifies to the right panel of the figure.

The components of the scattering vector are explicitly given by

$$\begin{aligned} \mathrm{q}_y &= k\left(\cos\theta_i - \cos\theta_f\right) \\ \mathrm{q}_z &= k\left(\sin\theta_i + \sin\theta_f\right) \end{aligned} \tag{3.33}$$

where $k = 2\pi/\lambda$. With figure 3.8 and equation (3.33) the important features of the geometry are introduced. The resolution of the experimental setup can be computed for $\mathrm{q}_{y,z}$ to [59]

$$\begin{aligned} \delta_{\mathrm{q}_y} &= \Delta\lambda/\lambda \mathrm{q}_x + k(\theta_i \Delta\theta_i + \theta_f \Delta\theta_f) \approx \mathrm{q}_z/2 \max(\Delta\theta_i, \Delta\theta_f) \\ \delta_{\mathrm{q}_z} &= \Delta\lambda/\lambda \mathrm{q}_z + k(\Delta\theta_i + \Delta\theta_f) \qquad \approx k \max(\Delta\theta_i, \Delta\theta_f) \end{aligned} \tag{3.34}$$

using the total differentials of equation (3.33) under the assumption of small angles (e.g. $\sin\theta_{i,f} \approx \theta_{i,f}$). For surface X-ray experiments, the wavelength spread $\Delta\lambda/\lambda$ given by

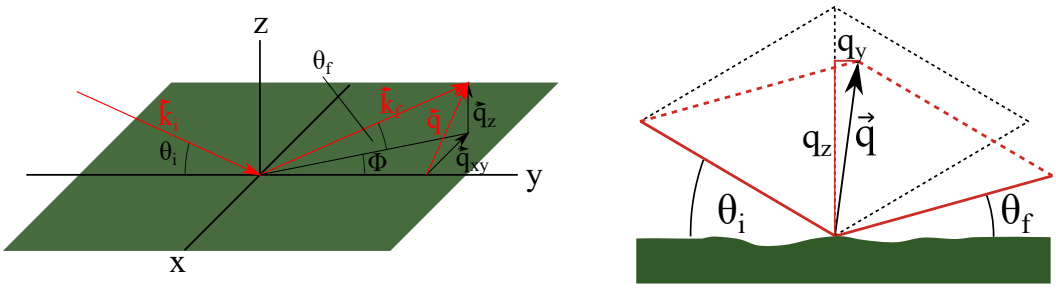

Figure 3.8: The left panel shows the scattering geometry for an incoming wave $\vec{k}_i$ in the yz-plane scattered at a rough interface in the xy-plane. The scattering vector $\vec{q}$ has a lateral q_{xy} and a perpendicular q_z component to the interface. In the right panel the same geometry is simplified to experimental conditions. The detector automatically integrates over all q_x simplifying the geometry and the lateral scattering vector component to q_y.

the monochromator is very small ($< 10^{-4}$) and can therefore be neglected. Furthermore, the angular divergence $\Delta\theta_i$ and acceptance $\Delta\theta_f$ are mainly determined by geometry, slit sizes and optical elements in front of the source and detector. The resolution is defined by the larger divergence which is usually given by the primary beam profile measured in the detector without sample ($\Delta\theta_i$).

A Gaussian function is used quite often to model the resolution function $\tilde{R}(\vec{k})$ in reciprocal space:

$$\tilde{R}(\vec{k}) = \frac{1}{2\pi\delta_{q_y}\delta_{q_z}} e^{-\frac{1}{2}k_y^2/\delta_{q_y}^2} e^{-\frac{1}{2}k_z^2/\delta_{q_z}^2} \tag{3.35}$$

The q_y and q_z directions are treated independently avoiding complicated cross terms which is legitimate as long as angular divergence/acceptance is not too far apart. For the setup used in this work this is the case. The measured intensity $I(\vec{q})$ in a detector is now defined by

$$I(\vec{q}) = \int \tilde{S}(\vec{k})\tilde{R}(\vec{q}-\vec{k})\,d\vec{k} \tag{3.36}$$

as the convolution of the resolution function with a scattering law $\tilde{S}(\vec{k}) = \left|\tilde{\rho}(\vec{k})\right|^2$ (e.g. Fresnel reflectivity). With an infinitely good resolution ($\delta_{q_{y,z}} \to 0$), the resolution function becomes a δ-distribution, thus leading to the measured intensity being equivalent to the model. On the other hand a finite resolution smears out the scattering law and is equivalent to an averaging over a certain area in real space

$$I(\vec{q}) = \iint \rho(\vec{r})\rho(\vec{r}')R(\vec{r}'-\vec{r})\,e^{i\vec{q}(\vec{r}'-\vec{r})}\,d\vec{r}\,d\vec{r}', \tag{3.37}$$

where the function $R(\vec{r})$ acts as a cutoff function in real space defining the area within which coherent scattering is possible. With the setup used in this work coherent scattering is able to occur on a lateral length scale up to several μm ($y_{max} = 2\pi/\delta q_y \approx 30\,\mu$m) in q_y and only several nm ($y_{max} = 2\pi/\delta q_x \approx 6\,$nm) in q_x direction.

Existence of Artifacts in the Scattering Data

The existence of two different scattering phenomena will be mentioned that have their origin in the experimental setup. The first one is that the footprint of the incoming rectangular shaped beam may not be completely on the sample. For very small incident angles the sample surface is almost parallel to the incident beam which may lead to part of the intensity not being reflected at the surface. In an experiment this feature can easily be identified by a decreasing reflectivity in the total-external reflection regime of the sample with decreasing incident angle θ_i. This can be prevented by a good adjustment of the beam geometry which is generally the case for the experimental data on the liquid interface.

The second artifact is the existence of a small kapton peak for $\theta_i + \theta_f = 7.5^\circ$ caused by two kapton windows of the box covering the Langmuir experiment. This peak exists for all measurement on the air-water interface but can be neglected since it is not in the interesting angular range during the experiments.

3.2.5 Off-specular Scattering from Soft Matter Surfaces

It has been mentioned before that the specular intensity from rough surfaces is damped considerably. The missing intensity is diffusely scattered at exit angles $\theta_f \neq \theta_i$. While it is enough to consider the rms roughness σ of the sample for specular intensity, it is necessary to use the full height-height profile $C(X,Y)$ to understand the off-specular intensity.

The electron density of a sample interface can be separated into a lateral and perpendicular component. It may be written as

$$\rho(\vec{r}) = \Delta\rho\, H[z - z(x,y)] \tag{3.38}$$

where the step function is $H[z] = 0$ for $z \leq 0$ and 1 otherwise. Within the Born approximation where only single scattering events are taken into account, the scattering function $S(\vec{\mathrm{q}})$ is the Fourier transformation of the density-density autocorrelation function. Assuming that $z(x,y)$ is a Gaussian random variable the scattering law can be expressed as [47]

$$S(\vec{\mathrm{q}}) = \frac{(\Delta\rho)^2}{\mathrm{q}_z^2} \iint e^{-\mathrm{q}_z^2 g(X,Y)/2}\, e^{i(\mathrm{q}_x X + \mathrm{q}_y Y)}\, \mathrm{d}X\mathrm{d}Y \tag{3.39}$$

where $g(x,y)$ is the height difference correlation function from equation (3.20). To obtain the scattered intensity, the scattering law has to be adapted to experimental conditions. Therefore, it has to be integrated over all potential angles in the detector $\Delta\Omega$ while taking into account the geometry of the experiment using the real-space cutoff functions $R(X,Y)$ from equation (3.37). This leads to an additional $1/\mathrm{q}_z^2$ term in the function. Furthermore, the height difference correlation function $g(x,y)$ can be expressed by equation (3.20) yielding to

$$I(\mathrm{q}_y, \mathrm{q}_z) = I_0 \frac{(\Delta\rho)^2}{\mathrm{q}_z^4} e^{-\mathrm{q}_z^2\sigma^2} \iint e^{\mathrm{q}_z^2 C(X,Y)}\, e^{-\left(X^2\delta_{\mathrm{q}_x}^2 + Y^2\delta_{\mathrm{q}_y}^2\right)} e^{i\left(\mathrm{q}_x X + \mathrm{q}_y Y\right)}\, \mathrm{d}X\mathrm{d}Y \tag{3.40}$$

with I_0 being the intensity of the tube. In most of the X-ray reflectivity setups the beam is limited by a combination of slits which are wide-open in the out-of-plane x direction.

Effectively this means an integration over all q_x. In this setup, soller slits with an angular acceptance of $\Delta\theta_x = 25\,\mathrm{mrad}$ are placed in front of tube and detector. As a consequence the effective length scale over which constructive interference may occur is given by $2\pi/\delta_{q_x} = \lambda/\Delta\theta_x \approx 6\,\mathrm{nm}$ which is a length scale not relevant for the observable q_y range in our setup. Consequently, only X=0 in equation (3.40) gives a contribution to the integral which just leaves the integration over Y. The intensity within the Born approximation can then be expressed as: [45,59]

$$I(q_y, q_z) = I_0 \frac{(\Delta\rho)^2}{q_z^4} e^{-q_z^2\sigma^2} \int e^{q_z^2 C(0,Y)}\, e^{-Y^2\delta_{q_y}^2}\, e^{iq_y Y}\, \mathrm{d}Y \tag{3.41}$$

Equation (3.41) is the most general form for the intensity in a reflectivity experiment. For further calculations one hast to insert an explicit form for the height-height correlation function $C(X,Y)$. There are a lot of correlation functions for which $C(X,Y) \to 0$ when $(X,Y) \to \infty$ and the integral in equation (3.41) contains a delta-function contribution. The intensity can then be separated into a specular (delta-function contribution) and an off-specular part:

$$I(q_y, q_z) = I_{\text{spec.}}(q_y, q_z) + I_{\text{off-spec.}}(q_y, q_z) \tag{3.42}$$

For the specular component it is enough to calculate the rms roughness σ which reduces the intensity by a factor of $e^{-q_z^2\sigma^2}$, it is equivalent to equation (3.17) apart from terms corresponding to the experimental setup. The diffuse off-specular component may only be calculated if the functional form of the height-height correlation function $C(X,Y)$ is known. The two components are given by: [45]

$$\begin{aligned} I_{\text{spec.}}(q_y, q_z) &= I_0 \frac{(\Delta\rho)^2}{q_z^4} e^{-q_z^2\sigma^2} \delta(q_y) \\ I_{\text{off-spec.}}(q_y, q_z) &= I_0 \frac{(\Delta\rho)^2}{q_z^4} e^{-q_z^2\sigma^2} \int \left(e^{q_z^2 C(0,Y)} - 1 \right) e^{-Y^2\delta_{q_y}^2}\, e^{iq_y Y}\, \mathrm{d}Y \end{aligned} \tag{3.43}$$

For a liquid interface excited by capillary waves the correlation function is given by equation (3.31). Even for $(X,Y) \to \infty$ the correlations of $C(X,Y)$ do not vanish, so the intensity cannot be separated into a specular and an off-specular part. The logarithmic approximation for the capillary waves has to be inserted directly in equation (3.41) to calculate the full scattering profile. For the exact profile it is also necessary to include dynamical scattering effects from the *distorted wave Born approximation* [53] (*DWBA*) by multiplying the equation with the respective transmission functions $|t_i(\theta_i)|^2 |t_f(\theta_f)|^2$ from equation (3.9). Considering the experimental setup with the instrumental resolution yields to [58]

$$I_{\text{CW}}(q_y, q_z) = I_0 \frac{q_c^4}{16 q_z^4} |t_i(\theta_i)|^2\, |t_f(\theta_f)|^2\, e^{-\sigma^2 q_z^2}\, {}_1F_1\left(\frac{1-\eta}{2}; \frac{1}{2}; -\frac{q_y^2}{2\Delta q_y^2} \right) \tag{3.44}$$

for the scattered intensity. The equation includes the instrumental resolution $\Delta q_y = 1/4\, q_z\, \Delta\theta_y$, the *rms roughness* σ of the water interface and the parameter $\eta = (k_B T q_z^2)/(2\pi\gamma)$ which is determined by the surface tension γ of the liquid. ${}_1F_1(x; y; z)$ denotes the confluent hypergeometric function also known as the Kummer function and I_0 is the initial intensity of the X-ray tube.

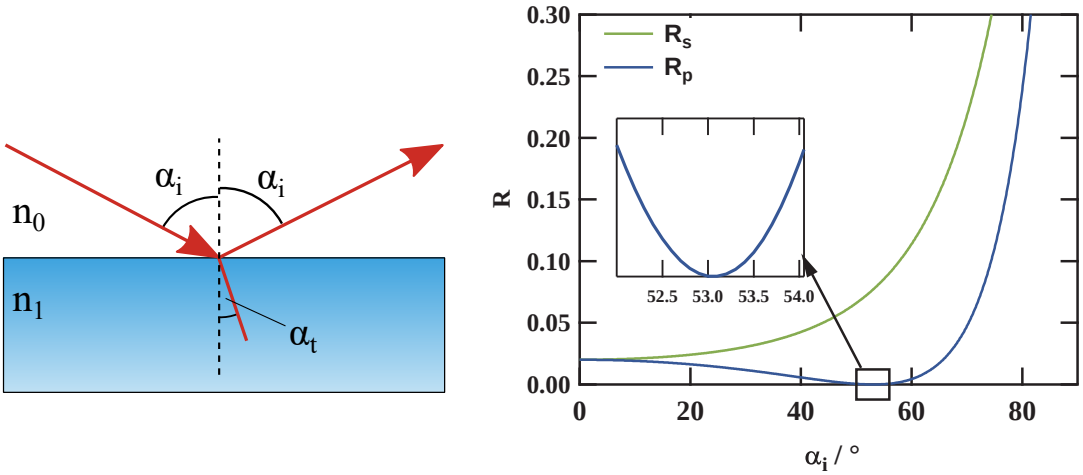

Figure 3.9: The left panel shows the reflection of a laser beam from medium n_0 at medium n_1. In optics the angles $\alpha_{i/t}$ are defined using the normal vector perpendicular to the interface. The right panel shows the reflectance $R_{s/p}$ as a function of incident angle α_i. The p-polarized component of the reflectance vanishes for the Brewster-angle α_B.

3.3 Brewster-Angle-Microscopy

As already mentioned before coherent scattering for X-rays may occur on lateral length scales up to 30 μm. Brewster-Angle-Microscopy (BAM) is a direct visualizing technique that is able to access the lateral structure of thin films locally on a μm scale. A laser beam illuminates the interface to obtain real time images of the film. This is also the difference to off-specular scattering where the structures are averaged over the illuminated area.

A Brewster-Angle-Microscope takes advantage of the vanishing reflection of p-polarized light when it is reflected at an interface with a higher refractive index ($n_1 > n_0$). The Fresnel equations for the reflection coefficient of s- and p-polarizations are

$$r_s = \frac{n_0 \cos\alpha_i - n_1 \cos\alpha_t}{n_0 \cos\alpha_i + n_1 \cos\alpha_t} \quad \text{and} \quad r_p = \frac{n_0 \cos\alpha_t - n_1 \cos\alpha_i}{n_0 \cos\alpha_t + n_1 \cos\alpha_i} \tag{3.45}$$

for a laser beam that comes from medium n_0 and is reflected at medium n_1. It is worth mentioning that in optics the angle $\alpha_{i,t}$ is defined as illustrated in the left panel of figure 3.9. Furthermore, the right panel of the figure shows the reflectance $R_{s/p} = |r_{s/p}|^2$ for the air-water interface ($n_{\text{air}} = 1, n_{\text{water}} = 1.33$). For the p-polarization the reflectance R_p vanishes at the Brewster-angle α_B. It can be shown that the Brewster-angle can easily be determined by

$$\tan\alpha_B = \frac{n_1}{n_0} \tag{3.46}$$

with its value for the air-water interface being $\alpha_B = 53.13\,°$.

If a monolayer ($n' \neq n_{\text{water}}$) is placed on the water surface it modifies the Brewster angle condition and light reflection will be observed. It can be shown that the reflected intensity I_r of the laser beam with an intensity I_0 is given by [60]

$$I_r = I_0 |r_s(\alpha_B)|^2 \left[\cos\phi \cos\psi \overline{\rho_B} + \sin\phi \sin\psi\right]^2 \tag{3.47}$$

with $r_s(\alpha_B)$ as the reflection coefficient for s-polarized light at the Brewster-angle, ϕ and ψ as the tilt angles for polarizer and analyzer whereas 0 corresponds to p-polarized light and the ellipticity[60]

$$\overline{\rho_B} = \frac{\pi}{\lambda} \frac{\sqrt{n_0^2 + n_1^2}}{n_0^2 - n_1^2} \int_{-\infty}^{+\infty} \frac{[n(z)^2 - n_1^2] \cdot [n(z)^2 - n_0^2]}{n(z)^2} \, \mathrm{d}z. \tag{3.48}$$

For a monolayer with thickness l and a homogeneous refractive index n', the integral in equation (3.48) can be calculated and $\overline{\rho_B} \sim l$. This leads immediately to an important correlation between the reflected intensity I_r and the thickness of the layer l. For a perfect p-polarized alignment of polarizer ($\psi = 0$) and analyzer ($\phi = 0$) the reflected intensity corresponds to the thickness of the layer as

$$I_r \sim l^2. \tag{3.49}$$

Another possibility for reflected intensity from the monolayer is that optical anisotropies are present in the film. They change the polarization of the reflected light and may also be observed in the reflected intensity. However, equation (3.47) shows that either polarizer or analyzer need to allow some s-polarized intensity to pass in order to observe those anisotropies. They are also a powerful tool to reveal substructures with long range orientation order[61].

4 Experimental Methods

The fundamental technique used for almost all investigations in this work was the Langmuir technique. Thin films consisting of polymers, nanoparticles and polymer nanocomposites have been characterized at the air-water interface using compression isotherms from Langmuir experiments, surface X-ray scattering and Brewster-Angle-Microscopy. The Langmuir-Blodgett technique was used to transfer films on silicon substrates for further investigations by X-ray reflectometry. A small-angle X-ray scattering experiment was used to determine particle sizes of the iron oxide nanoparticles used in this work. In this chapter, the setup of all experiments used will be briefly introduced including data processing of reflectivity data.

4.1 Langmuir-Blodgett Technique

As already introduced in chapter 2, a variety of systems are able to form stable monolayers at the air-water interface. Langmuir experiments provide an easy access to investigate the pressure-area isotherms of these systems. Recording Langmuir isotherms can be achieved using two different approaches, namely compression or concentration isotherms. The difference between the two record techniques will be discussed after the general idea has been presented.

In a Langmuir experiment the *Wilhelmy technique* is used to measure the surface tension. When a platinum plate with a perimeter $l = (2x + 2y)$ is placed in the air-water interface, its surface will be wetted by water with a contact angle θ. The resulting force F is directed towards the water and is given by the gravitational force F_G, the buoyancy F_A by the liquid and the surface tension γ:

$$F = F_G - F_A + \gamma l \cos\theta \tag{4.1}$$

In some of the experiments a platinum rod (diameter: d) is used instead of a plate which changes the perimeter to $l = \pi d$. A disadvantage is that due to the smaller perimeter the resolution of the measured tension reduces. As described in chapter (2.2), the surface pressure Π is the interesting measuring variable. Using its definition in equation (2.8) and combining it with equation (4.1) leads to the surface pressure being defined as

$$\Pi = \gamma_0 - \gamma = \frac{\Delta F}{l \cos\theta}. \tag{4.2}$$

ΔF is the difference between the two measured forces for the pure subphase and the one with a substance spread on the interface.

Two different experimental setups were used to record the surface pressure. The pressure-area isotherms (compression and concentration isotherms) and hysteresis measurements were performed on a KSV NIMA trough system (KSV NIMA, Langmuir Trough

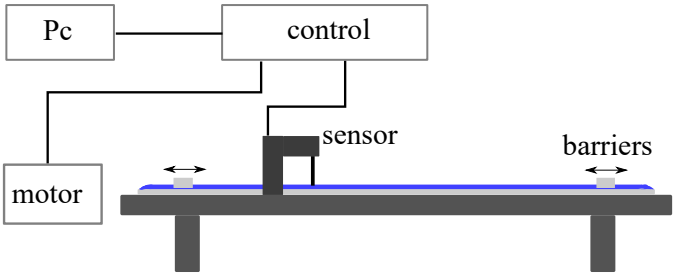

Figure 4.1: Sketch of the experimental setup for the KSV NIMA trough system used for Langmuir isotherm and Brewster-Angle-Microscopy measurements.

KN 1006, Biolin Scientific) equipped with two hydrophobic symmetrically-moving barriers and a Wilhelmy platinum plate placed in-between those barriers (tilted by an angle of 45 ° with respect to the direction of compression). The trough dimensions are $(58\,x\,14.5)\,\mathrm{cm}^2$. A sketch of the setup is shown in figure 4.1. For the X-ray reflectivity measurements, the pressure-area isotherms were recorded on a Kibron μTroughXS system equipped with one hydrophobic barrier and a Wilhelmy rod placed on one side of the trough. The trough dimensions are $(23\,x\,19.7)\,\mathrm{cm}^2$. In both cases a piezoelectric force sensor measures the surface tension and the available area A for the monolayer can be controlled by moving the barriers. The systems can be fully controlled by a computer software. During all experiments the temperature of the laboratory was being monitored at $T = (22 \pm 1)\,^\circ\mathrm{C}$. This is quite important since the surface tension shows a temperature dependency that has been empirically described by the Eötvös equation [62] and confirmed through several exerpiments [63–65]. Upon increasing temperature, the surface tension of water linearly reduces with $0.166\,\mathrm{mN/m/K}$ [65]. For all presented Langmuir experiments the surface tension of the subphase was adjusted to the usual reference value $\gamma_0 = 72.8\,\mathrm{mN/m}$ for the temperature in the laboratory. This procedure was performed prior to each measurement.

Preparation of a Langmuir Monolayer

For each measurement the barriers and the trough are first cleaned with ethanol and rinsed with purified water. Deionized Millipore water (Millipore Direct-Q) with a specific resistivity of $18.2\,\mathrm{M\Omega\,cm}$ at 25 °C was used for rinsing and the subphase. All isotherms were measured on a water surface and the purity of the surface was checked prior to each measurement by a compression of the water surface with $2175\,\mathrm{mm^2\,min^{-1}}$ while the surface pressure was monitored ($\Delta\Pi < 0.3\,\mathrm{mN/m}$). The samples used in this work were dissolved in chloroform (concentration: $c = 1.0\,\mathrm{mg/ml}$ for polymers; $c \approx 5\,\mathrm{mg/ml}$ for nanoparticles) and mixed before each measurement (Vortex 2000 mixer). A specified volume V was spread in drops of $1.5\,\mu\mathrm{l}$ on the water subphase with a hamilton syringe (maximum volume $5\,\mu\mathrm{l}$). The chloroform evaporates quickly and a stable monolayer is formed. The available surface for each polymer molecule is given by the mean molecular area mmA, which is defined as:

$$\mathrm{mmA} = \frac{AM}{cV\mathrm{N_A}} \tag{4.3}$$

A is the actual area enclosed by the two barriers, M the molecular weight of the polymer and $\mathrm{N_A}$ the Avogadro constant. The mean molecular area is inversely proportional to the surface concentration ($\mathrm{mmA} \sim c_m^{-1}$) used in chapter (2.2.1).

Compression and Concentration Isotherms

As already mentioned before there are two different recording techniques for Langmuir isotherms. In the case of the compression isotherm, all of the sample material $m = cV$ is spread on the interface at the beginning of the experiment. The isotherms are only measured after a waiting time of 30 minutes after spreading the sample. The mean molecular area mmA is now reduced by moving the barriers at a constant velocity. The velocity for all shown isotherms was $C_S = 435\,\mathrm{mm^2 min^{-1}}$. Due to the constant compression of the monolayer the surface pressure Π is not in equilibrium.

In contrast to that the concentration isotherm measures the equilibrium surface pressure Π. This is accomplished because the barriers are not used to reduce mmA, instead, the amount of sample is subsequently increased with a hamilton syringe. Each time after a new drop of solution is spread on the water subphase, the surface pressure is monitored until it reaches equilibrium. This value is recorded for the specific mmA. At first it seems like this technique is more suited to record Langmuir isotherms, however, there are two flaws that cannot be easily corrected. First, the number of points obtained for concentration isotherm is limited due to the recording procedure. Secondly, with increasing surface pressure a homogeneous spreading of the samples in the monolayer becomes more difficult. Chloroform has a spreading coefficient $S \approx 13\,\mathrm{mN/m}$ (for room temperature) at the air-water interface [66] which technically means that samples solved in chloroform can only be spread on the water surface until Π reaches the value of the spreading coefficient. Afterwards, chloroform will not wet the interface anymore which makes it very difficult for the polymer or nanoparticles to homogeneously spread at the interface. Regions of collapsed material are most likely formed already inside the evaporating chloroform droplet.

Langmuir-Blodgett Film Preparation

Langmuir-Blodgett (LB) films were produced on a Langmuir trough system (μTrough System Kibron Inc., Helsinki Finland). The silicon wafers were cleaned for 2 minutes in piranha solution and their surface was characterized by X-ray reflectivity measurements prior to the transfer of the monolayers. For the transfer, the silicon wafers were first dipped through the monolayer in the subphase with a dipping speed of 2 mm/min, and then pulled out of the subphase through the monolayer again at the same speed. The molecular area of the film was controlled and monitored by a software to guarantee a constant pressure during the transfer. The data shows that the monolayer was transferred when the silicon wafer was pulled out of the subphase (Z-type LB film) and all transfer ratios were close to 1.

4.2 Surface X-ray Scattering

All surface X-ray scattering experiments were performed on a modified D8 Advance reflectometer (Bruker AXS, Germany). The reflectometer has been modified during the PhD work of Martin Kraska and a detailed description of the setup can be found in his work [65]. Therefore, only a brief outline will be given here. A sketch of the setup is presented in figure 4.2 including the settings for its operating mode. The design of the setup makes it possible to measure reflectivities in $\theta - \theta$ geometry with the X-ray source and detector attached at goniometer arms which can be moved independently with a precision of 0.001°.

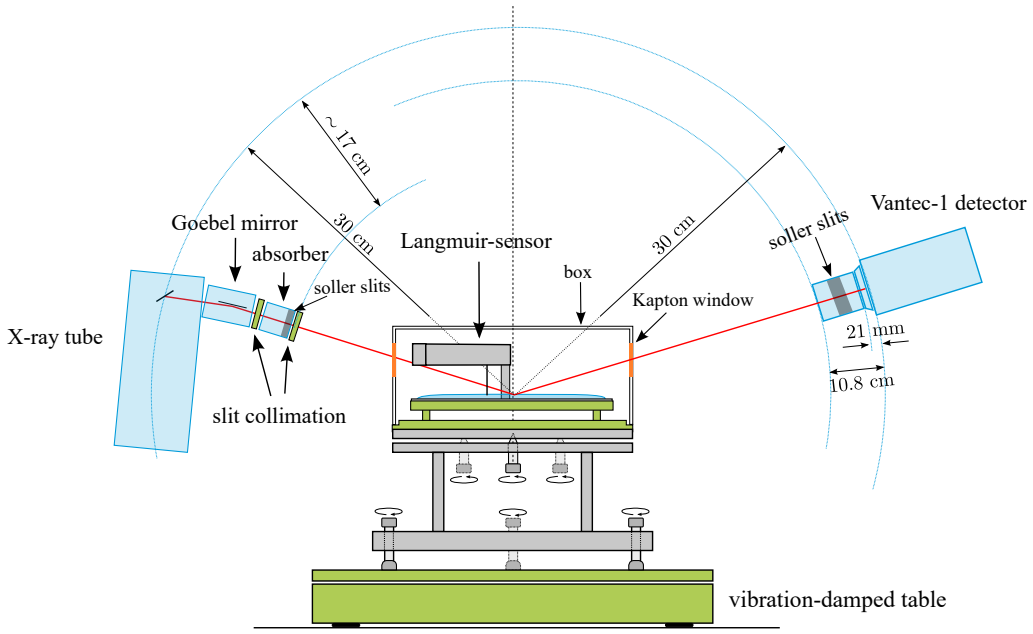

operating voltage	40 kV at anode current of 40 mA
wave length λ	1.5406 Å
adsorption factors	6200: used for primary beam adjustments
	80: used for small angles
	8.86: used for medium angles
detector	Vantec-1 with an angular range of $2-10^\circ$
instrumental resolution	$\Delta\theta_f = 0.733$ mrad

Figure 4.2: Sketch of the experimental setup for the modified D8 Advance reflectometer taken from [65]. The sample stage for the air-liquid interface was the Kibron μTroughXs system mounted on a vibration-damped table TS-150-g-25-a/LP from HWL Scientific Instruments. A cover box of PMMA with two kapton windows is place on top of the trough. All important margins are highlighted in the sketch. The important settings for the operation mode are listed in the table below the sketch.

A conventional X-ray tube with a Cu anode (CuK$_\alpha$, wavelength of $\lambda = 1.54$ Å) is used to generate a X-ray beam with a line focus. The beam is further monochromized by a Goebel mirror (W/Si multilayer mirror). Through a narrow horizontal slit of 0.1 mm, the beam passes an absorber (calibrated Cu attenuator) which is necessary for high intensities near the critical angle in order to maintain a linear response of the detector. A second 0.1 mm horizontal slit is placed after the absorber to cut out the K$_\beta$-line (which is also reflected by the monochromator). Soller slits ($\Delta\theta_x = 25$ mrad) are placed after the last horizontal slit and directly in front of the detector.

A Våntec-1 line detector (Bruker AXS, Germany) was used to measure the specularly reflected intensity $I(q_z)$ and the diffuse intensity $I(q_y)$ simultaneously in an angular range of $2-10^\circ$ for a given incident angle θ_i (see figure 3.8). Within one measurement the detector integrates intensity over all q$_x$ (line focus). The primary beam profile is shown in figure 4.3. The beam divergence is within the range of the instrumental resolution $\Delta\theta_f$ for the instrument as provided by *Bruker*.

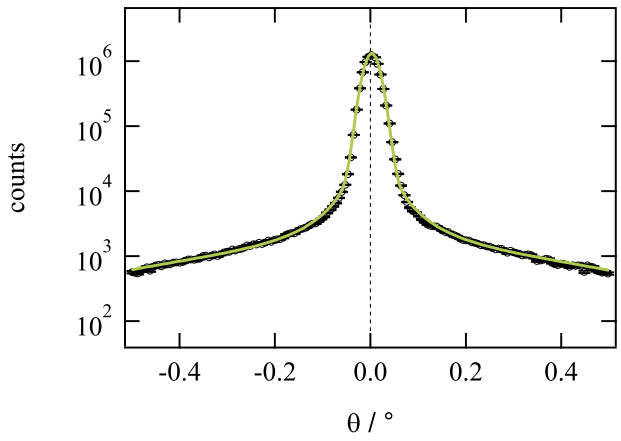

Figure 4.3: Primary beam profile measure of the modified D8 reflectometer with an accumulation time of 10 s [65]. A Pseudo-Voigt profile is used to fit the experimental data with a full width half maximum of 0.0378 °.

The investigation of films at the air-water interface were performed on a modified sample stage with the Kibron μTroughXS. Footsteps, vibrations from the building or other factors increase the background noise during a reflectivity experiment. To decrease the influences of these vibrations, the sample stage was mounted on a vibration-damped table (*HWL Scientific Instruments TS-150-g-25-a/LP*). This system reduces the background noise significantly which is specifically important for the interpretation of the diffuse scattered intensity. Besides vibration, evaporation of the water subphase is another factor that is important to be controlled during an experiment. The position of the reflection maximum shifts when the water level reduces due to evaporation. In order to control this effect a PMMA box was used as a cover on top of the Langmuir trough. This reduces the influence of evaporation so that experiments can be performed for up to 5 hours. The X-ray beam enters the box trough two kapton windows which leads to a small kapton peak at $\theta_i + \theta_f = 7.5\,^\circ$.

Performing and Evaluating a Specular Reflectivity Experiment

The advantage of using the Våntec-1 line detector is that it can simultaneously record specular and off-specular signal from the films. Using this advantage, an automated script was used to perform reflectivity measurements and the separation between specular and off-specular signal can be performed later. For each position θ_i of the X-ray tube the detector records the intensity in a range of either $2\,^\circ$ or $10\,^\circ$ for θ_f. Depending on θ_i, different accumulation times Δt, angular steps and adsorber values need to be used. The standard script used for most of the experiments is summarized in table 4.1. For small angles

Table 4.1: Standard script used for reflectivity measurements at the air-water interface. The time Δt describes the accumulation times for each angular step.

angular range θ_i	stepsize	No.	Δt/s
$0.08\,^\circ - 0.5\,^\circ$	$0.01\,^\circ$	51 (8 overlapping)	10 s
$0.51\,^\circ - 1.0\,^\circ$	$0.01\,^\circ$	50	10 s
$1.02\,^\circ - 1.50\,^\circ$	$0.02\,^\circ$	25	40 s
$1.525\,^\circ - 2.0\,^\circ$	$0.025\,^\circ$	20	30 s
$2.05\,^\circ - 3\,^\circ$	$0.05\,^\circ$	20	60 s

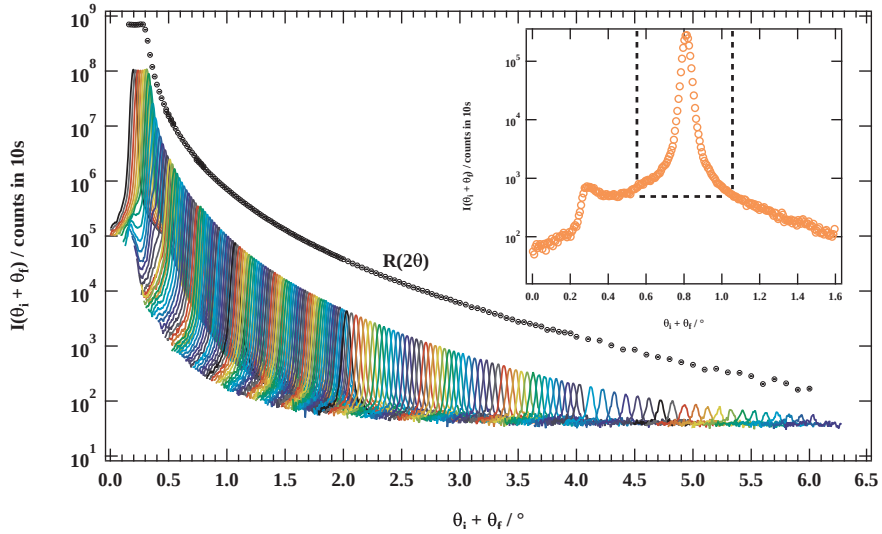

Figure 4.4: Reflectivity measured at the air-water interface. The 166 reflectivity curves as used in the standard script described in table 4.1 are shown. For each curve the background correction was performed separately as described and the reflectivity R(2θ) of the film was calculated.

(steps 1-20: absorption factor 80; steps 21-37: absorption factor 8.86) the adsorber was switched for fixed position in order to protect the detector from too intense reflections. An overlapping angular range was measured at the positions where the absorber switched. A full script takes a total time of 3810 s not including software delays between absorber switches and goniometer movements.

Calculating the specular reflectivity from the raw data was performed by a script written in *IGOR Pro* by Martin Kraska in his phD thesis [65]. This procedure works very well for interfaces or films with a weak off-specular signal. The general procedure will be briefly introduced in the following whereas a detailed description can be found here [65].

- After loading the raw data, each reflection signal is equally processed. For each angular step, the reflection maximum ($\theta_f = \theta_i$) with 50 points on each side is cut out of the initial data. This leads to a total angular range of 0.6 ° for each θ_i position which is illustrated in the inset of figure 4.4. A statistical error $\sqrt{I}$ is calculated for each of those 100 points.

- In a second step the raw data is corrected for absorber factors and different accumulation times in the script. In the data shown in figure 4.4, all reflection curves are normalized for an accumulation time of 10 s.

- The most important feature of the script is its reliability for calculating the reflectivity R(2θ) from the 166 different raw data curves. It is possible to measure R up to $2\theta = 5 - 6°$ due to a script used for background correction of the data. The background correction works as described in the following. As long as the ratio between background level and maximum intensity is small, a constant factor (lowest intensity of the 100 data points marked by the dashed lines in figure 4.4) is substracted from the data. If the ratio increases up to a threshold k (adjustable in the software), a polynomial function of fourth order is used for the background correction. This is

especially useful for an asymmetrical background. Finally, the reflected intensity is calculated by integrating the background corrected scattering profile.

As already mentioned before the script works very well for liquids like water, shown in figure 4.4, but also polymer films without any strong diffuse scattering. The specular reflectivities obtained by this procedure have been analyzed using the Motofit Reflectometry package, rev. 409 [67] for IGOR Pro. For strong diffuse signals the background correction fails and the data from the films have to be processed individually. In this work this was the case for the reflectivity experiments on iron oxide nanoparticles.

4.3 Small Angle X-Ray Scattering

Small angle X-ray scattering (SAXS) was performed using a laboratory X-ray set-up by Molecular Metrology. The K_α-line of a conventional copper X-ray tube with a wave length of $\lambda = 1.54\,\text{Å}$ is used and further monochromated by a Goebel mirror. The point focus is further collimated by three pinholes focussing the beam on the sample. The detector-sample distance is 1.5 m and the q calibration of the instrument is done by measuring the first peak of silver behenate as a calibration sample [68]. The scattered intensities are measured with a two-dimensional multi-wire gas detector (1024 *x* 1024 pixels). The minimum q resolution of $0.0012\,\text{Å}^{-1}$ of the detector is given by the distance between two pixels. However, the overall instrumental resolution is estimated to be $\Delta q = 0.01\,\text{Å}^{-1}$ by the full width half maximum of the silver behenate peak during calibration. The accessible q range is $0.007\,\text{Å}^{-1} \leq q \leq 0.25\,\text{Å}^{-1}$ and the data was radially averaged because the scattering was isotropic [69].

4.4 Brewster-Angle-Microscopy

Brewster Angle Microscopy (BAM) measurements were performed on an Accurion Nanofilm Ultrabam. The optical setup is placed on the already described Langmuir setup (KSV NIMA Langmuir Trough Large, (58 *x* 14.5) cm^2). Sample preparation and cleaning process were performed as described for the preparation of a Langmuir monolayer. In the optical setup, a laser (max. Power: 50 mW) with a wavelength of 658 nm illuminates an area of (800 *x* 430) μm^2 and the reflected beam is detected by a CCD camera with 1360 *x* 1024 pixels. Special imaging optics are used that guarantee a true lateral resolution of 2 μm for the Brewster angle of water (53.1°).

The measurements were performed under two different experimental conditions. In the first one only p-polarized light is allowed to pass polarizer and analyzer. Under this condition no light is reflected from the water surface and the image is black. When a film is prepared, any changes in the intensity are directly related to the optical properties of the film. In the second setup, a small amount of s-polarized light is merged into the detected light, thus tuning the contrast and leading to images for visualizing purposes. This way optical anisotropies of the layer are revealed that correspond to substructures with long range orientation order. In all images shown it will be specified under which conditions they were obtained [70].

5 Solvent Properties of the Air-Water Interface

This chapter focuses on the solvent properties of the air-water interface for different polymers. A brief introduction on the theoretical approach of de Gennes's *Scaling Concepts in Polymer Physics* is given in Chapter 2.2.1, however, experimental proof of this in two dimensions (2D) is still part of current research [5,29,30]. Suitable polymer systems to probe de Gennes's theory need to be insoluble in water while also forming single monomer-thick films at the air-water interface. Therefore, a major challenge for the research on 2D polymer films is to ensure a strict 2D conformation of the polymer films. Experiments indicate that in the most promising cases the polymer films are only in a quasi 2D state at the interface because it is almost impossible to restrict the spatial degree of freedom perpendicular to the interface.

In the following part, three different cases are presented. At first, poly(methyl methacrylate) (PMMA) is presented as an example for θ-solvent conditions at the air-water interface. PMMA is a hydrophobic polymer that is not soluble in water. It belongs to the group of acrylate polymers that are known as a promising group for experiments on 2D properties such as polymer scaling laws or glass transition in thin films [30,71–75]. Secondly, poly(2-vinylpyridine) (P2vP) is discussed being an example for good solvent conditions at the air-water interface. P2vP belongs to the group of hydrophilic polymers, however, it's solubility in water strongly depends on the pH of the water subphase. In a slightly acidic environment of $pH = 4.9$, the solubility of P2vP is very good [76]. This leads to the third case of intermediate conditions. Poly(*n*-butyl acrylate) (P*n*BA) homopolymers and diblock copolymers of P*n*BA and poly(ethylene glycol) (PEG) are investigated. In the diblock copolymers, the PEG anchor has a constant size of six monomers and is covalently attached to P*n*BA blocks of different molecular weights. The design of the polymers leads to an increasing hydrophilic (PEG) volume fraction in the diblock copolymers. Additionally, two homopolymers with molecular weights comparable to two of the block copolymers (one small and one large molecular weight) were used to understand the intermediate case.

A detailed study on the three systems being spread on the water interface is presented using the Langmuir technique. Results from concentration isotherm, compression isotherms and BAM imaging are used to provide a full description of the film properties. This allows for a test of the scaling laws for polymer solutions in two dimensions proposed by de Gennes in 1979 [7].

5.1 θ-Solvent Conditions: PMMA at the Air-Water Interface

Poly(methyl methacrylate) (PMMA) samples were purchased from *Polymer Standards Service (PSS) GmBH* located in Mainz. The molecular weight of a PMMA monomer unit

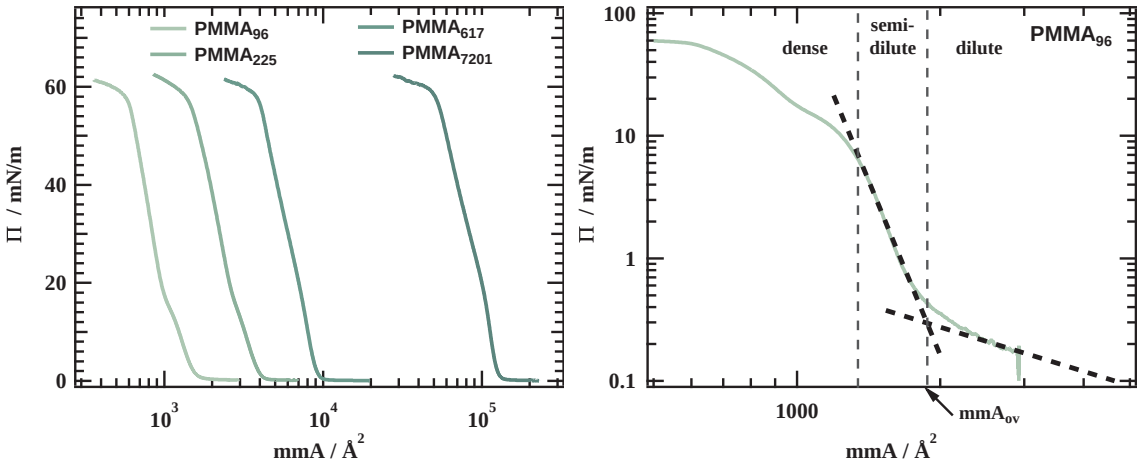

Figure 5.1: In the left panel compression isotherms as Π vs. mmA are shown for PMMA homopolymers with different molecular weights summarized in table 5.1. The right panel shows a detailed investigation of $PMMA_{96}$. The isotherm can be separated in three different regimes: dilute, semi-dilute and dense. The dashed lines present characteristic power laws for the surface pressure in the respective regime.

$(C_5H_8O_2)_n$ is $M_{mon} = 100.12\,g/mol$ and the tacticity of the samples is atactic. In Table 5.1, the molecular properties of the polymers used are summarized as provided by the supplier. As described in chapter 4.1, the samples were solved in chloroform at a concentration of $c \approx 1\,mg/ml$ and then spread on the water surface. First, results from the compression isotherms will be discussed.

Compression Isotherms

In the left panel of figure 5.1 compression isotherms are shown as surface pressure Π vs. *mean molecular area* mmA. The isotherms shift to larger areas with increasing molecular weight but their overall shape is similar for all molecular weights. For large areas, the surface pressure is almost zero and the monolayer can be compressed without any considerable changes in the surface pressure. With decreasing area the slope of the isotherm changes and the surface pressure increases steadily until it reaches a value of $\Pi \approx 60\,mN/m$. Apparently, in this part of the isotherm it can be seen that the individual shape of the isotherm changes slightly with molecular weight. For a surface pressure of $14\,mN/m < \Pi < 18\,mN/m$, a small kink is clearly visible for $PMMA_{96}$ that vanishes with increasing molecular weight. The same kink has been observed in other studies on PMMA corresponding to an additional phase transition[73,77]. This transition will be discussed later on in more detail.

Table 5.1: Names, molecular weights M_n, number of PMMA monomers N_{PMMA} and polydispersities (PDI) of the PMMA polymers used in this work.

sample name	M_n [kg/mol]	N_{PMMA}	PDI
$PMMA_{100}$	9.66	96	1.03
$PMMA_{230}$	22.5	225	1.03
$PMMA_{620}$	61.8	617	1.05
$PMMA_{7200}$	721	7201	1.10

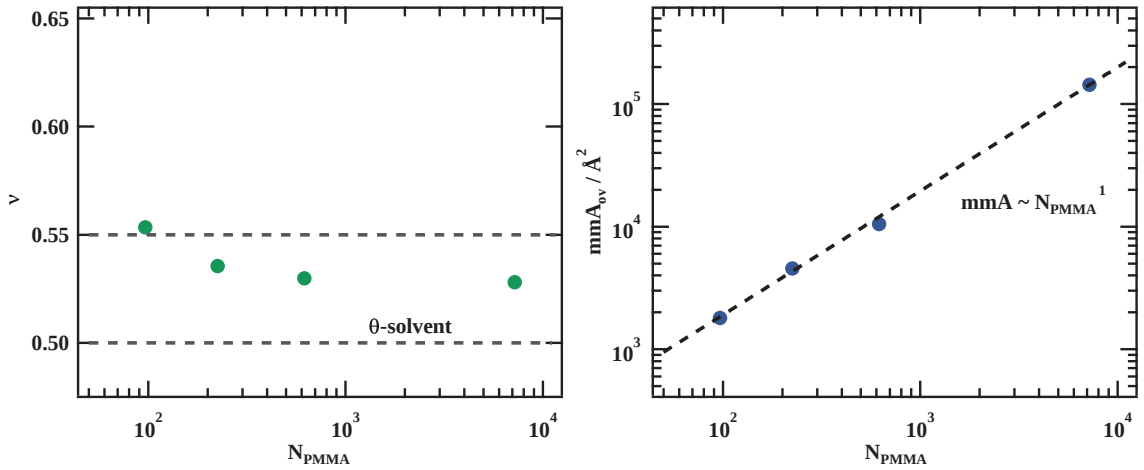

Figure 5.2: The left panel shows the 2D Flory exponent ν vs. the number of PMMA monomers N_{PMMA} in the samples. The exponents are within the expected range for the air-water interface acting as a θ-solvent. The right panel presents the area scaling of mmA_{ov} vs. N_{PMMA} for all samples. The area mmA_{ov} represents the area occupied at the overlap concentration. The error bars are within symbols.

In the right panel of figure 5.1, $PMMA_{96}$ is used as an example to illustrate the detailed characterization of each isotherm. Compared to the left panel the isotherm is now plotted in the double logarithmic presentation to identify possible power laws. The isotherms can be separated in three different regimes (dilute, semi-dilute and dense regime). In the dilute regime the polymer chains are well separated and each chain occupies a relatively large area. Reducing the area for each chain leads to an increasing surface pressure due to interaction between different chains. In the dense regime the quasi 2D conformation is usually broken leading to a film collapse or a transition into a 3D conformation. In the simplified picture of a two dimensional (2D) polymer film, the dilute regime can be interpreted as a 2D analogy of an ideal gas. The surface pressure in the dilute regime is supposed to follow a power law ($\Pi \sim \mathrm{mmA}^{-y}$ with $y=1$ in the dilute regime). For compression isotherms it is usually difficult to verify this behaviour due to the limited data in this regime. In the semi-dilute regime, the surface pressure can be determined with great accuracy over a wide range. As described in equation (2.16), the surface pressure Π in the semi-dilute regime can be expressed in terms of mmA ($\mathrm{mmA} \sim c_m^{-1}$) through a power law

$$\Pi \sim \mathrm{mmA}^{-y} \quad \text{with} \quad y = \frac{2\nu}{2\nu - 1} \tag{5.1}$$

that only depends on the solvent quality of the interface characterized by the 2D Flory-exponent ν.

Figure 5.1 shows that the power laws in the dilute and semi-dilute regime are able to describe the experimental data very well. In the dilute regime the exponent obtained from the power law is $y = 1.5 \pm 0.2$. This result is within an acceptable range for the predicted ideal gas behaviour, especially taking into account that the film is already prepared close to the crossover into the semi-dilute regime where the slope increases. Of greater interest is the power law in the semi-dilute regime. For a surface pressure ranging between $0.5 - 8\,\mathrm{mN/m}$, it can be perfectly described by equation (5.1). The 2D Flory-exponents

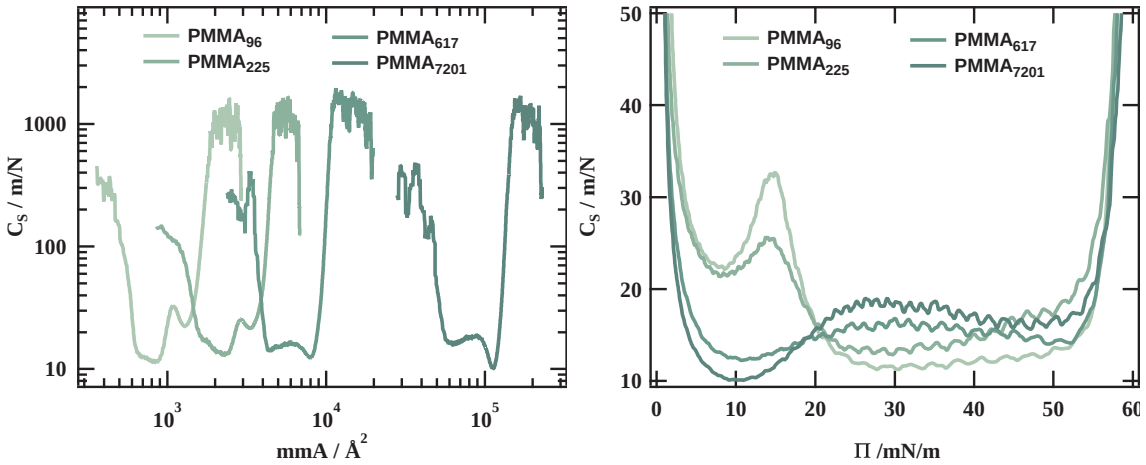

Figure 5.3: Compressibility C_S calculated from the compression isotherms in figure 5.1. In the left panel C_S plotted vs. mmA and vs. Π in the right panel. For a surface pressure of $\Pi \approx 15\,\mathrm{mN/m}$ a clear maximum characteristic for a phase transition becomes visible with decreasing molecular weight.

ν of the samples are displayed in figure 5.2. We get Flory exponents that are within the experimentally measured limits for a θ-solvent for all molecular weights. It becomes also apparent that ν slightly decreases with increasing molecular weight. On average the Flory exponent of the film is $\nu_{\mathrm{PMMA}} = 0.53 \pm 0.01$ with PMMA_{96} being the exception with an Flory exponent of 0.55. This slightly higher value might be the influence of the phase transition (plateau at $\Pi \approx 15\,\mathrm{mN/m}$) in the isotherm.

Another important quantity is the crossover from dilute to semi-dilute regime that can be identified by the intersection of the two power laws. $\mathrm{mmA_{ov}}$ is the area where different polymer chains start to overlap and therefore marks the beginning of the semi-dilute regime. We can relate $\mathrm{mmA_{ov}}$ to the Flory radius $\mathrm{R_F}$ ($\mathrm{mmA_{ov}} = \pi \mathrm{R_F^2}$). As described in equation (2.5), the Flory radius scales with the number of monomers N as $\mathrm{R_F} \sim kN^{\nu}$ with k as the Kuhn length. The right panel of figure 5.2 points out that $\mathrm{mmA_{ov}} \sim \mathrm{N_{PMMA}^1}$ scales as expected for the air-water interface as a θ-solvent confirming the results from the pressure scaling. Furthermore, using the relation between mmA and $\mathrm{R_F}$ it is possible to determine a Kuhn length of $k_{\mathrm{comp}} = (2.4 \pm 0.2)\,\text{Å}$ which is close to the monomer size and values reported in literature for the 2D [72] and 3D case [78].

Compressibility of the Films

A different approach to separate the isotherm in regimes is given by the compressibility of the films. The compressibility C_S can be directly calculated from the compression isotherm as described in chapter 2.2. In figure 5.3, C_S is plotted vs. mmA in the left panel and vs. Π in the right panel. The general shape of C_S in the double logarithmic plot is similar for all molecular weights. The high compressibility $C_S \approx 1000\,\mathrm{m/N}$ for large areas indicates that the film can be easily compressed. This is in agreement with the picture of the polymer chains in the dilute regime. Upon compression, the compressibility reduces to $C_S \approx 10 - 30\,\mathrm{m/N}$ with slightly different shapes for the studied molecular weights. The small oscillations (visible in the right panel) are produced by the numerical calculation of the compressibility. Finally, it rises again to values around $200 - 400\,\mathrm{m/N}$. The different behaviour becomes more apparent if C_S is plotted vs. Π on a linear scale.

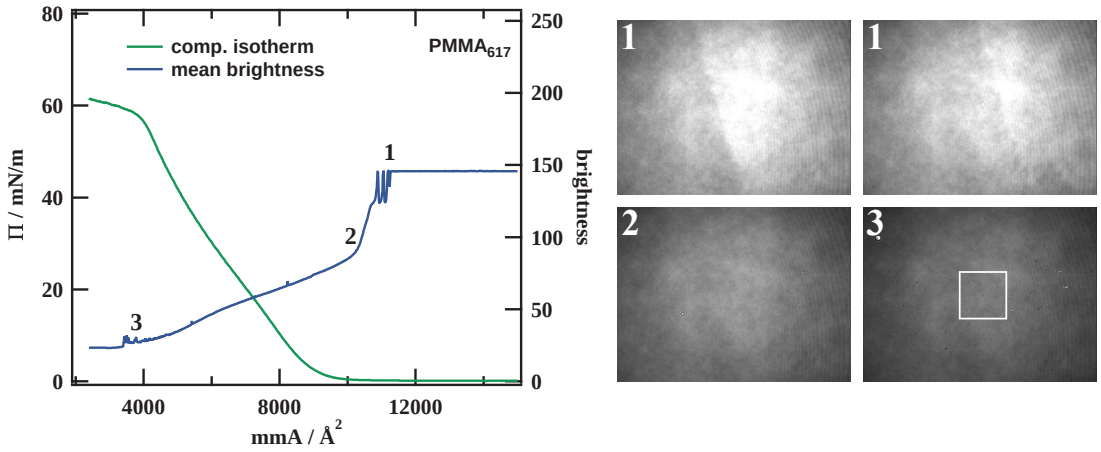

Figure 5.4: The left panel presents the compression isotherm of $PMMA_{617}$ and the respective brightness values (greyscale from 0 to 255) during compression. The right panel shows 4 images taken during compression. The images represent the positions marked by the numbers in the isotherm on the left side. The white rectangle shown in picture 3 ($150\,x\,150\,\mu m^2$) illustrates the area over which the brightness was derived. Here, the value for the reflection from a bare water surface was roughly 146.

A maximum is visible at $\Pi \approx 15\,mN/m$ for the two smaller polymers ($N_{PMMA} = 96, 225$) that vanishes with increasing molecular weight. The two largest samples do not show the maximum at all. A maximum in C_S is characteristic for a phase transition in the monolayer. Upon compression the conformation of the polymer chains changes which leads to a film structure that can be compressed more easily due to the coexistence of two phases in the transition. After the transition has occurred the compressibilty reduces again which indicates that the new conformation is already a closely packed one.

As already mentioned in the discussion of the isotherms, the phase transition has also been observed in literature [77]. Two molecular weights ($N_{PMMA} = 150, 1200$) of syndiotactic PMMA at 30 °C were compared with a similar transition occurring in the smaller molecular weight. The transition can also be triggered in the larger molecular weight if the isotherm is recorded for temperatures over 40 °C. The conclusion is that the transition is connected to the mobility of the chains. Miñones et al. suggest that during the transition the polymer segments are getting strongly folded and directed out of the interface forming loops and tails. Hence, the number of contact points with the water subphase reduces. They come to this conclusion because they observe a steady increase in film thickness during compression instead of a pronounced increase into a two layer system during the phase transition (plateau regime) [72,77]. Additionally, Hsu et al. confirms this observation with their experiments on PMMA of different tacticity and large molecular weight ($N_{PMMA} = 1000$) at room temperature. The isotactic iPMMA and atactic aPMMA isotherms showed the phase transition while the syndiotactic sPMMA did not show it [73]. They conclude that iPMMA and aPMMA are able to form folded structures due to their higher flexibility compared to sPMMA. However, at higher temperature the flexibility of sPMMA increases and the phase transition can also be observed in the isotherm.

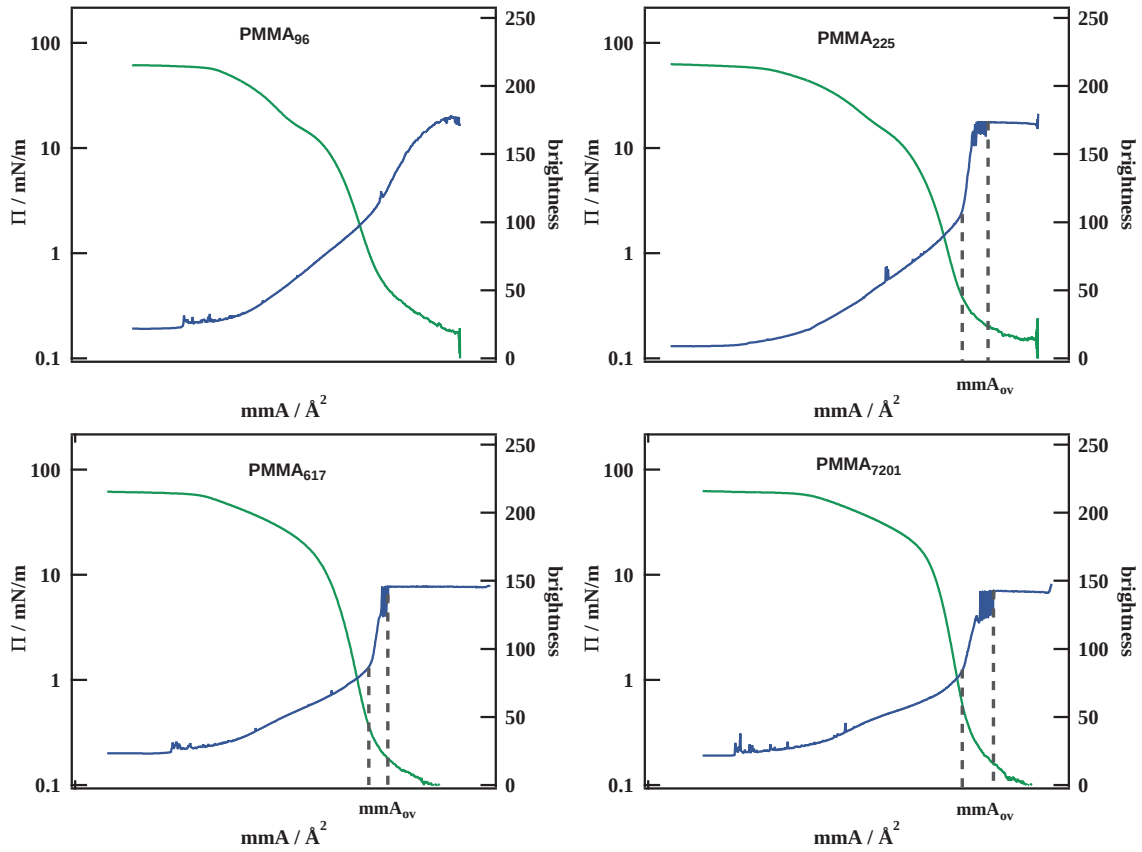

Figure 5.5: Comparison of the compression isotherm with simultaneous brightness measurement for all samples of PMMA. The slope of the brightness curve for $PMMA_{96}$ is qualitatively different from the other three samples. The data is presented in the double logarithmic axis representation.

Brightness Measurements

Further characterization of the films is also possible if Brewster-Angle-Microscopy is performed simultaneously to the compression isotherm. Such a measurement is shown in figure 5.4 with $PMMA_{617}$ being a representative example. Additional to the compression isotherm the corresponding brightness values are plotted against the right axis. The mean brightness is calculated in a frame of $150\,x\,150\,\mu m^2$ with the maximum value of 255. The mean value for the pure water surface is 146 since polarizer and analyzer were adjusted in a way that the reflection of the water was not suppressed.

Upon compression of the film, there is no change in the mean brightness at first, however a kink appears where the intensity starts to fluctuate first and then starts to decrease. Looking at the pictures taken at the point where the fluctuations in the brightness start (number 1 in figure 5.4), dark wave fronts enter and leave the picture frame leading to these fluctuations until a wave-front enters the picture frame without leaving it again. These dark wave-fronts are regimes where a PMMA layer has already formed and they are compressed together until the surface is fully covered by them. This raises the question whether the polymer chains in the dilute regime are really well separated from each other. In this compression isotherm it looks like macroscopic polymer regions are formed first, which are then compressed until they fully cover the interface. Right after the interface

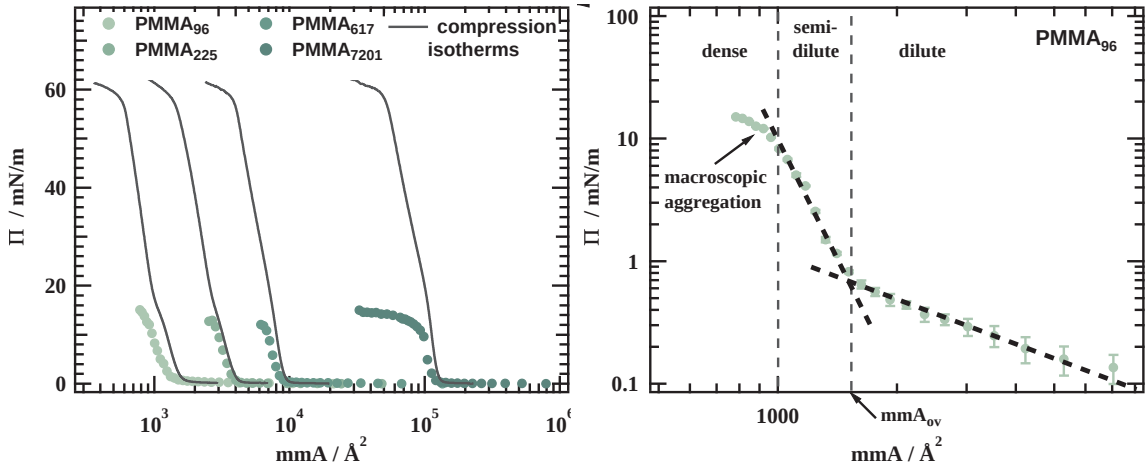

Figure 5.6: In the left panel concentration isotherms as Π vs. mmA are shown for PMMA homopolymers with different molecular weights summarized in table 5.1.The previous discussed compression isotherms are plotted as grey lines for comparision. The right panel shows a detailed investigation of $PMMA_{96}$. The isotherm can be separated in three different regimes: dilute, semi-dilute and dense. The dashed lines present characteristic power laws for the surface pressure in the respective regime. In the dense regime ($\Pi \approx 12\,\mathrm{mN/m}$) macroscopic aggregation visible by naked eye occurs while increasing the surface pressure with the hamilton syringe.

is fully covered, the intensity at the interface decreases very fast until the slope changes once again at a well defined point. Looking at the double logarithmic representation of the data in figure 5.5, it seems like the crossover region between dilute to semi-dilute regime is confined by these two characteristic points in the brightness measurements for $PMMA_{225,617,7201}$. After the kink, the intensity reduces steadily without any more noteworthy changes. Occasionally small aggregates can be observed in the BAM images and their number slightly increases with rising surface pressure (see picture 2 and 3 in figure 5.4). The appearance of aggregates is usually an indicator of structural changes in the monolayer, however here, their number stays quite small and it is more likely that they are regions where the film is partially ruptured.

While the mean brightness value during compression is almost the same for the three larger molecular weights, the slope of $PMMA_{96}$ is different (see figure 5.5). No plateau exists in the brightness during the dilute regime and there is also no kink in the slope. In the crossover region no wave-fronts are visible that could be related to island-like structures but a steady decrease of the mean brightness. This observation indicates that the conformation of the polymer chains is different for the smallest molecular weight. The mobility of the smaller chains is faster compared to the larger chains and therefore, it is easier for the chains to be well separated due to entropic forces. Upon compression they move closer to each other which leads to a steady decrease of the mean brightness.

Concentration Isotherms

Concentration isotherm measure the equilibrium surface pressure and are therefore another recording technique that is able to complement the non-equilibrium measurements of the compression isotherm. Details on how to record them are described in chapter 4.1. In the left panel of figure 5.6 compression and concentration isotherm are shown simulta-

Table 5.2: Comparison of parameters obtained from power law fits in the dilute and semi-dilute regime. Upper section: Dilute regime with $\pi \sim \mathrm{mmA}^{-y}$, expected value of $y = 1$ for an ideal gas. Lower section: Semi-dilute regime $\Pi \sim \mathrm{mmA}^{\frac{2\nu}{2\nu-1}}$ with the Flory-exponent $\nu_{\theta-\mathrm{solvent}} = 0.5$—$0.55$ expected for a θ-solvent.

Exponent y (dilute)	$PMMA_{96}$	$PMMA_{225}$	$PMMA_{617}$	$PMMA_{7201}$
compression isotherm	1.7	1.3	1.5	1.6
concentration isotherm	1.1	0.9	0.7	0.6
Flory-exponent ν				
compression isotherm	0.55	0.54	0.53	0.53
concentration isotherm	0.58	0.55	0.55	0.54

neously for comparison. In contrast to the compression isotherm, the surface area can only be increased step-wise which leads to much less recorded points in the isotherm. With a concentration isotherm the surface pressure cannot be increased above a value of around 12 mN/m before macroscopic drops remain in the film that are visible by the naked eye. This is in agreement with the spreading coefficient $S = 13\,\mathrm{mN/m}$ [66] for chloroform limiting the effective Π range in which concentration isotherms can be recorded to the dilute and the semi-dilute regime. Compression isotherms in comparison can be compressed up to a surface pressure of 60 mN/m (dense regime). However, the concentration isotherms provide a much better resolution of the dilute regime because low surface coverage can be accomplished easily (see right panel of figure 5.6). The concentration isotherms are slightly shifted to smaller areas, especially visible for $PMMA_{96}$.

For a detailed comparison the isotherms were also individually characterized as shown in the right panel of figure 5.6. The polymer scaling laws for dilute and semi-dilute regime are able to describe isotherms perfectly. Even at the crossover from dilute to semi-dilute regime, the power laws perfectly match the experimental data which is different to what has been observed for the compression isotherm in figure 5.1. In the dilute regime a scaling exponent of $y = 1$ for $PMMA_{96}$ that decreases to $y = 0.61$ with increasing molecular weight can be determined, while the average Flory-exponent in the semi-dilute regime is $\nu_{\mathrm{PMMA}} = 0.55 \pm 0.01$. As already observed for the compression isotherms, $PMMA_{96}$ gives a slightly larger $\nu = 0.58$. The crossover from dilute to semi-dilute $\mathrm{mmA_{ov}}$ can also be determined with high accuracy. Again, the scaling for $\mathrm{mmA_{ov}}$ vs $\mathrm{N_{PMMA}}$ verifies the power law determined for the compression isotherms in figure 5.2 ($\mathrm{mmA_{ov}} \sim \mathrm{N_{PMMA}^1}$). Calculating the area for a single monomer leads to a Kuhn length of $k_{\mathrm{conc}} = (2.1 \pm 0.2)\,\text{Å}$ slightly smaller compared to $k_{\mathrm{comp}} = (2.4 \pm 0.2)\,\text{Å}$.

Comparison of Results

- Dilute regime: The concentration isotherm provide a much larger data range to analyze the power law in the dilute regime. Compared to compression isotherms the slope is smaller and matches the expectations for the air-water being a θ-solvent (see table 5.2) within the virial expansion (see equation (2.12)). The beginning of the semi-dilute regime characterized by $\mathrm{mmA_{ov}}$ is also a sharp transition compared to a more steady one for the compression isotherms. The Kuhn length obtained by the two techniques are $k_{\mathrm{comp}} = (2.4 \pm 0.2)\,\text{Å}$ and $k_{\mathrm{conc}} = (2.1 \pm 0.2)\,\text{Å}$ which are within error range of each other. The Kuhn length is in good agreement with values from literature [72,78].

- Semi-dilute regime: The power law in the semi-dilute regime can be described very well for both, compression and concentration isotherms. The exponents obtained for the compression isotherms are slightly larger than for the concentration isotherm as already observed in the dilute regime. This seems reasonable since the compression isotherm do not measure the equilibrium pressure, however another effect has to be considered at this point. For the concentration isotherm macroscopic aggregation can be observed by naked eye if the pressure is increased to $\Pi \approx 12\,\mathrm{mN/m}$. In a dense layer local aggregation might already occur on a smaller length scale leading to a decrease of the power law exponent. Still, in both cases the air-water interface can be characterized as a θ-solvent and no clear advantage can be pointed out between both techniques.

- For $PMMA_{96}$ and $PMMA_{225}$, the compression isotherm shows a phase transition for $\Pi \approx 15\,\mathrm{mN/m}$. The plateau cannot be observed in concentration isotherms because it is not possible to increase the surface pressure to this value. There have been reports on this phase transition in literature connecting it to different tacticities, molecular weights and temperatures for PMMA[73,77]. The idea is that the chain is able to form folded structures upon compression to reduce the contact area with the water subphase. The ability of the film to form those structures depends on its flexibility. The brightness measurements indicate that the larger polymer chains are already aggregated in the dilute regime. Therefore, folded structures between different chains might already exists while the film is prepared. The brightness measurement of the smallest molecular weight indicates that the chains are separated in the dilute regime and upon compression into a dense state folded structures start to form to reduce the contact area to the water. Increasing the temperature in the experiment leads to a higher flexibility so that the transition can also be observed in higher molecular weights and even for less flexible stereoisomers.

5.2 Good Solvent Conditions: P2vP at the Air-Water Interface

To investigate good solvent conditions at the air-water interface, six different P2vP homopolymers were synthesized in the group of Dr. Markus Gallei from the Ernst-Berl-Institute at the TU Darmstadt. The molecular weight of a P2vP monomer unit $(C_7H_7N)_n$ is $M_{mon} = 105.13\,\mathrm{g/mol}$. The chemical structure of the monomer is a carbon chain with a pyridine side group. Under neutral or alkaline conditions P2vP is insoluble in water, however at a *pH* beneath five, P2vP is protonated rendering it soluble in water[76]. Monolayers

Table 5.3: Names, molecular weights M_n and number of P2vP monomers N_{P2vP} of the P2vP polymers used in this work.

sample name	M_n [kg/mol]	N_{P2VP}
$P2vP_9$	0.94	9
$P2vP_{47}$	4.9	47
$P2vP_{250}$	26.3	250
$P2vP_{472}$	49.6	472
$P2vP_{822}$	86.4	822
$P2vP_{2853}$	300	2853

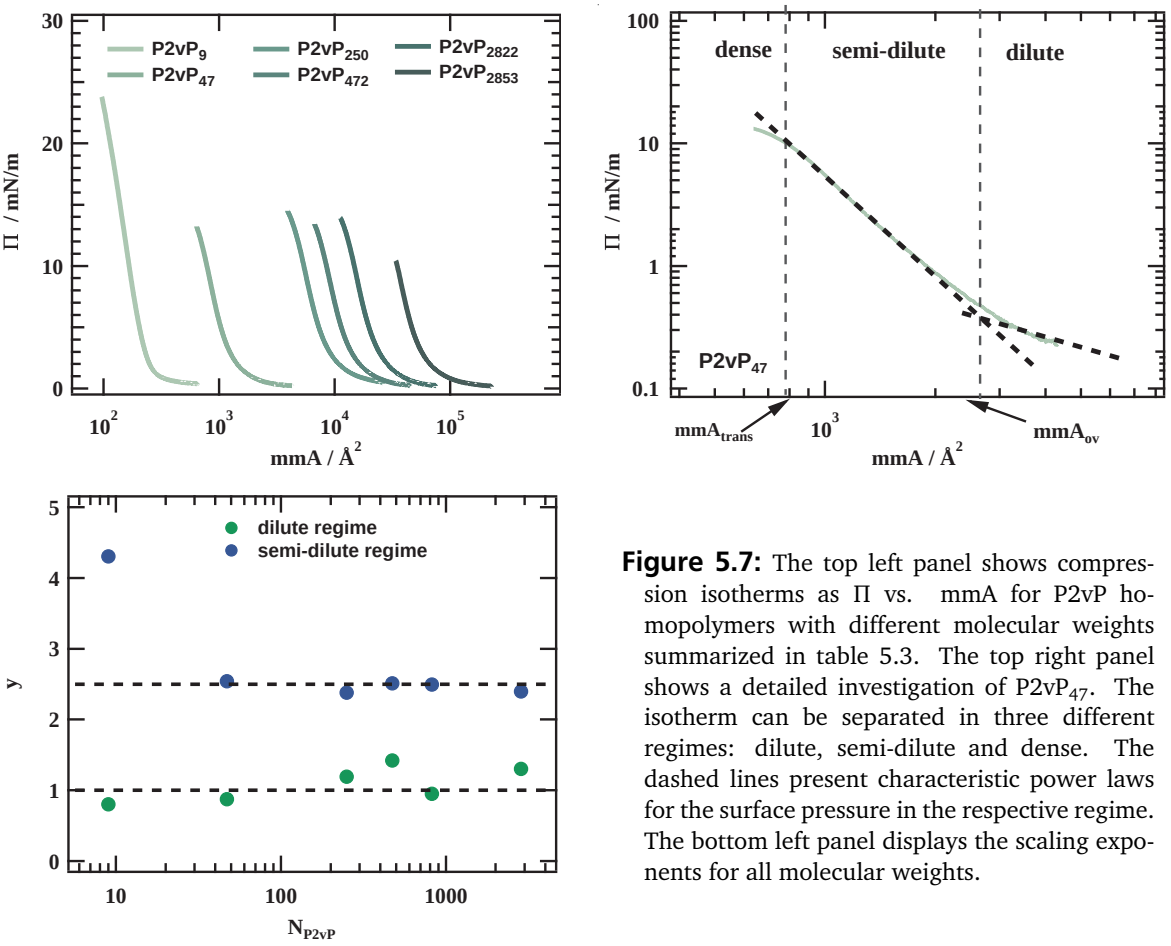

Figure 5.7: The top left panel shows compression isotherms as Π vs. mmA for P2vP homopolymers with different molecular weights summarized in table 5.3. The top right panel shows a detailed investigation of $P2vP_{47}$. The isotherm can be separated in three different regimes: dilute, semi-dilute and dense. The dashed lines present characteristic power laws for the surface pressure in the respective regime. The bottom left panel displays the scaling exponents for all molecular weights.

of PvFc-b-P2vP block copolymers have shown good solvent conditions at the air-water interface[5]. In Table 5.1 the properties of the synthesized polymers are summarized. As described in chapter 4.1, the samples were dissolved in chloroform at a concentration of $c \approx 1\,\mathrm{mg/ml}$ and then spread on the water surface. First, results of the compression isotherms will be discussed.

Compression Isotherms

The isotherms obtained during compression apparently display a comparable shape independent of molecular weight. The left panel in figure 5.7 shows the isotherms as surface pressure Π vs. mean molecular weight mmA. With increasing molecular weight the isotherms shift to larger values of mmA. The molecular weights reach different maximum surface pressures due to the limits of the trough. The semi-dilute regime is limited to the region of $\Pi < 10 - 12\,\mathrm{mN/m}$, so that all isotherms provide a sufficient Π range for the following investigations.

In the right panel of figure 5.7, $P2vP_{47}$ is shown to illustrate the further characterization of each isotherm. The isotherm can be separated in three regimes, however, the third regime is not clearly visible in all molecular weights due to the limits set forth by the trough. In the dilute regime all polymer chains are well separated occupying a large area. This leads to the surface pressure slowly increasing upon compression. When the area

for each chain is reduced further, polymer chains start to interact and the slope changes. In the semi-dilute regime, the surface pressure steadily increases until the slope starts to deviate at a pressure of $\Pi \approx 10\,\mathrm{mN/m}$. Later it will be shown that there is indeed a dense regime using data of the concentration isotherms.

The surface pressure in the dilute and semi-dilute regime can be described by power laws as shown in figure 5.7. Due to the limited data in the dilute regime it is difficult to accurately determine the scaling in this regime. The number of points is not sufficient to use the virial expansion from equation (2.12) extended to the second term. Herein, only the first term of the virial expansion is treated ($\Pi \sim mmA^{-y}$) while the focus is on how much does the exponent deviates from the expected -1 scaling. In the semi-dilute regime, the accessible Π range between $1-10\,\mathrm{mN/m}$ allows a good description of the pressure scaling using equation (5.1). The exponents obtained for both regimes are plotted in figure 5.7. In the dilute regime the exponent is $y \approx 1$ and increases slightly with molecular weight. In the virial expansion in equation (2.12), we expect an exponent being a little larger than 1 due to interactions between different chains as an effect of the second virial coefficient. It is reasonable that this influence is stronger for larger chains. In the semi-dilute regime, the exponent is $y \approx 2.5$ for the five larger molecular weights. Only the smallest sample $\mathrm{P2vP_9}$ shows a larger exponent slightly above 4.

This polymer only has 9 monomer units and it is questionable whether the theory based on coil statistics is suitable for describing this system. The exponent of the other samples is below the limit of $y = 3$ for good solvent conditions at the air-water interface[71]. This raises the question on how the exponent can be smaller than the expectations for good solvent conditions. The solubility of P2vP in a slightly acidic water environment ($pH = 4.9$) is very good[76]. Water under the influence of the atmosphere has a pH value of around $pH = 5.6$[79] which leaves the question how strong is the solubility of P2vP in water already influenced. The lower slope might indicate that polymers are able to submerge into the water like it has been observed for PEG in various cases[13,74,80,81]. If a fraction of polymers is already able to be dissolved into the subphase, then the polymers can even start to absorb again on the other side of the barrier again during a compression experiment. Consequently, the surface pressure would be affected in a way that cannot be monitored.

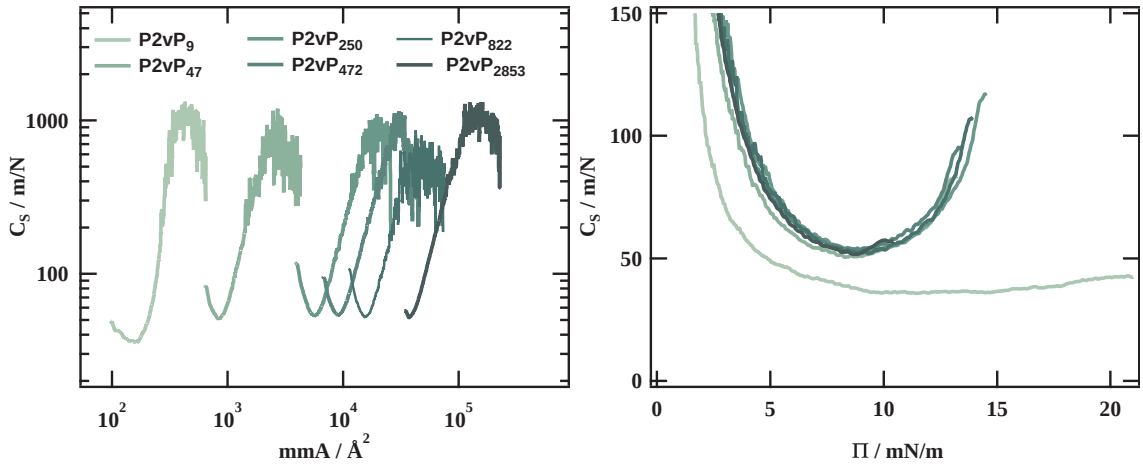

Figure 5.8: Compressibility C_S calculated from the compression isotherms in figure 5.7. In the left panel C_S plotted vs. mmA and vs. Π in the right panel. For a surface pressure of $\Pi \approx 8\,\mathrm{mN/m}$ a clear minimum is observed for all molecular weights except $P2vP_9$. The compressibility of $P2vP_9$ decays until reaching a plateau at $C_{S,min} \approx 40\,\mathrm{m/N}$ for surface pressures $\Pi > 10\,\mathrm{mN/m}$.

Compressibility of the Films

The compressibility of all molecular weights are displayed in figure 5.8. At first sight they all show a shape independent of molecular weight when shown vs. mmA, however when plotted over Π on a linear scale the compressibility of $P2vP_9$ deviates from the rest. A distinct minimum is visible for all samples for $C_{S,min} = 51\,\mathrm{m/N}$ at $\Pi \approx 9\,\mathrm{mN/m}$ with exception of $P2vP_9$. Instead of the minimum, the slope for $P2vP_9$ decays and shows a plateau of $C_S \approx (40 \pm 2)\,\mathrm{m/N}$ for the surface pressure in the range of $8 - 20\,\mathrm{mN/m}$. This value is in the characteristic range of a Langmuir monolayer in the liquid-expanded state [77]. The broad plateau in the compressibility is also equivalent to a linear slope of the surface pressure-area isotherm which is often observed in isotherms of short amphiphilic molecules (e.g. behenic or stearic acid).

Brightness Measurements

Brewster-Angle-Microscopy was performed simultaneously to the compression isotherms. In figure 5.9 the results of such an experiment are shown with $P2vP_9$ as an example. The mean brightness is calculated in a frame of $100\,x\,100\,\mu m^2$ in a range between 0 and 255. The mean value for the pure water surface was 126. After preparation of the film, the averaged reflected intensity roughly matches the bare water interface. Upon compression the intensity reduces steadily without the appearance of any characteristic features that could be related to the isotherm measurements. The two images on the right panel of figure 5.9 represent the situation in the low and high pressure regime. For low surface pressures, small aggregates (see picture 1: black dots) are visible in the layer, however upon compression the BAM images do not indicate aggregation thus simply reducing the amount of light being reflected at the interface. There are no signs of aggregation or inhomogeneities in the images.

It was not possible to identify the crossover from the dilute to semi-dilute regime as for PMMA, however, in case of the two largest molecular weights strong aggregation was revealed due to the imaging of the film. The isotherms measured for this case were also

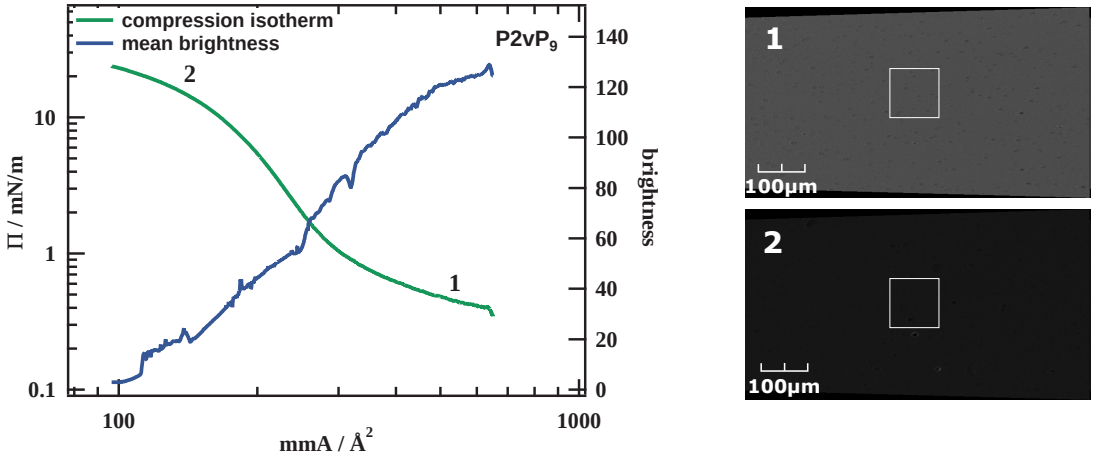

Figure 5.9: The left panel presents the compression isotherm of $P2vP_9$ and the respective brightness values (greyscale from 0 to 255) during compression. The right panel shows 2 images taken during compression. The images represent the positions marked by the numbers in the isotherm on the left side. The white rectangle shown in the images ($100\,x\,100\,\mu m^2$) illustrates the area over which the brightness was derived. Here, the value for the reflection from a bare water surface was roughly 126.

contradicting compared to the lower molecular weights which was explained by large regions of aggregated polymer on a macroscopic length visible for low surface pressures (see figure 5.10). Because of both observations, the initial samples solved in chloroform were mixed using ultrasonic waves for 30 minutes. In the second measurements no more signs of aggregation were visible with BAM imaging and the isotherms also shifted. This is an important information because it shows that the polymer can aggregate in the solvent before being spread on the interface. The aggregated samples show a different behaviour than the non-aggregated ones. A similar phenomenon has been observed in literature. Depending on the solvent used for preparation, it was possible to observe different morphologies on a macroscopic length scale in Langmuir films [66]. For all isotherms shown the samples were in the non aggregated state.

Concentrations Isotherms

The concentration isotherms for P2vP are shown in the left panel of figure 5.11. The shape of the concentration isotherms is similar to the compression isotherms that are plotted as grey lines and have been previously discussed. Although the shape is similar, the

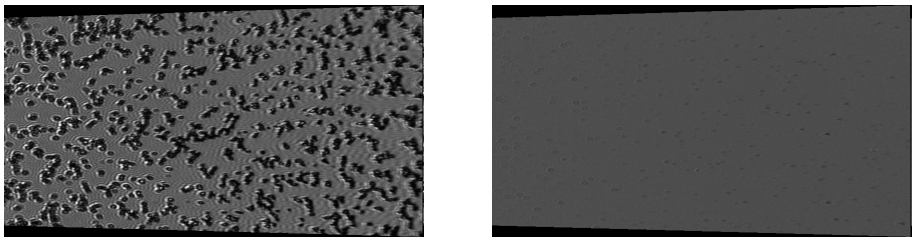

Figure 5.10: The left BAM image shows aggregation of $P2vP_{822}$ observed for low surface pressures. After treating the samples solved in chloroform with ultrasonic waves the observed film by BAM imaging was the one on the right hand side (similar surface pressure).

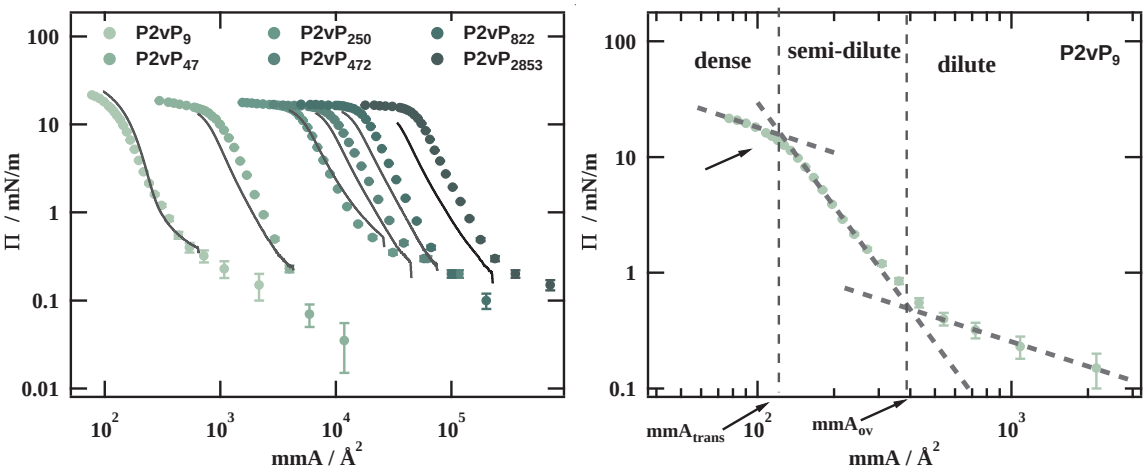

Figure 5.11: In the left panel concentration isotherms as Π vs. mmA are shown for P2vP homopolymers with different molecular weights summarized in table 5.3. The previously discussed compression isotherms are plotted in grey for comparison. The right panel shows a detailed investigation of $P2vP_9$. The isotherm can be separated in three different regimes: dilute, semi-dilute and dense. The dashed lines present characteristic power laws for the surface pressure in the respective regime.

compression isotherms seem to shift to smaller areas with increasing molecular weight. When the surface pressure increases above $\Pi \approx 10\,\mathrm{mN/m}$, the slope of the concentration isotherms changes and flattens out. Comparing the different molecular weights, it is possible to observe a plateau-like behaviour for large molecular weights while the surface pressure still increases for the smaller molecular weights. In the double logarithmic presentation, the isotherms of the $P2vP_9$ can be divided in three regimes. The right panel of figure 5.11 displays the three different regimes: dilute, semi-dilute and dense separated by the areas mmA_{ov} and mmA_{trans}. Again, we can use the simplified picture of a 2D gas, where the surface pressure can be characterized by the virial expansion (2.12) in the dilute and equation (2.16) in the semi-dilute regime. The data points in the dilute regime are restricted to a small number as it becomes apparent looking at low pressures in figure 5.11. This makes it impossible to characterize the dilute regime using the virial expansion. In the semi-dilute regime equation (2.16) can be used to determine a scaling exponent. There are two more important areas used to characterize the isotherms. One is mmA_{ov} given by the intersection of the power law in the dilute and semi-dilute regime. However, due to the limitation of the data in the dilute regime it is difficult to accurately identify it. The second area characterizes the crossover from the semi-dilute to the dense regime at mmA_{trans}. It can be well estimated using the crossover from a phenomenological power law used for the dense region and the characteristic scaling in the semi-dilute regime.

The scaling exponents y for the semi-dilute and dense regime are plotted in the left panel of figure 5.12. In the semi-dilute regime, all molecular weights lead to a consistent picture for the pressure scaling with an average exponent $y = 2.8$. This leads to a Flory-exponent of $\nu_{P2vp} = 0.78$ characterizing the air-water interface as a good solvent for P2vP. The exponents determined for the dense regime show that with increasing molecular weight the scaling of the surface pressure reduces to 0. The area scaling for mmA_{ov} and mmA_{trans} is presented in the right panel of figure 5.12. Both characteristic areas show more or less the same scaling with the number of monomers $N_{P2vP}^{1.1}$. The prediction for

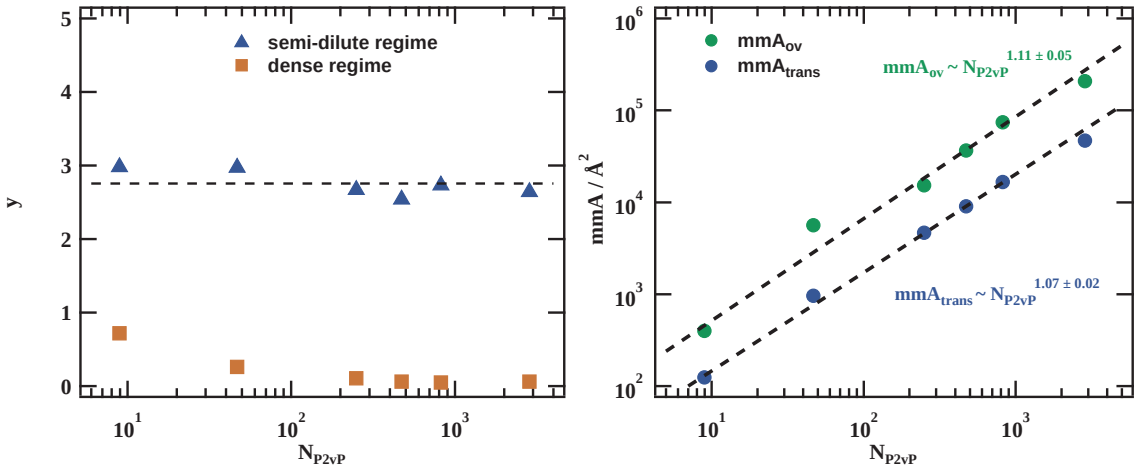

Figure 5.12: In the left panel shows the exponents for the power law fits in the semi-dilute and dense regime. The right panel displays the area scaling of two characteristic areas. The overlap from the dilute to the semi-dilute regime, $\mathrm{mmA_{ov}}$ and the overlap from the semi-dilute into the dense regime, $\mathrm{mmA_{trans}}$.

good solvent conditions is a scaling of $\mathrm{mmA} \sim \mathrm{N}^{1.5}$ [82] which we cannot confirm with our measurements. The results do not show that chains are in a swollen state at the interface. However, due to the uncertainty on the solubility of P2vP in water it is simply impossible to take any further conclusions.

Comparison of results

- Dilute regime: With both recording techniques it was difficult to obtain reliable data for the dilute regime. Results from the compression isotherms were more promising than from concentration isotherms. They indicate a scaling exponent of $y = 1$ slightly increasing with molecular weight as expected for the air-water interface being a good solvent. The reason for a slightly stronger pressure scaling is due to the effect of the second virial coefficient in the virial expansion. For PMMA, the concentration isotherms proved themselves to be more useful in this regime, however this might not be the case for P2vP because the characteristic scaling for the semi-dilute regime starts for surface pressures of around $\Pi \approx 0.3\,\mathrm{mN/m}$. Consequently, it would be necessary to measure the surface pressure with very high precision which is extremely difficult using the Langmuir technique.

- Semi-dilute regime: The power law in the semi-dilute regime can be described very well for both, compression and concentration isotherms. The Flory-exponent is $\nu_{\mathrm{P2vP}} = 0.78$ for concentration isotherms. The Flory-exponent for compression isotherms is even slightly higher.

  The problem for P2vP is its pH dependent solubility in water. For further experiments it is absolutely necessary to adjust the pH of the subphase so that the possibility of polymer dissolving is excluded. However, this would change the characteristics of the air-water interface.

5.3 Intermediate Conditions: PEG-b-P*n*BA and P*n*BA at the Air-Water Interface

For the intermediate conditions, a series of poly(*n*-butyl acrylate) (P*n*BA) homopolymers and diblock copolymers where a small hydrophilic anchor of poly(ethylene glycol) (PEG) is covalently attached to the P*n*BA block were synthesized by the group of Dr. Markus Gallei. P*n*BA is a soft amorphous polymer with a glass transition temperature of $T_G = -54\,°C$[78] and a molecular weight of $M_{mon} = 128.17\,g/mol$ for the monomer unit $(C_7H_{12}O_2)_n$. Four block copolymers with increasing PEG volume fraction were prepared to investigate the influence of the hydrophilic anchor. Additionally, two homopolymers of comparable size to two of the block copolymers were synthesized (a small and a large molecular weight). P*n*BA based monolayers (homopolymers and diblock copolymers) form stable films at the interface and share a unique phase transition in their isotherm[30,83–86]. In this section the series of P*n*BA based monolayers is investigated for the solvent properties of the air-water interface. In table 5.4, the molecular properties of the polymers are summarized. The volume fraction of PEG in the diblock copolymers is varied by the size of the P*n*BA block. All samples were dissolved in chloroform at a concentration of $c \approx 1\,mg/ml$ and spread on the water surface as described in detail in chapter 4.1. Results on the compression isotherms will be discussed first.

Compression Isotherms

The isotherms obtained during compression apparently display a universal shape independent of molecular weight. In figure 5.13 (left panel) the isotherms are shown with the homopolymers represented by the blue colors. With increasing molecular weight the isotherms shift to larger values of mmA. In particular, there is a plateau over a wide range of mmA for all samples. Such a plateau is characteristic for a phase transition in the monolayer and its structure will be further investigated in chapter 6. There is almost no difference in the compression behaviour of homopolymers and diblock copolymers with exception of the slightly lower plateau pressure Π_c for the block copolymers. This can be explained as a certain influence of the PEG block.

At high values of mmA the surface pressure Π is very low $\Pi < (1-1.5)\,mN/m$ and it increases monotonically to $\Pi_c \sim (22-23)\,mN/m$ with decreasing mmA. A characteristic change occurs at the kink (mmA_{trans}), see right panel of figure 5.13, which marks the beginning of a constant pressure regime indicating a phase transition in the monolayer. For the diblock copolymers containing a PEG block, the plateau pressure Π_c is slightly

Table 5.4: Names, molecular weights M_n, polydispersity indices (PDI), degree of polymerization N for poly(*n*-butyl acrylate) (P*n*BA) or poly(ethylene glycol) (PEG) and the volume fraction Φ_{PEG} of the polymers used in this study.

sample name	M_n [kg/mol]	PDI	N_{PnBA}	N_{PEG}	Φ_{PEG}[%]
PEG_6-*b*-P*n*BA_{37}	5.0	1.06	37	6	5.26
PEG_6-*b*-P*n*BA_{58}	7.7	1.07	58	6	3.42
P*n*BA_{66}	8.4	1.22	66	-	-
PEG_6-*b*-P*n*BA_{132}	17.2	1.08	132	6	1.53
PEG_6-*b*-P*n*BA_{224}	29.0	1.09	224	6	0.91
P*n*BA_{255}	32.7	1.14	255	-	-

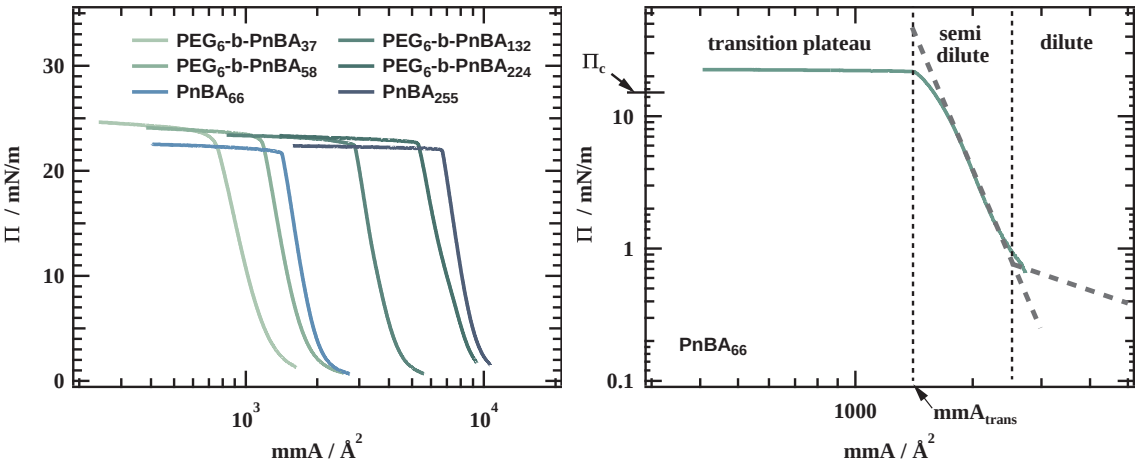

Figure 5.13: The left panel shows compression isotherms (Π vs. mmA) for P*n*BA homopolymers and PEG-*b*-P*n*BA diblock copolymers with different molecular weights summarized in table 5.4. The right panel illustrates the detailed investigation of $PnBA_{66}$. The isotherm can be separated in three different regimes: dilute, semi-dilute and transition plateau. The dashed lines present characteristic power laws for the surface pressure.

higher indicating an influence of PEG. Lee et al. also reported on an increasing plateau pressure for a diblock copolymer PEO-*b*-P*n*BA with a volume fraction of $\phi_{PEO} = 0.28$ [85]. The increase of the plateau pressure can be understood as a result of a decrease in the surface tension of the water surface due to the presence of the covalently bonded PEG chains extended into the subphase. Although for our diblock copolymers the PEG volume fraction is very small ($\phi_{PEO} < 0.06$), the plateau value indicates the same microphase separated structure. In this microphase separated structure, the PEG block is extended into the water subphase while the P*n*BA remains at the interface. This has been confirmed for block copolymers with larger volume fractions of PEG by neutron reflectivity [85], but we do not expect that it is possible to observe this phase separation with XRR due to the small length of our PEG block and the low scattering contrast.

With the variation of the molecular weight of P*n*BA, we focus on further understanding the influence of the PEG block on the compression behaviour. Therefore, the power law analysis as already described for PMMA and P2vP is applied on this set of molecular weights. A representative example is given in the right panel of figure 5.13 for $PnBA_{66}$. We quantitatively analyze the isotherms in detail to reveal all differences between the homopolymers and diblock copolymers. In Figure 5.13 (right panel), $PnBA_{66}$ is used as an example to illustrate the characterization. In the dilute regime the data points are not sufficient to describe the pressure scaling, while it is possible in the semi-dilute regime. The semi-dilute regime can be separated in two parts. In the first one the surface pressure, ranging between $1 - 8\,mN/m$, can be perfectly described by the power law in equation (5.1). The second part begins with the deviation of Π from the power law behaviour and ends in the constant surface pressure plateau. To confirm that an analysis in terms of power laws is justified, X-ray reflectivity and BAM measurements confirm a homogeneous thin film of less then 2 nm thickness (see chapter 6) for all samples. Furthermore, specular and off-specular XRR experiments as well as BAM measurements (see figure 5.16) show no sign of microphase separation of the films in the semi-dilute regime.

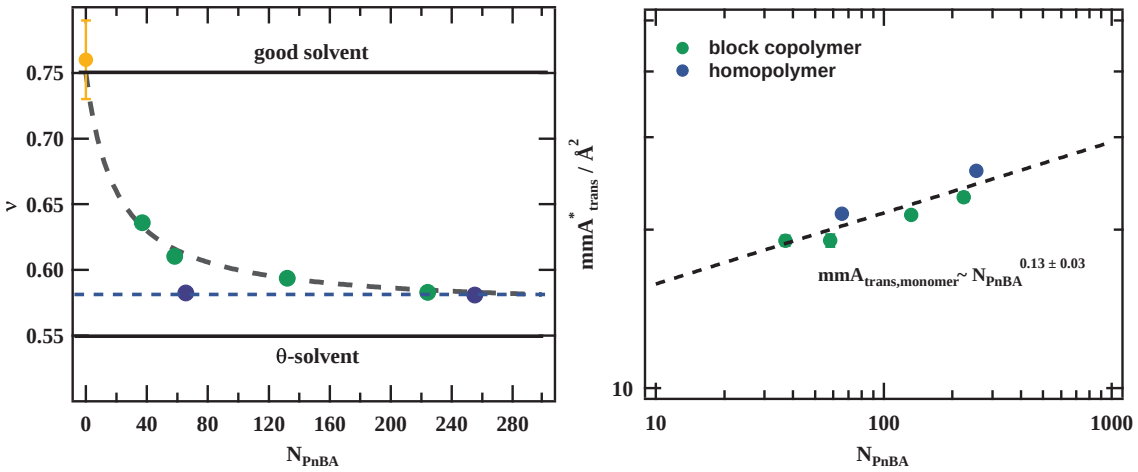

Figure 5.14: The left panel displays the 2D Flory-exponent ν vs. the number of P*n*BA monomers N_{PnBA} in the samples. Additionally, the Flory-exponent ν_{PEG} is shown which was computed from published data on PEG isotherms [80]. The right panel shows the area occupied by each monomer at the transition point mmA_{trans} vs. the number of monomers N_{PnBA} in the polymer chain. The error bars are within symbols.

The 2D Flory-exponents ν of our samples are displayed in figure 5.14 (left panel). For both homopolymers the same Flory exponent of $\nu_{PnBA} = 0.58 \pm 0.01$ is obtained. This value is expected for P*n*BA as it describes the air-water interface as a θ-solvent being consistent with results for other acrylate polymers [29]. Looking at the diblock copolymers, the behaviour of the Flory-exponent changes as a function of molecular weight. While the largest diblock copolymer shows the same Flory exponent as the homo polymers, its value increases steadily for smaller blocks. Here, the influence of the PEG block can be clearly seen as its volume fraction increases for smaller P*n*BA blocks. The Flory exponent of a pure PEG monolayer $\nu_{PEG} = 0.76 \pm 0.03$ was computed from published data of Xu et al [80]. The air-water interface obviously acts as a good solvent for the PEG monolayer. The investigations show that in the diblock copolymers both blocks contribute to the compression behaviour within the first part of the semi-dilute regime. The PEG block in the polymer is able to tune the air-water interface from approximately θ-solvent conditions to good solvent conditions. When the surface pressure further increases, the PEG block descends into the water phase and, therefore, does not contribute to the compression behaviour any longer.

In the second part of the semi-dilute regime the surface pressure starts to flatten in comparison to the predicted power law, until the pressure reaches Π_c at mmA_{trans}. A clear kink is visible at this area that has been observed for P*n*BA homopolymer monolayers as well as diblock copolymers with different hydrophilic block partners [30,84,85,87,88]. When the layer is solely composed of PnBA at this area, it is more adequate to look at molecular weight independent units - mmA^*: area per monomer (mmA/N_{PnBA}). In the right panel of figure 5.14, mmA^*_{trans} is plotted versus the number of P*n*BA monomers for homopolymers and diblock copolymers. With increasing molecular weight we see a weak increase of mmA^*_{trans} with N_{PnBA}. It can be observed independent of the polymer type as expected for a pure P*n*BA layer. The weak increase is consistent with the scaling characteristics of an area within the semi-dilute regime ($mmA^* \sim R_F^2/N \sim N^{2\nu-1}$). We find a Flory-exponent of $\nu = 0.58$ for mmA^*_{trans}, which agrees very well with $\nu_{PnBA} = 0.58$ obtained from the

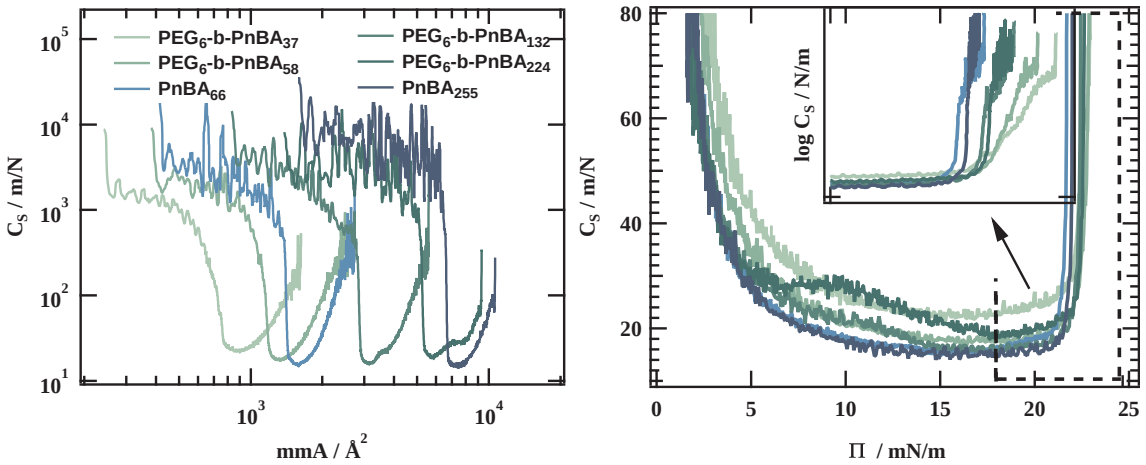

Figure 5.15: Both panels show the compressibility C_S computed from the compression isotherms using equation (2.10). In the left panel it is displayed vs. mmA and in the right one vs. Π. The overall shape of the curves is similar for all molecular weights, however in detail differences in the broad maximum become apparent for the larger diblock copolymers. The inset in the right panel shows the different behaviour of the compressibility when crossing into the plateau.

surface pressure scaling of the P*n*BA homopolymers. The kink at mmA_{trans} is a property of the P*n*BA block which completely covers the water interface with a densely packed layer at this area. The PEG block does not contribute to the compression anymore which confirms our picture of the PEG block to be immersed in the subphase. However, it is interesting to note that the scaling laws for the air-water interface as a θ-solvent for the P*n*BA layers are still applicable at mmA_{trans}, even though the pressure scaling no longer holds.

Compressibility of the Films

The compressibility C_S provides another tool to characterize different phases in a monolayer as we have already discovered for PMMA. In figure 5.15 the compressibility is plotted as C_S vs. mmA in the left panel and C_S vs. Π in the right panel. Plotted versus mmA the overall shape of C_S already indicates that there are small differences in the compression behaviour that were not clearly visible in the isotherms before. For both homopolymers the shape of C_S is almost identical independent of molecular weight. This feature becomes even more apparent in the representation versus Π. With increasing surface pressure C_S decreases and forms a broad minimum with values around $C_{S,min} \approx 14\,m/N$ for Π ranging between $10-21\,mN/m$. Upon reaching the plateau pressure of $\Pi_C \approx 21.3-21.7\,mN/m$ (for the homopolymers), C_S diverges and increases to high values of over $5000\,m/N$.

The situation for the diblock copolymers is different and can be described in two steps. For the two smaller diblock copolymers a similar broad minimum can be observed, however, the minimum value of $C_{S,min}$ is higher than for the homopolymers. The two larger blocks show a step-like behaviour in the same region. The minimum value $C_{S,min}$ for the blocks decreases from $25\,m/N$ to $16\,m/N$ with increasing block length but at the same time a maximum at $\Pi \approx 10\,mN/m$ appears for the larger blocks that changes the slope of the compressibility. Such an occurrence is usually the sign for a phase transition in the film and it is interesting that it appears for the larger diblocks for which the solvent

conditions at the air-water interface have been confirmed to be the same as for the homopolymers (θ-solvent conditions). Since we clearly observe a different behaviour in the compressibility of the blocks, the maximum must be related to the PEG block. Furthermore, the surface pressure of around $\Pi \approx 7-10\,\mathrm{mN/m}$ for the PEG block submerging into the water subphase is in agreement with existing work on diblock copolymers containing a PEG block[9,13,81]. The question still remains why the maximum emerges with increasing molecular weight and cannot be observed for the smaller blocks with higher volume fractions of PEG. Although it is not backed up with scattering data, it is possible that microphase separated structures exist in the film and differ for the different molecular weights. In case of small molecular weight and high volume fraction of the PEG block, several blocks of different chains could form small micelles at the interface due to the higher mobility of the chains. When the PEG blocks start to submerge into the subphase it is a collective motion that does not occur at a specific surface pressure but a broad range. For the larger molecular weights, the PEG blocks are more separated leading to a sharp transition for a surface pressure of $\Pi \approx 7-10\,\mathrm{mN/m}$. The PEG blocks submerge into the subphase almost at the same time.

Another effect of the PEG block can be observed upon reaching the critical surface pressure of the plateau $\Pi_C \approx 22.3-22.7\,\mathrm{mN/m}$ where the compressibility increases strongly. However, compared to the homopolymers the slope of C_S for the blocks is less steep and does not reach the same maximum value. This can be observed in the inset of figure 5.15 (right panel). The effect is stronger for the small molecular weights with larger volume fraction of the PEG block. While the interface is purely covered by P*n*BA chains in the plateau, the PEG blocks are submerged into the water subphase close to the interface. Logically, the coverage of PEG increases with PEG volume fraction. The PEG block acts as a resisting element upon compressing the film in the plateau.

Brightness Measurements

To obtain more information on the films, Brewster-Angle-Microscopy was performed simultaneously while recording the compression isotherms. Figure 5.16 (left panel) displays the compression isotherm of PEG_6-*b*-P*n*BA_{132}. With respect to the right axis, the figure shows the integrated p-polarized intensity of a rectangular frame ($360x188\,\mu m^2$). It is a measure of the optical properties of the film. Two BAM images, one in the semi-dilute regime and one when the film is compressed in the plateau, are shown in the right panel of the figure. The rectangular frame is appended to visualize the area over which the mean brightness ranging from 0 to 255 is calculated. Analyzer and polarizer were both aligned the same so that only the p-polarization was able to pass. The mean brightness value for the bare water surface was roughly 2.5.

The data clearly shows two different regimes separated by the transition point mmA_{trans}. The average intensity in the semi-dilute regime is low (brightness < 3) and essentially identical to that of the bare water surface. When crossing mmA_{trans} a fundamental change is visible in the intensity. During compression of the monolayer in the plateau, the intensity increases steadily. In the raw images, shown in Figure 5.16, we can see the difference of the macroscopic structure in both regimes. The first snapshot taken in the semi-dilute regime is essentially black, although occasionally small micrometer-size bright domains are visible in the images. The number of bright domains suddenly increases dramatically when crossing mmA_{trans}. Intensity continues to increase along the

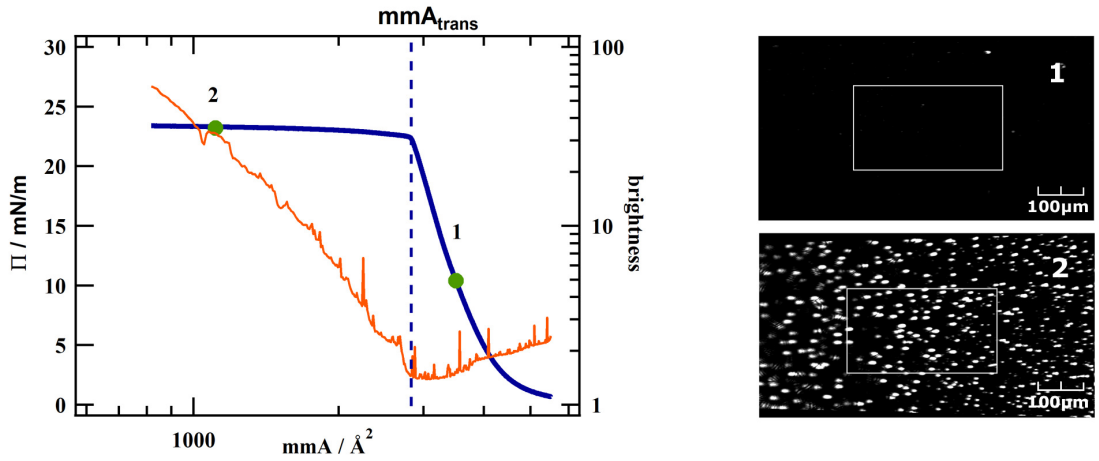

Figure 5.16: The left panel shows the compression isotherm of PEG_6-*b*-P*n*BA_{132} and the respective brightness values (greyscale from 0 to 255) during compression. The right panel shows two images taken during compression that are marked by green points in the isotherm. The images illustrate how the brighness value was derived by taking an average over the white rectangular area ($360\,x\,188\,\mu m^2$). For this experiment the analyzer and polarizer of the setup allow only p-polarized light to pass. Here, the mean brightness for the reflection from the bare water interface was roughly 2.5.

plateau. The domains are a manifestation of structural changes in the optical properties of the film. The structure formation in the plateau regime will be investigated further in chapter 6.

Concentration Isotherms

The concentration isotherms for all samples are shown in the left panel of figure 5.17 and directly compared to the compression isotherms. Similar to the experiments on PMMA ,it is only possible to prepare the isotherms to a maximum surface pressure of $\Pi \approx 15\,mN/m$ safely. Afterwards, the evaporation behaviour of the chloroform changes and a successful preparation of a monolayer cannot be guaranteed. The position and shape of the concentration isotherms approximately match the previously presented compression isotherms. There are small shifts in the area and the slope that will be further dicussed in the following.

In the right panel of figure 5.17, P*n*BA_{66} is presented as an example for the further characterization of the concentration isotherms. It illustrates that the dilute and semi-dilute regime are well presented and can easily be distinguished by the two different power laws for the surface pressure scaling in these regimes (see equations (2.12) and (2.16)). The crossover from dilute to semi-dilute given by mmA_{ov} can be determined with great accuracy by the intersection of the two power laws. The pressure scaling in the semi-dilute regime validates the results on the Flory-exponent ν that have been discussed for the compression isotherms. The absolute values for ν are slightly lower (e.g. $\nu_{PnBA} = 0.575 \pm 0.015$) however the data leads to the same conclusion. The PEG block is able to tune the solvent properties of the air-water interface from θ-solvent conditions to good solvent conditions with increasing volume fraction.

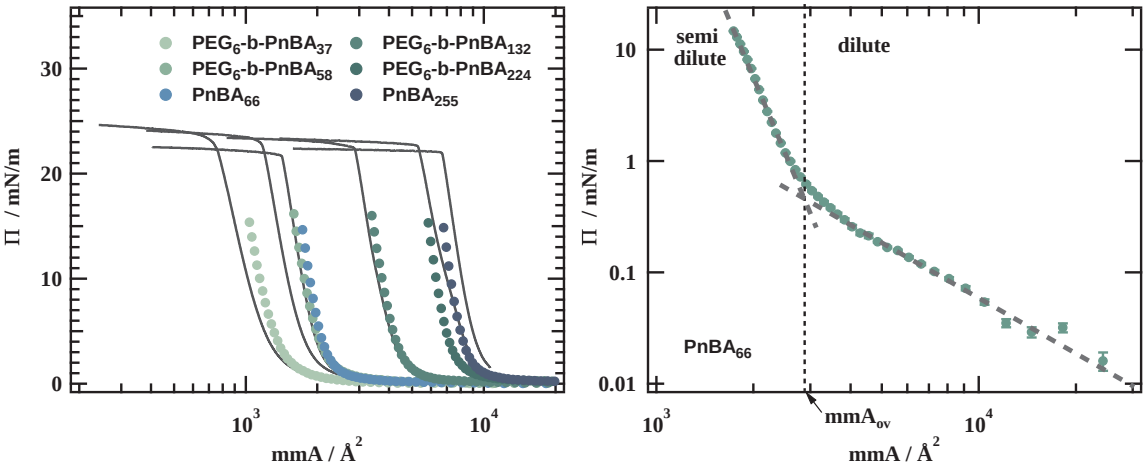

Figure 5.17: The left panel shows the concentration isotherms of P*n*BA homopolymers and diblock copolymers compared to the previously discussed compression isotherms. The concentration isotherms can only be recorded up to surface pressures of $\Pi \approx 15\,\mathrm{mN/m}$ before the chloroform drops cannot be spread properly anymore. The right panel illustrates the detailed investigation of P*n*BA$_{66}$. Two different regimes (dilute and semi-dilute) are visible clearly separated by mmA$_{ov}$ which is given by the intersection of the predicted power laws in dilute and semi-dilute regime.

A big advantage given by the concentration isotherms is that they make it possible to analyze the scaling behaviour in the dilute regime and their accurate determination of mmA$_{ov}$. For the block copolymers the exponent is $y \approx 1.5$. The two homopolymers give an exponent of $y = 1.5$ for P*n*BA$_{66}$ and $y = 0.9$ for P*n*BA$_{255}$. The expected scaling for a θ-solvent scaling ($\Pi \sim \mathrm{mmA}^1$) can only be confirmed for the largest homopolymer, but not for the smaller molecular weight. For good solvent conditions the exponent is expected to increase, however, due to the results on P*n*BA$_{66}$ which also show a higher exponent, a detailed investigation of the scaling behaviour in this regime is not possible without further experiments. The area characteristic for the overlap mmA$_{trans}$ scales to the power of 1 with the number of P*n*BA monomers N$_{PnBA}$. This is roughly in agreement with the expected behaviour of $\mathrm{mmA}_{trans} \sim N_{PnBA}^{2\nu}$ with $\nu_{PnBA} = 0.575$. In the area scaling the two smallest blocks were excluded and the PEG block in the larger blocks have been neglected. It is also possible to calculate the expansion of a single monomer for P*n*BA at the air-water interface using equation (2.5) ($\mathrm{mmA}_{ov} = \pi R_F^2$). It leads to a Kuhn length of $k_{PnBA} = (4.8 \pm 0.2)\,\text{Å}$ which is more than twice as big as values found for the 3D case in literature [89]. However, for its isomeric polymer P*t*BA, a Kuhn length of $k_{PtBA} = 4.5\,\text{Å}$ can be found for a Langmuir monolayer in literature [82]. It is still contradicting because the air-water interface is characterized as a good solvent for P*t*BA in this reference.

Comparison of Results

- Dilute regime: The data in the dilute regime is limited and only accessible by measuring concentration isotherms. It was possible to determine an exponent for a power law, however it was not possible to verify the expected behaviour as stated from the virial expansion (2.12)). It was not possible to accurately describe the solvent properties of the air-water interface in the dilute regime (see table 5.5). The data from the area scaling for the overlap concentration leads to a Kuhn length of

Table 5.5: Comparison of parameters obtained from power law fits in the dilute and semi-dilute regime. Dilute regime with $\pi \sim \mathrm{mmA}^{-y}$, expected value of $y = 1$ for an ideal gas (θ-solvent). Semi-dilute regime $\Pi \sim \mathrm{mmA}^{\frac{2\nu}{2\nu-1}}$ with the Flory-exponent $\nu_{\theta-\mathrm{solvent}} = 0.5 - 0.55$ expected for a θ-solvent.

Exponent y (dilute)	comp. iso.	conc. iso.	Flory-exponent ν	comp. iso.	conc. iso.
PEG_6-*b*-P*n*BA_{37}	-	1.49		0.64	0.62
PEG_6-*b*-P*n*BA_{58}	-	1.54		0.61	0.60
P*n*BA_{66}	-	1.55		0.58	0.58
PEG_6-*b*-P*n*BA_{132}	-	1.36		0.59	0.59
PEG_6-*b*-P*n*BA_{224}	-	1.51		0.58	0.59
P*n*BA_{255}	-	0.9		0.58	0.58

$k_{\mathrm{PnBA}} = 4.8\,\text{Å}$ for a P*n*BA monomer. This agrees with the Kuhn length determined for its isomeric polymer P*t*BA at the air-water interface [82].

- Semi-dilute regime: For both P*n*BA homopolymers the air-water interface acts as a θ-solvent. However, an interesting effect is observed for the block copolymers. With increasing volume fraction of the PEG block, the solvent properties of the interface can be tuned from θ to good solvent conditions. This can be observed in compression but also concentration isotherms.

- BAM imaging does not show any reflected intensity as long as the film is in the dilute or semi-dilute regime. This changes completely upon crossing the transition point point $\mathrm{mmA}_{\mathrm{trans}}$ where an increasing number of bright spots emerges within the film leading to a continuous increase of the average mean intensity. The bright spots are characteristic for the plateau and the beginning incease in intensity matches the kink at ($\mathrm{mmA}_{\mathrm{trans}}$) very well.

5.4 Comparison and Conclusions of the 3 Systems

In the previous sections three different polymer systems with a wide range of molecular weights were investigated using Langmuir isotherms. Polymer scaling laws in 2D were used to characterize the solvent properties of the air-water interface for all systems while the results were also compared for two different recording techniques (concentration and compression isotherms). Computing the compressibility from the compression isotherm was a very useful tool to identify phase transitions in the isotherms. Using BAM imaging to calculate the average reflected intensity from the monolayer proved to be a good complementary method to identify phase separation and aggregation in the layer.

2D Polymer Scaling Laws

In this work it was shown that Langmuir isotherms are a very handy tool to investigate 2D polymer films at the air-water interface. Compression and concentration isotherms complement each other to characterize the dilute and semi-dilute regime. However, the data in the dilute regime is usually limited so that a proper analysis using the virial expansion for a dilute polymer solution in 2D is not really possible. The situation is different in the semi-dilute regime where a clear power law dependency can be identified in all

systems that is reproducible for both recording techniques. The solvent quality of the interface can be determined for all three systems (P2vP: good, PMMA and P*n*BA: θ-solvent and PEG-*b*-P*n*BA as an intermediate case between θ and good solvent). Furthermore, the Kuhn length k determined for P*n*BA and PMMA agrees with values found in literature for 2D measurements[72,90], but for P*n*BA it is around two times larger than its caluclated value in 3D[89].

A very interesting phenomenon can be observed for the PEG-*b*-P*n*BA block copolymers. Upon increasing the volume fraction of the PEG block, the solvent properties of the interface change from θ to good solvent conditions. This can be very useful to control the solvent properties of the interface by adjusting the volume fraction in block copolymers. However, further experiments on different block copolymers would have to confirm this observation first. After computing the compressibility for the block copolymers another feature is revealed that suggests a phase separated structure in the film. A sharp transition corresponding to the PEG block submerging into the subphase can be observed for the blocks with a low volume fraction while a collective motion is observed for the higher volume fractions. The idea is that the mobility of the chains is higher due to the larger volume fraction of the PEG block. PEG blocks might be able to form surface micelles that start to submerge into the subphase as a collective motion. Due to this no sharp transition is observed. Rheology experiments might help to test this hypothesis.

Phase Transitions in the films

P*n*BA based monolayers (homopolymer and diblock copolymer) all have a characteristic constant pressure plateau. This can be easily identified by measuring the compression isotherm with the Langmuir technique, however since the value of the surface pressure remains almost constant the Langmuir technique is not suitable for further characterizing the transition. A slightly higher plateau value for the diblock copolymers can be explained by the PEG block submerged into the subphase. As a consequence of that the surface tension of the water layer right beneath the interface is reduced which leads to a slightly higher plateau pressure compared to the homopolymer films. This microphase separated structure in the plateau has also been confirmed by neutron reflectometry experiments published in literature[84]. BAM imaging shows that upon compressing the films into the plateau an increasing number of macroscopic bright spots appear within the film. A detailed study on the structure of the P*n*BA layer at the interface will be given in the following chapter.

The results from the PMMA samples are also very interesting. A phase transition can be observed for the two smaller molecular weights but it vanishes for the larger ones. There have already been reports about this transition in literature that it is most likely a transition from a flat layer to a folded structure at the interface[73,77]. The idea is that the contact area to the water subphase is reduced. The studies showed that whether the transition can be observed or not strongly depends on the mobility of the chains, respectively how close was the temperature during the experiment compared to the 3D glass transition temperature. The tacticity, molecular weight and temperature of the experiment play an important role. The experiment in this work indicate that the folded structure already exists in the larger molecular weights, because they already appear in form of large islands in the dilute regime. This is confirmed by BAM imaging. The smallest molecular weight shows a different behaviour in the images and has also the strongest sign for the phase

transition. For the smaller molecular weights the chains are still able to form those loops upon compression to reduce the stress in the film. The maximum in the compressibility clearly indicates this. Further temperature dependent measurements would be able to confirm the origin of the phase transition.

6 Structure in Densely Packed P*n*BA Films during Compression

P*n*BA homopolymers and diblock copolymers have been investigated focusing on the solvent quality of the air-water interface within the semi-dilute regime. There is however, another unique feature in this series of polymers which is the broad constant pressure plateau in the Langmuir isotherms (see figure 5.13). Its existence is characteristic for a phase transition in the sample and it is a unique feature in a Langmuir isotherm. Structural changes have to take place if a film can be compressed over such a wide range without notable changes in the surface pressure. The plateau pressure for the block copolymers is slightly higher than for the homopolymers which has already been discussed in chapter 5.3. The slightly higher pressure can be connected to the submerged PEG blocks beneath the P*n*BA films because they reduce the surface tension of the subphase. However, this is the only information that we can obtain from the Langmuir isotherms. The surface pressure is no longer a good measurement quantity since it does not show notable changes upon compression. The brightness measurements in figure 5.16 show that macroscopic changes occur in the isotherm while crossing into the plateau. An increasing number of bright spots with a magnitude of several micrometer become visible in the BAM images.

In this chapter Surface X-ray scattering and BAM imaging will be used to investigate the structure of the film parallel and perpendicular to the air-water surface. The necessary theoretical aspects are presented in chapter 3. The following part starts with in-situ and ex-situ specular reflectivity measurements on the P*n*BA homopolymers and diblock copolymers. Specular reflectivities of the films have been measure in-situ and ex-situ and results of those experiments have already been published in the Phd thesis of Martin Kraska [65]. Since they are important to understand the film structure they will be shown on the first few pages of this chapter. Afterwards, the macroscopic lateral structure of the films is investigated using BAM imaging. The stability in the plateau is investigated by apllying hysteresis experiments on the Langmuir films. The focus of the chapter is on the off-specular scattering from structures at the air-water interface. This part is divided into two sections. First, results on PEG_6-*b*-P*n*BA_{132} will be shown and used as an example to show the evaluation of the data. In a second part, experiments on all molecular weights are shown and compared to each other.

6.1 Specular Reflectivity on P*n*BA and PEG-b-P*n*BA Monolayers

To analyse the structure, in-situ and ex-situ specular reflectivity experiments were performed on the polymer films. In the previous chapter it was assumed that the polymer forms monolayer thick films at the interface, however, experimental proof of this can only be obtained by performing X-ray scattering on the films.

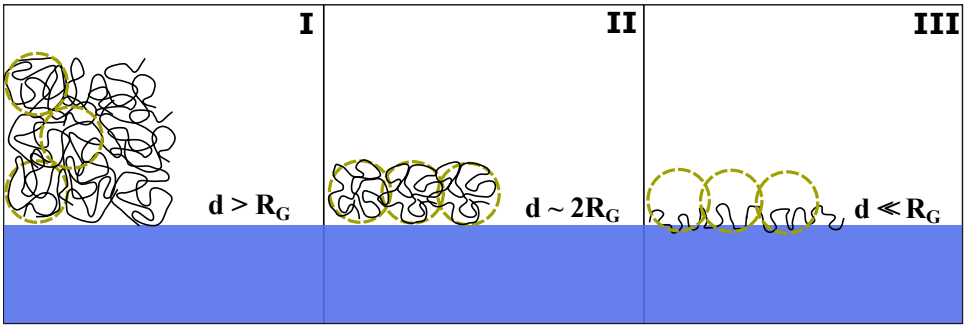

Figure 6.1: Different conformations of polymer films on a water subphase. R_G is the radius of gyration. I. $d > R_G$: no confinement. II. $d \sim R_G$: intermediate state. III. $d \ll R_G$: strong confinement.

In a quasi 2D system the film thickness is small compared to the actual size of the chain. As a measure for the confinement of the polymer in a film of thickness d, d is compared to R_G. In general, three different situations can be imagined. In the first situation, the film thickness is much larger than R_G which is comparable to the situation in a bulk solution. Another possibility is that the thickness is comparable to its own size, respectively $2R_G$. Here, the polymer is already in a weak confinement at the interface. In the last situation the film thickness may be much smaller than R_G, leading to a strong confinement of the polymer at the interface (2D confinement). These three situations are illustrated in the sketch in figure 6.1.

The aim is to determine the film thickness at the air-water interface which is expected to be a few Ångström. Therefore, in-situ X-ray reflectometry (XRR) measurements were performed on the polymer films at the air-water interface and ex-situ measurements on Langmuir-Blodgett (LB) films. For the ex-situ measurements, the polymer films were transferred on silicon wafers at mmA_{trans} (see figure 5.13). The films were transferred while the wafer was pulled out of the monolayer (Z-type deposition) as expected for a monolayer consisting of hydrophilic groups in the backbone. The process was monitored and the transfer ratio for all films was close to one, indicating a successfully transferred film from the water surface. The ex-situ measurements were performed because of the lack of scattering contrast between water and the polymer film, as will be briefly shown in the following. The scattering length density of P*n*BA is $\rho_{PnBA} = 10.0 \cdot 10^{-6}\,\text{Å}^{-2}$, which gives a contrast of around 5 % to the water subphase ($\rho_{H_2O} = 9.427 \cdot 10^{-6}\,\text{Å}^{-2}$) [30]. This makes it difficult to differentiate the thin monolayer from the water subphase. Furthermore, for PEG the scattering length densities is $\rho_{PEG} = (9.6 - 10) \cdot 10^{-6}\,\text{Å}^{-2}$ for thin film measurements [91], which is in between the two above mentioned scattering length densities.

Results on the LB films, shown in the left panel of figure 6.2, will be discussed first. In this representation of the data the reflectivity R is multiplied by q^4 to take the overall decay of R according to the Fresnel reflectivity $R_F \sim q_z^{-4}$ into account. The raw data already shows the appearance of a first minimum of Kiessig fringes that slightly shifts to larger q_z with increasing molecular weight. As the scattering length density of the PEG and P*n*BA blocks are very similar, we use a one layer model for both homopolymers and diblock copolymers in order to extract reliable results for the film thickness. The model calculates the reflectivity of an electron scattering density profile along the surface

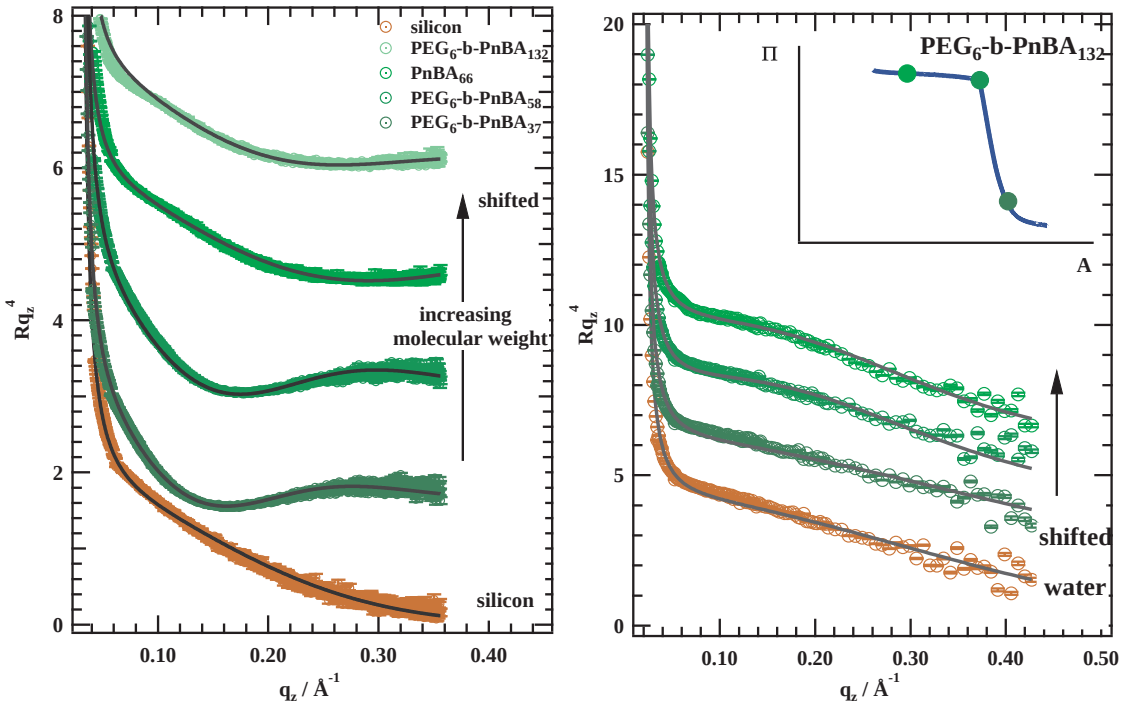

Figure 6.2: The left panel shows the ex-situ reflectivity curves of P*n*BA$_{66}$ and PEG$_6$-*b*-P*n*BA$_{37,58,132}$ Langmuir-Blodgett films, produced at the transition point mmA$_{\text{trans}}$, on a silicon wafer. The right panel displays the reflectivity curves of PEG$_6$-*b*-P*n*BA$_{132}$ at the air-water interface for different surface pressures of $\Pi \approx (5, 22, 24)\,\text{mN/m}$. In both panels the reflectivity is multiplied by q_z^4 to emphasize the appearance of Kiessig fringes (see equation (3.16)) in the curves.

normal using the in section 3.2.1 introduced Parratt formalism. It consists of a layer with a thickness d, a scattering length density ρ_{SLD}, a roughness of the layer-silicon interface σ_0 and of the layer-air interface σ_1. The solid lines in Figure 6.2 are calculated reflectivities according to this model. For better comparison the same model is used for all molecular weights, although small deviations can be observed for the largest molecular weight when q_z is small ($q_z < 0.09\text{Å}^{-1}$). The scattering length density of the films is constrained to $\rho_{SLD} = 10.0 \cdot 10^{-6}\,\text{Å}^{-2}$ for all films. The results for σ_0, σ_1 and d are shown in figure 6.3 and the thickness found for all films is smaller than 2 nm. A trend can be observed, namely d decreases with increasing molecular weight for the blocks to the thickness of the P*n*BA homopolymer layer. Obviously, the thickness is influenced by the existence of the PEG block. At mmA$_{\text{trans}}$, only a water-free P*n*BA layer exists at the interface with the PEG block submerged into the subphase. However, for the block copolymers the PEG block is also transferred on the wafer. This can lead to a slightly larger thickness of the layer because the transferred volume increases with increasing volume fraction of PEG. Another possible explanation is that microphase separation occurs for the block copolymers. The underlying structure can depend on the volume fraction of PEG in the blocks as similarly observed for PS-PEG diblock copolymers [92]. The roughness at the silicon interface ranges between $\sigma_0 = 2.5 - 5\,\text{Å}$ with smoother values for the two small diblock coplymers. The initial roughness of the silicon wafers determined in a separated XRR experiment was

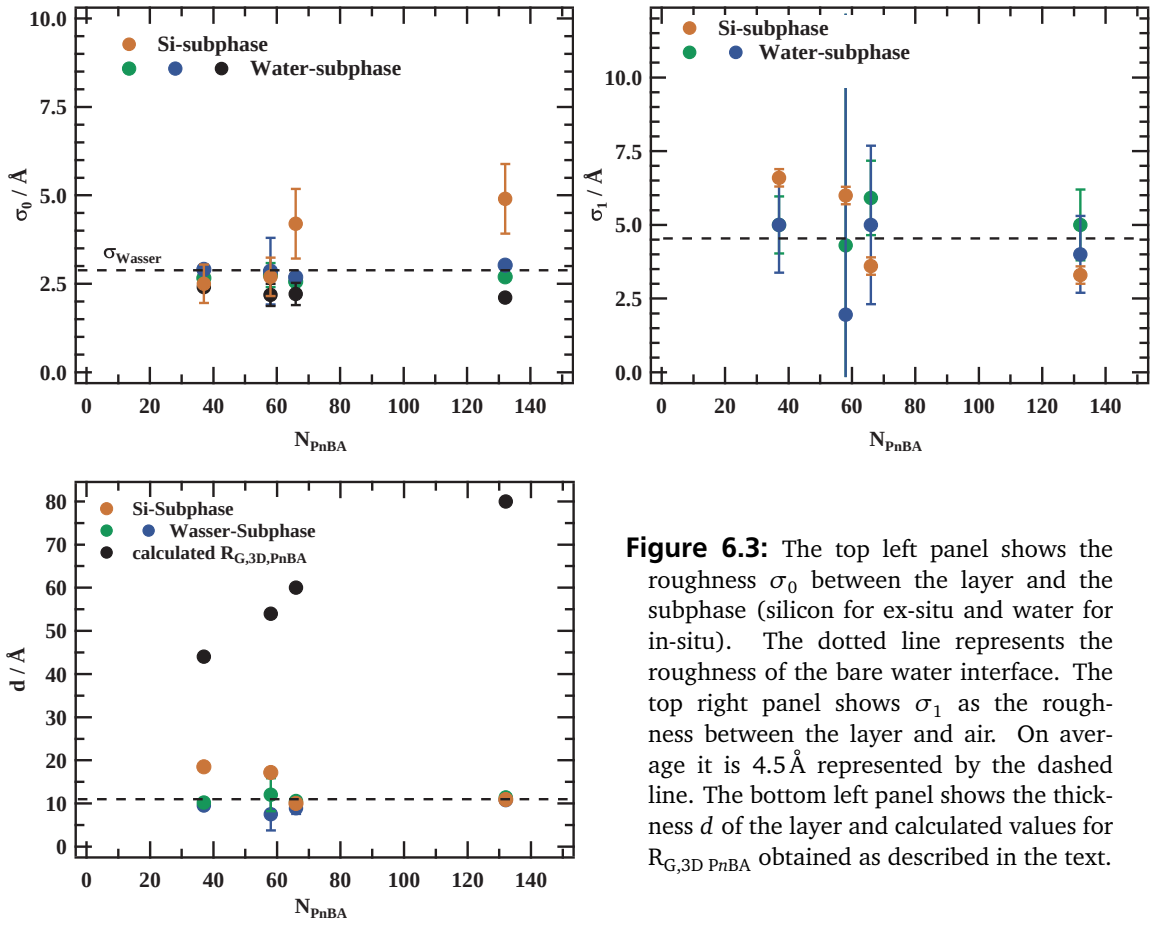

Figure 6.3: The top left panel shows the roughness σ_0 between the layer and the subphase (silicon for ex-situ and water for in-situ). The dotted line represents the roughness of the bare water interface. The top right panel shows σ_1 as the roughness between the layer and air. On average it is 4.5 Å represented by the dashed line. The bottom left panel shows the thickness d of the layer and calculated values for $R_{G,3D\ PnBA}$ obtained as described in the text.

around 4.5 Å. The roughness at the air interface decreases with increasing molecular weight from 6.5 Å to 4 Å.

The right panel of figure 6.2 shows the in-situ reflectivity of the films at air-water interface for PEG_6-*b*-P*n*BA_{132}. As expected the reflectivity of different positions in the isotherm is hardly different from a bare water surface. Still, it is possible to distinguish small changes in the curve. For the first measurement point in the semi-dilute regime at a surface pressure $\Pi \approx 5\,\mathrm{mN/m}$, the reflectivity reduces a little less compared to water. With increasing surface pressure small changes become visible that can be fitted with the already described one layer model. The scattering length density of the layer is constrained to $\rho_{SLD} = 10.0 \cdot 10^{-6}\,\text{Å}^{-2}$. The roughness $\sigma_0 = 2.6\,$Å is in agreement with the roughness of the bare water interface and towards air the roughness $\sigma_1 = 3 - 5\,$Å is similar to the ex-situ results.

The film thickness d for in-situ and ex-situ measurements can be compared to calculated values of $R_{G,3D\ PnBA}$ (see figure 6.3). The values are calculated with a power law fitted to light scattering data on P*n*BA dissolved in Tetrahydrofuran [93]. The results show that for all samples d is smaller than the respective radius of gyration R_G for both in-situ measurements on the water surface and ex-situ measurement on silicon wafers. Obviously, the polymers are strongly confined into a thin layer. Consequently their chain conformation will have to adapt to this 2D situation.

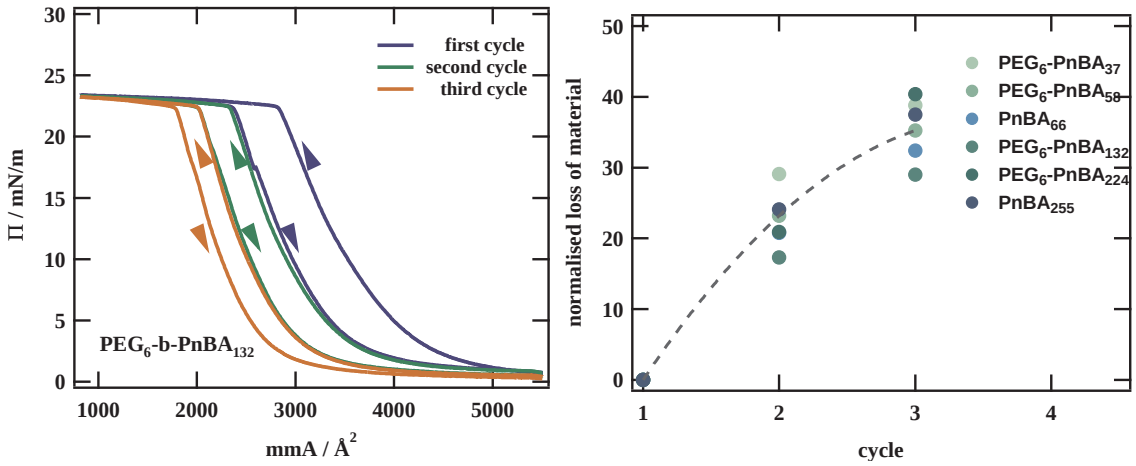

Figure 6.4: The left panel shows the hysteresis cycles of PEG_6-*b*-P*n*BA_{132}. Subsequent expansions and compressions in the hysteresis cycle overlap but the characteristic area mmA_{trans} is shifted to smaller areas after each cycle. This means the amount of polmyer in the film is reduced. The right panel displays the shift of the characteristic area mmA_{trans} in dependency of the cycle number.

6.2 Stability and Macroscopic Structure in the Transition Plateau

To investigate the stability of the film in the transition plateau, hysteresis experiments were performed on all samples. In the left panel of figure 6.4 the data on PEG_6-*b*-P*n*BA_{132} is used as a representative example. Three compression/expansion cycles were repeated without any delay at the smallest and highest area in the isotherm. With each compression/expansion cycle the general slope of the isotherm stays the same but is being shifted to smaller areas. Using the characteristic area mmA_{trans} this shift can be quantified and is displayed in the right panel of figure 6.4 based on its relative shift from the position in the first cycle. The characteristic area mmA_{trans} shifts with respect to the initial area to $17-29\,\%$ after the first to $29-40\,\%$ after the second cycle. Furthermore, subsequent compressions of the monolayer perfectly overlap with previous expansions. These observations indicate that a fraction of the polymer is permanently removed from the compressible film in the plateau. The removed amount depends on the absolute area being compressed in the plateau and therefore reduces from the first to the second hysteresis cycle. Similar results have been reported in reference for P*n*BA films [30]. The results for the different polymers vary a little but it was not possible to observe a molecular weight trend or differences between diblocks and homopolymers.

With hysteresis experiments it is also possible to calculate the work performed by the system. The necessary work dW_A to increase the surface area by a small quantity dA is given by $dW_A = \gamma\, dA$, with the work performed during one hysteresis cycle:

$$W_{A,i} = \int_A \Pi_{\text{compression},i}(A) - \Pi_{\text{expansion},i}(A)\, dA \approx \Pi_c \cdot \Delta A_i \tag{6.1}$$

Here, Π_c and ΔA_i are the plateau pressure and the shifting area mmA_{trans} as shown in the left panel of figure 6.5. There is almost no difference between the slope of the expansion and compression curve which is illustrated by the overlap of the second compression and

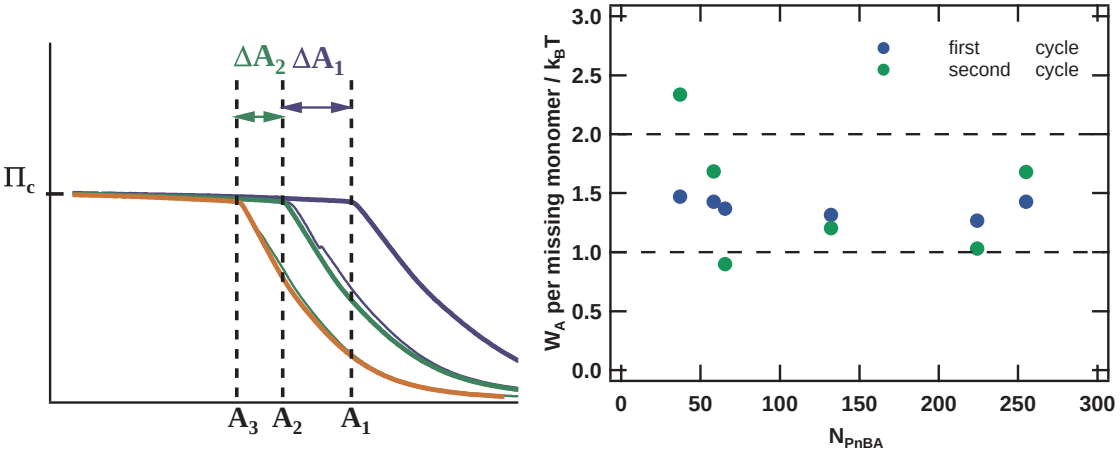

Figure 6.5: The left panel shows a sketch of the hysteresis cycles and all necessary values for equation (6.1) to calculated the work W_A performed by the system. The right panel displays the energy per missing monomer vs the number of PnBA monomers in the chain for the first and second hysteresis cycle.

the first expansion. Due to this the integral can be described very good by multiplying the plateau pressure with the area shift ΔA_i. The right panel of figure 6.5 shows the in the system deposited energy for each missing monomers for the first and second cycle. The number of missing polymer can be calculated from the data shown in figure 6.4.

The data shown in figure 6.5 illustrates that the energy per missing monomer ranges between $1-2\,k_\mathrm{B}T$. In the plateau, the surface pressure Π_c is equivalent to the spreading coefficient S reaching 0. As a consequence no additional energy is necessary to remove a P*n*BA monomer from the interface. The monomers excluded from the layer can either move towards the air-polymer or polymer-water interface. The surface tensions $\gamma_{\text{polymer-water}} < \gamma_{\text{air-polymer}}$ suggest that the monomers move towards the water subphase [30]. This being the case one has to consider the hydrophobic interaction in order to understand how much energy is necessary to move a monomer into the subphase. Data on the hydrophobic interaction of *n*BA was not available so that its side chain *n*-butyl will be used to estimate the energy necessary for one molecule to be moved into the water subphase. Due to the hydrophobic interaction, the energy necessary to move one *n*-butane molecule from pure butane into water is around $10\,k_\mathrm{B}T$. However, 85 % of the contribution to the energy arise from a decrease in entropy because the water molecules need to arrange a cage around butane [21]. A thermodynamic model considering the entropic penalty of confining polymer chains to a monolayer suggest that the excess polymer should form a single large domain in order to minimize the large surface at the water-polymer interface [30]. However, the mechanism is not only determined by thermodynamics but also by hydrodynamics of the water and the film. As a consequence, it is likely that the polymer is locally trapped forming globular domains as observed in BAM imaging. For the hydrophobic interaction this also means that the decrease in entropy is dramatically reduced. Taking into account that its contribution is 85% of the $10\,k_\mathrm{B}T$, the energy loss W_A measured by hysteresis experiments can be explained by hydrophobic interaction between subphase and polymer.

To reveal the structure in the plateau, BAM imaging has been performed simultaneously to the hysteresis experiments. Results from mean intensity measurements have

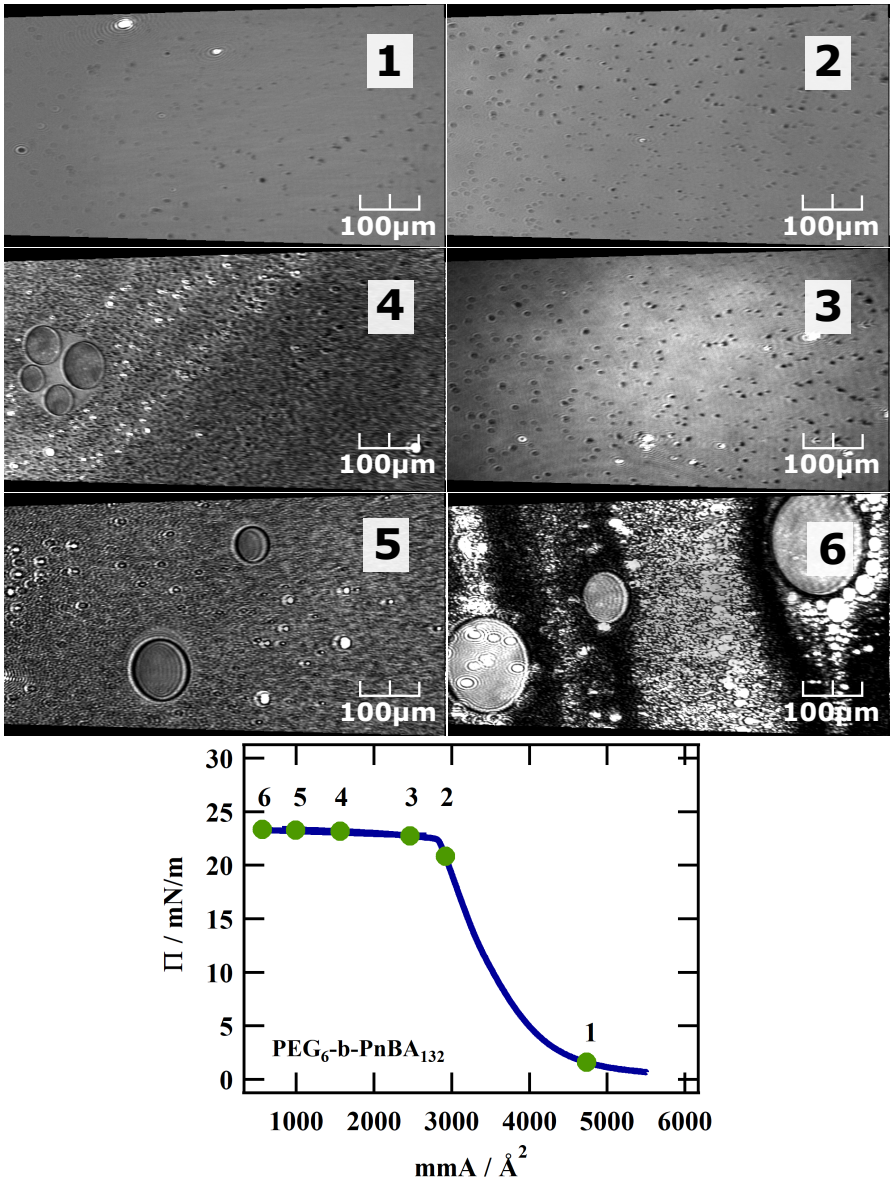

Figure 6.6: BAM pictures of PEG_6-*b*-P*n*BA_{132} during a compression isotherm are displayed. The position within the isotherm is given by the black number in each frame. The setup of the microscope is optimized for visualizing purposes, which means that the polarizor and analyzor allow some s-polarized intensity to expose structures in the monolayer.

been presented in chapter 5.3 for p-polarized light. They reveal that upon crossing into the plateau a fundamental change is visible in the mean intensity reflected at the interface. An increasing number of bright domains appear and intensity continues to increase along the plateau. The domains are a manifestation of structural changes in the optical properties of the film. Additionally to the these measurements, high-contrast images were taken of the macroscopic film structure by adding a small amount of s-polarized intensity. A series of images taken during compression of PEG_6-*b*-P*n*BA_{132} are displayed in Figure 6.6. In detail, small aggregates are already visible in the semi-dilute regime (image 1),

however, their number starts to increase dramatically when the isotherm crosses the transition point from image 2 to 3. Consequently, these aggregates can be associated to the small bright domains in the experiment with the p-polarized laser. Further in the plateau two different phases can be observed (image 4, 5 and 6). One of those phases consist of closely packed aggregates which can be barely distinguished from each other due to their size and distances being close to the resolution limit of the setup (lateral resolution $> 2\,\mu$m). The second phase consists of flat globular structures with a radius of $30-60\,\mu$m. Their thickness of $1-3\,\mu$m can be estimated by thin-film interference pattern. The ring pattern inside of the objects corresponds to interference of the laser being reflected at the interface and the bottom of the structure (see image 5 in figure 6.6).

These results are a visual confirmation of a controlled collapse in the film. The collapse is reversible apart from the amount of missing polymer as confirmed by the hysteresis measurements. It is initiated when the surface pressure reaches the critical value Π_c, which is slightly higher for the diblock polymers due to the influence of the PEG block on the surface tension of the water subphase [84,88]. Furthermore, the surface pressure in the transition plateau is equivalent to the surface tension change associated with the removal of P*n*BA chains from the air-water interface. This value is given by the already mentioned spreading coefficient S ($S = \Pi_c = \gamma_{\text{air-water}} - (\gamma_{\text{air-P}n\text{BA}} + \gamma_{\text{P}n\text{BA-water}})$). The surface pressure reaching the critical value Π_c means S is reaching 0. The polymer is now able to dewet from the interface. This is what most likely happens upon further compression. The P*n*BA chains dewet from the water surface instead of being further compressed in a uniform monolayer. A thermodynamic model considering the entropic penalty of confining polymer chains to a monolayer suggests that the removed polymer forms a single large domain in order to minimize the large surface at the water-polymer interface [30]. However, details of this mechanism of dewetting are not only controlled by thermodynamics but also by the hydrodynamics of subphase and film. The observed coexistence of monolayer and dewetted domains is caused by the slow kinetics of structure formation. The results indicate that the P*n*BA films at the air-water interface are in an initial stage of dewetting from the water interface. However, our BAM images show that although many small domains exist, larger ones are also present that seem to be able to grow with time by integrating smaller domains. We cannot exclude the possibility that these large objects in the BAM pictures represent regions of collapsed polymer already coexisting in the monolayer. Formation of such macroscopic structures have been observed for a block copolymer MEH-PPV depending on how the films were prepared [66].

6.3 Off-specular Scattering: Polymer Dewetting the Water Interface

To analyze the structure of the polymer films, off-specular XRR experiments were performed directly on the Langmuir trough. The advantage of off-specular towards specular experiments is that they are sensitive to the lateral structure in the film. However, the model calculations and experiments are highly demanding and strongly depend on the specific experimental scattering setup as described in section 3.2. During the course of this work, the setup was moved into a new laboratory and newly adjusted. This has to be mentioned because the form of the scattering depends on the scattering setup and adjustments. In the following, the off-specular scattering of PEG_6-*b*-P*n*BA_{132} and a model to describe the scattering will be presented first.

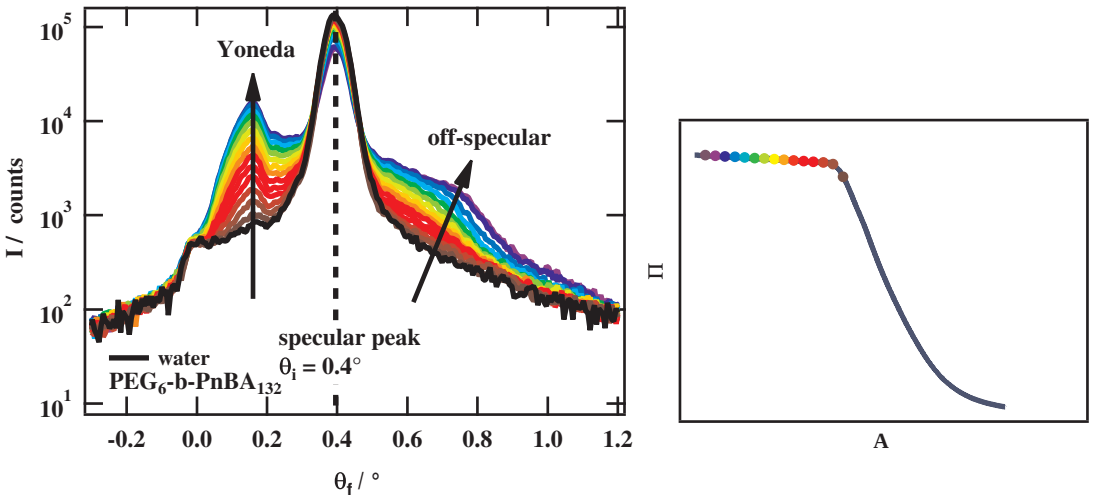

Figure 6.7: The left panel displays the reflected intensity of a PEG_6-*b*-P*n*BA_{132} monolayer during compression for an incident angle of $\theta_i = 0.4°$. The positions within the isotherm are marked in the right panel of the figure. For the duration of the scattering experiment (4 times 30 s) the compression was interrupted. Moreover, before each measurement a waiting time of 2 minutes was ensured to avoid non-equilibrium effects.

6.3.1 Transition Plateau of PEG_6-*b*-P*n*BA_{132}

The experiments were conducted at fixed θ_i (see figure 3.8) with variable θ_f (line detector) for a series of positions in the isotherm. Before moving the setup, the angular acceptance of the detector was $\Delta\theta_f = 2°$ while it was increased to $\Delta\theta_f = 10°$ in the new laboratory. Figure 6.7 displays the results for an incident angle of $\theta_i = 0.4°$ with a logarithmic intensity scale. Different colours refer to a series of measurements obtained during compression of the film. The corresponding points in the isotherm are shown in the same colour code on the right panel of the figure. The scattering curve of a bare water surface is shown in black colour.

The first reflectivity measurement on the polymer film was performed just before the crossover into the constant pressure plateau. As seen in the reflectivity of the film, at this area it is nearly identical with that of the bare water surface. Further compression of the film leads to a continuous decrease of the specular intensity ($\theta_f = \theta_i$) and increase of the off-specular intensity. The most prominent feature in the off-specular scattering can be differentiated into two phenomena. These two anomalous phenomena occur close to the specular peak. For a detector angle of $\theta_f = \theta_c$ (critical angle of total reflection), the reflected intensity increases dramatically. At the same time a shoulder becomes visible for $\theta_f \sim 0.7°$. Both phenomena are strongly enhanced by further compression of the film in the plateau. The maximum at $\theta_f = \theta_c$ is identified as the Yoneda peak. It was first detected by Yoneda in 1963 [94]. His observations indicated that the diffuse scattering of a rough surface is resonantly enhanced while the specular peak intensity decreases. In accordance with these observations it is possible to conlude that the roughness of the interface in the plateau strongly increases with compression of the film.

The importance of the roughness for the off-specular scattering has been introduced in chapter 3.2.3 & 3.2.5. It is only possible to calculate the off-specular component for the

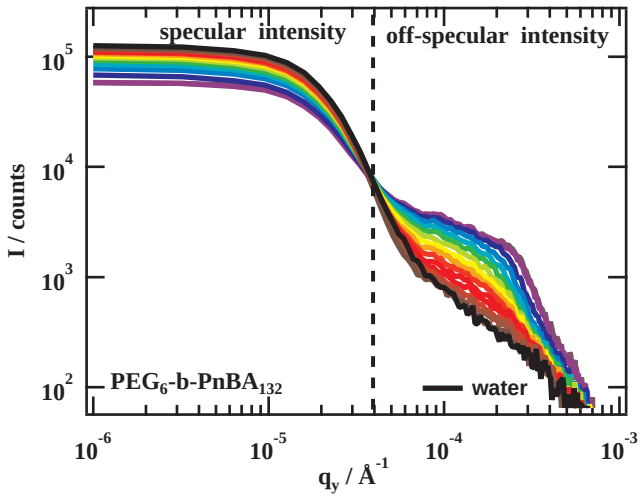

Figure 6.8: Off-specular intensity of PEG_6-*b*-P*n*BA_{132} vs. the in-plane scattering vector q_y for $\theta_i = 0.4°$. The colours refer to consecutive measuring points in the isotherm shown in figure 6.7.

intensity if a functional form of the height-height correlation function is known. Additionally the model has to be adapted to experimental conditions. If all contributions are taken into account correctly it is possible to characterise the lateral structure of an interface by analyzing the off-specular component. A good example is the contribution of capillary wave modes of a liquid interface given by equation (3.44) in section 3.2.5.

In the following the discussion will be splitted into two parts. First, the results of the shoulder appearing for $\theta_f > \theta_i$ will be discussed before turning the focus on the *Yoneda peak* at $\theta_f = \theta_c$. The scattered intensity for $\theta_f > \theta_i$ is displayed on logscale in figure 6.8 versus the scattering vector q_y in y-direction (see equation (3.33)). For the pure water surface and the data for low film compression the off-specular intensity obviously follows a power law decay with q_y. This power law is characteristic for the spectrum of capillary waves from a liquid interface. With further compression of the film an additional scattering component appears on top of the power law. Intensity increases in form of a shoulder with compression. This second contribution appears in addition to the spectrum of capillary waves and is clearly related to the structure formation of the film in the plateau.

The goal is to obtain a quantitative description of the scattering from the polymer film. A Gaussian shaped function with the instrumental resolution ($\Delta\theta_f = 0.733$ mrad) is used to account for the contribution of the specular peak. To model the off-specular intensity two independent parts are used. One is the contribution of capillary waves from the liquid water surface and the other one is scattering from micro-islands of the film being in an initial stage of dewetting. The measured intensity I_{dif} is assumed to be the sum of the scattering from the capillary wave spectrum I_{cap} and that of the micro-islands I_{isl}:

$$I_{dif} = I_{cap} + I_{isl} \tag{6.2}$$

For a liquid surface excited by capillary waves, the height-height correlation function $C(R)$ is well known and the scattering can be calculated considering dynamical scattering effects[53] within the distorted wave Born approximation (DWBA). In the case of our ex-

perimental setup taking into account the instrumental resolution, the scattering intensity is given by[58]

$$I_{cap}(q_y) = C\frac{q_c^4}{16q_z^4}|T_i(\theta_i)|^2|T_f(\theta_f)|^2 e^{-\sigma_{eff}^2 q_z^2}\,{}_1F_1\left(\frac{1-\eta}{2};\frac{1}{2};-\frac{q_y^2}{2\Delta q_y^2}\right) \tag{6.3}$$

and has been introduced in detail in chapter 3 (see equation (3.44)). The transmission functions $T_{i/f}(\theta_{i/f}) = 2\sin(\theta_{i/f})/(\sin(\theta_{i/f}) + \left(\sin^2(\theta_{i/f}) - \sin^2(\theta_c)\right)^{1/2})$ are introduced within the DWBA. Furthermore, the equation includes the resolution of the instrument $\Delta q_y = 1/4\, q_z\, \Delta\theta_y$, the roughness σ_{eff} of the water interface and the parameter $\eta = k_B T q_z^2/2\pi\gamma$ which is determined by the surface tension γ of the liquid. ${}_1F_1(x;y;z)$ denotes the confluent hypergeometric function also known as the Kummer function. The model also contains a scaling factor C. As can be seen in the isotherm in figure 6.7, the first measurement was performed just before crossing into the plateau. For this point, the off-specular scattering is nearly identical to that of the bare water surface. This measurement was used to determine the scaling factor C and the roughness of the water surface $\sigma_{eff} = 2.8\,$Å, being the typical roughness for water measured with our setup[5]. Both values were fixed in our model for the scattering of the higher compressed films.

Langmuir and BAM experiments indicate the appearance of structural changes within the plateau. The off-specular intensity now provides access to the height-height correlation function of the polymer film at the surface during compression. Based on these observations a model for the height-height correlation function is introduced. Correlation is assumed to be isotropic in the layer and to be governed by a repeat distance $l = 2\pi/q_0$. l may be seen as an average size of the dewetted regions or islands. The range of order is described by a decay constant κ and the thickness of the islands is given by h. This results in a correlation function that has already been introduced for thin films dewetting solid substrates[42].

$$C(X,Y) = h^2 e^{-\kappa R}\cos(q_0 R) \quad \text{with} \quad R = \sqrt{X^2+Y^2} \tag{6.4}$$

Using equation (3.43) and the correlation function C(X,Y), the contribution I_{isl} to the diffuse scattering profile can be calculated as[45]

$$I_{isl}(q_y) = B\left(\frac{q_c}{q_z}\right)^4 e^{-q_z^2\sigma^2}\int_0^\infty \left(e^{q_z^2 h^2 e^{-\kappa Y}\cos(q_0 Y)} - 1\right) e^{-\delta_{q_y}^2 Y^2} e^{i q_y Y}\,dY \tag{6.5}$$

with the reciprocal vector for the critical angle q_c, the roughness of the polymer-air interface σ, a scaling factor B and the resolution of the experimental setup along the y axis ($\delta q_y = 1/4\, q_z\, \Delta\theta_y$ with $\Delta\theta_y = 0.733\,$mrad). As already discussed in chapter 3.2.5 only the Y direction contributes to the integral due to the experimental setup. The setup limits the area in which constructive interference at the interface can occur to roughly 6 nm along X and 30 μm along Y.

With equation (6.2) the sum of both contributions is used to describe the off-specular intensity. The growth of the maximum is described by the contribution of the island scattering I_{isl} from equation (6.5). It was even possible to simultaneously fit all four incident angles in a global fit procedure. The full curves in figure 6.9 demonstrate the very

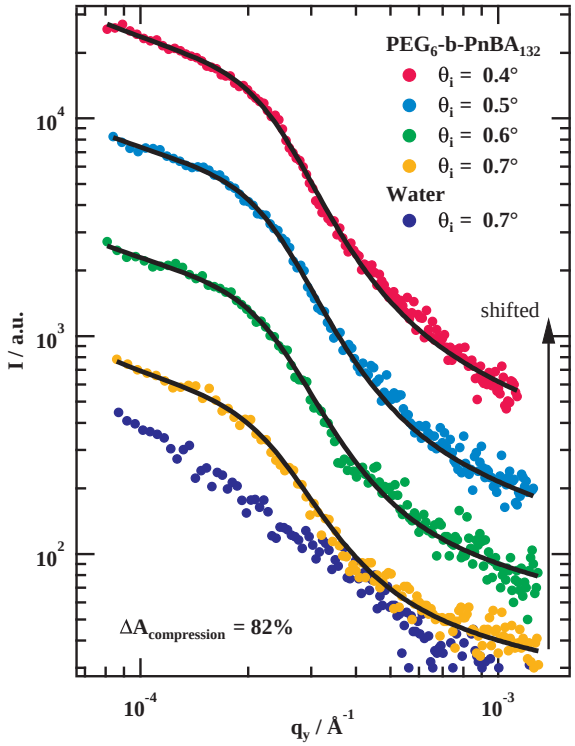

Figure 6.9: Off-specular intensity of PEG_6-*b*-P*n*BA_{132} for $\Delta A_{compression} = 82\,\%$ (all measured incident angles). Data from pure water for $\theta_i = 0.7°$ is also shown for comparison. The curves are shifted as indicated with exception of the data from pure water and $\theta_i = 0.7°$. Data from four different incident angles were fitted simultaneously in a global fit using equation (6.2) and the resulting fit curves are shown as full lines in the plot.

good description of the data by the model. The variables q_0, κ and σ were determined with great accuracy due to the global fit. The scaling factors B were fitted individually for each angle. The data shown in figure 6.9 represents an almost fully compressed film on the trough. The positions in the isotherm will be differentiated by their different degree degree of compression. $\Delta A_{compression} = 0\%$ corresponds to the position just before crossing into he plateau while 100% means the film is in its most compressed state in the plateau.

At the beginning of the plateau, the contribution of the island scattering is very small and the global fit does not converge with physically reasonable values. For films compressed more than $\Delta A_{compression} > 45\,\%$, the fitting procedure converged and the results are shown in figure 6.10. The left panel shows a selection of correlation function C(X,Y) from equation (6.4) with the two global variables q_0 and κ. The correlation functions are normalized by their island height h for better comparison. The first minimum represents the radius of the islands $l/2$ which shifts to smaller values with compression of the layer. It reduces from 3.2 μm to 2.5 μm. At the same time it is possible to interpret the decay constant κ as a measure for the size distribution in reciprocal space. The values for κ range between 50 % to 60 % of the island size. This rather large value of κ is demonstrated by the strong decay of the oscillation in the correlation function. The second minimum of the function is barely visible. The other two globally fitted parameters are presented in the right panel of figure 6.10. Upon compression the island height h represented by the blue

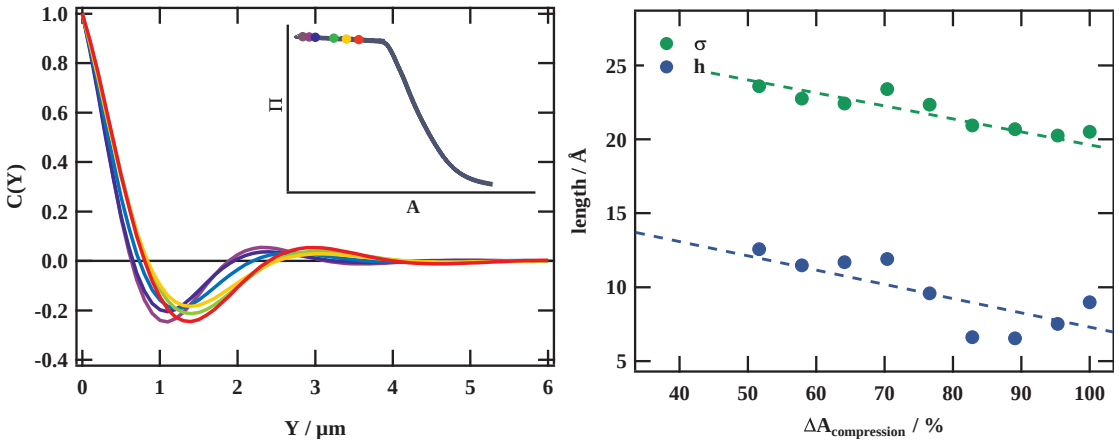

Figure 6.10: The left panel shows a selection of the normalized correlation functions $C(Y)$ obtained from the globally fitted parameters q_0 (reciprocal island size) and κ (damping coefficient). The positions in the isotherm are marked in the inset of the curve. The right panel displays the remaining global parameters σ (overall roughness) and h(island height) for compression rates (100 % corresponds to the most compressed state in the plateau) for which the fit converged.

dots reduces from 14 Å to values below 10 Å. The green dots represent the overall roughness of the layer σ which weakly reduces upon compression. Furthermore, it is roughly twice the value of the island height which indicates that there has to be another contribution to the roughness of the layer that is not included in the utilized model. Strictly speaking the overall roughness of the layer should be equal to $C(0) = h^2$. However, if this constraint was used in the model the fit did not converge.

This leads to the question how strong the different parameters of the model are correlated. For this purpose, the Pearson correlation coefficient (PCC) was computed within the fitting procedure which is a measure of the linear correlation between two variables. The coefficient ranges from -1 to 1, where 1 is total positive linear correlation, 0 is no correlation and -1 total negative linear correlation. In figure 6.11, PCC is presented for q_0, κ, h and σ for all measured areas in the plateau. The correlation will be discussed one at a time starting with q_0 in the upper left panel. There is a positive linear correlation between the island size q_0 and the island height h which is almost 1. An increase of q_0 follows an increase of the island height h so that smaller values of the island height h directly lead to a larger island size $l = 2\pi/q_0$. The observation that the island size l and height h decrease upon compression is clearly not a correlation effect of the two fitting parameters. The correlation for the other parameters is rather small $|PCC(q_0)| < 0.5$. Especially the fact that there seems to be little correlation between κ and q_0 indicates that those two parameters can be determined independently in the fitting procedure. For κ which is displayed in the upper right panel the situation is different. The PCC shows that there is a positive linear correlation between κ and the amplitudes (displayed as an average B_{avg} for all angles), a negative linear correlation with the island height h and a strong negative linear correlation with the layer roughness σ. This shows that κ is affected by almost all other fitting parameters except q_0. The correlation for h, displayed in the bottom left panel, shows a positive linear correlation for q_0 and a negative one for κ. There is also a weaker positive contribution by σ which decreases upon compression. The overall layer roughness σ shows a strong negative correlation with the amplitudes

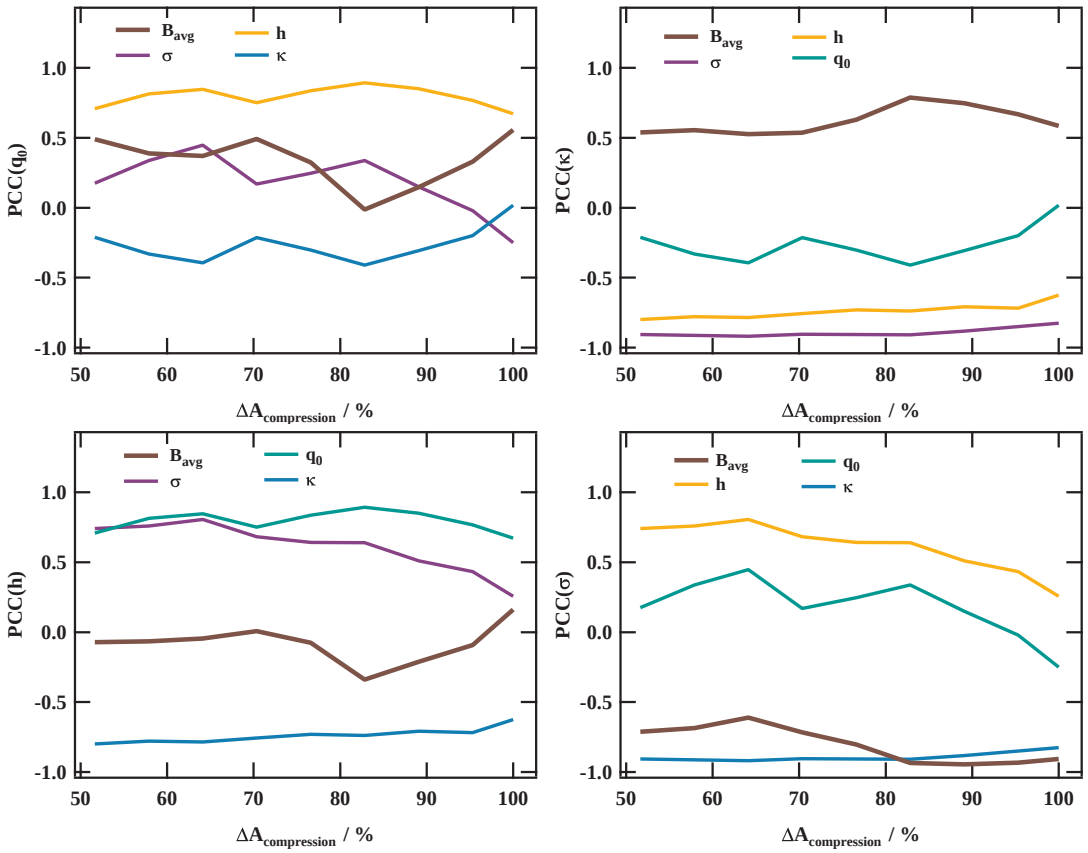

Figure 6.11: The four panels show the Pearson correlation coefficients PCC for PEG_6-*b*-P*n*BA_{132} with q_0 (top left panel), κ (top right panel), h (bottom left panel) and σ (bottom right panel). The PCC shows the correlation between the fitting parameters. The coefficient ranges between -1 and 1, where 1 is total positive linear correlation, 0 is no correlation and -1 total negative linear correlation.

B_{avg} and also κ. This is not too surprising since its contribution in the model is reducing the intensity similar to a Debye-Waller factor. The PCC showed that especially κ, h and σ are correlated with the other fitting parameters in the model. A concluding remark is that only the island size q_0 can be determined independently of the other fitting parameters. Conclusions on the size distribution κ, island height h and overall layer roughness σ have to be considered with care. Evidently, this becomes apparent in the fitting of the kinetic measurements where the fitting procedure is not used globally but for only one incident angle θ_i. The results on κ, h and σ vary slightly for that case as will be shown later on in this section.

After analysing the correlation between the different parameters it is still possible to come to a conclusion for the overall picture of the polymer film on the water surface. Islands of a preferred lateral length scale $l \approx 2.5 - 3.2\,\mu$m with a size distribution (κ/q_0) of around 50 % and 60 % are formed. Their size reduces upon compression. While their lateral size is a few μm, their height is just around 10 Å that also reduces slightly upon compression. It seems surprising that both parameters decrease upon compression, however there is no indication that this is an artifact produced by the fitting procedure. Since there are no measurements on the film thickness in this regime, it is also possible that

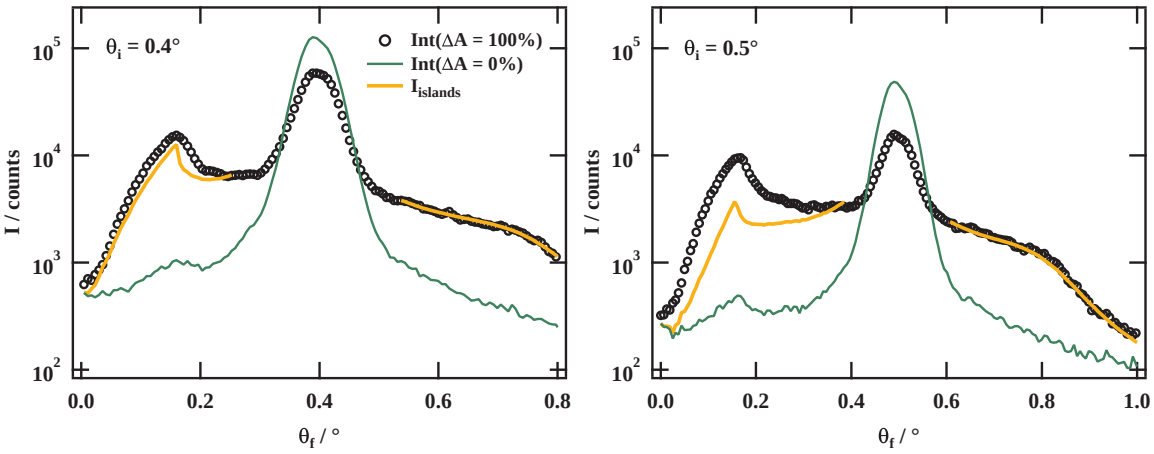

Figure 6.12: The panels show two full spectra reflected at the PEG_6-*b*-P*n*BA_{132} film for an incident angle of $\theta_i = 0.4\,^\circ$ in the left and $\theta_i = 0.5\,^\circ$ in the right one. The spectra represent the scattering before the plateau ($\Delta A_{compression} = 88\,\%$, green line) and for maximum compression of the film ($\Delta A_{compression} = 100\,\%$, black dots) in the plateau. The orange line presents the island model for off-specular scattered intensity for $\theta_f > \theta_i$ and its at the specular peak mirrored curve for $\theta_f < \theta_i$. The mirrored curve was also multiplied by the transmission function $|T_f(\theta_f)|^2$.

by increasing the thickness upon compression, the conditions for the dewetting of the polymers change since they also depend on the layer thickness. The overall roughness of the layer is around $\sigma = 20\,\text{Å}$ which is around twice the height of the island size. The fitting procedure for one incident angle as performed in the kinetic measurements leads to a different results where σ and h are almost the same. This shows how strongly the two parameters are correlated. At the same time it is very difficult since the correlation of the parameters also affects the size distribution κ. However, with this constraint it is not possible to fit all four incident angles globally. So far, a reason for this could not be found. One possibility is that a q dependent prefactor in equation 6.5 is not correctly implemented in the model.

Comments on the Yoneda Peak

It has already been discussed that the Yoneda peak is an anomalous scattering phenomena exhibiting in the form of a peak at $\theta_f = \theta_i$. It is a dynamic scattering effect that enhances the reflected intensity for the critical angle. Generally, the effect can be described by the product of the transmission functions $|T_f(\theta_f)|^2$ which increases the intensity by a factor of 4 at $\theta_f = \theta_i$. A rough surface leads to an additional increase of the Yoneda peak's intensity as already observed by Yoneda himself[94]. A theoretical approach formulated by Névot-Croce describes this enhancement of the transmission functions[95,96]

$$T'(\theta_f) = T(\theta_f) \cdot \exp\left(\left(q_z - \sqrt{q_z^2 - q_c^2}\right)^2 \frac{\sigma^2}{8}\right) \tag{6.6}$$

by a factor related to the roughness σ of the interface. In order to verify this relation it is necessary to have a full description of the off-specular scattered intensity arising from the height-height correlation function for $\theta_f < \theta_i$. In a first attempt, the model obtained for the fits in figure 6.9 was mirrored at the specular peak under the assumption that

the diffuse scattered intensity from the interface is symmetric around the specular peak. This is illustrated for $\theta_i = 0.4°$ and $\theta_i = 0.5°$ in figure 6.12. The reflected detector spectra are shown for $\Delta A_{compression} = 100\,\%$ and $\Delta A_{compression} = 0\,\%$ (situation before the film is compressed into the plateau). The mirrored intensity for the height-height correlation function is multiplied by the transmission functions $|T_{i,f}|^2$ without the additional enhancement of the Névot-Croce factor. It is easy to see that this approach did not work because the curve nearly describes the data for $\theta_i = 0.4°$ while this cannot be said for $\theta_i = 0.5°$. The additional Névot-Croce factor is only able to enhance the intensity by the same factor for both cases. The problem is that the off-specular component to the diffuse scattering profile is not as simply as mirroring the fits for $\theta_f > \theta_i$. The model in equation 6.5 is derived in the Born approximation. The approximation is valid for the weak scattering regime and it is legitimate to use it in the fits for figure 6.9. However, to calculate the contribution of the correlation function in the vicinity of the critical angle, it would be necessary to calculate the contribution of the model within the DWBA. Furthermore, as already mentioned before there are contradicting results between globally fitted curves and single fits for the correlation of the fit parameter (experiments on the kinetics shown at the end of this chapter). It is possible that a prefactor is not implemented correctly which is absolutely necessary to calculated the scattering in the vicinity of the critical angle using the parameter obtained from the correlation function. To conclude, a full description of the Yoneda peak was not possible within the model used to describe the off-specular scattered intensity for $\theta_f > \theta_i$.

6.3.2 Fourier Analysis of PEG_6-*b*-P*n*BA_{132} BAM Images

The off-specular scattering results indicate that polymer is dewetting the water interface on a macroscopic length scale. This was shown in the previous section by introducing a model for a height-height correlation function C(X,Y) (see equation (6.4)) that is able to describe the diffuse scattered intensity. The X-ray scattering occurs in reciprocal space and averages over the whole footprint of the X-ray beam. The scattering experiment does not measure the correlation function directly so that visualizing methods, such as BAM imaging, are very suitable to complement the results from the X-Ray scattering experiment. Furthermore, as there is evidence for a structure while measured as an averaged over the footprint of the X-ray beam, it has to be visible on a local length scale aswell. Prior to the discussion of the scattering data, BAM images of PEG_6-*b*-P*n*BA_{132} have already been shown in figure 6.6 for different positions in the isotherm. The images reveal small aggregates in the film. Upon compression they are getting closely packed in the film. In a simplified approach the intensity for each pixel can be associated with the height of the film z(x,y). Using image processing, periodic structures within the film can be revealed in the images.

The two-dimensional fourier transformation of the image $\tilde{z}(q_x, q_y)$ is calculated in order to separate structures on different length scales. The fourier transformed picture reveals if there are structures of a preferred length scale in the image. The so called power spectral density (*PSD*)

$$\tilde{C}(q_x, q_y) = |\tilde{z}(q_x, q_y)|^2 \tag{6.7}$$

can by directly computed from the fourier transform of the image and it represents the fourier transform of the correlation function C(X,Y). Using the PSD, the results from the two techniques can be directly compared and complement each other.

The fourier transform of the images was calculated using the fast fourier transform algorithm implemented in the *numpy package* for *Python*. The specifics of the algorithm are described in the package manual[1]. The algorithm uses a discrete *fast fourier transformation* (*fft*). The zero frequency term $|\tilde{z}(0,0)|^2$ represents the total intensity in the image. In order to avoid spatial aliasing, the largest accessible frequency in the transformed image (the *Nyquist frequency*) is given by half of the sampling rate of the images. In case of a $400\,x\,400$ px image, the *Nyquist frequency* is $q = 585\,nm^{-1}$ corresponding to a real space distance of $1/q = 1.71\,\mu m$. The *fft* of an image consists of complex numbers. Half of the image represents the complex conjugated frequencies, however, since it is not possible to know in which direction a waves propagates in our images, half of the information is redundant. Furthermore, once the PSD is calculated the phase information in the transformed image is lost anyway due to its definition as the absolute squared of the *fft*.

The algorithm was used to derive the PSD for the images of the PEG_6-*b*-P*n*BA_{132} isotherm shown in figure 6.6. Two representative examples (image 3 and 5 from figure 6.6) are shown in figure 6.13 as an example for the structure. The left side of the figure shows the images obtained for the begin (top) and the end (bottom) of the plateau, while the respective PSD performed over the white rectangle in the image is shown on the right hand side. The zero frequency term ($q_x = q_y = 0$) is in the middle of the PSD. The different behavior of the *fft* can be easily distinguished for the two images of the structure in the plateau. The top images representing the situation at the beginning of the plateau will be discussed first.

Two different features can be identified in the raw image. There are a number of aggregates visible as black dots in the top left image of figure 6.13. Furthermore, a faint wave spectrum is visible which origins from an interference effect from the reflection of the laser at the interface. The wave spectrum can be easily identified by its q-vector (q_x, q_y) in the fourier transformation. While a single wave length would transform into a single pixel in the *fft*, it is broadened for this wave spectrum. In the upper part of the image the wave front propagates in the y-direction, however there is an additional x-component when one looks at the bottom part of the image. Therefore, the wave is represented by the two spots at $(30\text{—}65, -(90\text{—}130))$ and $(-(30\text{—}65), 90\text{—}130) \cdot 10^3\,\mu m^{-1}$ in the *fft*. One of the spots is redundant since it is the absolute squared of the complex conjugated value. The interference phenomena demonstrates nicely how the *fft* works. Secondly, we can clearly identify a bright elliptically formed area in the middle of the image. The most outer region of the area corresponds to the size of the small aggregates in the image. Its elliptical form means that the shape of the aggregates is extended in the y-direction. Their size obtained from the *fft* is $8.8\,\mu m$ in x and $5.5\,\mu m$ in y direction which fits well with the size of a single aggregate when zoomed into the image.

In the second image at the bottom, much more structure can already be observed in the direct image of the interface. The white rectangle was chosen so that the large round aggregate is not part of the transformation because it would lead to a pattern charac-

[1] https://docs.scipy.org/doc/numpy/reference/routines.fft.html

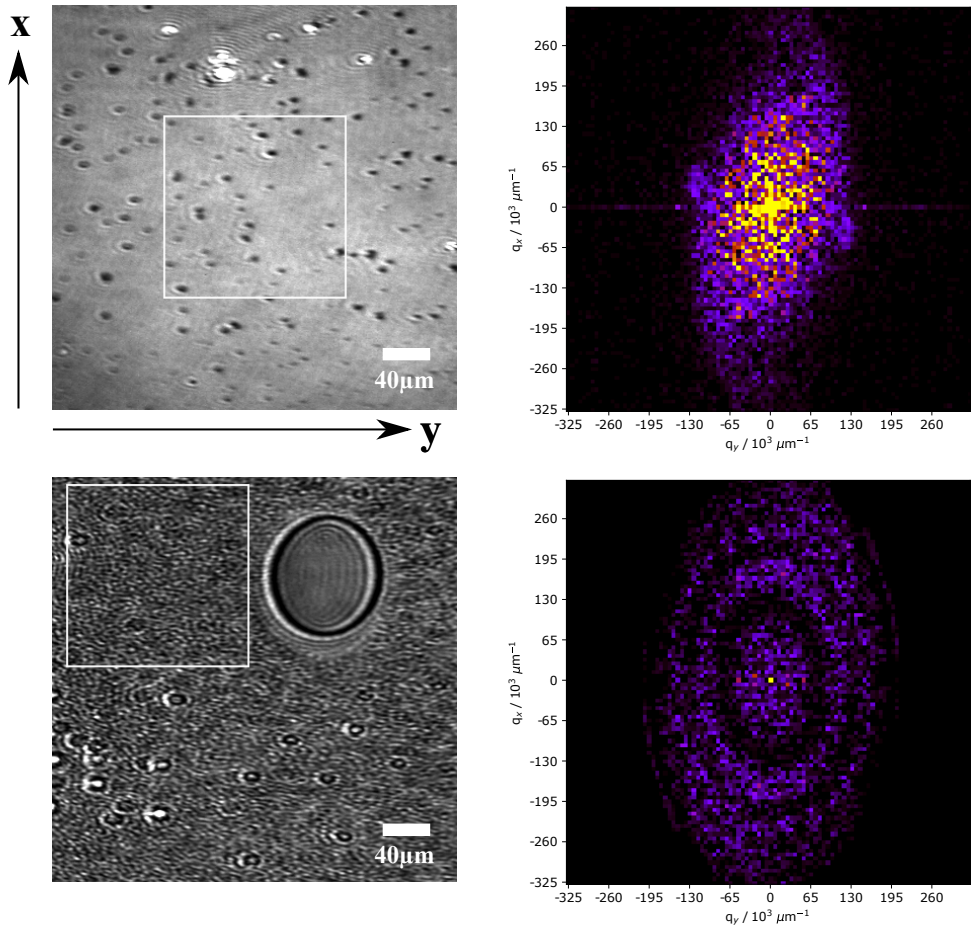

Figure 6.13: Two images recorded in the plateau of the PEG_6-*b*-P*n*BA_{132} isotherm are shown with the upper picture obtained at the beginning and the lower and the end of the plateau. The images were already shown and discussed in figure 6.6. The respective Power spectral densities (PSDs) over the white rectangle frame are shown on the right hand side of the image. The PSDs are the squared fourier transformations of the images. The zero frequency term (sum over all intensity in the image) is located in the middle of the PSD.

teristic for a lens. The section in the rectangular frame represent the typical structure in the compressed state of the plateau. In the *fft* spectrum, correlation is detected for small q, but additionally two halos are revealed for larger q values. These halos are proof that structures of preferred length scale are hidden within in the film. The larger halo limits the size of the structures and the characteristic wavelength is $q_x = 260 \cdot 10^3\,\mu m^{-1}$ and $q_y = 160 \cdot 10^3\,\mu m^{-1}$. The corresponding size of the structures is around $4\,\mu m$ in x-direction and $6\,\mu m$ in y-direction. Rectangular shaped structures are indeed visible on this length scale when zoomed into the frame. It is interesting that the orientation of the longer part is parallel to the compression direction of the film (y-direction). Furthermore, the *fft* results are in very good agreement with the data obtained from the scattering experiments. The size of the islands was determined to be $3\,\mu m$ with a size distribution

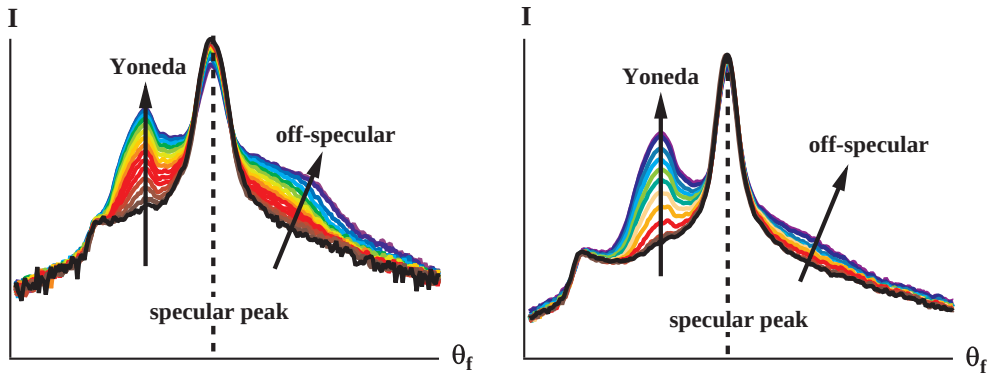

Figure 6.14: Direct comparison of the intensity recorded in the detector as I vs. θ_f before (left panel) and after (right panel) the instrument was moved into a new laboratory. After moving into a new laboratory it was necessary to do a new alignment and calibration of the setup. The scattering from the same film shows a considerably weaker off-specular scattering.

of 50 %. X-ray and BAM experiments both see this structure that appears to be similar to a thin polymer film dewetting a solid substrate. This further consolidates the idea of the PEG_6-b-P*n*BA_{132} film being in an initial stage of dewetting while compressed into the plateau of the isotherm.

6.3.3 Transition Plateau for all Samples

In the course of this work the XRR setup was moved into a new laboratory and a new alignment of all components was performed. In figure 6.14, two measurements before and after moving the setup are shown for the same sample (PEG_6-*b*-P*n*BA_{132}). Apparently, the same scattering phenomena is visible, however, the intensity of the shoulder for $\theta_f > \theta_i$ is considerably smaller compared to before. The increasing Yoneda peak intensity is almost the same in both experiments. This was really surprising at first, however, one has to keep in mind that the form of the intensity measured depends on properties of the experimental setup (see chapter 3.2.4) such as detector or instrumental resolution. The primary beam profile of the setup before and after moving the setup are almost identical. Furthermore, no parts of the experiment were exchanged so that it is safe to say that the experimental setup is not responsible for the difference in the spectra. The reproducibility of the experiments have also been assured in both laboratories. Some remaining external factors that are able to influence the experiment can be water quality or temperature. Both were controlled during the experiments and it is unlikely that they have such a strong influence on the scattering profile. What can not be excluded is an aging effect of the samples, however, the isotherms do not indicate this at all which is also difficult because the surface pressure Π is not a good quantity anymore within the plateau. It is also possible that the gas detector efficiency has been affected while moving the setup. This may be a possible explanation aswell. However, it was not possible to fully understand why the intensity of the shoulder decreased for the two measurements.

With this in mind additional experiments on the remaining molecular weights were performed. For the experiments performed after moving the setup the detector acceptance

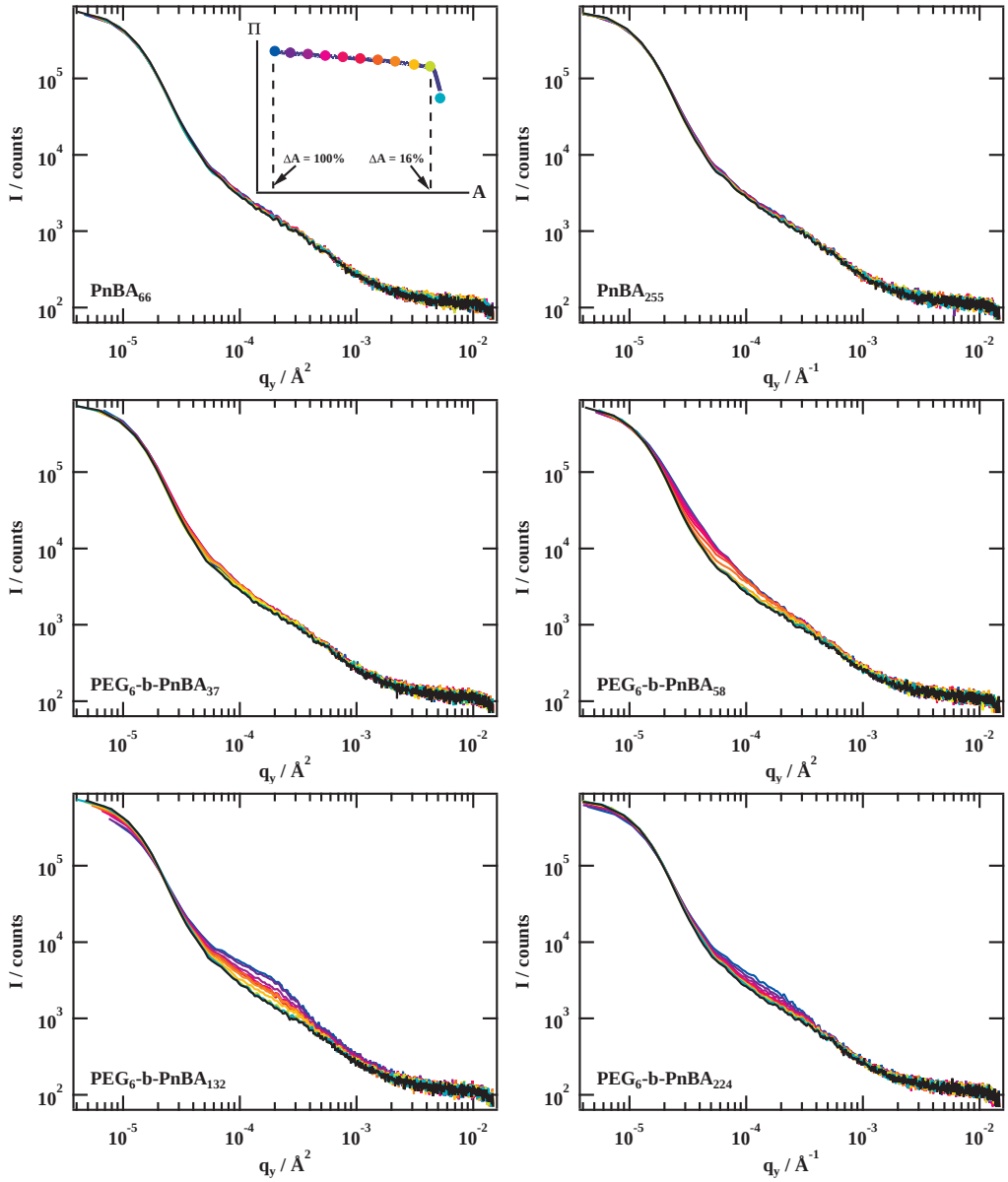

Figure 6.15: Off-specular intensity for all molecular weights displayed vs. the in-plane scattering vector q_y for $\theta_i = 0.4°$. The colors refer to consecutive measuring points in the isotherm shown in the inset of the top left panel. The two top figures are the homopolymers and the remaining four figures are the diblock copolymers both arranged for increasing molecular weight. The off-specular signal of the homopolymers does not show a contribution of island structures to the scattering profile while it can be observed for the diblock copolymers on a different length scale for all molecular weights.

angle was increased from 2° to 10° leading to an higher accessible q_y range up to an order of magnitude. A constant background scattering can be clearly observed in all measurements that are shown in figure 6.15. The figure displays the off-specular scattering for $\theta_f > \theta_i$ as I vs. q_y in the double logarithmic representation. The black curve is the off-specular scattering from the bare water surface while the different colours correspond to a series of measurements obtained during compression of the film. The positions in the

isotherm are marked in the inset of the top left panel in the figure. The first scattering curve was measured just before the isotherm crosses into the constant pressure plateau. The first measurement in the plateau is at an area of $\Delta A_{compression} = 16\,\%$ for all films and the smallest one is $\Delta A_{compression} = 100\,\%$. The two top panels present the diffuse scattering of the homopolymers P*n*BA$_{66}$ and P*n*BA$_{255}$. For both molecular weights the offspecular scattering is equivalent to that of the bare water surface. The contribution of the capillary wave spectrum is enough to describe the diffuse signal and there is no additional contribution from islands to the intensity. The off-specular scattering from the four diblock copolymers shown in the middle and bottom panel of the figure is different. While the diffuse intensity of PEG$_6$-*b*-P*n*BA$_{37}$ is only weakly affected upon compression into the plateau, a clear contribution can be identified for the three larger blocks. There are two important conclusions that can be named after looking at the raw diffuse scattering of all samples. The first one is that the contribution of the islands to the off-specular intensity can only be observed in the diblock copolymers. This is apparent by comparing the scattering of the similar molecular weights P*n*BA$_{66}$ to PEG$_6$-*b*-P*n*BA$_{58}$ and P*n*BA$_{255}$ to PEG$_6$-*b*-P*n*BA$_{224}$. In both cases a contribution of the islands to the scattering can only be observed in the diblock copolymers. Taking into account that the PEG block is necessary for the formation of the islands we can observe that its q_y dependency shifts to smaller values with increasing volume fraction of the PEG block. In case of the smallest block copolymer PEG$_6$-*b*-P*n*BA$_{37}$, this contribution even vanishes under the specular peak (see middle left panel of figure 6.15). It was also not possible to differentiate between specular and off-specular scattering for PEG$_6$-*b*-P*n*BA$_{58}$ because the diffuse intensity merges with the specular peak.

The diffuse scattering for the two largest diblock copolymers (PEG$_6$-*b*-P*n*BA$_{132,224}$) can be fitted by the sum of the two contributions, namely the capillary wave spectrum and the island scattering. The above described global fit procedure is also able to describe the off-specular intensity using equation (6.2). For PEG$_6$-*b*-P*n*BA$_{132}$, the full curves in figure 6.16 ($\Delta A_{compression} = 84\,\%$, left panel) demonstrate the very good description of the data by the model. However, since the contribution of the islands is much smaller compared to before moving the setup, the fitting procedure only converged with reasonable parameters for small areas in the plateau. For films compressed more than $\Delta A_{compression} > 66\,\%$ the fit converged properly and the results are shown in the left panel of figure 6.16. The correlation function $C(Y)$ from equation (6.4) is shown in the right panel. In the inset of the figure the isotherm is shown with the 4 positions marked for the scattering experiment. In the correlation function the first minimum shifts slightly to larger Y indicating that the islands slightly increase in size upon compression. Their size $l = 2\pi/q_0$ increases from 2.1 μm to 2.8 μm. At the same time the size distribution κ/q_0 slightly increases from 40 % to 50 %. The island height h decreases from 19 Å to 17 Å upon compression and the overall roughness from 22.5 Å to 20.5 Å. The Pearson correlation coefficient for q_0, κ, σ and h are shown in the appendix in figure 9.1. It shows that q_0 only shows a weak positive linear correlation with the average amplitude B_{avg} while κ, σ and h are stronger correlated with more than one of the fitting parameters. Although the amplitudes of the scattering process is now considerably smaller, the parameters obtained from the fit are similar to the earlier results before moving the experiment. The trend of increasing island size upon compression is the opposite of what has been observed earlier, however, it is very small in both cases and can be neglected. The most eye-catching difference is that

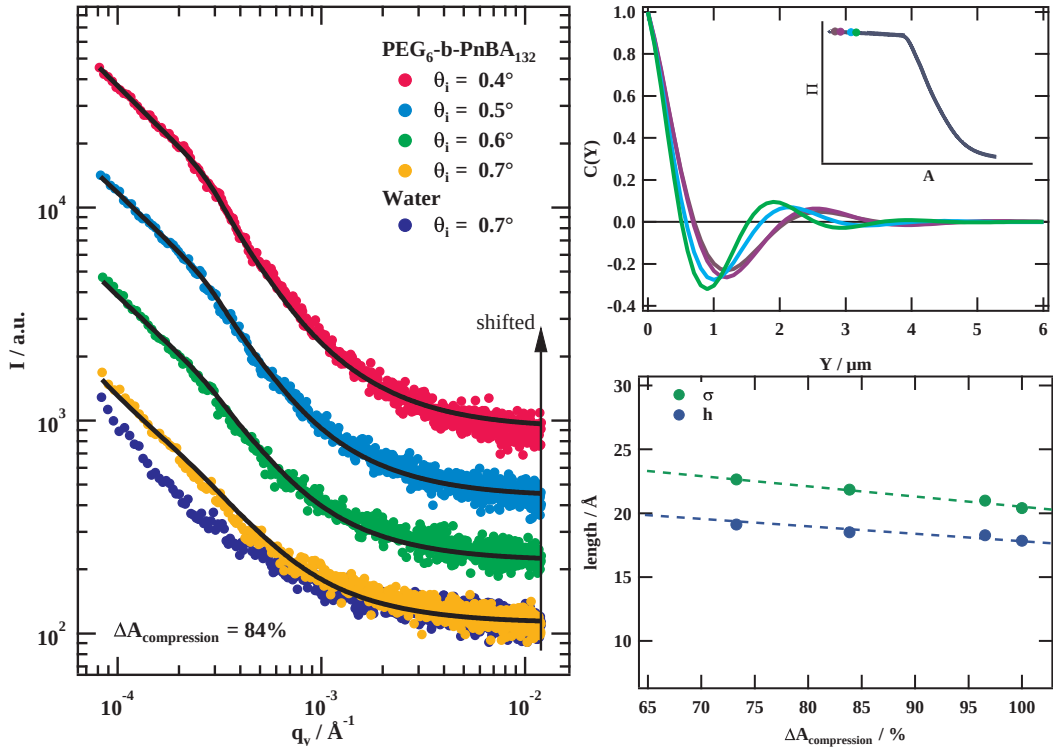

Figure 6.16: The left panel shows the off-specular intensity of PEG$_6$-*b*-P*n*BA$_{132}$ for $\Delta A_{compression} = 84\,\%$ (all measured incident angles) after moving into a new laboratory. Data from pure water for $\theta_i = 0.7°$ is also shown for comparison. The curves are shifted as indicated with exception of the data from pure water and $\theta_i = 0.7\,°$. Data from four different incident angles were fitted simultaneously in a global fit using equation (6.2) and the resulting fit curves are shown as full lines in the plot. The left top panel shows the normalized correlation functions $C(Y)$ obtained from the globally fitted parameters q_0 (reciprocal island size) and κ (damping coefficient). The positions in the isotherm are marked in the inset of the curve. The left bottom panel displays the remaining global parameters σ (overall roughness) and h(island size) for all areas in which the fit converged properly.

the island height h is almost twice as large as before even though the scattering observed is smaller. But the strong correlation of the parameter h makes it difficult to come to a specific conclusion regarding this difference.

In the left panel of figure 6.17 the diffuse scattering for PEG$_6$-*b*-P*n*BA$_{224}$ is shown for $\Delta A_{compression} = 82\,\%$ with the full curves representing the global fit to the raw data. The fit converged for films compressed more than $\Delta A_{compression} > 75\,\%$ and the results are shown in the right panel of the figure. The correlation functions $C(Y)$ look similar to the already discussed ones. However, the first minimum is slightly shifted to smaller Y which means the island size is smaller for this sample. Again it can be observed that the island size slightly increases from 1.6 μm to 2.1 μm upon compression. The size distribution κ/q_0 is around 33 % slightly smaller than for the other samples in all measurements. The overall layer roughness σ slightly increases upon compression from 21 Å to 24 Å while the island height h also increases from 15 Å to 19 Å. Looking at the Pearson correlation coefficient one has to realize that for these three fits all parameter are strongly correlated to each. While this was also the case for κ, h and σ for PEG$_6$-*b*-P*n*BA$_{132}$ before and after moving

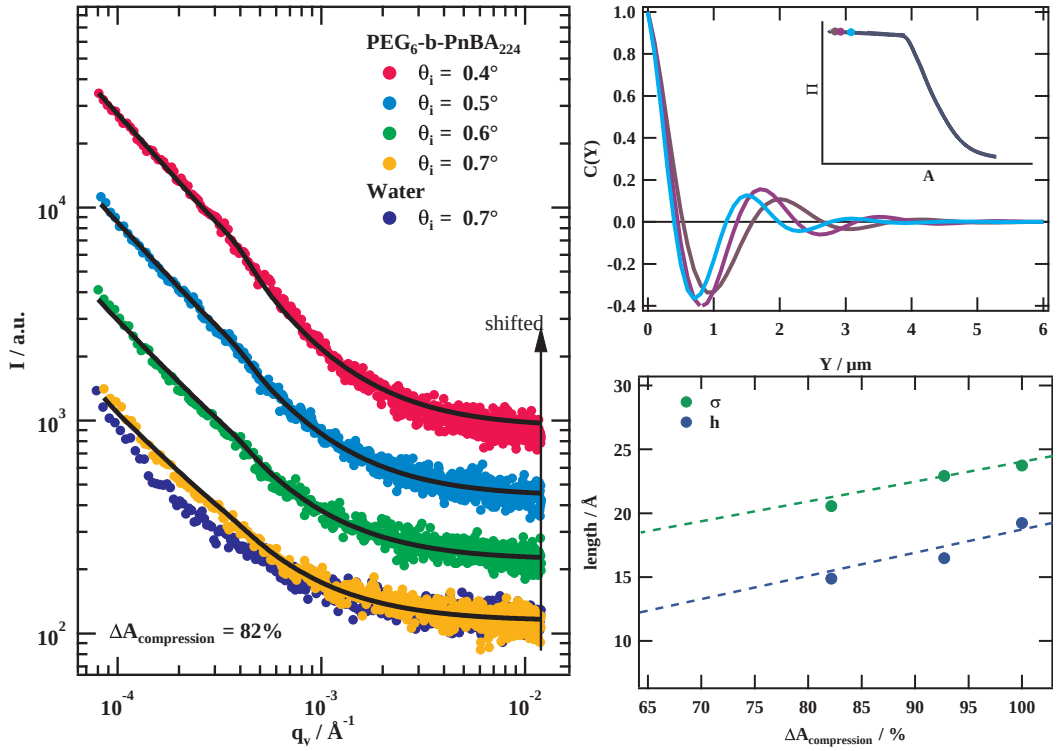

Figure 6.17: The left panel shows the off-specular intensity of PEG$_6$-*b*-P*n*BA$_{224}$ for $\Delta A_{compression} = 82\,\%$ (all measured incident angles) after moving into a new laboratory. Data from pure water for $\theta_i = 0.7°$ is also shown for comparison. The curves are shifted as indicated with exception of the data from pure water and $\theta_i = 0.7°$. Data was fitted as already stated in the last figure and the resulting fit curves are shown as full lines in the plot. The correlation functions $C(Y)$ and the overall roughness σ plus island size h are shown in the right panel for all areas in which the fit converged properly.

the setup, q_0 was only weakly correlated to one of the other fitting parameters. The fits converged with larger q_0 which means smaller island sizes.

An interesting question is what kind of difference exists for the diffuse scattering of the different samples. The normalized correlation functions $C(Y)$ for $\Delta A_{compression} = 82$ & $93\,\%$ for the three discussed cases are shown in figure 6.18. For both areas the correlation functions of PEG$_6$-*b*-P*n*BA$_{132}$ are almost identical to before. This confirms once again that the observed scattering phenomena is indeed the same, however, for some reason its signal was greatly reduced after the instrument was moved. The correlation function of PEG$_6$-*b*-P*n*BA$_{224}$ clearly indicates that smaller islands are formed for both areas. This general trend can also be observed in the presentation of the raw data in figure 6.15. For the two smallest molecular weights, the scattering process approaches respectively vanishes within the specular peak. Since comparable molecular weights of the P*n*BA homopolymers do not show any diffuse scattering from island structures, the formation of the islands can be clearly related to the existence of the PEG block. The existence of the PEG block increases the mobility of the polymers on the surface which in return enables them to arrange on longer length scales. In a theoretical model that considers the penalty for confining into a monolayer suggested that upon compression into the plateau P*n*BA chains are able to leave the interface and the excess polymer should form a single large

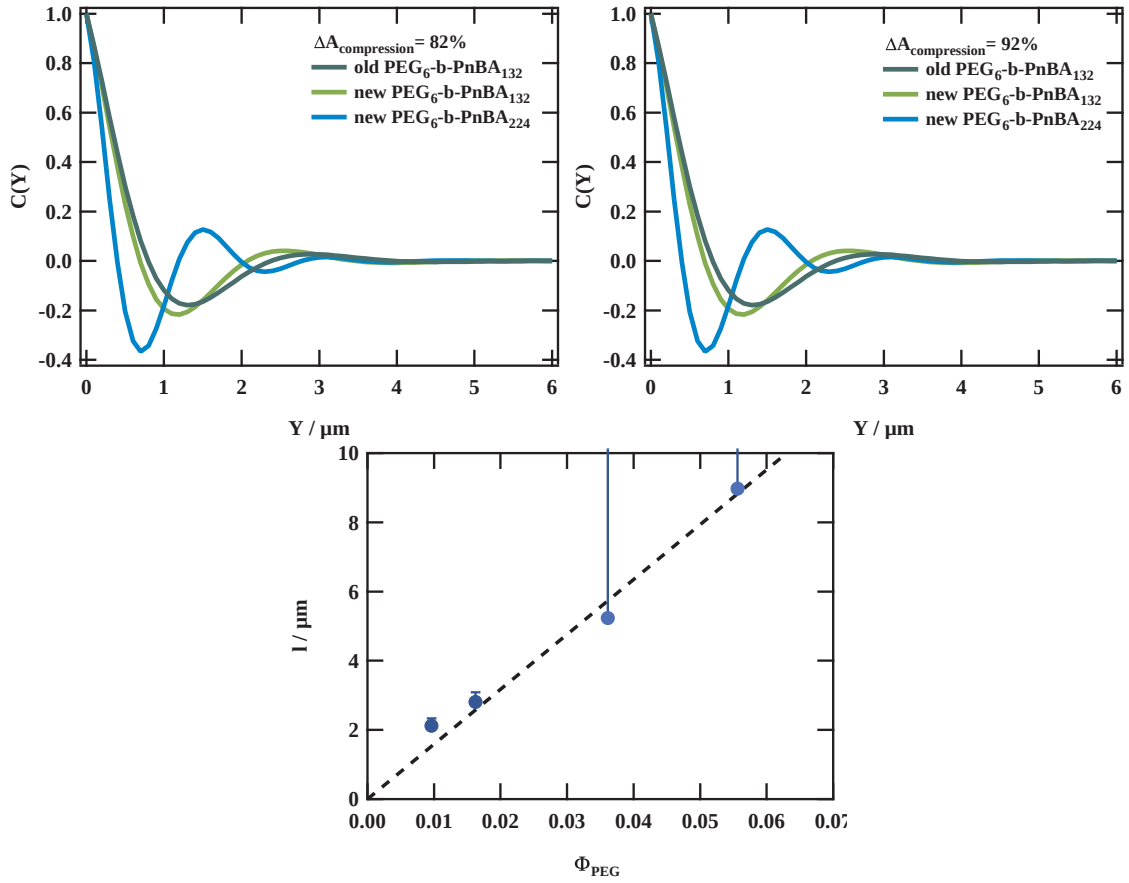

Figure 6.18: In two top panels the normalized correlation function C(Y) is displayed for PEG_6-*b*-P*n*BA_{132} before and after moving the setup and PEG_6-*b*-P*n*BA_{224}. Two different positions in the isotherm ($\Delta A_{compression}$ = 82 & 93 %) are used to compare the results for the different samples. While the correlation function for PEG_6-*b*-P*n*BA_{132} is almost identical in both cases, the minimum for PEG_6-*b*-P*n*BA_{224} is clearly shifted to smaller values indicating that smaller islands are formed for the larger diblock copolymer. The bottom panel shows the island size l in dependency of the PEG volume fraction Φ_{PEG} for the most compressed film. The minimum island size for the two smaller diblock copolymers ($\Phi_{PEG} = 0.036 \& 0.056$) was estimated from the raw data since it was not possible to separated specular and off-specular intensity for these samples. The island sizes are almost on a straight line from the origin.

domain in order to reduce the polymer water interface [30]. However, due to the slow kinetics the polymers are locally trapped in domains. Logically the mobility of the polymers increases with volume fraction of the PEG block. Therefore, it is interesting to compare the island size l to the volume fraction ϕ_{PEG} in the diblock copolymers.

It was not possible to get a fit for the two smaller molecular weights, the minimum size of the islands could only be estimated from the raw data to $q_0 \leq 0.7 \cdot 10^{-4}$ for PEG_6-b-$PnBA_{37}$ and $q_0 \leq 1.2 \cdot 10^{-4}$ for PEG_6-b-$PnBA_{58}$. In the bottom panel of figure 6.18 the island size l for the most compressed film is plotted over the volume fraction ϕ_{PEG}. The island sizes are almost on a straight line from the origin. Even though two points in the plot can only be estimated, a positive correlation between the island size l and the PEG volume fraction can be confirmed. The idea of higher mobility in the diblock copolymers is reasonable and can explain why the contribution of the islands to the diffuse scattering

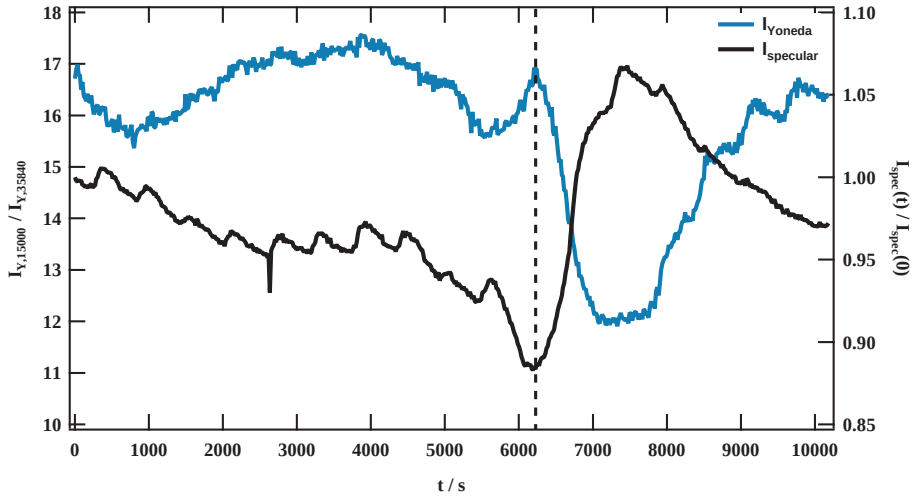

Figure 6.19: Time evolution of the Yoneda peak's intensity after the film was compressed to an area of $\Delta A_{compression} = 88\,\%$ into the plateau. The intensities were normalized by the Yoneda peak's intensity of the film before it was compressed into the plateau. A broad minimum can be observed for a long times at $6000\,s < t < 9000\,s$. The intensity of the specular peak normalized by its value for t=0 is plotted for better comparison vs the right axis of the plot.

between homopolymers and diblock copolymers is completely different. The underlying mechanism for the dewetting is controlled by the hydrodynamics between subphase and film and luckily for two of our samples it was possible to observe the island formation within the limited q_y range of the XRR setup. All shown scattering curves were measured after an equilibrium time of 100 s which makes it easy to compare them between each other. However, if the mobility of the chains play an important role it is also necessary to look into the kinetics of the mechanism. For this purpose a series of measurements were performed which will be described in the following.

Time Evolution of the Off-Specular Intensity

Identifying the kinetics of the mechanism might also help to further characterize the specific mechanism of dewetting. The appearance of a well defined length scale in the structuring process of the thin polymer film is of course reminiscent of an underlying spinodal process. This scenario would imply a fluctuation length scale with strong growth rate dominating the process. Such a scenario has been discussed, as an analogous mechanism to liquid-liquid demixing of a bulk solution, to be responsible for the dewetting of thin films [97,98] and has been successfully applied for thin films dewetting solid substrates [42]. The capillary instability mechanism driven by thermal fluctuation is responsible for the breakup of these thin films. The analogy to the mechanism of spinodal decomposition in fluid mixtures is that height fluctuations of the thin film correspond to composition fluctuations in the fluid mixture. In order to investigate the kinetics the polymer film was compressed into the plateau until the overall area of the trough was at $\Delta A_{compression} = 88\,\%$. Right after the barriers were stopped, a series of full diffuse spectra were recorded for $\theta_i = 0.4°$. The series consist of 600 subsequent measurements with accumulation times of 17 s recording the evolution of the diffuse profile on a time scale up to 10200 s.

Presenting the raw data for all 600 measurements at the same time is practically impossible. It is more convenient to look at the evolution of the different phenomena starting with the intensity of the Yoneda peak and the specular peak that are plotted in figure 6.19 as a function of the time after compressing the film. The intensity of the Yoneda peak is normalized by its intensity before the film was compressed into the plateau ($\Delta A_{compression} = 0\,\%$). The Yoneda peak is enhanced by a factor of 16 to 17 to that before the film was compressed into the plateau. Its intensity fluctuates slightly over a long time frame until it changes suddenly for $t \approx 6200\,s$ (marked by the dashed vertical line). The peak intensity reduces around 25 % within a few hundred seconds and stays there for one thousand seconds. Afterwards it slowly increases again to the same level as before.

The intensity of the specular peak is plotted versus the right axis and normalized by its value for $t = 0\,s$. Apparently, the slope indicates that the decreasing intensity of the Yoneda peak for $t \approx 6200\,s$ is not due to intensity fluctuations of the X-ray tube but rather an effect of the film. Prior to this position, the intensity slightly decreases with time, however it suddenly increases at the same moment where the intensity of the Yoneda peak decreases. Both observations indicate the the structure of the film starts to change for a specific time. The reduction of the Yoneda peak's intensity indicates that the roughness of the film changes while the increase of the specular intensity indicates that the film thickness changes. The two phenomena are directly related and proof that the structure of the film is changing during the time period of $t > 6200\,s$.

To confirm this, it is also possible to check the time evolution of the off-specular intensity for $\theta_f > \theta_i$. This is plotted for a selection of measurements in the top panel of figure 6.20. The selection is reduced to one seventh of the measurements ($\Delta t \approx 120\,s$) and is plotted as a time evolution of intensity over θ_f. Again it is possible to see clear changes in the spectra for the time interval around $t \approx 6200\,s$. Two quantify these spectra two different approaches were pursued. In the first one, the intensity data is fitted by the capillary wave model with islands of polymers using equation (6.2). This has already been described in detail before. Each of the shown spectra were fitted this way and the parameter q_0, κ, h and σ are plotted in the middle panel of figure 6.20. The second approach is that the intensity averaged over six angles (as indicated by the grey lines for $\theta_f = 0.6, 0.8, 1.0, 1.2$ in the top figure) are plotted at the bottom of figure 6.20 as a function of time. Apparently, all three plots show a distinct feature (dashed vertical line) for the same time as it as already been observed for the intensity of the Yoneda and specular peak.

The normalized intensity curves as a function of time shown in the bottom panel are shifted so that the feature are more easily distinguishable. For the two largest angles ($\theta_f = 1.0, 1.2$) the averaged intensity almost does not change over time. However, this is different for the two smaller angles ($\theta_f = 0.6, 0.8$). At the beginning the intensity slowly increases for both angles until roughly 5000 s have passed. Then it starts to increase more strongly until it suddenly decreases for $t \approx 6200\,s$. Apparently, for the smallest angle this effect is the most evident. The parameters obtained from the contribution of the islands (see equation (6.5)) of the fit help to further understand what exactly happens in the film. The characteristic wave length for the island size q_0 (see height-height correlation function in equation (6.4)) slowly decreases at first until around 5000 s have passed. The kinetics change and its decrease is accelerated until the model fails to describe the data

for times larger than 6200 s. The contribution of the islands to the scattering profile is basically a Kelvin-Voigt profile that shifts to smaller q with increasing time. The kinetics of this shift change after 5000 s until it is not possible to fit the data any longer after passing 6200 s. This can be understood as a thin film breakup where the dewetting mechanism changes from an initial stage of dewetting to a thin film breakup into droplets characteristic for liquid films. At 6200 s the thin film ruptures due to the growing droplets. The same phenomena has been observed for 4.5 nm thin films of polystyrene on silicon wafer by AFM measurements [97]. It is interesting to note that the size distribution of the island in reciprocal space κ also deviates at the same time which clearly indicates that the model fails to describe the data. The island height h and overall roughness of the layer σ perfectly match each other which is different from what has been observed before for the global fit procedure. In total, the experiments on the kinetics of the film show that further studies are necessary to verify the time scale on which the dewetting mechanism changes. The collapse of the film can be clearly identified using the intensity of the Yoneda and specular peak. This first experiment was very promising but at the same time it proofed how complicated and time consuming the interpretation of experiments on the kinetics can be. The time span for which the kinetics change is very small and needs to be verified first before further discussions can be performed.

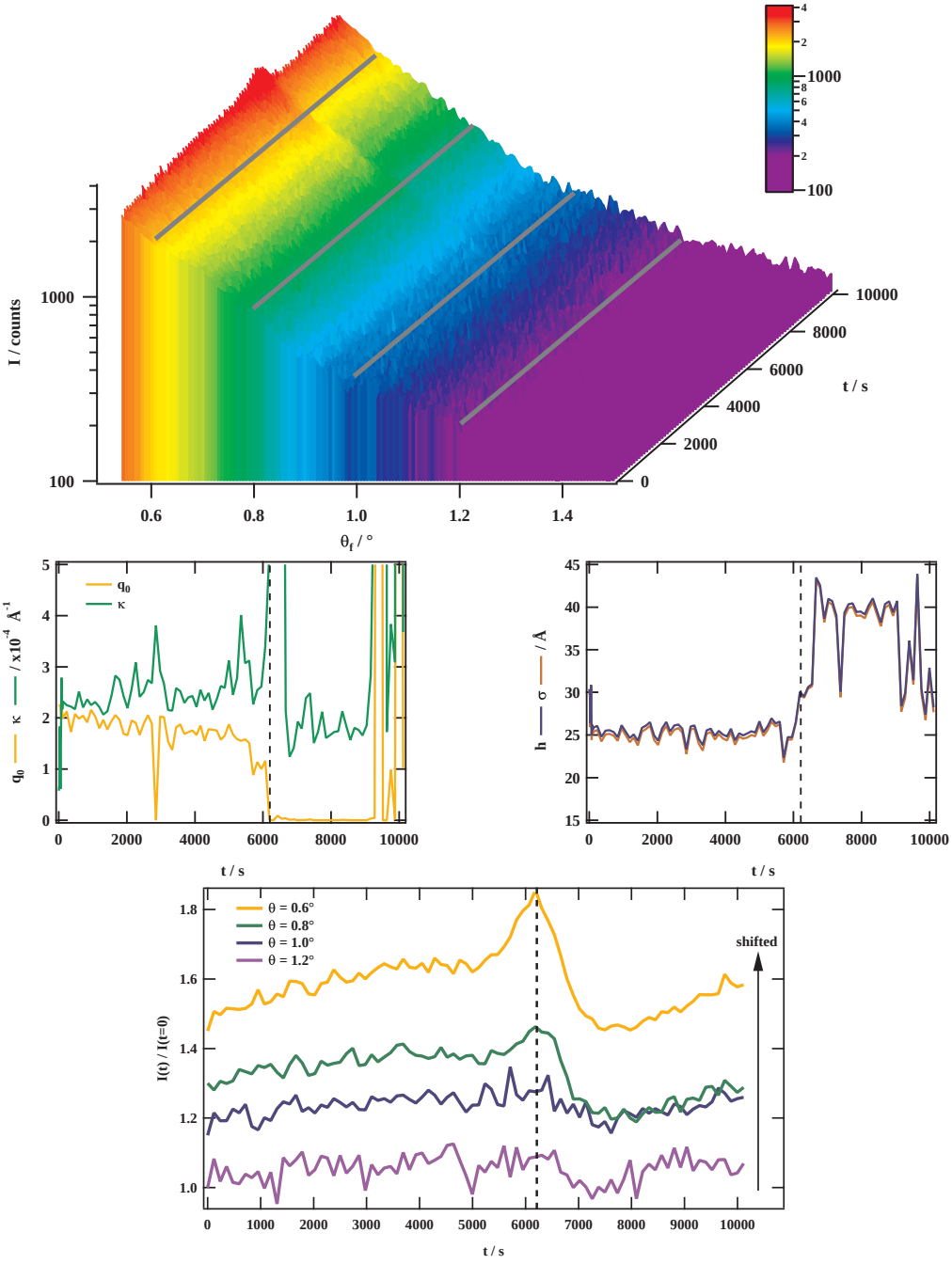

Figure 6.20: The top panel shows a selection of curves ($\Delta t = 120\,\mathrm{s}$) for the time evolution of the off-specular scattered intensity in a waterfall plot as intensity I vs θ_f and time t. Changes in the spectra are visible around $t \approx 6200\,\mathrm{s}$. The gray lines in the scattering profile present four angles were the average intensity over a number of angles (6) is used and plotted as a function of time in the bottom panel. The four curves are shifted for comparison reasons. In the middle panel, two plots present the parameters of a fit on all curves shown in the top panel. The model (see equation (6.2)) has already been introduced in this section. In the right panel the reciprocal island size q_0 and its size distribution κ are plotted as a function of time while the left panel summarizes the overall roughness of the layer σ and the island height h.

7 Iron Oxide Nanoparticles and Polymer Nanocomposites at the Air-Water Interface

The controlled assembly of nano-objects is getting more and more important with further progress in the development of nanoelectronic devices. Furthermore, interesting new physical phenomena are often revealed in single particle films of (magnetic) nanoparticles that have no analogies in bulk material. Therefore, it is very interesting to investigate the possibilities of arranging iron oxide nanoparticles in monolayers. In general, nanoparticles are able to self assemble at the air-water interface. Their ability to form monolayers at the interface depends on their size, hydrophobicity and particle-particle interactions. With increasing size the particles tend to stick to the interface due to an increase of the adsorption free energy[34]. The hydrophobicity of particles is given by their contact angle at the interface. The systems used are stabilized by an oleic acid shell ($\sim 2.5\,\mathrm{nm}$) which increases the hydrophobicity of the particles so that they can be absorbed at the air-water interface. Despite that, it is possible that interactions between particles exist which can promote or prevent the formation of a layer at the interface. Work on spherical iron oxide nanoparticle spread into a single particle film at the air-water interface has already been pusblished for 10, 15 and 20 nm large spherical particles[17]. It is stated that the 10 nm large particles form a uniform monolayer while this is prevented due to interactions between the particles for the two larger systems. Iron oxide nanoparticle are also very interesting due to their magnetic properties which has already been taken advantage of for self assembly into chains[99].

In this chapter three different sizes (5, 10 and 20 nm) of iron oxide nanoparticles purchased from *Ocean Nanotech* will be investigated for their ability to form monolayers at the air-water interface. The 5 nm large nanoparticle consist of a mixture of Fe_2O_3 and Fe_3O_4, while the 10 nm and 20 nm large particles only consist of Fe_3O_4 nanocrystals. The particles were purchased as solutions dissolved in chloroform. The size and shape of the particles were characterised with TEM experiments by *Ocean Nanotech*. Therefore, their structure in solution is investigated first by small angle X-Ray scattering experiments. Then the particles are spread at the air-water interface and characterised by Langmuir experiments to understand their compression behaviour. BAM imaging is performed to visualize the macroscopic structure of the nanoparticle films before specular X-ray reflectivity experiments will be presented to investigate the structure perpendicular to the interface on a nanometer length scale. In a second step, the 5 and 10 nanometer large particles will be introduced into a polymer matrix of a PEG_6-*b*-P*n*BA_{132} at the air-water interface. Studies are necessary to understand whether these particles are able to form polymer nanocomposites with iron oxide particles homogeneously distributed in the polymer matrix or if phase separation occurs in the mixed films. Langmuir isotherms, BAM imaging and surface X-ray scattering experiments were performed to investigate this.

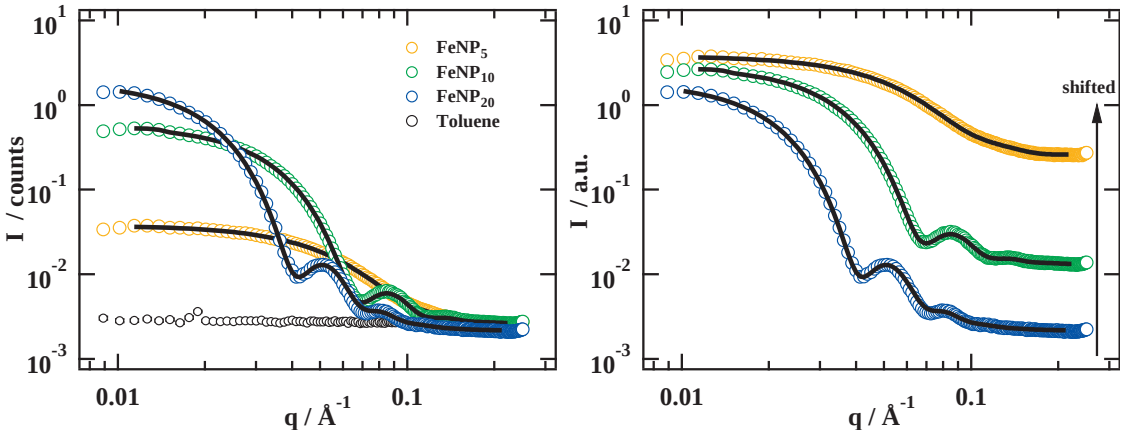

Figure 7.1: Both panels show Small angle X-ray scattering data from the three different sizes of iron oxide nanoparticles (FeNP5, FeNP10 and FeNP20). The black points present the q independent background scattering from toluene. The full lines demonstrate the very good agreement of the fits to the experimental data using a polydisperse form factor for a sphere (FeNP10 & FeNP20) and a thick disk (FeNP5) visible in the shifted data in the right panel.

7.1 Iron Oxide Nanoparticles in Solution

To check the size and form of the nanoparticles small angle X-ray scattering was performed with the setup described in section 4.3. Since chloroform strongly absorbs X-rays, the solvent solution was changed to toluene. For this a small amount of the highly concentrated solution of nanoparticles ($c = 25\,\mathrm{mg/ml}$) was diluted in toluene until the concentration of nanoparticles was $c = 1\,\mathrm{mg/ml}$ in the chloroform toluene mixture.

The results for the three iron oxide nanoparticles and pure toluene are shown in figure 7.1. The scattering data of pure toluene shows no q dependency and can be treated as a constant background. The raw data on the 5 nm particle is fundamentally different compared to 10 and 20 nm. Clear oscillations are visible for 10 and 20 nm particles while there is none for the 5 nm ones. Furthermore, the intensity decays much faster in case of the two larger particles ($I \sim q^{-4}$) compared to the small one ($I \sim q^{-2}$). This indicates that there has to be a difference between the smallest particles and the larger ones. In a first attempt to describe the scattering data, the oleic acid shell of the particles was ignored due to its electron density being almost identical to toluene. A form factor model was used to describe the core of the particles. A thick disk (see equation (3.6)) was used for 5 nm particles (FeNP5) and a sphere (see equation (3.5)) for the 10 and 20 nm particles (FeNP10, FeNP20). Both models were extended for a polydisperse system of either disks or spheres. The full curves in both panels demonstrate the very good description of the data by the two form factor models. The sphere form factor fit leads to a polydispersity of

Table 7.1: Fit parameters for the form factor model used to describe the SAXS data in figure 7.1.

sample name	fit type	diameter	height	PDI
FeNP$_5$	flat disc	8 ± 0.1 nm	3 ± 0.1 nm	10 % (fixed)
FeNP$_{10}$	sphere	12.8 ± 0.05 nm	-	10 ± 0.3 %
FeNP$_{20}$	sphere	21.4 ± 0.05 nm	-	10 ± 0.2 %

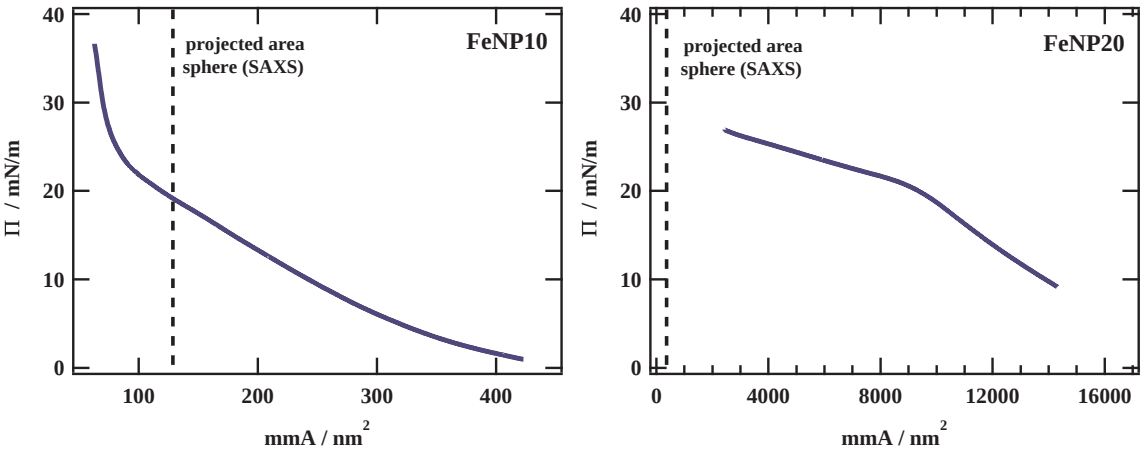

Figure 7.2: The panels show the surface pressure isotherm as Π vs. mmA for FeNP10 in the left panel and FeNP20 in the right panel. The dashed line marks the calculated projected area for the spheres taken from the form factor model obtained by bulk scattering.

10 % for both samples FeNP10 and FeNP20. The radius obtained from the fit was 6.4 nm for FeNP10 and 10.7 nm for FeNP20. The results agree with the claimed sizes provided by *Ocean Nanotech*. For FeNP5 the polydispersity was fixed to 10 % during the fit. The best fit leads to a thick disks with a thickness of 3 nm and a radius of 4 nm. The fit parameters are summarized in table 7.1.

From the form factor fits it can be concluded that there is no aggregation between neighboring particles in the solution since no structure factor contribution is seen. This is an important information since particle aggregation in the solvent would have been problematic for the preparation of the following Langmuir experiments. With aggregated particles in the solution the formation of monolayers would already be constraint in various ways. Furthermore, the shape of the 5 nm particles is interesting for the following Langmuir experiments. Due to their shape two different conformations with the radius parallel or perpendicular to the interface are imaginable.

7.2 Iron Oxide Nanoparticles at the Air-Water Interface

The three iron oxide nanoparticles dissolved in chloroform were diluted to concentrations around $c \approx 5\,\mathrm{mg/ml}$ and spread on the water surface as described in detail in chapter 4.1. First, the isotherms of the two spherical particles FeNP10 and FeNP20 will be discussed which are displayed in figure 7.2. The isotherm of FeNP10 is shown in the left panel of the figure. The film was prepared for low surface coverage, so that the area available for each particle is much larger than the projected area calculated from the form factor of the bulk scattering experiment ($A_{\mathrm{particle}} \approx \pi R^2$, with $R = 6.4\,\mathrm{nm}$). After spreading the sample, the surface pressure equilibrated within minutes and remained at $\Pi \approx 1\,\mathrm{mN/m}$ for around 30 min. The compression isotherm was recorded with a compression rate of $5\,\mathrm{mm^2 min^{-1}}$ (same for all nanoparticle sizes). Compressing the FeNP10 film leads to a steadily increasing surface pressure up to a value of 20 mN/m. The area equivalent to this surface pressure roughly marks the projected area of $129\,\mathrm{nm^2}$ for a single particle calculated from the results of the scattering experiment. This approximation can be used

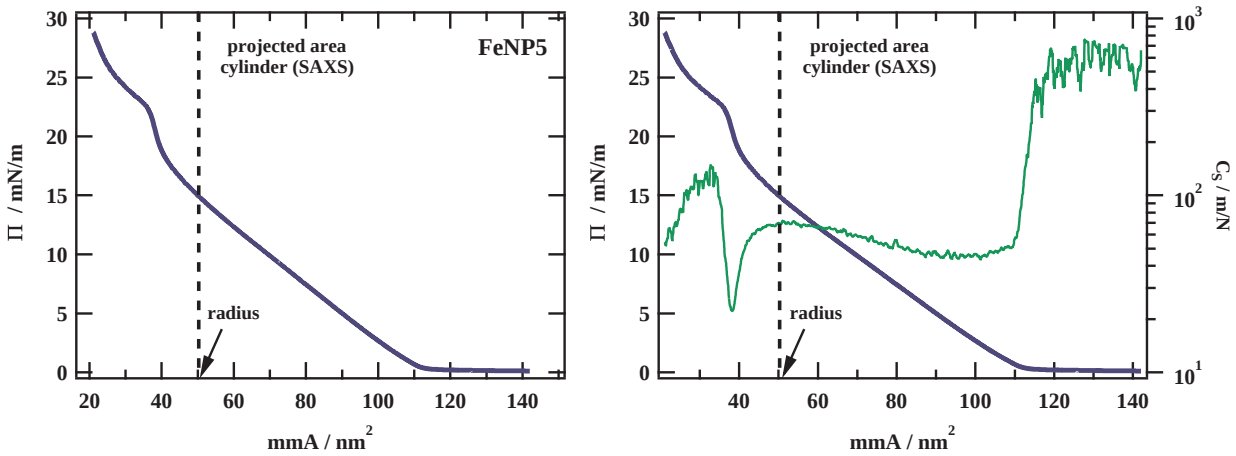

Figure 7.3: The left panel shows the surface pressure isotherm as Π vs. mmA for FeNP5. The dashed line marks the calculated projected area for the radius of the disks taken from the form factor model obtained by bulk scattering. The right panel shows the same isotherm with the compressibility C_S displayed vs the right axis of the plot.

since the overall error in mmA is smaller than 10 % which includes potential loss of sample while preparing the film. Further compressing the film also leads to an steady increase of the slope of the isotherm. The qualitative change in the surface pressure may indicate that the particles cores approach each other instead of a compression of the shell for larger areas. The sudden increase represents a strong resistance which can be related to the sterical resistance from the oleic acid shell close to the core.

The same procedure was repeated for FeNP20. Again the idea was to prepare the film for low surface coverage, however, the surface pressure already increased to nearly 10 mN/m even though only a small amount of sample was spread on the interface. The surface pressure remained constant even after waiting for more than 30 min and the compression experiment was started with the low surface coverage. The isotherm for the sample is shown in the right panel of figure 7.2. The surface pressure steadily increases until its slope slightly changes at a surface pressure of 20 mN/m. Afterwards, the pressure still increases but slower compared to before. Due to the limitation of the trough size it was not possible to compress the film to areas comparable to the calculated projected area of 360 nm^2 for a single FeNP20 particle. These results indicate that the FeNP20 particles do not form a uniform monolayer at the interface but instead form a more complex three dimensional structure. This has also been observed for FeNP20 films in literature [17].

The FeNP5 nanoparticle films were also prepared for a low surface coverage. The surface pressure remained constant over a long period of time at 0.1 mN/m before the compression isotherm was started. The isotherm is shown in the left panel of figure 7.3. For large areas the surface pressure remains constant. The surface is not completely covered by particles yet and upon compression the unoccupied surface area reduces. At mmA $\approx$ 110 nm^2, a change occurs and the surface pressure increases with a linear slope. The surface pressure steadily increases up to 15 mN/m where it reaches the calculated projected area of 50 nm^2 from the scattering experiment. For the scattering experiment on FeNP5 a thick disk form factor was used to describe the data with a radius of 4 nm and a thickness of 3 nm. The first idea was that the particles are oriented in a way to minimize

the film thickness, respectively the disks are oriented parallel to the interface. Therefore, the calculation of the projected area is performed with the radius of the disks. After crossing this point the slope in the isotherm increases and a small kink becomes visible in the isotherm. This is usually an indication for a phase transition in the isotherm. Two different scenarios are imaginable. The first one is that multilayer structures are formed due the overlap of single regions upon compression of the film. The other one takes into account that the FeNP5 particles are not spherical. There is the possibility that the particles may flip their orientation into a different structure that allows a closer packing of the particles. For the thick disks this would mean that the thickness of the film after the transition has to increase from the thickness of the disks to their diameter. To identify phase transitions, the compressibilty has proven to be a powerful tool for polymer films. Therefore, the compressibility of the nanoparticle films will be discussed in the following.

Compressibility at the Air-Water Interface

The compressibility of FeNP5 is shown in the right panel of figure 7.3. Just to recapitulate, the compressibility C_S is a measure for the resistance of the film to an external force. Consequently, when the surface is not fully covered by sample large values are observable for C_S. This becomes apparent for large areas (mmA $> 110\,\mathrm{nm}^2$) with $C_S \approx 600\,\mathrm{m/N}$. During the steady increase of the surface pressure, C_S drops down to a broad almost plateau like regime with values around 50 m/N. The magnitude is comparable to a polymer film in the semi-dilute regime as already discussed for PMMA or P*n*BA in chapter 6. The interesting region begins when the area is reduced below the projected area of the particles. At this point the oleic acid chains from different particles have to come into contact if the particles are in a single layer at the interface. And indeed there is a change in the compressibility that is connected to the already mentioned kink in the isotherm. A sharp minimum with a minimum value of $C_{S,\mathrm{min}} \approx 22\,\mathrm{m/N}$ appears. It is reasonable to connect this minimum to compressing the shell of the nanoparticles, although the value is around twice as big as typical values for the liquid expanded state in a fatty acid Langmuir layer. What is even more interesting is that the layer does not break, but instead the compressibility increases again to a value around 100 m/N before it starts to reduce again. This is characteristic for a phase transition in the layer as also been observed for the small molecular weight of PMMA in section 5.1. The phase transition can be identified by the increasing compressibility due to the reduction of the resistance during compression while the particles in the film rearrange as a consequence of the external force.

In the two panels of figure 7.4, C_S is shown for all samples plotted vs mmA in the left and vs Π in the right panel. In the left panel the qualitatively different behaviour for FeNP20 is becoming clear once again. Its compressibility looks similar to that of a series of step functions. With increasing compression the film gets more compressed and its resistance gets smaller which is reasonable for films being in a collapsed stage where the film is able to form three dimensional structures. The slopes of FeNP5 & FeNP10 appear to be rather similar and they can be directly compared in the right panel displayed over Π. Both have large values of C_S for small surface pressures that decrease to a broad plateau at $50 - 60\,\mathrm{m/N}$ upon compression. The minimum for $\Pi \approx 20\,\mathrm{mN/m}$ in FeNP5 associated with the compression of the oleic acid shell is clearly visible. The general slope for FeNP10 is similar and the compressibility also decreases but not as fast as for FeNP5. The compressibilty reduces down to $C_{S,\mathrm{min}} \approx 15\,\mathrm{m/N}$, but does not increase again as

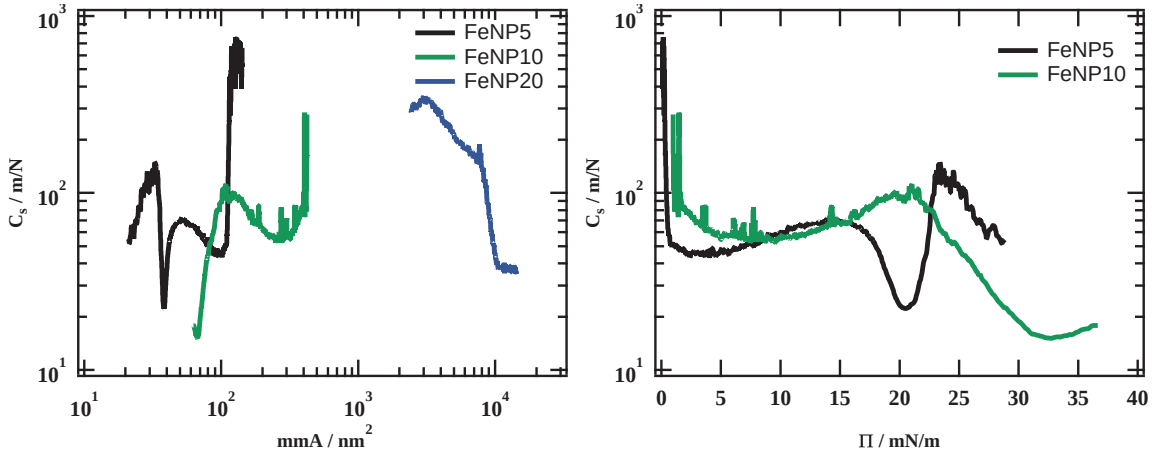

Figure 7.4: Both panels show the compressibility C_S vs mmA in the left and Π in the right panel. While it is shown for all sizes in the left panel, the right panel only displays the qualitatively similar slopes of FeNP5 & FeNP10. The slope for FeNP20 indicates that the particles do not form a uniform layer at the interface.

observed for FeNP5. Consequently, the film for FeNP10 particles only shows the feature of compressing the oleic acid shell. The sphere shaped particles do not show a transition because they cannot change their arrangement at the interface to reduce the occupied area.

Brightness Measurement during Compression

The brightness measurements were performed simultaneously to the recording of the isotherms. The setup used for this is described in section 4.4. The mean brightness value was obtained by averaging the intensity over a region of $(150\,x\,150)\,\mu m^2$ in the images obtained during compression. In case of FeNP10 & FeNP20, the p-polarized intensity reflected by the interface was constantly at the maximum value of 255 (arbitrary intensity scale 0...255) while recording the isotherm. Before spreading the sample at the interface, the intensity of the bare water interface was around 5. The intensity measurement will be illustrated by the example of FeNP5 where the surface was not fully covered by nanoparticles at the beginning of the measurement. The isotherm with the respective brightness measurement plotted against the right axis is shown in the left panel of figure 7.5. Right after spreading the particles on the interface the BAM images show an interface similar to the bare water surface with low values for the p-polarized intensity (< 5). Upon compression very bright regions appear where the reflected intensity is at its maximum value. This is shown in the first image in the right panel for which its position is marked by the number 1 in the isotherm. Within a short time more bright regions appear and merge together until the reflected intensity is constantly at its maximum value of 255 for mmA $\approx 120\,nm^2$ (illustrated in image 2). The second picture could also be used to represent the reflected p-polarized intensity from the FeNP10 & FeNP20 films. Unfortunately the brightness measurements did not help characterizing the structure of the film further. However, high contrast images for visualizing purposes were also taken from the different films. For the images shown in figure 7.6 different combinations of polarizer and analyzer positions were used to illuminate the interface by a combination of s- & p-polarized light.

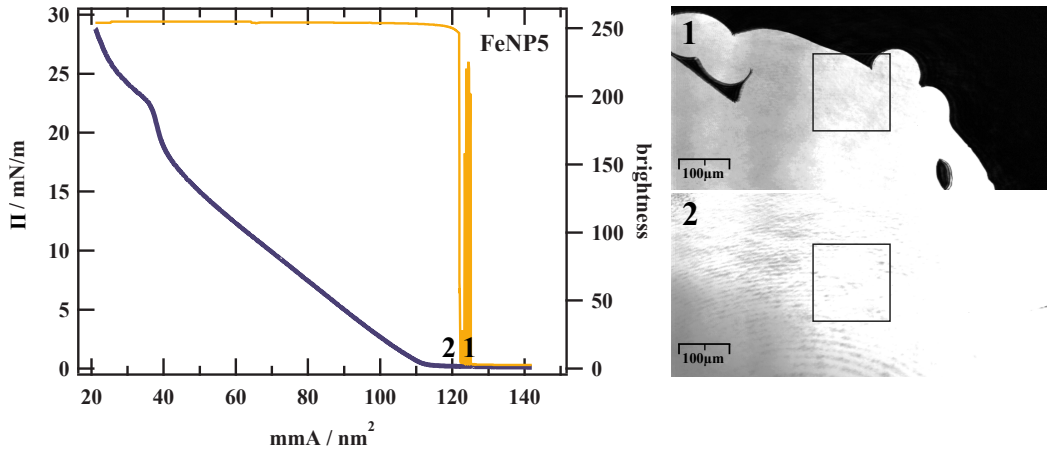

Figure 7.5: Compression isotherm of FeNP5 as Π vs mmA with the over a frame of $(150\,x\,150)\,\mu m^2$ averaged mean intensity (scale 0...255) shown vs the right axis. The reflected p-polarized intensity immediately increases to its maximum value due to bright regions of nanoparticle covering the interface. The first picture on the right hand side represents the region where the mean intensity starts to fluctuate due to the nanoparticle islands entering the frame. The second image shows the image of a fully covered interface roughly 20 seconds later.

Under some conditions the images provided an overall picture of the nanoparticle films. The bright spots in the images can either correspond to the bare water surface or defects within the film. Very dark spots can generally be associated to small optical defects of the film. The first three images show different position in the FeNP5 isotherm. The first one shown is for a relatively low surface pressure where the bright regions indicate that the interface is not uniformly covered by the particles yet (image 1). This changes for the second position right before the phase transition. Here, the second image shows an uniformly covered interface with small anisotropies in the refraction coefficient of the film. During and after the phase transition the optical properties of the film change fundamentally. It was necessary to readjust the polarizer and analyzer so that it is difficult to compare the second and third image taken. However, the two images show a fundamentally different film which proves that a phase transition indeed occurs within the film in agreement with the results from the isotherm. Due to the lateral resolution of around $2\,\mu m$ for the images, they cannot provide a direct visualisation of the structural changes in the film. Therefore, the question remains whether the phase transition is the formation of multilayer structures or flipping of the disks.

The images for the FeNP10 isotherm show a uniform layer that is getting compressed so that the overall reflected intensity of the images increases with increasing surface pressure. Furthermore, the videos show that the mobility of the film is quite fast for low surface pressures while it almost stagnates for the last image taken at around 20 mN/m. This agrees with the idea of a dense layer of nanoparticles that is compressed. The third image also shows a lot of heterogeneties on a macroscopic length scale indicating that the film may be ruptured or formed regions were particles are stacked on top of each other. The image taken for FeNP20 shows the situation for the lowest surface pressure measured in the isotherm. It looks fundamentally different compared to FeNP5 & FeNP10. Worm-like structures are visible which are typical for samples that aggregate after spreading at the interface. The images of the macroscopic length scale confirm that FeNP20 particles

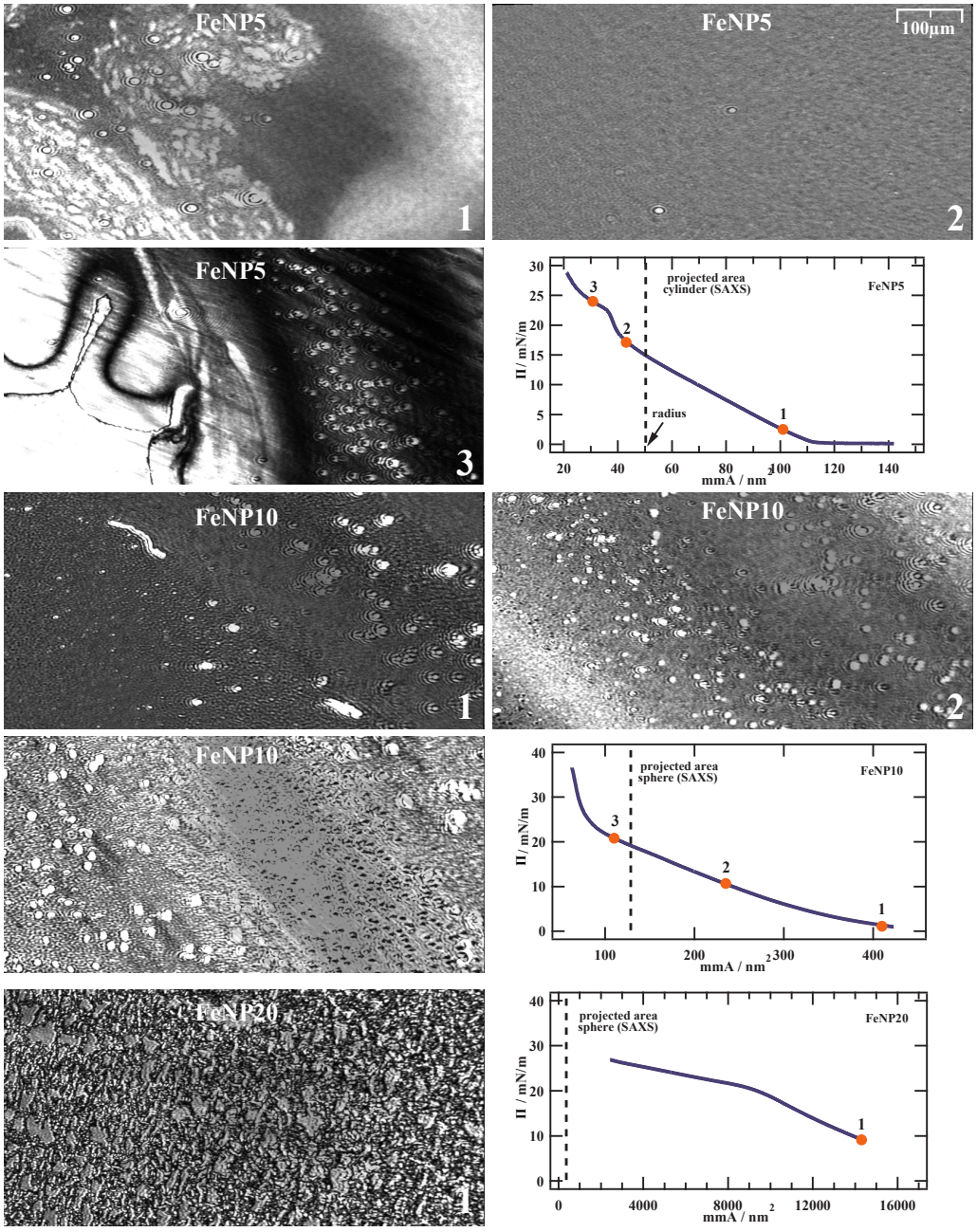

Figure 7.6: BAM Images for all FeNP nanoparticle films. The analyzator and polarizator are adjusted so that the interface is also illuminated by s-polarized light. These values were adjusted so that the reflected images give an idea of the structure at the interface. Bright white or dark black spots can be associated with either bare water or defects in the film. The images are shown for all sizes of FeNP nanoparticles and different positions in the isotherms that are individually highlighted.

do not form a uniform layer as already presumed from the results of the compression isotherm.

In order to understand the structure of the films not only on a macroscopic length scale but also on the nanometer scale, X-ray scattering experiments were performed for

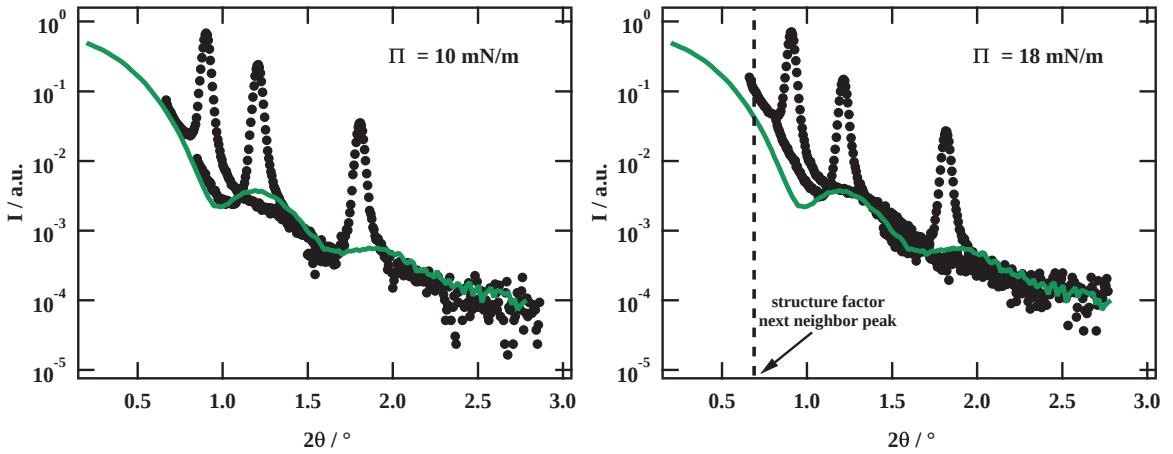

Figure 7.7: Both panels show three detector spectra of FeNP10 for two different measurement positions in the isotherm. The left panel shows data of $\Pi \approx 10\,\mathrm{mN/m}$ and the right one $\Pi \approx 18\,\mathrm{mN/m}$. The green curve is the form factor model obtained from scattering of the diluted particles in solution. The form factor is scaled. For $\Pi \approx 10\,\mathrm{mN/m}$ the form factor demonstrates a very good agreement with the background scattering while deviations are visible for the second measurement point at $\Pi \approx 18\,\mathrm{mN/m}$.

different positions in the isotherm. The results from these experiments are presented in the following.

7.2.1 Background Correction for Reflectivity Data on Nanoparticle Films

Surface X-ray scattering experiments were performed on all three samples for three different positions in the isotherm. Iron oxide nanoparticles have a large electron density contrast at the air-water interface compared to the polymer films that were discussed in the previous chapter. Due to the high contrast between particles and water, pronounced curves are expected for the reflectivity. However, the setup for the reflectivity experiment is also a small angle X-ray scattering setup. One has to keep in mind that the scattered intensity may include more than one contribution. The form factor already measured in the small angle setup is one contribution that has to be taken taken care of. In a reflectivity experiment the intensity is collected in the detector at an angle of $2\theta = \theta_i + \theta_f$ which is equivalent to the scattering angle in a SAXS experiment. Additionally to the small angle scattering, specular and off-specular reflected intensities are collected in the detector. Usually the intensity of the reflectivities is much larger than the small angle scattering so that it can be neglected, however, for nanoparticles this has to be confirmed for each measurement. It is necessary to identify the small angle intensity and check whether it is possible to separate the two intensities cleanly. Single scattering spectra for all samples will be shown and compared to the bulk scattering of the respective nanoparticles.

The results will be discussed in an order that is most suitable for the data. The discussion will focus first on FeNP10, then FeNP20 and finally FeNP5 because of the intensity in the background scattering. The detector collects data for a range of θ_f for one θ_i, which makes it easy to identify the specular reflected intensity at $\theta_i = \theta_f$. Three full detector spectra are plotted in figure 7.7 for FeNP10 at a surface pressure of $\Pi = 10\,\mathrm{mN/m}$ and $\Pi = 18\,\mathrm{mN/m}$. They are compared to the form factor from the small angle experiment

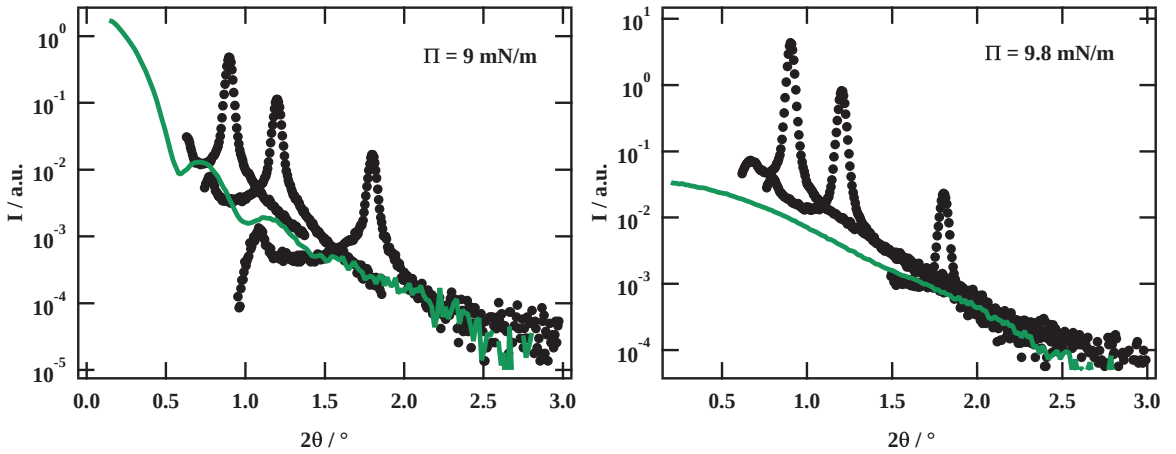

Figure 7.8: Both panels show three detector spectra of FeNP20 at $\Pi = 9\,\mathrm{mN/m}$ in the left panel and FeNP5 at $\Pi = 9.8\,\mathrm{mN/m}$ in the right panel. The green curve is the form factor model obtained from scattering of the diluted particles in solution. The form factor is scaled. For both particle sizes the form factor does not match the background data in the reflectivity spectra.

of FeNP10. The absolute intensity of the reflectivity and small angle experiment cannot be directly compared because in both cases the intensity of the primary beam is not monitored, therefore only relative intensities are measured. The three detector spectra of the reflectivity experiment were multiplied by the same constant factor to compensate for this. Furthermore, a constant background level was substracted for reflectivity and small angle experiment. The background in the $\Pi = 10\,\mathrm{mN/m}$ measurement shown in the left panel agrees very well with the form factor from the SAXS. In the right panel the form factor is still able to describe the background scattering of the reflectivity experiment. However, it already deviates slightly especially visible for small angles $2\theta < 1.0°$. The deviations can be explained by two different phenomena. The first one is related to the rougher interface that can lead to off-specular scattering becoming another additional component to the scattering. The Yoneda peak increases in intensity and changes its form upon compression and its position is roughly in the region where the deviations become visible. Another factor can be related to higher compressed films. The position in the isotherm is comparable to the projected area of a single particle which could give rise to a structure factor peak corresponding to the next neighbor distance of ordered particles. The dotted vertical line roughly corresponds to the next neighbor distance for the particle size 12.8 nm obtained from the form factor fits in the SAXS experiment. The background scattering for the third position in the isotherm which is not shown separately can still be described by the form factor. However, the deviations between form factor and background in the reflectivity spectra increase even more.

In the left panel of figure 7.8 three spectra and the form factor of FeNP20 are plotted. The data is obtained for the lowest surface pressure in the isotherm ($\Pi \approx 9\,\mathrm{mN/m}$). The background of the detector spectra only roughly fit to the form factor of the particles. Especially for the largest angle, the oscillation of the form factor is not visible in the left flank of the curve. This indicates that the background scattering is not dominated by the particles. The mass per area fraction of FeNP20 in the films is roughly five times smaller compared to the FeNP10 films. This can be calculated from the sample spread on the

surface while taking their different size into account. The surface pressure for FeNP20 already increases for a relatively low surface coverage. Logically, the contribution of the form factor to the intensity is decreased by a large degree.

The situation for FeNP5 is displayed in the right panel of the figure. Here, the background of the detector spectra and the form factor do not match. However, one has to remember that the form factor is not a spherical particle but instead a thick disk. In the scattering experiment from solution the particles are randomly oriented which leads to an isotropic scattering. For oriented disks the form factor depends on the orientation of the particles in respect to the X-ray beam because of their anisotropically shape.

Only the background scattering for FeNP10 can be clearly associated with the form factor of the particles while deviations become visible with increasing surface pressure. For FeNP5 & FeNP20 the background scattering cannot be explained by the respective form factors. However, in order to be consistent during the background subtraction the following procedure (see section 4.2 for comparison) is maintained for all three different particle sizes. A frame consisting of 40 points on each side is used to cut out the reflection maximum ($\theta_f = \theta_i$). The lowest intensity in this ensemble of 80 points was used to substract a constant background in the scattering profile. Reflectivity for each angle is obtained by integrating over the background corrected spectra. Data from this procedure is shown for FeNP10 and water in figure 7.9 by the black points (*standard procedure*). It is directly compared to a different method where the intensity of the form factor for the particles is used as a background signal. Here, reflectivities are calculated by simply substracting the form factor intensity from the specular peak intensity ($\theta_f = \theta_i$) for each angle. No integration over the detector profile is performed. Figure 7.9 presents the comparison for three different films, namely water and FeNP10 at two different pressures. The curves are shifted for comparison reasons. Due to experimental reasons, some points are missing in the reflectivity profile because the intensity reflected from the nanoparticle film was too high. The detector was no longer in its linear response regime. For water and the low surface pressure of FeNP10, the two procedures lead to similar reflectivity curves. FeNP10 at a high surface pressure shows that the two procedures deviate from each other for $q_z > 0.2\,\text{Å}^{-1}$. The two minima at $q_z = 0.2\,\text{Å}^{-1}$ and $q_z = 0.3\,\text{Å}^{-1}$ are still evident with the standard procedure but already deformed when the form factor is used for the background correction. The explanation for this is that the standard procedure accumulates more intensity due to the integration over the specular peak. The results for the reflectivity is greatly improved by the integration instead of simply taking the intensity of the maximum. The procedure leads to good results even for larger q values as long as the background scattering can be accurately determined. Using a model for a roughened interface to describe the water measurement shows that the data from the standard procedure can be perfectly described with a roughness of $\sigma = 2.8\,\text{Å}$. When the model is used for the data corrected by the form factor, it is not able to describe the slope in the range of $0.05\,\text{Å} < q_z < 0.1\,\text{Å}$ very well. Furthermore, the roughness in the model increases slightly to $\sigma = 3.4\,\text{Å}$. When the procedure is applied for the FeNP20 films, the deviation between the two approaches is even stronger. Due to these observations, reflectivities were calculated using the standard procedure. For all sizes of iron oxide nanoparticles, a constant background was substracted from the detector profile before reflectivity was calculated by an integration over the selected frame of 80 points.

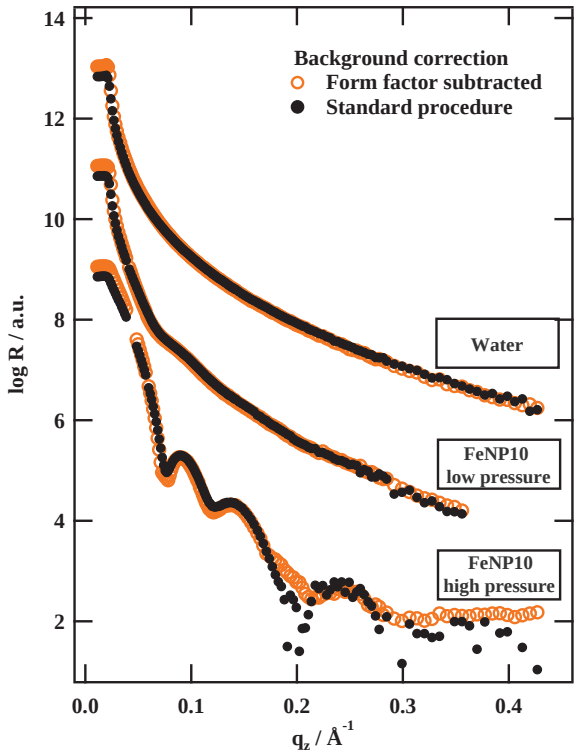

Figure 7.9: The reflectivities obtained for two different background correction procedures which are described in the text are directly compared. In total three differnt measurements are shown being water and FeNP10 particles for $\Pi = 1.6\,\mathrm{mN/m}$ and $\Pi = 20\,\mathrm{mN/m}$. The curves are shifted for better comparison. The standard procedure leads to more promising results especially in the case of low intensities and large q values ($q_z > 0.2\,\text{Å}^{-1}$).

In the previous discussion it was shown that the FeNP particle films have a strong off-specular scattering signal. However, it is not possible to cleanly separate the different contributions in the data. It is only possible to determine a background level using the in our group established background correction and use the specular reflectivities to determine the electron density profile perpendicular to the interface. Detailed investigation of the off-specular intensities are not possible for the nanoparticle films.

7.2.2 Specular Reflectivity of Iron Oxid Nanoparticles Films

The specular reflectivities for three points in the FeNP20 isotherm are shown in figure 7.10 with the bare water surface before spreading for comparison. The data is presented as log R vs q_z and the positions in the isotherm are marked in the top right panel. The reflectivity of the FeNP20 films reduces slightly compared to that of the bare water surface. Furthermore, upon compression the reflectivity in the range of $0.05\,\text{Å}^{-1} < q_z < 0.2\,\text{Å}^{-1}$ reduces a little more. The effect of the FeNP20 particles is however very weak when it is compared to the reflectivity of the FeNP5 and FeNP10 films (see figure 7.11 and 7.12).

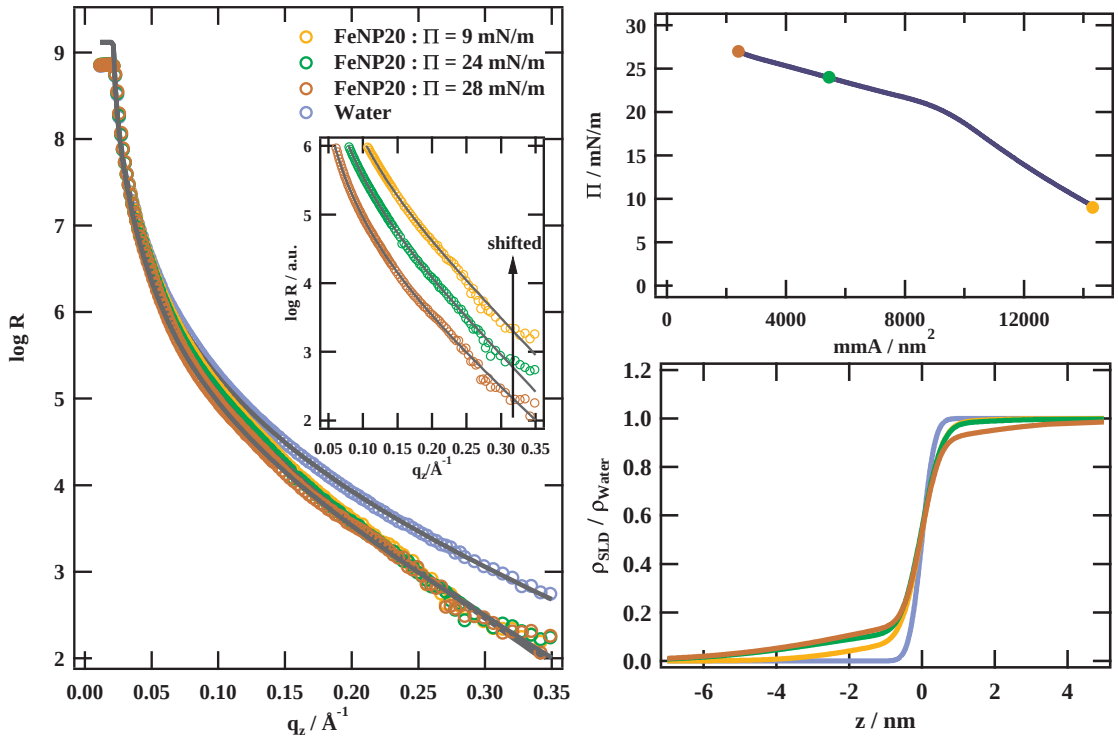

Figure 7.10: Results for the reflectivity measurement for three different positions in the isotherm (top right panel) of FeNP20 are shown. The bare water surface before spreading the sample is shown for comparison. The reflectivities are plotted as log R vs q_z in the left panel with the inset demonstrating the good agreement of the fits to the data. The bottom right panel displays the results for the electron density profiles obtained by the one layer fit.

Due to the small effect of the particles, a relatively simple model was used to modify the electron density profile

$$\langle\rho(z)\rangle = \frac{\rho_0}{2}\left(1+\mathrm{erf}\left(\frac{z-z_0}{\sqrt{2}\sigma_0}\right)\right)+\frac{\rho_{\mathrm{water}}-\rho_0}{2}\left(1+\mathrm{erf}\left(\frac{z}{\sqrt{2}\sigma_1}\right)\right) \tag{7.1}$$

with two error functions which is equivalent to a one layer model. The layer thickness is given by z_0 while the roughness σ_1 is the one towards water and σ_0 the one towards air. The Motofit Reflectometry package rev. 409 [67] for IGOR PRO takes the density profile to calculate a reflectivity curve using the Parratt formalism [44] introduced in section 3.2.1 modified by an error function for the reflectivity of each interface. The very good agreement of the fits is demonstrated in the inset of figure 7.10. Results for the electron density profile are plotted in the bottom right panel as a function of the distance to the water surface. Apparently, the electron density at the interface (z=0) is broadening with increasing surface pressure. In the model the position z_0 of the additional interface varies between 1 and 2 nm above water while its roughness σ_0 increases from 1.8 to 3.3 nm upon compression. The electron density of the layer is around 10 % to 20 % that of the water subphase. The profile indicates that although the electron density at the interface is slightly modified, no uniform particle layer is formed. This complies with the results of the isotherm and BAM imaging that also indicated that FeNP20 does not form a sin-

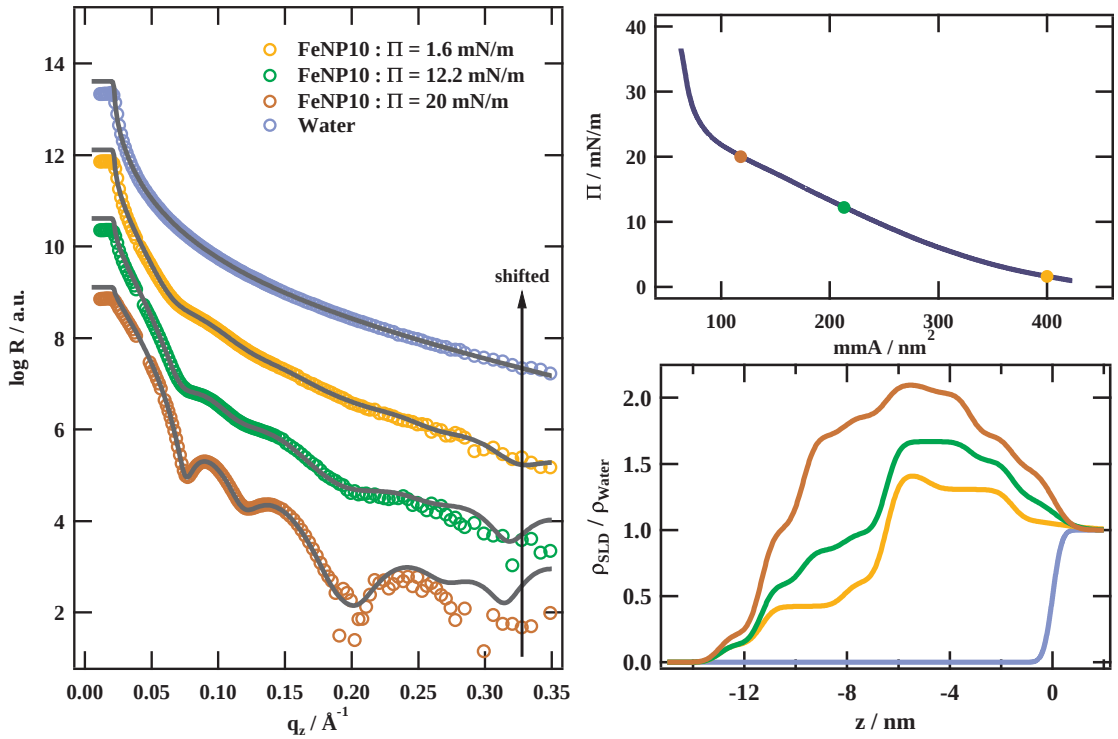

Figure 7.11: Results for the reflectivity measurement for three different positions in the isotherm (top right panel) of FeNP10 are shown. The bare water surface before spreading the sample is shown for comparison. In the left panel the reflectivities are plotted as shifted curves with log R over q_z. The full lines demonstrate the very good agreement of the fits to the data. The bottom right panel displays the results for the electron density profiles obtained by a box model consisting of 8 boxes.

gle particle layer. The particles aggregate on a macroscopic length scale into wormlike structures shown in figure 7.6.

In the left panel of figure 7.11 the reflectivity curves of a FeNP10 film are shown for three different positions in the isotherm as log R vs q_z with the bare water surface measured before spreading the sample for comparison. The measurement positions are highlighted in the isotherm shown in the top right panel of the figure. The reflectivities show a completely different behaviour compared to FeNP20. The specularly reflected intensities of the film are clearly affected after spreading the particles at the interface. For the highest surface pressure of 20 mN/m several minima can be detected in the curve. Upon closer inspection, one can also identify the same minima in the two other measurements of the film which means that the general structure perpendicular to the interface is similar for the three positions in the isotherm. In the Born approximation discussed in section 3.2.2, a series of minima corresponds to a film thickness. The most simple case is a single layer with a homogeneous electron density and thickness d. The period of the oscillation corresponds to the film thickness $\Delta q_z = 2\pi/d$. However, it is not possible to describe the curve by a single oscillation. A double layer was also not able to describe the series of minima observed in the reflectivity.

Due to the composition and shape of the spherical nanoparticles with an oleic acid shell, it is unlikely to expect a homogeneously distributed electron density perpendicular to the interface. A model for a multilayer system is used where the electron density is

divided into a number of boxes N with an equal size a is much more suitable to describe the particle films. The edge of each box is modulated by an error function with a constant roughness σ to smooth the electron density change between two neighboring boxes. Preferable the number of boxes is minimized to keep the model as simple as possible. The general formulation of the electron density profile for this multilayer system is given by

$$\langle\rho(z)\rangle = \sum_{j=1}^{N} \frac{\Delta\rho_j}{2}\left(1+\mathrm{erf}\left(\frac{z+j\cdot a}{\sqrt{2}\sigma}\right)\right) + \frac{\rho_{\mathrm{water}} - \sum_{j=1}^{N}\Delta\rho_j}{2}\left(1+\mathrm{erf}\left(\frac{z}{\sqrt{2}\sigma_0}\right)\right) \quad (7.2)$$

with $\Delta\rho_j$ as the increase or decrease of the electron density between each box and z as the distance from the air-water interface. Negative values of z are related to the structure in the air. The last term makes sure that the electron density of the system matches the water subphase. The roughness σ_0 facing the water interface was fitted independently from the roughness between each of the boxes. Reflectivity can be calculated using Parratt's formalism which was introduced in chapter 3.2.1 [44]. It was possible to describe all three surface pressures with this model while using $N = 8$ boxes with a size of $a = 1.625\,\mathrm{nm}$. The size of the boxes was constant during the fitting and their total size of 13 nm matches the particle diameter from the form factor measurements in the SAXS (see table 7.1). The roughness for each box was fixed to $\sigma = 0.4\,\mathrm{nm}$. The thickness and roughness of the boxes were slowly adjusted while improving the fit. The particle size was used as an initial guess for the overall thickness of the particle layer and results from the fit agreed very well with the experimental data.

The full curves in figure 7.11 show the best fit of the model to the data. The best results were obtained for a particle size of 13 nm which neglects the size of the shell (estimated to be around 2.5 nm). The results for the electron density profiles show that a model for a single particle layer is able to describe the specular reflectivity curves for all three surface pressures. The density profile is shown in the bottom right panel as a function of the distance z to the water interface. For the lowest surface pressure the electron density at the interface slightly increases at first before steadily decreasing with increasing distance to water. Since the X-ray experiment averages over a broad range, the layer of FeNP10 particles has to be weakly packed at this point. The electron density for solid iron oxide (Fe_2O_3 or Fe_3O_4) is roughly four times larger then ρ_{water}. After compression of the film the contrast increases while it still shows a similar shape. With closer getting particles, the average electron density in each box increases. The area per particle where the highest surface pressure is measured is comparable to the size of a single particle. The reflectivity curve for the highest pressure also shows the most pronounced minima and the electron density profile resembles a gaussian function. This indicates that particles in the film are highly compressed. The maximum of the electron density profile is roughly half of what would be expected for a pure solid iron oxide layer. It can be concluded that the oleic acid shell still has to be within the film acting as a sterical hindrance between the particles. This leads to a lower mean electron density of the layer. The deviation from the fit to the reflectivity for $q_z > 0.25\,\mathrm{\AA}^{-1}$ is not problematic because this represents already the resolution limit for the setup because of the low intensities. Although the model used was constraint for several parameters, the results give a reasonable explanation on how FeNP10 films are formed at the air-water interface. The electron density profile provide a consistent picture of a single particle layer at the air-water interface. Upon compression,

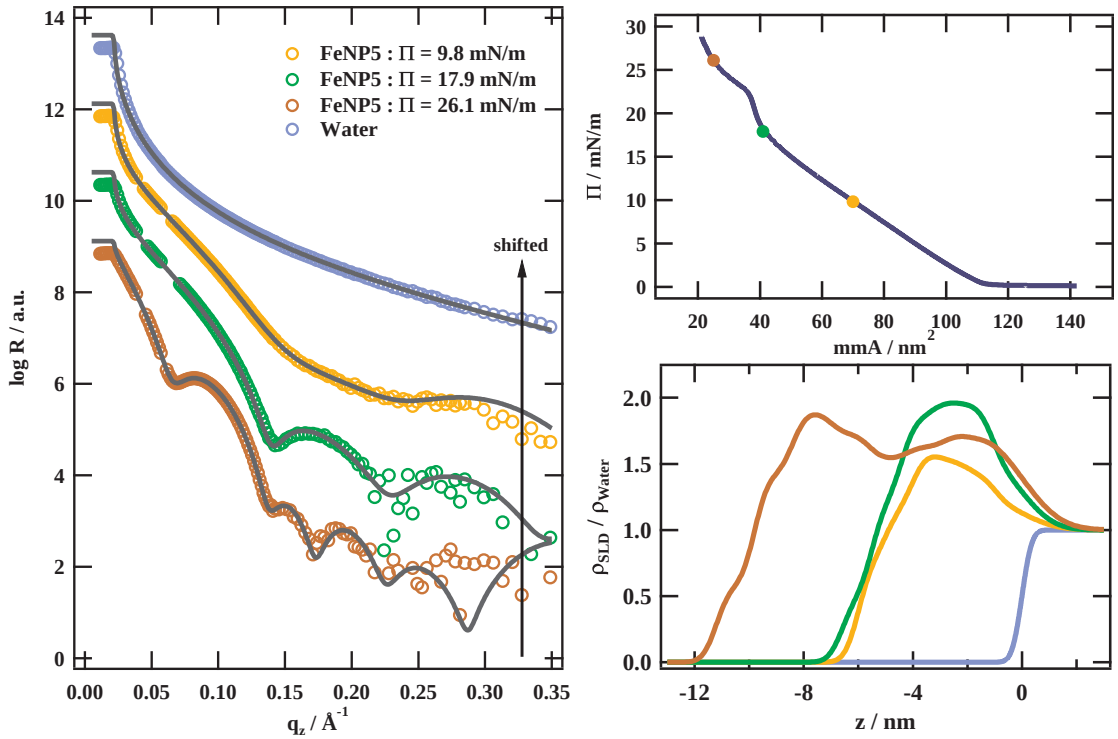

Figure 7.12: Results for the reflectivity measurement for three different positions in the isotherm (top right panel) of FeNP5 are shown with the bare water surface for comparison. In the left panel the reflectivities are plotted as shifted curves with log R over q_z. The full lines demonstrate the very good agreement of the fits to the data. The bottom right panel displays the results for the electron density profiles obtained by a box model consisting of N boxes (see text for details).

the particles in the layer are being compressed into a closely packed layer clearly demonstrated by the electron density profile and compression isotherm. The results are in good agreement with recently published data for FeNP10 nanoparticle films [17].

The specular reflectivity curve of the FeNP5 film has also been measured for three positions in the isotherm and they are shown with the reflectivity of water in the left panel of figure 7.12. The positions in the isotherm were chosen for three different surface pressures with the second and the third pressure being right before and after the phase transition in the isotherm. For a low surface pressure of 9.8 mN/m the specular reflected intensity develops a broad minimum for $0.1\,\text{Å}^{-1} < q_z < 0.25\,\text{Å}^{-1}$. Upon further compression the broad minimum separates into two different minima for the measurement at $\Pi = 17.9\,\text{mN/m}$. The position in the isotherm is just before the phase transition occurs. BAM imaging indicates that the film is densely packed on a macroscopic length scale for this position in the isotherm. After compressing the film further, the number of visible minima in the reflectivity curve increases from 2 to 4. This already indicates that the structure of the film changed in between the two measurement positions. The same electron density model from equation (7.2) is used for fitting. For a surface pressure of 9.8 mN/m six boxes ($N = 6$) with a size of $a = 1.0\,\text{nm}$ were necessary to describe the specular reflected intensity. The model for the second position ($\Pi = 17.9\,\text{mN/m}$) also consisted of six boxes ($N = 6$), however it was necessary to slightly increase their size to $a = 1.1\,\text{nm}$. After the phase transition eight boxes ($N = 8$) were necessary with a size of

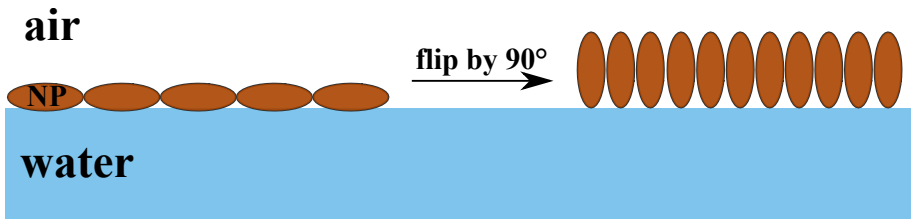

Figure 7.13: Idealized sketch for FeNP5 particles arranged at the air-water interface. During the phase transition they flip their conformation by 90° to reduce the contact area to the water interface.

$a = 1.4\,\text{nm}$ for each of them. The roughness in between the boxes remained at $\sigma = 0.4\,\text{nm}$ for all measured positions in the isotherm. The full lines in the left panel of figure 7.12 illustrates the very good agreement of the model to the experimental data. Again we see a small deviation for $q_z > 0.25\,\text{Å}^{-1}$ in the reflectivity curve of $\Pi = 26.1\,\text{mN/m}$ which is the same resolution effect described for FeNP10 film. The four minima before are perfectly described by the model.

The results for the electron density profiles are shown in the bottom right panel of the figure. For the first two positions in the isotherm the density profile resembles a gaussian shaped function for the thick disks. For the second position the electron density increases to almost two times of the one from water which has been similarly observed for FeNP10 in a highly compressed film. Compared to the profile for the spherical shaped particles in figure 7.11, the maximum is broadened while the density decreases quite fast on both flanks. The profile resembles the expected structure of thick disks oriented parallel to the water surface. The bulk scattering provided a thickness of 3 nm. With an oleic acid shell on both sides with a total thickness of roughly 2.5 nm, the overall thickness used in the model appears reasonable for this orientation. The second position illustrates a denser packed film, however the orientation of the particles is still the same. The model used for the last position in the isotherm had to change which can also be seen in the density profile. The overall thickness of the layer is around 11.2 nm and the density profile shows a broad plateau with the two flanks being similar to the ones for the lower surface pressure. The form of the profile indicates that the thick disks flip their orientation by 90° for high surface pressures. The overall thickness agrees with the diameter of 8 nm adding the oleic acid shell of roughly 2.5 nm. The transition is illustrated as a sketch in figure 7.13 in an idealized way. It is very interesting that the phase transition leads to a dense layer of flipped disks without a collapse of the layer. If multilayer structures would be formed, the density profile should not have such a broad maximum. It is also unlikely that the nanoparticle form a perfect double layer when the film breaks and its regions are pushed over each other. All results indicate that particles indeed perform a flipping process similar to the one illustrated in figure 7.13.

The three different sizes of iron oxide nanoparticles have been investigated on their ability to form uniform layer at the air-water interface. The results show that the largest particles, FeNP20, do not form a uniform particle layer but instead agglomerate into wormlike structures on a macroscopic length scale. This confirms the measurements published in reference [17]. The FeNP5 and FeNP10 particles form single uniform particle layers at the interface. A electron density model consisting of several boxes is able to describe the density profile perpendicular to the interface for both particles. The disk

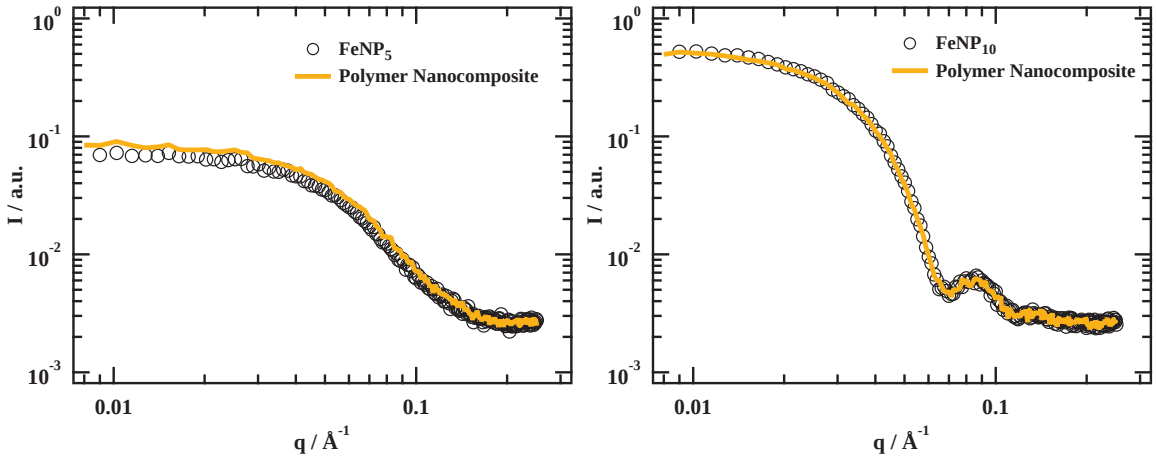

Figure 7.14: Small angle X-Ray scattering data is shown in both panels for iron oxide nanoparticles and polymer nanocomposites solved in toluene. In the left panel the scattering from FeNP5 and the nanocomposite of FeNP5 and PEG_6-*b*-P*n*BA_{132} is directly compared to verify that no particle aggregation occurs in the composite films. The right panel shows the same in case of FeNP10. The results proof that the particles do not aggregate in the nanocomposite solutions.

shaped FeNP5 particles exhibit a phase transition that can be associated to a conformation change by their orientation. They flip by 90° from flat slices with their radius parallel to the water interface to it being perpendicular to it. This study could not answer the question why FeNP20 particles are not able to form single particle films at the interface, while it was possible for FeNP5 and FeNP10. One possibility is that the particles are simply to large and they rather agglomerate into 3D structures instead of forming a thin film when the solvent evaporates. It is also possible that the magnetic properties of the particles are affected by their size. When the solvent evaporates the magnetic interaction between neighboring particles may prevent the FeNP20 particles to form a single particle film. The film structure of the three particle films could be transferred on solid substrates using the Langmuir-Blodgett technique. Afterwards, SQUID (*superconducting quantum interference device*) measurements could be performed to investigate the magnetic properties of the transferred films and they could be compared to SQUID bulk measurements on the particles.

7.3 Polymer Nanocomposite Films

The results from the previous section show that FeNP5 and FeNP10 form uniform particle films at the water interface. The idea is to mix these particles into a polymer matrix of the diblock copolymer PEG_6-*b*-P*n*BA_{132} investigated in chapter 6. The FeNP20 particles were not used for this study because they do not form a uniform layer at the air-water interface. To prepare the sample, the polymer was dissolved in a diluted solution of iron oxide nanoparticles in chloroform so that for each particle roughly 7 polymer chains in case of FeNP5 and 21 in case of FeNP10 are in the solution. The concentrations were chosen in a way that the particle area fraction is comparable for the two systems. The projected area of the FeNP10 spheres is around 2...3 times larger than the projected area of the thick disks. The solution were completely black due to the nanoparticles. Before

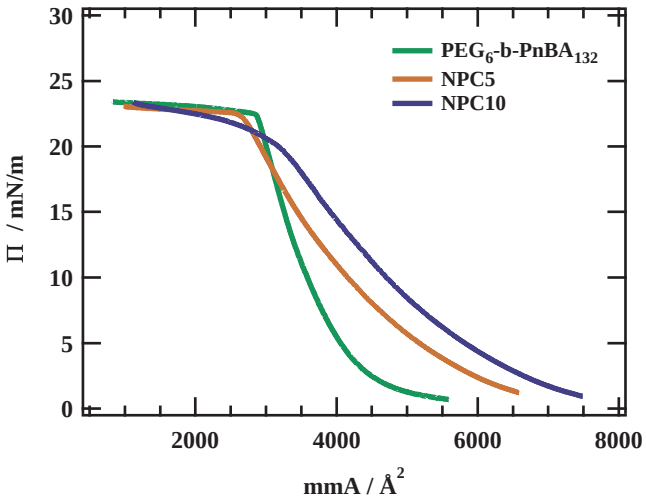

Figure 7.15: Langmuir isotherms as surface pressure Π vs mean molecular area mmA are shown for the diblock copolymer PEG_6-*b*-P*n*BA_{132} and the nanocomposite films the diblock combined with FeNP5 (NPC5) and FeNP10 (NPC10). mmA was corrected in case of the composite films so that it is equivalent to the area of a polymer chain in the film.

preparing the Langmuir films, SAXS experiments were performed to make sure that particles do not aggregate in the polymer nanoparticle solution. The solvent was exchanged to toluene and the solutions were measured with the setup described in chapter 4.3. Figure 7.14 shows the scattering of the polymer nanoparticle solutions for FeNP5 & FeNP10 directly compared to a measurement of the solution before the polymer was added. The two scattering curves are almost identical with the shape of the disk form factor for the FeNP5 composite and the sphere form factor for the FeNP10 composite. Consequently, the nanoparticles do not aggregate. The oleic acid shell prevents the aggregation even in mixtures of nanoparticles and polymers.

Langmuir Compression Isotherms

The two different polymer nanoparticle composites (NPC) were spread at the air-water interface. The sample with FeNP5 particles will be referred to as NPC5 and the one with FeNP10 as NPC10. BAM imaging was performed simultaneously to recording the Langmuir isotherms. The results for the Langmuir isotherms will be presented first before the images help to understand the macroscopic structure in the film. The Langmuir isotherms of NPC5, NPC10 and PEG_6-*b*-P*n*BA_{132} are shown in figure 7.15. In the presentation of the data the surface pressure Π is plotted over the mean molecular area (mmA) for each polymer to compare the NPC isotherms to the isotherm of the polymer. The slope of the isotherms for NPC5 and NPC10 are slightly different compared to the polymer isotherm. The NPC5 isotherm is displayed by the brown curve and the NPC10 isotherm by the blue curve. For low surface coverage the surface pressure already increases in case of the composite films but the gradient of the slope is smaller in the semi-dilute regime ($1\,mN/m < \Pi < 23\,mN/m$). The isotherm of the polymer has been discussed in detail in chapter 5 and 6. A characteristic feature is the constant pressure plateau in which the P*n*BA chains dewet from the interface. The same transition can be observed in the NPC5 composite isotherm. The crossover into the plateau almost exactly matches the area for

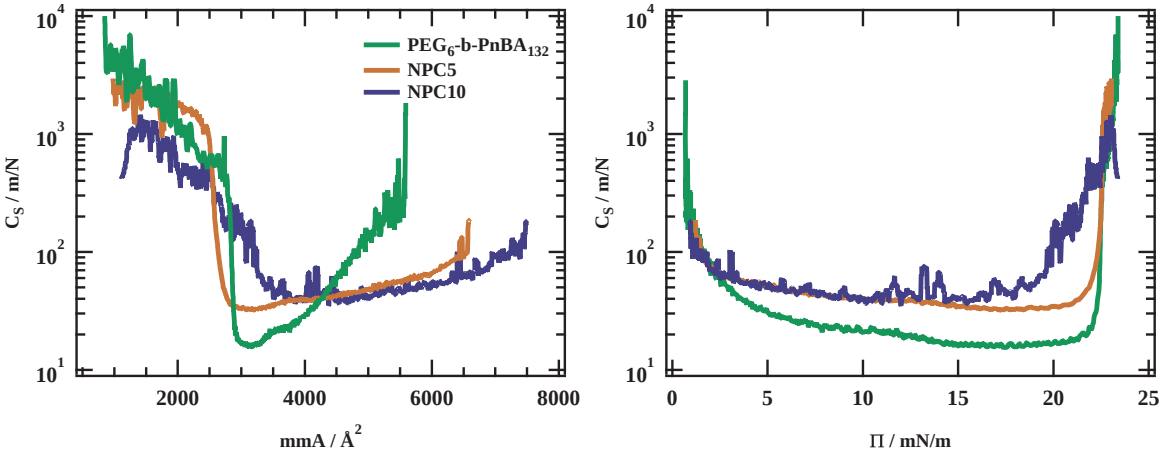

Figure 7.16: The compressibilities C_S of the PEG$_6$-*b*-P*n*BA$_{132}$ film and the two composite films (NPC5 & NPC10) are presented vs mmA in the left and Π in the right panel. The different behaviour of the composite films is visible in the right panel where C_S increases earlier before crossing into the constant pressure plateau characteristic for the pure PEG$_6$-*b*-P*n*BA$_{132}$ films.

which this happens in the pure polymer films. The surface pressure in the plateau fully agrees for the NPC5 and PEG$_6$-*b*-P*n*BA$_{132}$ isotherms. This verifies that the NPC5 composite indeed consist of both particle and polymer. The isotherm of NPC10 shows a slighlty different behaviour. Instead of a clear kink, the slope of the surface pressure slowly decreases. No clear plateau is observable before the record of the isotherm stops due to the limits for the barriers. However, the surface pressure does not increase to values larger than in the plateau which means NPC10 is most likely a mixture of particles and polymer too.

The compression behaviour of the films is clearly influenced by the particles in both composite films. For the NPC5 composite films the gradient of the slope is reduced, however the constant pressure plateau still remains. This is only reasonable since it can be associated to P*n*BA polymers dewetting from the interface. Upon crossing into the plateau the nanoparticles are not compressed closer together but instead the polymer chains dewet the interface as already observed in the pure PEG$_6$-*b*-P*n*BA$_{132}$ films. In case of NPC10 the particles are larger and interact earlier with each other. Therefore, the isotherm of the NPC10 composite is already affected by compressing the nanoparticles before the pressure reaches the plateau pressure of 23 mN/m which is necessary for P*n*BA chains to dewet the interface. In both cases the particles seem to be integrated into the polymer matrix for low surface pressure, however the deviation of the surface pressure for the NPC10 film indicates that FeNP10 particles might be pushed out of the matrix for this composite mixture. This statement has to be checked in the following investigations.

Compressibility

The compressibility C_S of the composite films can be directly calculated from the compression isotherms. It is shown in figure 7.16 as C_S vs mmA in the left panel and vs Π in the right panel. In the presentation of the data vs the area mmA, similar features of the compressibility can be observed for part of the composite films and the polymer film. However, it is much easier to compare the data plotted over the surface pressure Π in the

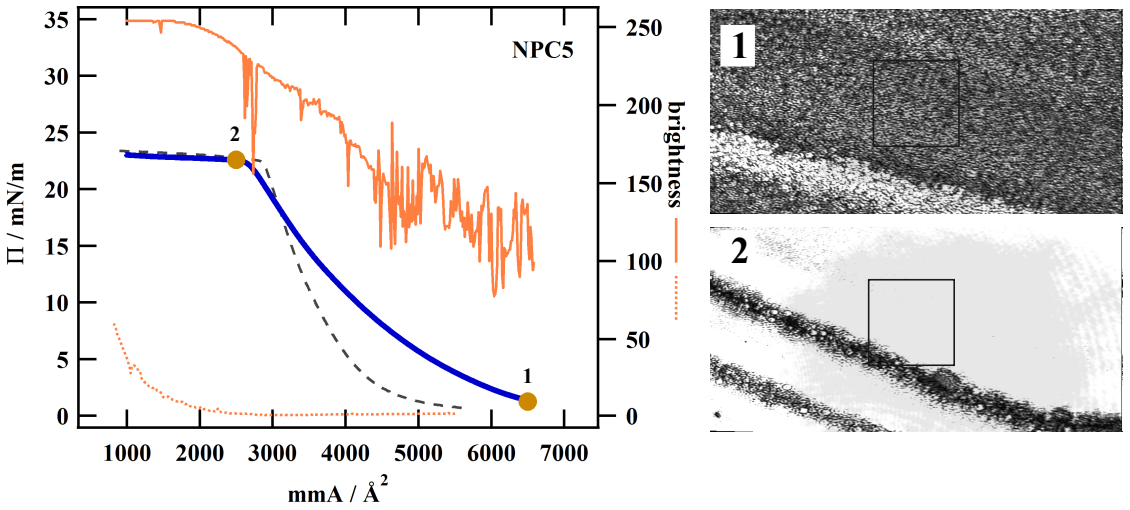

Figure 7.17: Compression isotherm of NPC5 as Π vs mmA with the mean intensity (scale 0...255) averaged over a frame of $(150\,x\,150)\,\mu m^2$ shown vs the right axis. The dotted black line is the isotherm of the pure polymer film with its brightness in orange points at the bottom. The reflected p-polarized intensity shows a complete different behaviour compared to the pure polymer film. It increases steadily from 120 until reaching its maximum value after the isotherm is already in the plateau regime. The first image on the right hand side represents the region for a low surface pressure while the second image was taken right after crossing into the plateau.

right panel. Here, two different observations can be reported. By directly comparing the compressibility of NPC5 & NPC10 the slopes are almost identical until the surface pressure reaches 15 mN/m. The absolute value of the compressibility for the two composite films is comparable to the value of the pure nanoparticle layers for medium surface pressures ($\Pi \approx 10$ mN/m). However, in case of NPC10 the compressibility fluctuates much more compared to the smooth slope of NPC5. For $\Pi > 15$ mN/m, C_S increases which could indicate that the FeNP10 nanoparticles are pushed out of the polymer matrix and remain on top of the film. The slope of C_S for FeNP5 is very similar to that of the pure polymer film. However, an offset of around $\Delta C_S \approx 16$ m/N exists between the two slopes. This indicates that the FeNP5 particles are indeed spread in the polymer matrix but it is easier compressible compared to the pure polymer film. However, once the surface pressure reaches the critical value of $\Pi \approx 23$ mN/m the P*n*BA are able to dewet from the interface and the composite film reacts as if it were a pure PEG_6-*b*-P*n*BA_{132} film.

Brightness Measurements during Compression

BAM imaging was performed simultaneously to recording the previously discussed Langmuir isotherms. The averaged intensity reflected by the film is calculated over a rectangular frame of $150x150\,\mu m^2$ illuminated by a p-polarized laser. The rectangular frame is illustrated in the picture frame on the right hand side of figure 7.17. The averaged mean intensity is displayed on the left side of the figure vs the right axis for the NPC5 film with the position for the pictures marked in the isotherm. The absolute scale for the brightness ranges between 0 and 255. The dotted black and orange lines are the isotherm of PEG_6-*b*-P*n*BA_{132} and its respective brightness. The macroscopic structure in the first image shows that the optical properties of the film are fundamentally different

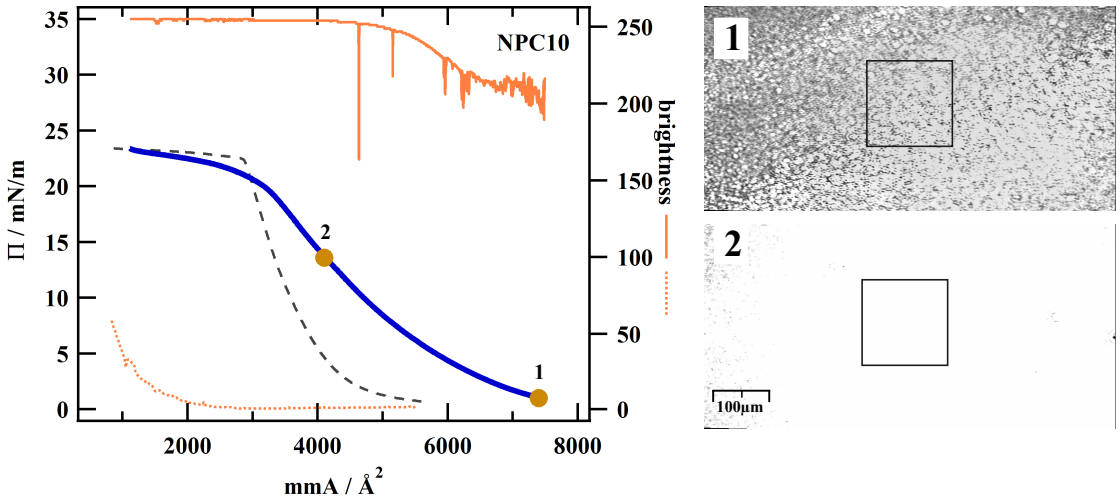

Figure 7.18: Compression isotherm of NPC10 as Π vs mmA with the mean intensity (scale 0...255) averaged over a frame of $(150\,x\,150)\,\mu m^2$ shown vs the right axis. The dashed black line is the isotherm of the pure polymer film with its brightness in orange points at the bottom. The reflected p-polarized intensity is already much higher for low surface pressures compared to the NPC5 film. The p-polarized intensity is more reflected by FeNP10. The intensity already reaches its maximum value while the surface pressure is still lower than the plateau pressure. The first image on the right hand side represents the region for a low surface pressure while the second image was taken for a surface pressure of $\Pi \approx 14\,mN/m$.

compared to the pure polymer film. However, it is also surprising that for low surface pressures the intensity is not at its maximum value right from the start as it has been observed for the pure FeNP5 films. This indicates that the composite film does not consist of regions of FeNP5 films and polymer films but instead a proper mixture of both of them. When the film is compressed the particles are closer to each other which results in an increase of the reflected intensity. The intensity increases to its maximum value after crossing into the plateau where dewetted regions of polymer also contribute to the increased reflected intensity (see figure 5.16 for comparison). In the second picture frame on the right hand side of the figure black lines are visible in the image. They might indicate that on a macroscopic length scale the nanoparticles are not equally distributed in the polymer matrix which becomes visible once the particles are compressed close to each other. The image was taken right after crossing into the plateau.

The results for BAM experiments on NPC10 are shown in figure 7.18. Again two representative images taken during compression are shown in the right panel with their positions marked in the isotherm. The mean averaged intensity from the rectangular frame is plotted vs the right axis in the plot and the dashed lines represent the isotherm of PEG_6-*b*-P*n*BA_{132} and its brightness for comparison. For low surface pressure the nanoparticles are equally distributed within the film as it can be observed in the first image in the figure. However, compared to NPC5 the overall reflected p-polarized intensity is already considerably higher for low surface pressures. Upon compression the reflected intensity is at its maximum value even before the surface pressure reaches the plateau value.

Unfortunately, it is not possible to obtain more information of the film in this regime in order to understand why the shape of the isotherm changes compared to NPC5 or the pure polymer film. The strong reflection of the film might agree with the idea of FeNP10

particles forced out of the polymer matrix as already mentioned for the compressibility measurements. In the NPC5 films the slope of the isotherm with the clear kink into the constant pressure plateau indicates that nanoparticles and polymer coexist in a mixed film. Once the plateau pressure is reached, P*n*BA chains are able to dewet the interface and the nanoparticles are not compressed any further. This might explain the similarity between the shape of the NPC5 and polymer isotherm. For NPC10, the particles change the slope of the isotherm more strongly. Particles being pushed out of the film may explain the slower increase of the surface pressure. Reflectivity measurement can help to further understand this mechanism.

Specular Reflectivity of NPC Films at the Air-Water Interface

Surface X-Ray scattering was performed for four different positions in the isotherm for both composite films. The first position was for low surface pressure, then two reflectivity measurements were performed while crossing into the constant pressure plateau and the last one for the compressed layer in the plateau. The results for the NPC5 films are shown in figure 7.19. The specular reflectivities are plotted in the left panel with the bare water surface before spreading the sample for comparison. In the right panel, the positions in the isotherm are marked in the same colour and the bottom shows the electron density profile perpendicular to the interface obtained by the model used to fit the experimental data.

In the raw data one can observe that for $q_z \approx 0.15\,\text{Å}^{-1}$ the reflectivity reduces upon compression of the film. A single or double layer model was not able to describe this so that the box model already established for FeNP particles was used for fitting. Six boxes with a size of $a = 0.9\,\text{nm}$ and a roughness of $\sigma = 0.3\,\text{nm}$ each were used as fixed parameters during the fitting. The electron density profile described in equation (7.2) was used to calculate the reflectivity by the Parratt formalism. The very good agreement of the model to the experimental data is demonstrated by the full lines. The profiles are shown in the bottom right panel of figure 7.19 with the profile for the bare FeNP5 film at low surface pressure ($\Pi = 9.8\,\text{mN/m}$) as the dashed line for comparison. The profiles for the different positions in the isotherm are quite similar, however the contrast increases upon compression of the film. Especially after the film is compressed into the plateau a clear maximum can be observed in the profile which is equally high as the one for the profile of the FeNP5 films at low surface pressure. Directly comparing the profile from the bare particle films to the composites shows that the maximum is much broader for the pure nanoparticle films. This is also reasonable for a composite film where the particles are quite homogeneously distributed in the polymer matrix. The pure polymer film has a thickness of roughly $2-3\,\text{nm}$ (see section 6.1) and an electron density similar to that of water. With FeNP5 nanoparticles distributed in the polymer matrix the electron density increases in the region close to the interface. However, for larger distances from the interface only the remaining part of the particles contributes to the average electron density because air is in between the particles for these values of z. Therefore, the average electron density is much lower compared to the pure FeNP5 film at the interface.

The measurements indicate that NPC5 forms a mixed film at the air-water interface. No information is accessible on the lateral structure of particles in the film using off-specular intensities. As already discussed before off-specular experiments are not able to help because it is not possible to separate the off-specular reflected intensities from the

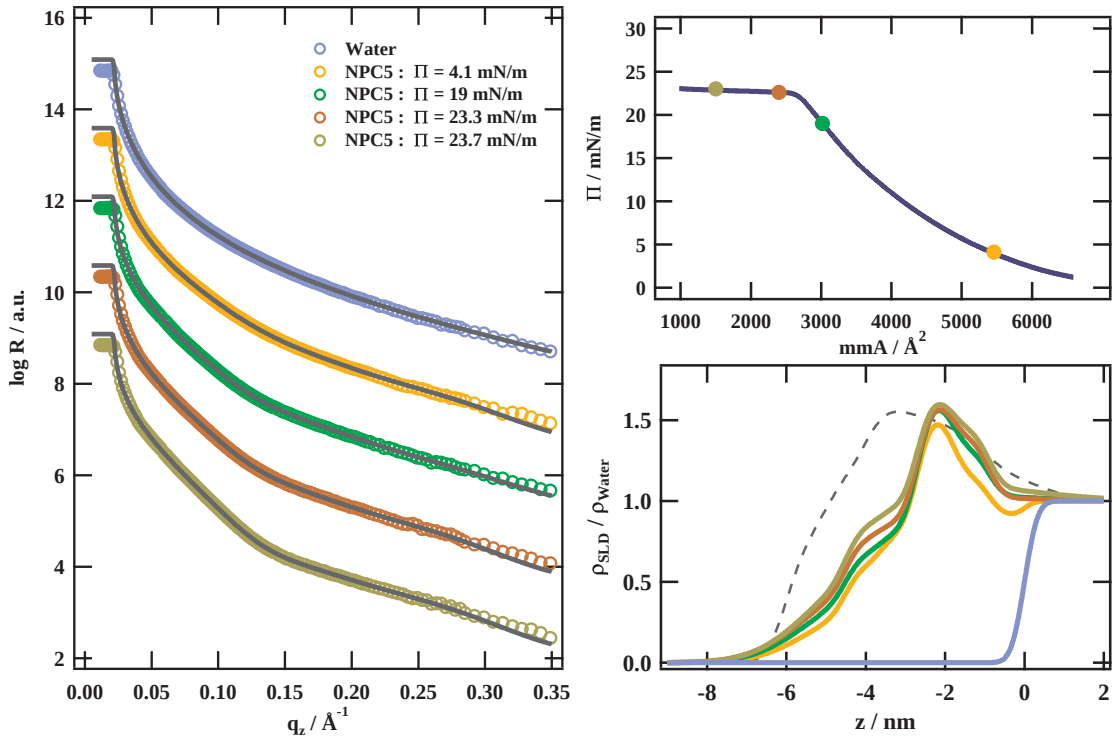

Figure 7.19: Results for the reflectivity measurement for four different positions in the isotherm (top right panel) of NPC5 are shown with the bare water surface for comparison. In the left panel the reflectivities are plotted as shifted curves with log R over q_z. The full lines demonstrate the very good agreement of the fits to the data. The bottom right panel displays the results for the electron density profiles obtained by a box model consisting of N boxes (see text for details). The dotted line represents the density profile for a FeNP5 film at low surface pressure ($\Pi = 9.8\,\mathrm{mN/m}$).

form factor of the particles. AFM measurements on transferred films may help to further increase our understanding of the distribution of particles in the film.

The reflectivity curves for the NPC10 composite film are shown in figure 7.20. In the raw data two minima get more and more pronounced upon compression of the film. The positions for the measurements are marked with the same colours in the isotherm on the top right of the figure. The model used to describe the data was the same as the one for the FeNP10 films. Eight boxes of equal size $a = 1.2\,\mathrm{nm}$ and a roughness of $\sigma = 0.4\,\mathrm{nm}$ were used in equation (7.2) for a electron density profile. The size and the roughness of the boxes were fixed in the model. The model is able to describe the experimental data very well as the full lines demonstrate in the left panel of figure 7.20. The results for the profiles are shown at the bottom right of the figure with the profile of pure FeNP10 for low pressure ($\Pi = 1.6\,\mathrm{mN/m}$) as the dashed line. As already observed for NPC5 the contrast of the film increases upon compression of the film into the plateau. The maximum of the profile is around 4 nm above the interface which agrees with the idea of the particles distributed in a polymer matrix. The two reflectivity measurements for high pressure show an increase in the density profile for a distance of $z = 5...10\,\mathrm{nm}$. This may indicate that particles are pushed out of the matrix which lead to the decrease of the slope in the isotherm while the electron density above the layer increases. However, the effect visible in the density profile is only small and cannot be clearly linked to this mechanism.

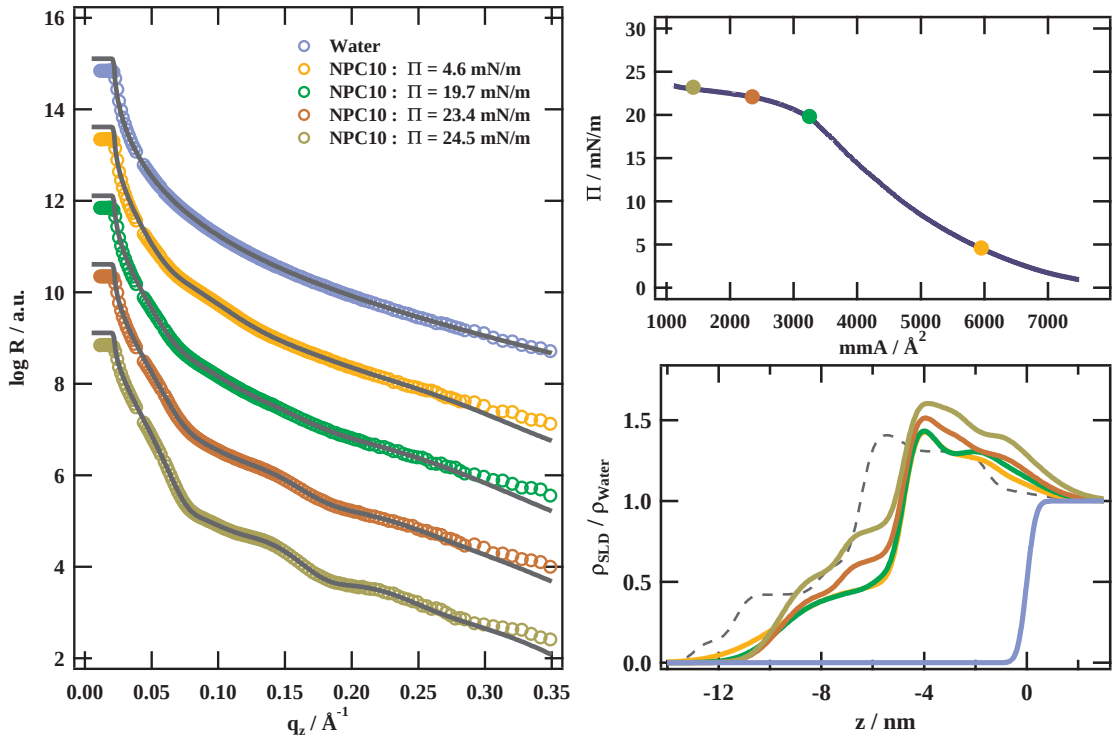

Figure 7.20: Results for the reflectivity measurement for four different positions in the isotherm (top right panel) of NPC10 are shown with the bare water surface for comparison. In the left panel the reflectivities are plotted as shifted curves with log R over q_z. The full lines demonstrate the very good agreement of the fits to the data. The bottom right panel displays the results for the electron density profiles obtained by a box model consisting of N boxes (see text for details). The dotted line represents the density profile for a FeNP10 film at low surface pressure ($\Pi = 1.6\,\mathrm{mN/m}$).

Although it would be a reasonable explanation since the entropy for mixing nanoparticles in a polymer matrix increases with decreasing particle size (see section 2.3). Therefore, it is more difficult to introduce the FeNP10 nanoparticles into a polymer matrix and with increasing surface pressure they may indeed be pushed out of the film as a reaction to the external force.

The off-specular scattering of the films may help to reveal whether particles are pushed out of the film or not. The same measurement script as already described for the P*n*BA homopolymer and diblock copolymer films was used to investigate the off-specular scattering in the vicinity of the constant pressure plateau. The first measurement position was right before the pressure reaches the plateau value and then subsequent positions were measured in the isotherm. Four different incident angles were investigated to differentiate between surface scattering and volume scattering. The raw data plotted as intensity over q_y is shown in the figure 9.3 for NPC5 and figure 9.4 for NPC10 in the appendix (chapter 9). The data shows that there is indeed off-specular intensity scattered for a q range that has also been observed for the pure polymer films. Therefore, one can expect that the polymers also dewet the interface in case of the composite films. However, after taking a closer look it becomes evident that this is only the case for NPC5 for all incident angles. For NPC10 and an incident angle of $\theta_i = 0.7\,^\circ$ there is almost no diffuse scattered intensity for this q range. This may also be due to the slower increase in surface pressure so that

the polymer chains are not able to dewet yet in the NPC10 films. The experiments started at the same surface pressure slightly lower than the plateau pressure $\Pi_c \approx 23\,\mathrm{mN/m}$ and due to the flatter slope of the isotherm the surface pressure in case of NPC10 is below the critical value for all measurement positions. The other incident angles for the NPC10 films show a maximum in a similar region which illustrates that it is almost impossible to separate the volume scattering from the particles and the off-specular scattering from the surface. Additionally, the intensity in the specular peak is also modified due to constructive or destructive interference which makes the separation between specular and off-specular intensity even more difficult. The variation of the specular peak's intensity is the same for the NPC5 films which makes it also impossible to cleanly separate the different contributions in the off-specular intensity.

The specular reflectivity on the NPC10 films also indicates that a mixed polymer and particle film exists at the air-water interface. For further characterizing its lateral structure, AFM measurements on transferred films seem to be to most suitable approach. The electron density profile of the NPC10 films indicate that for the two measurements with the highest surface pressure the profile around $5 - 9\,\mathrm{nm}$ above the interface shows a stronger increase than for the NPC5 films. This might indicate that the 10 nm particles are being pushed out of the film upon compression before the plateau pressure is reached and P*n*BA is able to dewet the interface. The increase of the stretching energy from equation (2.23) is higher for the larger particles. This may be the reason for the different behavior of the NPC5 and NPC10 composite films.

8 Conclusion

This thesis deals with the structure of polymer and polymer nanocomposite films at the air-water interface. The conformation of three polymer systems confined to the water surface was investigated using scaling theory for polymer solutions revealing three different solvent properties of the interface[7]. In the simplified picture of a two dimensional film, chain conformation can be expressed by power laws characterising the solvent properties of the air-water interface to be either good or a θ-solvent. P*n*BA based monolayers exhibit a clear phase transition in its Langmuir isotherm. The combination of in-situ and ex-situ X-Ray surface scattering as well as light scattering from the surface leads to a consistent picture of this phase transition being a mechanism of thin film dewetting from the air-water interface. Eventually, iron oxide nanoparticles that are able to form a uniform layer at the air-water interface are introduced into the polymer matrix of the dewetting film. The point of interest is whether the particles are equally distributed in the polymer matrix or phase separate and their influence on the polymer film and phase transition.

In chapter 5, the solvent properties of the air-water interface were characterised for three different polymer systems. In the first system, atactic poly(methyl methacrylate) (PMMA), the air-water interface acts as a θ-solvent. The coils adopt a flat conformation at the water interface with a Kuhn length of 0.24 nm close to the monomer size[72,78]. Upon further compression of the film, the two smaller molecular weights exhibit a phase transition: Due to their higher mobility, a folding of polymer segments into loops and tails is able to reduce the contact points with water. As a results the chain conformation at the interface changes and a plateau is visible in the isotherm. Studies on PMMA samples of different tacticity showed that the tacticity can similar alter the conformation of chains as observed for decreasing molecular weight in this work[73,77]. This consolidates the argument that mobility of the chain is the important quantity. Another observation is that large polymer chains are not well separated in the dilute regime but instead stick together in large islands. This may be related to entanglements during the preparation since it is not observed for the smallest molecular weight. For the second system, poly(2-vinylpyridine) (P2vP), the air-water interface acts as a good solvent. Handling the system was a little problematic because the solubility of P2vP is pH dependent and it is possible that part of the polymer starts to dissolve into the water subphase. The most reliable results for the power law analysis were obtained for concentration isotherms of the samples. The third system, poly(*n*-butyl acrylate) (P*n*BA) homopolymers and diblock copolymers with a small poly(ethylene glycol) (PEG) anchor attached to P*n*BA, represents the intermediate case. The air-water interface is approximately a θ-solvent for P*n*BA homopolymers. However, a remarkable effect is found for the diblocks where the Flory exponent ν grows with increasing volume fraction of PEG. The PEG block is able to tune the solvent properties in case of the diblock copolymers towards good solvent conditions. Similar to PMMA, the polymer coils adopt a flat conformation at the interface with a Kuhn length of 0.48 nm close to what has been measured for its stereoisomeric PtBA[82]. Addi-

tionally, the third polymer system showed a broad constant pressure plateau characteristic for a phase transition rarely seen in polymer films.

The focus in chapter 6 was the structural development in the phase transition of P*n*BA homopolymer and PEG-*b*-P*n*BA diblock copolymer films. In the plateau a water-free P*n*BA layer exists at the interface with the PEG block of the diblocks submerged into the subphase. X-Ray reflectometry (XRR) was performed in-situ on the films at the water surface and on films transferred on silicon wafers by the Langmuir-Blodgett technique. For both cases the film thickness in the plateau is smaller than 2 nm which is much smaller than their radius of gyration. This indicates that the films are strongly confined to the water surface. The stability of the plateau was investigated by hysteresis experiments showing that the transition is reversible apart from a small amount of polymer that is constantly removed from the film. BAM imaging on the films reveals an increasing number of islands on a macroscopic length scale upon compressing the film into the plateau. The surface pressure in the plateau is equivalent to the energy change necessary for P*n*BA chains to be removed from the water surface which indicates that the polymer is dewetting the interface. This agrees with a thermodynamic model suggesting that polymers dewet the interface, however, they are locally trapped in non equilibrium and form island like structures on a micrometer scale [30]. Details of the mechanism of dewetting are not only controlled by thermodynamics but also by the hydrodynamics of subphase and film. The mechanism was further investigated by off-specular XRR experiments. A series of measurements were performed in the constant pressure plateau revealing a roughening of the film for the diblock copolymers which manifests in a resonantly enhanced intensity of the Yoneda peak. Furthermore, the off-specular intensity is found to increase by scattering from islands of a preferred size of several micrometer. This height-height correlation function model has also been used for thin films dewetting solid substrates [42]. The island size linearly increases with volume fraction of the PEG block indicating that the mobility of the chains is important for the structure mechanism. The height of the islands is only around 1 to 2 nm. As opposed to the diblock copolymers, the P*n*BA homopolymers did not show the formation of islands in the observable q range. The underlying mechanism for the dewetting is controlled by the hydrodynamics between subphase and film. Furthermore, experiments on the kinetics of the mechanism were also performed using XRR spectra over a time scale of 10^4 s. The results show that the island size increases very slowly, however the kinetics are accelerated after 5000 s. Unfortunately, the film ruptures after 6200 s which highly restricts the available data on the kinetics. The little data indicates that the process is quite similar to the thin film breakup for 4.5 nm thick polystyrene films dewetting a silicon wafer [97]. Further experiments are necessary to confirm whether the mechanism can really be compared to the one reported for polymer dewetting solid substrates.

In chapter 7, the controlled assembly of iron oxide nanoparticles into single particle films and polymer nanocomposite films was investigated. Thick disks with a thickness of 3 nm and a radius of 4 nm as well as two different sizes of spherical particles with a radius of 6.4 nm and 10.7 nm were used in the experiments. Spread at the air-water interface, the thick disks and the 6.4 nm spheres formed uniform single particle layers while the 10.7 nm spheres agglomerated instead, which has also been reported in literature [17]. The 6.4 nm particle films can be compressed until the shells of the particles touch each other which leads to a strong increase of the surface pressure. The electron density pro-

file perpendicular to the water surface was measured by specular XRR experiments and confirms a single layer particle film with a thickness of 13 nm in agreement with the particle size from bulk scattering. The thick disks films exhibit an additional phase transition upon compression. Initially, the disks are oriented parallel to the water surface. For high surface pressures the disks flip their orientation by 90° to reduced the necessary area for each particle. The transition is confirmed by specular XRR measurements in an increase of the layer thickness from 6.8 nm to 11.2 nm being consistent with the thickness and diameter of the disks considering the shell size of 2.5 nm. The 6.4 nm spheres and the disks were both introduced into a polymer matrix of the investigated PEG_6-*b*-P*n*Ba_{132} diblock copolymer. The particles and polymers were both solved in chloroform and polymer nanocomposite films successfully formed at the air-water interface. In case of the thick disks the Langmuir isotherm, BAM imaging and XRR measurements indicate that the particles are equally distributed in the polymer matrix. The characteristic constant pressure plateau is clearly preserved and only the slope of the composite isotherm in the semi-dilute regime is slightly different compared to the pure polymer film. In case of the spherical particles the isotherm is affected stronger. The composite isotherm does not have a distinct plateau characteristic for the polymer films. It is possible that the particles are pushed out of the polymer matrix upon compression of the film. XRR measurements indicate this mechanism, however, no clear evidence was found. Still, the idea is reasonable since the entropy for mixing nanoparticles in a polymer matrix increases with decreasing size of the particles so that demixing is more likely for larger particles.

In conclusion, studying thin polymer films at the air-water interface led to important findings on the conformation of polymers under two dimensional confinement. De Gennes polymer scaling laws[7] can be extended to two dimensions and used to describe the surface pressure scaling of the films. A remarkable effect has been observed for PEG-*b*-P*n*BA diblock copolymers where the solvent properties of the interface can be tuned by the volume fractions of the blocks. A unique phase transition of polymer dewetting the water interface has been observed for PEG-*b*-P*n*BA diblock copolymers. Since the kinetics of the mechanism are not yet fully understood, dynamical measurements during the phase transition will be interesting for future investigations. Furthermore, it was shown that iron oxide nanoparticles are not only able to form uniform single particle layers at the air-water interface, but it is also possible to introduce them into a polymer matrix at the water interface. This provides the possibility of controlling the distance between the magnetic iron oxide particles in a film that can be transferred from the water interface to a solid substrate. A variety of application such as nanosensors may benefit from the possibilities emerging with these assembled structures.

9 Appendix

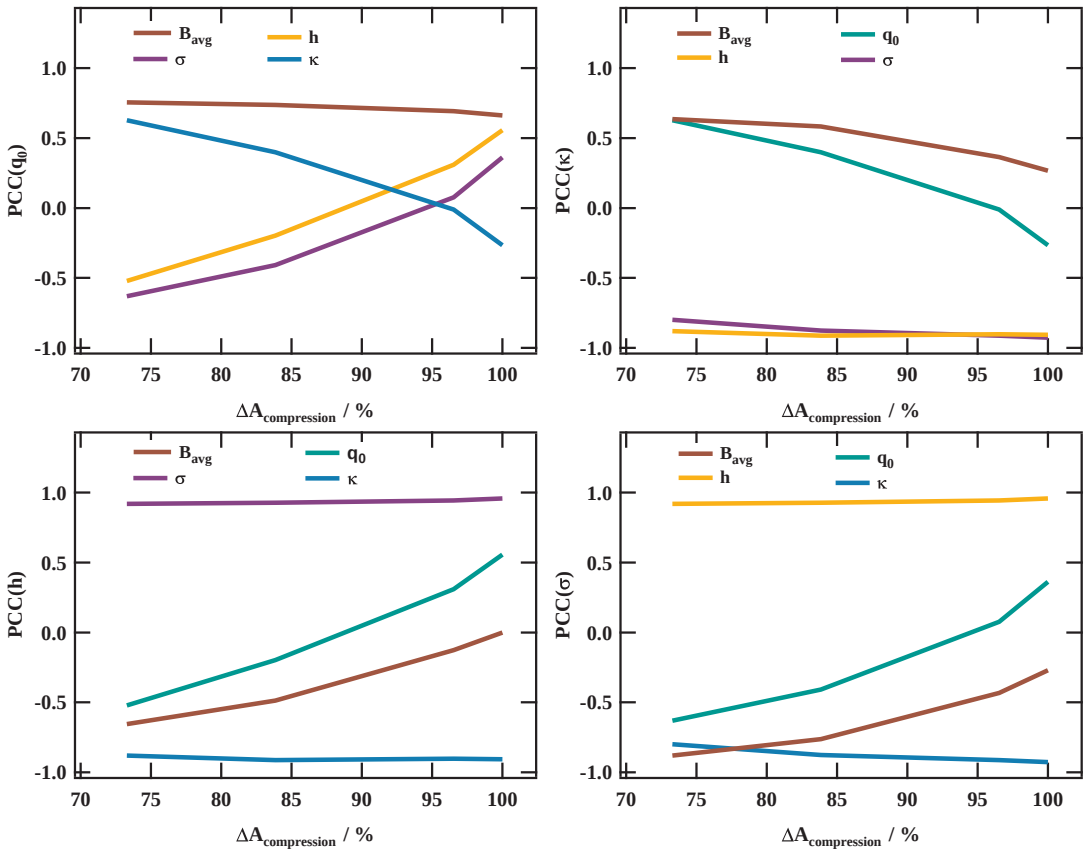

Figure 9.1: The four panels show the Pearson correlation coefficients PCC for PEG_6-*b*-P*n*BA_{132} after the experiment was moved into a new laboratory with q_0 (top left panel), κ (top right panel), h (bottom left panel) and σ (bottom right panel). The PCC shows the correlation between the fitting parameters. The coefficient ranges between -1 and 1, where 1 is total positive linear correlation, 0 is no correlation and -1 total negative linear correlation.

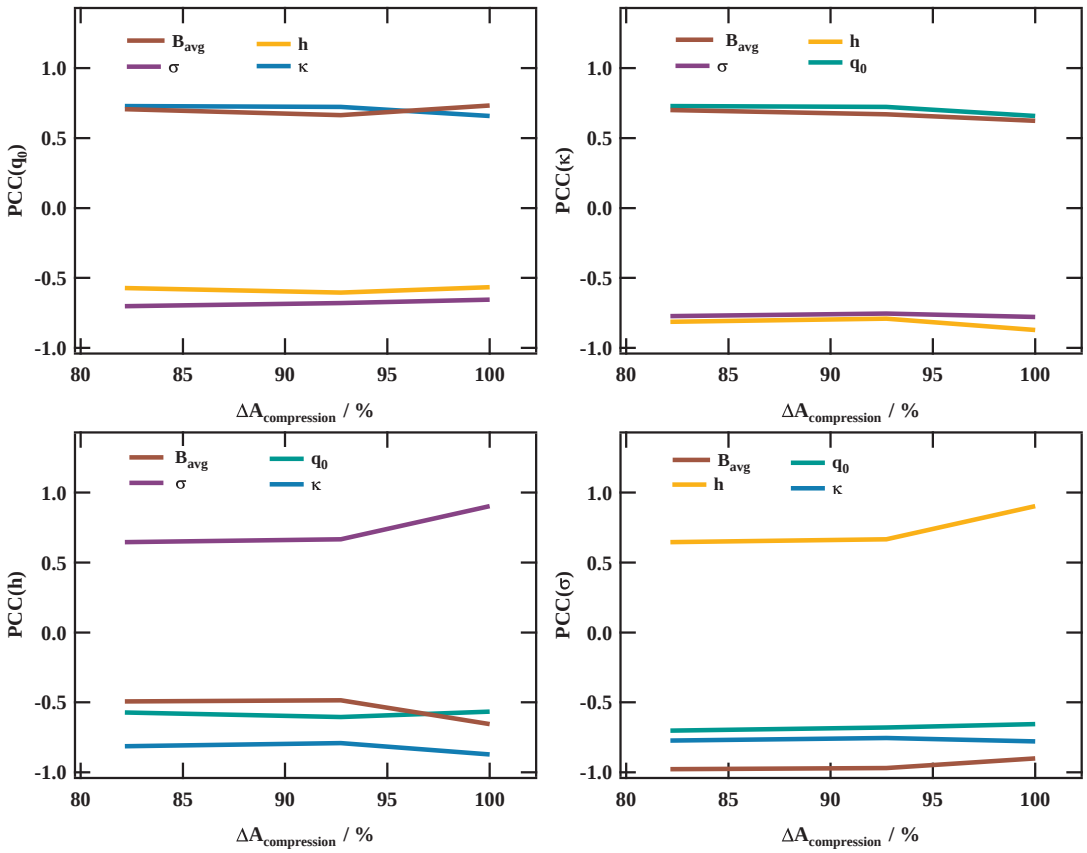

Figure 9.2: The four panels show the Pearson correlation coefficients PCC for PEG_6-*b*-P*n*BA_{224} after the experiment was moved into a new laboratory with q_0 (top left panel), κ (top right panel), h (bottom left panel) and σ (bottom right panel). The PCC shows the correlation between the fitting parameters. The coefficient ranges between -1 and 1, where 1 is total positive linear correlation, 0 is no correlation and -1 total negative linear correlation.

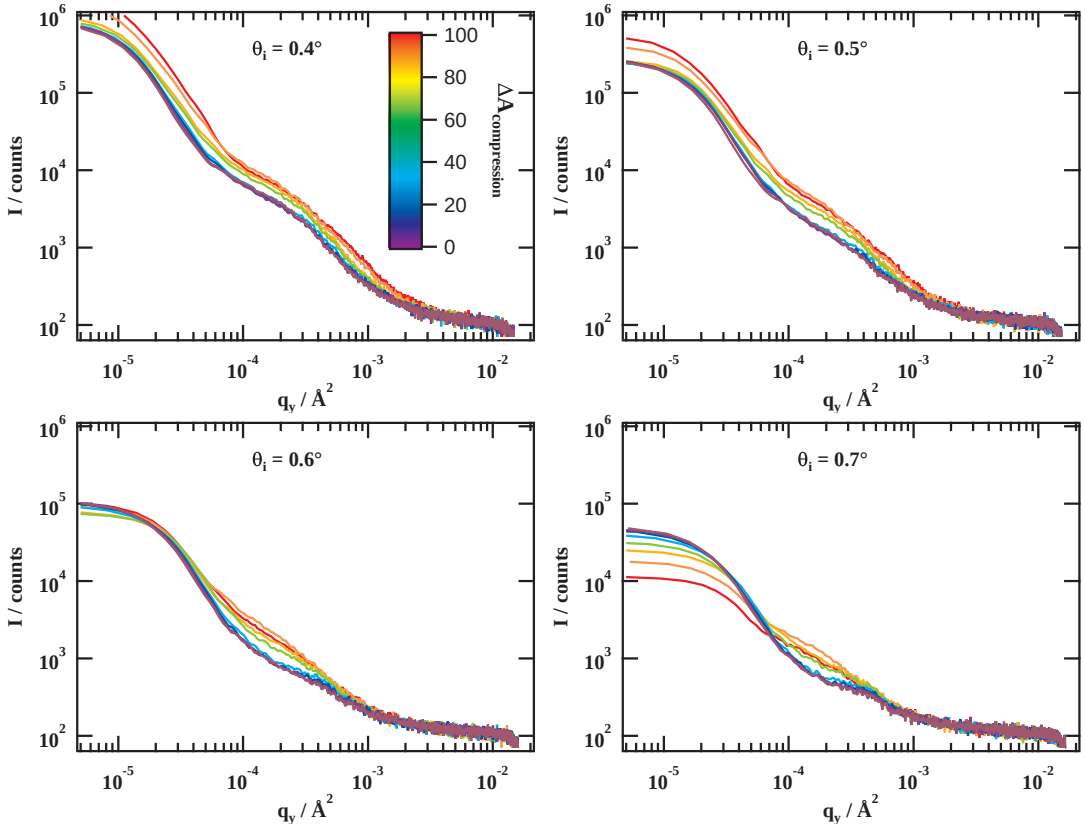

Figure 9.3: Off-specular intensity for NPC5 films vs. the in-plane scattering vector q_y for all incident angles with $\theta_i = 0.4°$ in the top left, $\theta_i = 0.5°$ in the top right, $\theta_i = 0.6°$ in the bottom left and $\theta_i = 0.7°$ in the bottom right panel. The colors refer to consecutive measuring points in the isotherm. The color scale presents the percentage of compression while the first position was measured for $\Pi \approx 18\,\mathrm{mN/m}$ just before crossing into the constant pressure plateau. The small peak visible for $\theta_i = 0.7°$ at $q_y \approx 5 \cdot 10^{-3}$ is a scattering artifact of the experiment. It is visible in all spectra for $\theta_i + \theta_f \approx 1.8°$ moving to smaller q_y with increasing θ_i (see figure 9.4).

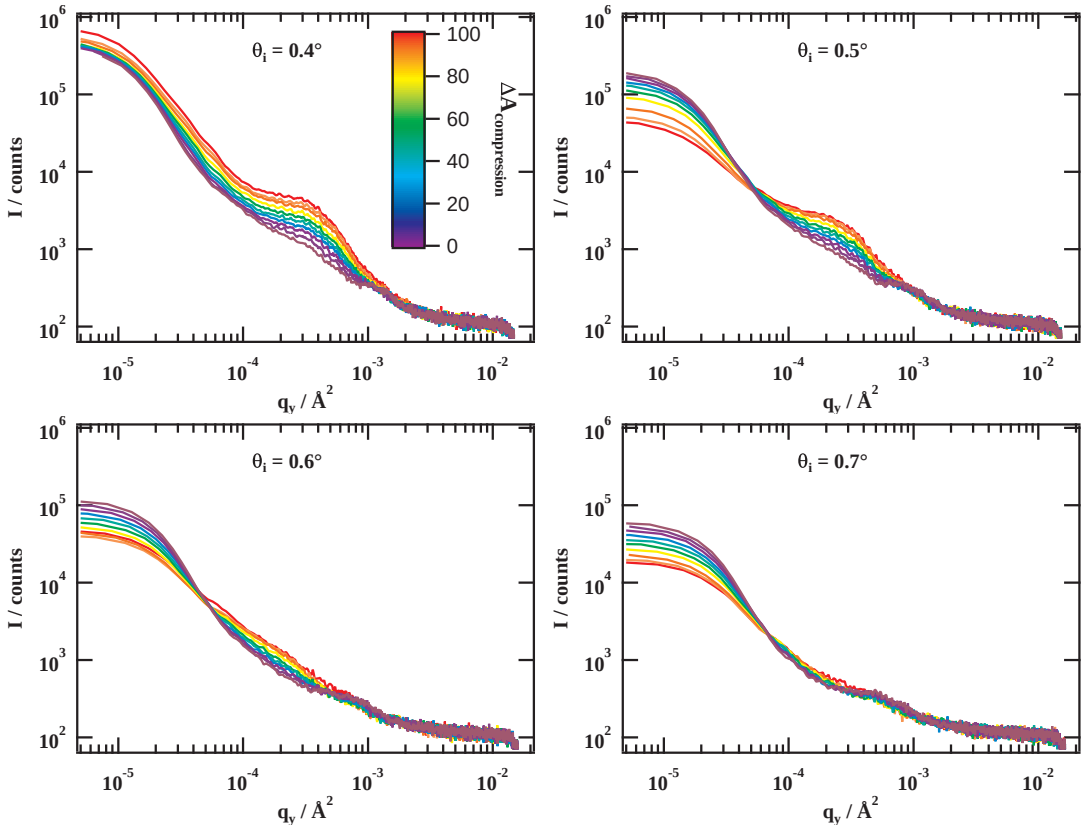

Figure 9.4: Off-specular intensity for NPC10 films vs. the in-plane scattering vector q_y for all incident angles with $\theta_i = 0.4°$ in the top left, $\theta_i = 0.5°$ in the top right, $\theta_i = 0.6°$ in the bottom left and $\theta_i = 0.7°$ in the bottom right panel. The colors refer to consecutive measuring points in the isotherm. The color scale presents the percentage of compression while the first position was measured for $\Pi \approx 18\,\mathrm{mN/m}$ with subsequent measurements comparable to the NPC5 films afterwards (the NPC10 film does not show a clear constant pressure plateau). The small peak visible for $\theta_i = 0.7°$ at $q_y \approx 1 \cdot 10^{-3}$ is a scattering artifact of the experiment. It is visible in all spectra for $\theta_i + \theta_f \approx 1.8°$ moving to smaller q_y with increasing θ_i.

Bibliography

[1] Rayleigh, Nature, 1891, **43**, 437–439.

[2] I. Langmuir, Journal of the American Chemical Society, 1917, **39**, 1848–1906.

[3] H. Zhang, R. Hao, J. K. Jackson, M. Chiao and H. Yu, Chemical Communications, 2014, **50**, 14843–14846.

[4] H. Z. Zhu, R. G. Sun, T. Zhang, C. C. Hao, P. L. Zhang, J. Wang and S. R. Li, Journal of Nanomaterials, 2015, 10.

[5] M. Kraska, M. Gallei, B. Stühn and M. Rehahn, Langmuir, 2013, **29**, 8284–8291.

[6] J. J. Giner-Casares, G. Brezesinski and H. Möhwald, Current Opinion in Colloid & Interface Science, 2014, **19**, 176 – 182.

[7] P. G. de Gennes, Scaling Concepts in Polymer Physics, Cornell University Press, 1979.

[8] M. C. Fauré, P. Bassereau, L. T. Lee, A. Menelle and C. Lheveder, Macromolecules, 1999, **32**, 8538–8550.

[9] T. J. Joncheray, K. M. Denoncourt, M. A. R. Meier, U. S. Schubert and R. S. Duran, Langmuir, 2007, **23**, 2423–2429.

[10] H. Yang, K. Shin, G. Tae and S. K. Satija, Soft Matter, 2009, **5**, 2731–2737.

[11] Y. Wang, G. Wen, S. Pispas, S. Yang and K. You, Journal of Colloid and Interface Science, 2018, **512**, 862–870.

[12] A. Watanabe and J. Kumaki, Journal of Colloid and Interface Science, 2017, **486**, 316–324.

[13] C. A. Devereaux and S. M. Baker, Macromolecules, 2002, **35**, 1921–1927.

[14] J. Als-Nielsen, D. Jacquemain, K. Kjaer, F. Leveiller, M. Lahav and L. Leiserowitz, Physics Reports, 1994, **246**, 251–313.

[15] M. Pauly, B. P. Pichon, P. Panissod, S. Fleutot, P. Rodriguez, M. Drillon and S. Begin-Colin, J. Mater. Chem., 2012, **22**, 6343–6350.

[16] S. Bedanta and W. Kleemann, Journal of Physics D: Applied Physics, 2009, **42**, 013001.

[17] A. Vorobiev, A. Khassanov, V. Ukleev, I. Snigireva and O. Konovalov, Langmuir, 2015, **31**, 11639–11648.

[18] C. Stefaniu, M. Chanana, D. Wang, D. V. Novikov, G. Brezesinski and H. Möhwald, ChemPhysChem, 2010, **11**, 3585–3588.

[19] V. Padmanabhan, A. Frischknecht and M. Mackay, Macromolecular Theory and Simulations, 2012, **21**, 98–105.

[20] B. Kuttich, A.-K. Grefe and B. Stühn, Soft Matter, 2016, **12**, 6400–6411.

[21] R. A. Jones, Soft Condensed Matter, Oxford University Press Inc., 2002.

[22] I. W. Hamley, The physics of block copolymers, Oxford University Press Inc., 1998.

[23] G. Strobl, The Physics of Polymers, Springer-Verlag Berlin Heidelberg, 2007.

[24] M. Kleman and O. D. Lavrentovich, Soft Matter Physics: An Introduction, Springer-Verlag New York, 2003.

[25] I. W. Hamley, Introduction to Soft Matter - Revised Edition: Synthetic and Biological Self-Assembling Materials, John Wiley & Sons, Ltd, 2007.

[26] V. M. Kaganer, H. Möhwald and P. Dutta, Rev. Mod. Phys., 1999, **71**, 779–819.

[27] K. N. Witte, J. Hur, W. Sun, S. Kim and Y.-Y. Won, Macromolecules, 2008, **41**, 8960–8963.

[28] J. des Cloizeaux, J. Phys. France, 1975, **36**, 281–291.

[29] A. R. Esker, C. Kim and H. Yu, Polymer Monolayer Dynamics, Springer, Berlin, Heidelberg, 2007, pp. 59–110.

[30] K. N. Witte, S. Kewalramani, I. Kuzmenko, W. Sun, M. Fukuto and Y.-Y. Won, Macromolecules, 2010, **43**, 2990–3003.

[31] I. Teraoka, Polymer Solutions: An Introduction to Physical Properties, 2002.

[32] B. P. Binks, Current Opinion in Colloid & Interface Science, 2002, **7**, 21 – 41.

[33] B. S. Murray and R. Ettelaie, Current Opinion in Colloid & Interface Science, 2004, **9**, 314–320.

[34] N. Zhongwei, J. He, T. P. Russell and Q. Wang, Angewandte Chemie International Edition, 2010, **49**, 10052–10066.

[35] P. G. de Gennes, Rev. Mod. Phys., 1985, **57**, 827–863.

[36] S. Chandran, N. Begam and J. K. Basu, Journal of Applied Physics, 2014, **116**, 222203.

[37] T. V. M. Ndoro, E. Voyiatzis, A. Ghanbari, D. N. Theodorou, M. C. Böhm and F. Müller-Plathe, Macromolecules, 2011, **44**, 2316–2327.

[38] A. Jayaraman and K. S. Schweizer, Macromolecules, 2008, **41**, 9430–9438.

[39] N. Stribeck, X-Ray Scattering of Soft Matter, Springer, 2007.

[40] R.-J. Roe, Methods of X-Ray and Neutron Scattering in Polymer Science, Oxford University Press, 2000.

[41] A. Guinier, X-Ray Diffraction in crystals, imperfect crystals, and amorphous bodies, Dover Books on Physics, 1963.

[42] M. Tolan, O. H. Seeck, J. P. Schlomka, W. Press, J. Wang, S. K. Sinha, Z. Li, M. H. Rafailovich and J. Sokolov, Physical Review Letters, 1998, **81**, 2731–2734.

[43] Abelès, Florin, Ann. Phys., 1950, **12**, 596–640.

[44] L. G. Parratt, Phys. Rev., 1954, **95**, 359–369.

[45] M. Tolan, X-Ray Scattering from Soft-Matter Thin Films, Springer-Verlag, 1999.

[46] K. Heinz, Annalen der Physik, 1931, **402**, 715–768.

[47] A. Gibaud and S. Hazra, Current Science, 2000, **78**, 1467–1477.

[48] S. K. Sinha, E. B. Sirota, S. Garoff and H. B. Stanley, Physical Review B, 1988, **38**, 2297–2311.

[49] G. Palasantzas and J. Krim, Phys. Rev. B, 1993, **48**, 2873–2877.

[50] G. Palasantzas, Phys. Rev. B, 1993, **48**, 14472–14478.

[51] G. Palasantzas, Phys. Rev. B, 1994, **49**, 10544–10547.

[52] A. Braslau, P. S. Pershan, G. Swislow, B. M. Ocko and J. Als-Nielsen, Phys. Rev. A, 1988, **38**, 2457–2470.

[53] M. K. Sanyal, S. K. Sinha, K. G. Huang and B. M. Ocko, Physical Review Letters, 1991, **66**, 628–631.

[54] D. K. Schwartz, M. L. Schlossman, E. H. Kawamoto, G. J. Kellogg, P. S. Pershan and B. M. Ocko, Phys. Rev. A, 1990, **41**, 5687–5690.

[55] B. M. Ocko, X. Z. Wu, E. B. Sirota, S. K. Sinha and M. Deutsch, Phys. Rev. Lett., 1994, **72**, 242–245.

[56] M. P. Gelfand and M. E. Fisher, Physica A: Statistical Mechanics and its Applications, 1990, **166**, 1 – 74.

[57] D. Beysens and M. Robert, The Journal of Chemical Physics, 1987, **87**, 3056–3061.

[58] Y. F. Yano and T. Iijima, J. Chem. Phys., 2000, **112**, 9607–9616.

[59] J. Daillant and O. Belorgey, The Journal of Chemical Physics, 1992, **97**, 5824–5836.

[60] S. Hénon and J. Meunier, Review of Scientific Instruments, 1991, **62**, 936–939.

[61] D. Hönig and D. Moebius, The Journal of Physical Chemistry, 1991, **95**, 4590–4592.

[62] S. R. Palit, Nature, 1956, **177**, 1180–1180.

[63] D. Gómez-Díaz and J. M. Navaza, Journal of Chemical & Engineering Data, 2004, **49**, 1406–1409.

[64] Y. Maham, A. Chevillard and A. E. Mather, J. Chem. Eng. Data, 2004, **49**, 411–415.

[65] M. Kraska, Mesostructures at the liquid/gas interface, Verlag Dr. Hut, Dissertation, Technische Universität Darmstadt, 2013.

[66] K.-P. Chao and S. L. Biswal, Langmuir, 2014, **30**, 4236–4242.

[67] A. Nelson, Journal of Applied Crystallography, 2006, **39**, 273–276.

[68] T. C. Huang, H. Toraya, T. N. Blanton and Y. Wu, Journal of Applied Crystallography, 1993, **26**, 180–184.

[69] B. Kuttich, I. Grillo, S. Schottner, M. Gallei and B. Stühn, Soft Matter, 2017, **13**, 6709–6717.

[70] C. Appel, M. Kraska, C. Rüttiger, M. Gallei and B. Stühn, Soft Matter, 2018, **14**, 4750–4761.

[71] R. Vilanove and F. Rondelez, Physical Review Letters, 1980, **45**, 1502–1505.

[72] A. Maestro, F. Ortega, R. G. Rubio, M. A. Rubio, J. Krägel and R. Miller, The Journal of Chemical Physics, 2011, **134**, 104704.

[73] W.-P. Hsu, Y.-L. Lee and S.-H. Liou, Applied Surface Science, 2006, **252**, 4312 – 4320.

[74] T. J. Joncheray, S. A. Bernard, R. Matmour, B. Lepoittevin, R. J. El-Khouri, D. Taton, Y. Gnanou and R. S. Duran, Langmuir, 2007, **23**, 2531–2538.

[75] H. M. Hilles, M. Sferrazza, F. Monroy, F. Ortega and R. G. Rubio, J Chem Phys, 2006, **125**, 074706.

[76] U. Borchert, U. Lipprandt, M. Bilang, A. Kimpfler, A. Rank, R. Peschka-Süss, R. Schubert, P. Lindner and S. Förster, Langmuir, 2006, **22**, 5843–5847.

[77] J. Miñones, M. M. n. Conde, E. Yebra-Pimentel and J. M. Trillo, The Journal of Physical Chemistry C, 2009, **113**, 17455–17463.

[78] Polymer Handbook, ed. J. Brandrup and E. Immergut, John Wiley & Sons, 3rd edn, 1989.

[79] R. Charlson and H. Rodhe, Nature, 1982, **295**, 683–685.

[80] Z. Xu, N. B. Holland and R. E. Marchant, Langmuir, 2001, **17**, 377–383.

[81] A. Malzert, F. Boury, P. Saulnier, J. P. Benoît and J. E. Proust, Langmuir, 2001, **17**, 7837–7841.

[82] A. Maestro, H. M. Hilles, F. Ortega, R. G. Rubio, D. Langevin and F. Monroy, Soft Matter, 2010, **6**, 4407–4412.

[83] D. J. Crisp, Journal of Colloid Science, 1946, **1**, 49–70.

[84] H. Lee, D. H. Kim, H. W. Park, N. A. Mahynski, K. Kim, M. Meron, B. H. Lin and Y. Y. Won, Journal of Physical Chemistry Letters, 2012, **3**, 1589–1595.

[85] H. Lee, D. H. Kim, K. N. Witte, K. Ohn, J. Choi, B. Akgun, S. Satija and Y. Y. Won, Journal of Physical Chemistry B, 2012, **116**, 7367–7378.

[86] G. T. Gavranovic, J. M. Deutsch and G. G. Fuller, Macromolecules, 2005, **38**, 6672–6679.

[87] D. J. Crisp, Journal of Colloid Science, 1946, **1**, 161–184.

[88] H. Lee, V. Tsouris, Y. Lim, R. Mustafa, J. Choi, Y. H. Choi, H. W. Park, M. Meron, B. H. Lin and Y. Y. Won, Soft Matter, 2014, **10**, 3771–3782.

[89] N. M. Ahmad, P. A. Lovell and S. M. Underwood, Polymer International, 2001, **50**, 625–634.

[90] F. Monroy, L. R. Arriaga and D. Langevin, Physical Chemistry Chemical Physics, 2012, **14**, 14450–14459.

[91] A. Wesemann, H. Ahrens, R. Steitz, S. Förster and C. A. Helm, Langmuir, 2003, **19**, 709–716.

[92] J. K. Cox, K. Yu, B. Constantine, A. Eisenberg and R. B. Lennox, Langmuir, 1999, **15**, 7714–7718.

[93] E. Penzel and N. Goetz, Die Angewandte Makromolekulare Chemie, 1990, **178**, 191–200.

[94] Y. Yoneda, Physical Review, 1963, **131**, 2010–2013.

[95] P. Croce and L. Névot, Rev. Phys. Appl. (Paris), 1976, **11**, 113–125.

[96] L. Névot and P. Croce, Rev. Phys. Appl. (Paris), 1980, **15**, 761–779.

[97] R. Xie, A. Karim, J. F. Douglas, C. C. Han and R. A. Weiss, Physical Review Letters, 1998, **81**, 1251–1254.

[98] S. Ralf, H. Stephan, N. Chiara, S. Stefan, P. Daniel, K. Renate, M. Hubert and J. Karin, Journal of Physics: Condensed Matter, 2005, **17**, S267.

[99] M. M. Schmauch, S. R. Mishra, B. A. Evans, O. D. Velev and J. B. Tracy, ACS Applied Materials & Interfaces, 2017, **9**, 11895–11901.

Publications

1. Christian Appel, Martin Kraska, Christian Rüttiger, Markus Gallei and Bernd Stühn, *Crossover from Semi-dilute to Densely Packed Thin Polymer Films at the Air-Water Interface and Structure Formation at Thin Film Breakup*, Soft Matter, 2018, **14**, 4750-4761.

2. Augustin Picco, Martin Kraska, Haiko Didzoleit, Christian Appel, Gustavo Silbestri, Omar Azzaroni, Bernd Stühn and Marcelo Ceolin, *On the supramacromolecular structure of core-shell amphiphilic macromolecules derived from hyperbranched polyethyleneimine*, Journal of Colloid and Interface Science, 2014, **436**, 243-250.

Curriculum vitae

Personal information

Name	Christian Appel
Birthday/ place of birth	01. January 1989 in Seligenstadt
Marital status	single
Nationality	german

Academic education

Nov. 2014 - Mar. 2018	Post-graduate student, TU Darmstadt, Germany
Oct. 2014	Master of Science (Physics), TU Darmstadt, Germany
Oct. 2012 - Oct. 2014	Physics studies, TU Darmstadt, Germany
Sep. 2012	Bachelor of Science (Physics), TU Darmstadt, Germany
Oct. 2009 - Sep. 2012	Physics studies, TU Darmstadt, Germany
Jul. 2008	Abitur, Einhard Gymnasium Seligenstadt, Germany

Practical work

Nov. 2014 -	Scientific staff member Institut für Festkörperphysik TU Darmstadt
Feb. 2014 - Apr. 2014	Internship Vacuumschmelze GmbH & Co. KG, Hanau, Germany
Feb. 2011 - Oct. 2014	Student assistant
Aug. 2008 - Apr. 2009	Civilian service